Variational data assimilation of satellite remote sensing observations for improving methane simulations in chemical transport models

by

Ilya Stanevich

A thesis submitted in conformity with the requirements
for the degree of Doctor of Philosophy
Department of Physics
University of Toronto

Abstract

Variational data assimilation of satellite remote sensing observations for improving methane simulations in chemical transport models

Ilya Stanevich
Doctor of Philosophy
Department of Physics
University of Toronto
2018

Atmospheric concentrations of methane (CH_4), the second most important anthropogenic greenhouse gas, have been rapidly rising since 1850, however, the rate of increase has varied in recent decades. In order to attribute these trends, significant effort has been put into characterizing CH_4 surface emissions using inverse modelling ("top-down") approaches, which rely on the ability of chemical transport models (CTMs) to simulate atmospheric CH_4 fields. However, systematic errors in models can significantly reduce the quality of the CH_4 simulation and result in biased CH_4 emission estimates. Until now, errors in models have been poorly characterized. The objective of this thesis was to characterize and investigate the origin of the CH_4 model errors in the GEOS-Chem CTM and quantify their impact on inferred CH_4 emission estimates. The weak constraint four-dimensional variational data assimilation scheme in GEOS-Chem, together with CH_4 data from the Greenhouse gases Observing SATellite (GOSAT), were used to characterize model errors in GEOS-Chem at the horizontal resolutions of $4^\circ \times 5^\circ$ and $2^\circ \times 2.5^\circ$. Large biases in CH_4 were found in the stratosphere and in vertical transport in the troposphere at mid-latitudes. The identified errors were significantly larger at $4^\circ \times 5^\circ$ than at $2^\circ \times 2.5^\circ$. It was determined that a major cause of the biases at $4^\circ \times 5^\circ$ is excessive mixing due to increased numerical diffusion manifested in enhanced stratosphere-troposphere exchange, and stronger quasi-isentropic mixing through the edges of the "tropical pipe" and the polar vortex in the stratosphere. Coarsening of the model grid also weakened vertical transport in the troposphere due to the loss of advective air mass fluxes and

sub-grid tracer eddy mass fluxes. A key outcome of this work is the recommendation that the $4^\circ \times 5^\circ$ version of GEOS-Chem should not be used for inverse modeling of CH_4 emissions. The thesis also investigated the sensitivity of North American CH_4 emission estimates in the nested version of GEOS-Chem (at the $0.5^\circ \times 0.67^\circ$ resolution) to biases in boundary conditions from the coarse global resolution model. It was shown that biases not fully mitigated in the global CH_4 simulation could result in biases as large as 30-35% in monthly mean surface emission estimates on local to regional scales.

Acknowledgements

This work was supported by the Canadian Space Agency (CSA) through the CAFTON project, the Natural Sciences and Engineering Research Council of Canada (NSERC), and Environment and Climate Change Canada (ECCC).

The work heavily relies on the data and codes from different people, research groups and agencies. I express my gratitude to the GEOS-Chem and STILT scientific communities for maintaining their models and making them publicly available, and to Rob Parker and the University of Leicester team for providing GOSAT satellite XCH_4 retrievals. I thank the TCCON team for providing ground-based trace gas measurements and the ACE-FTS team for providing solar occultation measurements. My work also greatly benefited from the HIPPO aircraft data provided by Steven C. Wofsy, from the Environment Canada surface in situ measurements shared by Doug Worthy, from the NOAA in situ aircraft data made available by Colm Sweeney and from the NOAA in situ surface measurements provided by Arlyn Andrews.

I really appreciate helpful feedbacks and discussions on my presentations from the members of the Earth, Atmospheric and Planetary Physics Group at the University of Toronto, and especially, from all members of the Atmospheric Physics and Composition Modelling Group as well as from Saroja Polavarapu and Ray Nassar.

I am grateful to my PhD committee member Paul Kushner for his invaluable input and advice in framing my research objectives, and to my final PhD exam committee members Lori Bruhwiler, Saroja Polavarapu and Debra Wunch for exciting discussions.

Many thanks to my great PhD supervisors Kim Strong and Dylan Jones, especially, for exposing me to both the experimental and modelling research in Atmospheric Physics and Remote Sensing, for supporting me financially, for guiding me in my work, for improving my presentation and writing skills, for the chance to travel the world and meet great people, for being open and available for discussions, for their enthusiasm and for sharing life experience and advice.

The greater half of this Section would ideally be devoted to my son Darius, my wife Hanna and my mother Svetlana. Although, you already know how much I appreciate your support, patience and motivation.

Contents

List of Tables

List of Figures

List of Acronyms and Abbreviations

3D-Var	Three-dimensional variational data assimilation
4D-Var	Four-dimensional variational data assimilation
ACE-FTS	Atmospheric Chemistry Experiment - Fourier Transport Spectrometer
AGCM	Atmospheric GCM
agl	above ground level
AIRS	Atmospheric Infrared Sounder
AK	Averaging kernel
AMF	Air mass flux
AMT	Argyle, Maine Tower
BAO	Boulder Atmospheric Observatory
BC	Boundary condition
CAI	Cloud and Aerosol Imager
CFL	Courant-Friedrichs-Lewy
CMF	Convective mass flux
CrIS	Cross-track Infrared Sounder
CTM	Chemical transport model
DAS	Data Assimilation System
DO	Dansgaard-Oeschger
DOFS	Degrees of freedom for signal
ECCC	Environment and Climate Change Canada
EDAS	Eta Data Assimilation System
EDGAR	Emission Database for Global Atmospheric Research
EnKF	Ensemble Kalman Filter
Envisat	Environmental Satellite
ESMF	Earth System Modelling Framework
ESRL	Earth System Research Laboratory

FOV	Field-of-view
FTIR	Fourier transform infrared
FV	Finite volume
GCM	General circulation model
GeoCarb	Geostationary Carbon Cycle Observatory
GEOS	Goddard Earth Observing System
GFED3	Global Fire Emissions Database Version 3
GGG/GFIT	Software suite for TCCON retrievals
GMAO	Global Modelling and Assimilation Office
GMI	Global Modelling Initiative
GOES	Geostationary Operational Environmental Satellites
GOSAT	Greenhouse Gases Observing Satellite
GSFC	Goddard Space Flight Center
GSI	Gridpoint Statistical Interpolation
hAMF	Horizontal air mass flux
HIAPER	High-Performance Instrumented Airborne Platform for Environmental Research
HIPPO	HIAPER Pole-to-Pole Observations
HITRAN	High-resolution transmission molecular absorption database
HYSPLIT	Hybrid Single-Particle Lagrangian Integrated Trajectory model
IASI	Infrared Atmospheric Sounding Interferometer
ILS	Instrument line shape
ITCZ	Inter-tropical convergence zone
KF	Kalman filter
KIT	Karlsruhe Institute for Technology
L-BFGS-B	Limited-memory Broyden-Fletcher-Goldfarb-Shanno algorithm for bound-constrained optimization
LIDORT	Linearized Discrete Ordinate Radiative Transfer
LMDZ	Laboratoire de Meteorologie Dynamique (zoom)
LR	Lin and Rood (1996)
MACC-II	Monitoring Atmospheric Composition and Climate - Interim Implementation
MAESTRO	Measurement of Aerosol Extinction in the Stratosphere and Troposphere Retrieved by Occultation
MERLIN	Methane Remote Sensing Lidar Mission

MeteoSat	Meteorological satellite
MIPAS	Michelson Interferometer for Passive Atmospheric Sounding
MODIS	Moderate-resolution imaging spectroradiometer
NASA	National Aeronautics and Space Administration
NCEP	National Centers for Environmental Prediction
NH	Northern hemisphere
NIES	National Institute for Environmental Studies
NIR	Near-infrared
NOAA	National Oceanic and Atmospheric Administration
NWP	Numerical weather prediction
OCO-2	Orbiting Carbon Observatory 2
OI	Optimal interpolation
OSSE	Observing System Simulation Experiment
p.d.f.	probability density function
PBL	Planetary boundary layer
PPM	Piecewise parabolic method
QCLS	Quantum cascade laser spectrometer
QuikSCAT	Quick Scatterometer satellite
RAS	Relaxed Arakawa-Schubert
RF	Radiative forcing
RT	Radiative transfer
SC	Strong constraint
SCIAMACHY	Scanning Imaging Absorption Spectrometer for Atmospheric Cartography
SCT	South Carolina Tower
SH	Southern hemisphere
SOM	Second-order moment
SRON	Netherlands Institute for Space Research
SSM/I	Special Sensor Microwave/Imager
STE	Stratosphere-troposphere exchange
STILT	Stochastic Time-Inverted Lagrangian Transport model
SWIR	Shortwave infrared
SZA	Solar zenith angle
TAMC	Tangent and Adjoint Model Compiler

TANSO-FTS	Thermal And Near-infrared Sensor for carbon Observation Fourier Transport Spectrometer
TAO	University of Toronto Atmospheric Observatory
TCCON	Total Carbon Column Observing Network
TES	Tropospheric Emission Spectrometer
TIR	Thermal infrared
TLM	Tangent linear model
TMI	TRMM Microwave Imager
TOA	Top of the atmosphere
TRMM	Tropical Rainfall Measuring Mission
TROPOMI	TROPOspheric Monitoring Instrument
UoL	University of Leicester
UTLS	Upper troposphere lower stratosphere
vAMF	Vertical air mass flux
VMR	Volume mixing ratio
WBI	West Branch, Iowa
WC	Weak constraint
WCB	Warm conveyor belt
WGC	Walnut Grove, California

Chapter 1

Introduction

1.1 CH_4 in the Earth's atmosphere

Atmospheric methane (CH_4) plays an important role in climate and air quality. Its concentration has increased from 722 ppb in 1750 to about 1860 ppb in January 2018 (Mitchell et al., 2011; Dlugokencky, 2018). However, the recent growth rate in CH_4 has not been steady. Figure 1.1 shows the recent changes in atmospheric CH_4 concentrations since 1983. The figure indicates that the rate of atmospheric increase slowed down in the late 20^{th} century, and went to zero between 2000-2007, but has since resumed. Various scenarios have been proposed to explain the slow-down, including a decrease in oil and gas emissions (Aydin et al., 2011; Simpson et al., 2012), a decrease in rice emissions (Kai et al., 2011), and an increase in concentrations of OH (Rigby et al., 2017), the major chemical sink of CH_4. Explanations for the renewed growth rate include an increase in microbial emissions (Nisbet et al., 2016; Schaefer et al., 2016; Schwietzke et al., 2016), or more specifically anthropogenic microbial emissions (Schaefer et al., 2016; Saunois et al., 2016b), an increase in global fossil fuel emissions (Rice et al., 2016), or a decrease in OH concentrations (Rigby et al., 2017; Turner et al., 2017). This remains an active area of research, and it is possible that some combination of these various factors could be responsible.

Understanding the recent CH_4 variations may also help improve projections of future CH_4 increase. Interpreting these changes is a challenging task. It is crucial to quantify the relative contribution of changes in CH_4 sources and sinks as well as to attribute changes in emissions to either anthropogenic or natural sources. Regulating emissions can control atmospheric CH_4 loading owing to the relatively short lifetime of CH_4 (about nine years). Anthropogenic emissions are the largest source of atmospheric CH_4. Efficient policy could target anthropogenic emissions of a particular type and location. This could include

better capturing CH_4 leaks at oil and gas mining sites, or collecting CH_4 emitted from landfills. Natural CH_4 sources cannot be directly controlled. Also, there are other factors that affect natural CH_4 variability, such as the El Niño Southern Oscillation and volcanic eruptions, which have to be taken into account when investigating the impact of climate warming on changes of natural CH_4 emissions. Generally, understanding the response of natural emissions to modern climate change may also help interpret the historic CH_4 variations in paleoclimate records, which may shed some light on how the natural CH_4 budget may change in the future. These issues highlight the importance of determining and monitoring present day CH_4 emissions. CH_4 emissions cannot be directly measured at a global scale, however, indirect methods can be used to do this. One such method, referred to as inverse modelling (or the top-down approach), is employed in this thesis.

1.1.1 CH_4 properties

Atmospheric CH_4 is a typical tetrahedral molecule of the XY_4 form. Any absorption or emissions by a molecule changes its energy due to translational, rotational or vibrational motion, or electronic energy state. All types of energy, except for translational, are quantized (take certain values). Electronic transitions are very energetic and happen only in the ultraviolet and visible spectral regions. Pure rotational transitions require a small amount of energy and occur only in the far-infrared and microwave spectral regions. Vibrational transitions happen mainly in the near- to mid-infrared region and are always coupled with rotational transitions. In order for a transition to happen, when interacting with electromagnetic radiation, a molecular dipole moment has to change by a discrete amount. The CH_4 molecule does not have a permanent dipole moment and, therefore, has no pure rotational spectrum. The dipole moment is also produced by molecular vibrations, which give rise to the vibrational-rotational spectral bands. CH_4 has four normal vibrational modes: a non-degenerate symmetric stretch (ν_1), a doubly degenerate bending vibration (ν_2), a triply degenerate asymmetric stretch (ν_3) and a triply degenerate symmetric bend (ν_4). However, only two (ν_3 and ν_4) of the four normal modes create an electric dipole moment, owing to their asymmetric structure. The transition to the next vibrational energy state is associated with a change of the vibrational quantum number ν_k, where k is a normal mode, by unity ($\Delta\nu_k = \pm 1$). A vibrational transition from the ground state ($\nu_k = 0$) to the next excited state ($\nu_k = 1$) gives rise to the so-called fundamental bands in spectra. For CH_4, transitions in these bands are centred at 2917 cm^{-1}, 1534 cm^{-1}, 3019 cm^{-1} and 1306 cm^{-1} for the ν_1, ν_2, ν_3 and ν_4 normal modes, respectively. In the near- and mid-infrared regions, CH_4 also possesses a large number of overtone and

combination bands. Transitions in overtone bands occur at a multiple of the fundamental band frequency ($\Delta\nu_k \geq 2$), while transitions in combination band require simultaneous change of two different vibrational quantum numbers ν_k.

The most important band for Earth's climate is ν_4, where CH_4 acts as a greenhouse gas, absorbing terrestrial thermal infrared radiation. The ν_3 band in the mid-infrared region is less important due to significantly weaker thermal radiation in this spectral range. Overtone and combination bands always contain weaker spectral lines relative to the fundamental bands due to a smaller probability of transitions and, therefore, are also less important for terrestrial climate. Figure 1.2 shows an example of Earth's emission spectrum at the top of the atmosphere (TOA) over the Sahara Desert. The reduced radiance in the spectral band at 1306 cm^{-1} is due to the presence of CH_4 in the atmosphere.

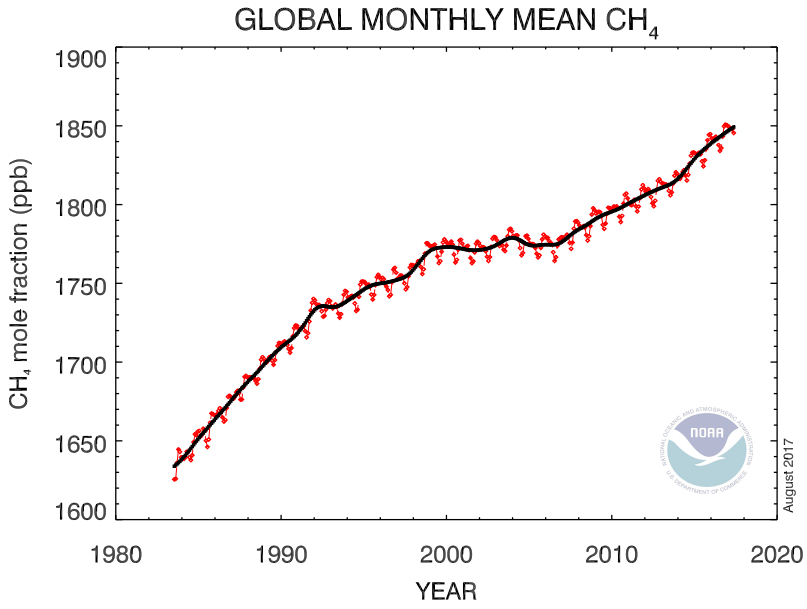

Figure 1.1: Red line: globally-averaged, monthly mean atmospheric CH_4 mole fraction based on data from the network of marine surface air sampling sites maintained by the Global Monitoring Division of NOAA's Earth System Research Laboratory (Dlugokencky et al., 1994); black line: long-term trend with seasonal cycle removed. The figure is taken from `https://www.esrl.noaa.gov/gmd/ccgg/trends_ch4/` on September 5, 2017.

CH_4 reacts with hydroxyl radicals (OH) throughout the entire atmosphere (Jacob, 1999). It also reacts with Cl radicals and excited atomic oxygen $O(^1D)$ in the stratosphere.

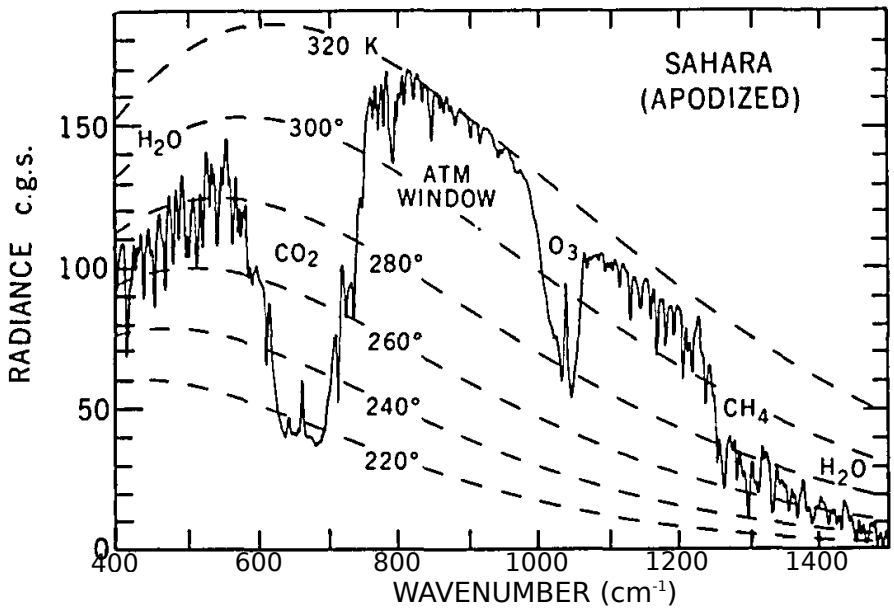

Figure 1.2: Earth's thermal emission spectrum over the Sahara Desert observed by the Nimbus 4 satellite (solid line). Blackbody radiances at different temperatures are depicted by dashed lines. Adapted from Hanel et al. (1971).

Oxidation by OH is initialized by the reactions

$$\mathrm{CH_4 + OH \longrightarrow CH_3 + H_2O} \qquad \{1.1\}$$

$$\mathrm{CH_3 + O_2 + M \longrightarrow CH_3O_2 + M} \qquad \{1.2\}$$

where M is any molecule, such as O_2 or N_2, that dissipates energy released in the reaction. The methylperoxy radical (CH_3O_2) reacts with peroxy radicals (HO_2) or nitric oxide (NO) to produce the methylhydroperoxide (CH_3OOH) or methoxy radical (CH_3O), respectively:

$$\mathrm{CH_3O_2 + HO_2 \longrightarrow CH_3OOH + O_2} \qquad \{1.3\}$$

$$\mathrm{CH_3O_2 + NO \longrightarrow CH_3O + NO_2\,\cdot} \qquad \{1.4\}$$

CH_3OOH photodissociates or is oxidized by OH:

$$\mathrm{CH_3OOH + OH \longrightarrow CH_2O + OH + H_2O} \qquad \{1.5\}$$

$$\mathrm{CH_3OOH + OH \longrightarrow CH_3O_2 + H_2O} \qquad \{1.6\}$$

$$\mathrm{CH_3OOH} + h\nu \longrightarrow \mathrm{CH_3O + OH} \qquad \{1.7\}$$

while CH_3O (including that produced in reaction (1.7) reacts with O_2:

$$CH_3O + O_2 \longrightarrow CH_2O + HO_2 \cdot \quad \{1.8\}$$

Reactions (1.5) and (1.8) produce formaldehyde (CH_2O) which also photodissociates or is oxidized by OH:

$$CH_2O + OH \longrightarrow CHO + H_2O \quad \{1.9\}$$

$$CH_2O + h\nu \xrightarrow{O_2} CHO + HO_2 \quad \{1.10\}$$

$$CH_2O + h\nu \longrightarrow CO + H_2 \cdot \quad \{1.11\}$$

Carbon monoxide (CO) is produced in reaction (1.11) as well as the reaction of CHO with the oxygen molecule (O_2)

$$CHO + O_2 \longrightarrow CO + HO_2 \quad \{1.12\}$$

and is later oxidized by OH to yield carbon dioxide (CO_2):

$$CO + OH \xrightarrow{O_2} CO_2 + HO_2 \cdot \quad \{1.13\}$$

In a high-NO_x environment, CH_4 also acts as a precursor of tropospheric ozone (O_3) as reaction (1.4) is favoured over reaction (1.3), producing NO_2. At high concentrations of NO_x, reaction of the peroxy radical (HO_2) with NO also produces NO_2,

$$HO_2 + NO \longrightarrow OH + NO_2, \quad \{1.14\}$$

which is readily photolyzed to produce O_3

$$NO_2 + h\nu \xrightarrow{O_2} NO + O_3 \cdot \quad \{1.15\}$$

Additional reaction of CH_4 with Cl and $O(^1D)$ atoms in the stratosphere yields hydrogen chloride (HCl) and OH, respectively:

$$CH_4 + Cl \longrightarrow CH_3 + HCl \quad \{1.16\}$$

$$CH_4 + O(^1D) \longrightarrow CH_3 + OH \cdot \quad \{1.17\}$$

This review above shows that in addition to being radiatively active, CH_4 is also a precursor of other greenhouse gases. In the stratosphere, CH_4 oxidation is a major source

of H_2O. In the troposphere, CH_4 oxidation is a important source of O_3, which is a harmful pollutant. Additionally, CH_4 (as well as CO) is the major sink of OH in the troposphere. Therefore, CH_4 oxidation affects the oxidative capacity of the troposphere and the ability to remove chemical pollutants. As a result, CH_4 has substantial impacts on both climate and air quality.

In terms of its radiative effect, 0.48 Wm^{-2} of additional radiative forcing (RF) since about 1750 AD is attributed directly to CH_4 (Myhre et al., 2013) (however, this value was recently revised by Etminan et al. (2016) and estimated at 0.61 Wm^{-2}) and, generally, represents the RF due to the increase in CH_4 concentrations alone from 722 ppb in 1750 to 1803 ppb in 2011. Changes in the actual CH_4 emissions since 1750 would yield a larger direct CH_4 RF of 0.641 Wm^{-2}, which also partly includes CH_4's impact on its own lifetime through the reduction of OH. Indirect RF due to CH_4 emissions would also include 0.241 Wm^{-2} due to production of tropospheric O_3, 0.07 Wm^{-2} due to production of stratospheric H_2O and 0.018 Wm^{-2} due to production of CO_2. The total emissions RF of 0.97 Wm^{-2} thus makes CH_4 the second most important anthropogenic greenhouse gas after CO_2 with a the total RF of 1.68 Wm^{-2}. While the CH_4 RF estimate has its own uncertainties, the cumulative forcing is significantly larger than the estimated average natural RF due to changes in solar irradiance since the Maunder Minimum in the 17^{th} century, which falls in the range from 0.08 to 0.22 Wm^{-2}. The impact of the CH_4 RF on Earth's climate depends on climate sensitivity and the initial climate state. However, the increase in CH_4 concentration since 1750 C.E. is assumed to be partly responsible for recent climate warming and is projected to continue in the future.

1.1.2 Origins and fate of CH_4

Unlike H_2O (or CH_4 on Titan), CH_4 under Earth's atmospheric temperatures is far from saturation pressure, and its abundance is mainly controlled by surface emissions and chemical loss. Atmospheric CH_4 is of both biogenic and non-biogenic origin, with the former sources accounting for about 70% of total emissions (Ciais et al., 2013). Biogenic CH_4 is mainly a product of metabolism of methanogenic Archaea organisms, which consume either hydrogen or acetate:

$$CH_3COOH \longrightarrow CH_4 + CO_2 \qquad \{1.18\}$$

$$CO_2 + 4\,H_2 \longrightarrow CH_4 + 2\,H_2O\,. \qquad \{1.19\}$$

Biogenic sources have natural (wetlands, oceans and termites) and anthropogenic (landfills, livestock and rice agriculture) origins. Non-biogenic sources can also be divided into

	Top-down	Bottom-up
Natural sources	231 [194–296]	384 [257–524]
Wetlands	167 [127–202]	185 [153–227]
Other sources	64 [21–132]	199 [104–297]
Freshwater (lakes and rivers)		122 [60–180]
Wild animals		10 [5–15]
Wildfires		3 [1-5]
Termites		9 [3–15]
Geological (incl. oceans)		52 [35–76]
Hydrates		2 [0-5]
Permafrost (excl. lakes and wetlands)		1 [0-1]
Anthropogenic sources	328 [259–370]	352 [340–360]
Agriculture and waste	188 [115–243]	195 [178–206]
Rice		30 [24–36]
Ruminants		106 [97–111]
Landfills and waste		59 [52–63]
Biomass burning (incl. biofuels)	34 [15–53]	30 [27–35]
Fossil fuels	105 [77–133]	120 [95-138]
Sum of sources	558 [540–568]	736 [596–884]

Table 1.1: Global CH_4 budget for 2003-2012 in Tg yr^{-1}. Reported values correspond to the mean estimates in the literature with the minimum and maximum values in square brackets. The estimates are obtained using the "top-down" and "bottom-up" approaches which are introduced in Section 1.2. Adapted from Saunois et al. (2016a).

anthropogenic (fossil fuel mining and burning and waste treatment) and natural (biomass burning and geological sources including natural seeps and volcanism). At present, the majority of CH_4 emissions (more than 50%) are of anthropogenic origin. Table 1.1 gives estimates of CH_4 emissions from different anthropogenic and natural sources.

In addition to atmospheric chemical loss, some CH_4 is also lost by oxidation in soils. According to Prather et al. (2012), CH_4 has a chemical lifetime of about 11.2 years against loss due to tropospheric OH oxidation, 150 years due to loss in the stratosphere, about 200 years against Cl oxidation, and 120 years due to soil uptake. CH_4 is well-mixed in the troposphere but not in the stratosphere. The total CH_4 emissions are constrained to within 10-15% by observations of its atmospheric growth rate and estimates of the OH budget (constrained by methyl chloroform (CH_3CCl_3) measurements) and account for about 560 Tg CH_4 yr^{-1} (Saunois et al., 2016a).

Additional CH_4 can be produced by methanogenic bacteria from the carbon stored in the Arctic permafrost soil. CH_4 is also stored in the deep ocean in the form CH_4 clathrates (icy solids with methane enclosed in the crystal structure of water) and is

hypothesized to have had a crucial impact on climate during certain periods of Earth's history, which will be discussed later. Destabilization of CH_4 clathrates and melting of permafrost, accompanied by release of massive amounts of CH_4 into the atmosphere, pose a danger for Earth's climate in the distant future (Ciais et al., 2013).

1.1.3 CH_4 natural variability and interaction with climate

CH_4 is believed to have been abundant in the early Archean atmosphere and has been proposed as a possible answer to the Faint Young Sun paradox (Kasting, 2005), which is the unresolved problem of how water in a liquid form could exist on Earth early in its history when the solar output was low (70% of the modern luminosity). Under low-O_2 conditions, the chemical lifetime of CH_4 would increase up to 10 kyr, which would allow the atmosphere to maintain high CH_4 abundances in the presence of a permanent emission source. CH_4 concentrations of about 100-1000 ppm would be required to keep temperatures above freezing, with the atmosphere containing modern concentrations of CO_2. Methanogenic bacteria have been proposed as a possible source of this CH_4 and could maintain levels of CH_4 as high as 1000 ppm. The Great Oxidation Event at about 2.3 Ga during the Paleoproterozoic, accompanied by a significant rise of O_2 in the atmosphere, destroyed much of the CH_4 in the atmosphere. This led to glaciation and plunged Earth into a cold (potentially, "snowball") climate state (Kopp et al., 2005). However, some studies also suggest the opposite, that the reduction of CH_4 biogenic emissions and weakening of the CH_4 greenhouse effect triggered the rise of O_2 (Zahnle et al., 2006). During the mid-Proterozioc era, CH_4 concentrations would have had to be higher than 100 ppmv in order to keep the Earth's temperature above the freezing point under conditions of low solar luminosity. However, as shown by Olson et al. (2016), the atmosphere could maintain CH_4 concentrations only below 10 ppm. Therefore, given that there is no geological evidence of glaciations during the mid-Proterozoic, CH_4 can not be the primary factor for sustaining the warm climate during that period, although variations in CH_4 could still have played a role in destabilizing the climate. During late neo-Proterozioc era between 650 and 635 Ma, the Earth could have been entirely covered with ice (the Marinoan glaciation). CH_4 release from destabilized low-latitude permafrost clathrates has been suggested as a possible mechanism for abrupt climate warming, which put an end to the glaciation (Kennedy et al., 2008). Another clathrate dissociation could have caused significant warming during the Late Paleocene around 55 Ma and could have taken place in the sub-tropical western North Atlantic ocean (Katz et al., 1999).

The record of modern ice core CH_4 measurements extends only to about 800 kyr before

present. However, even these measurements give a broad insight into the historical natural variability of atmospheric CH_4 and its connection to climate variations. Figure 1.3 shows Dome C (a site in East Antarctica with thick ice) records of CH_4 (Loulergue et al., 2008) and deuterium (δD) (Jouzel et al., 2007) ($\delta D = [(D/H)_{sample}/(D/H)_{standard}] - 1$) from 800 kyr to present. Here, δD is a proxy for temperature, with higher values corresponding to higher temperatures during interstadial periods and lower values being associated with cold temperatures during extended glaciation. The record shows that CH_4 varied from about 350 to 800 ppb and is highly correlated with the δD record.

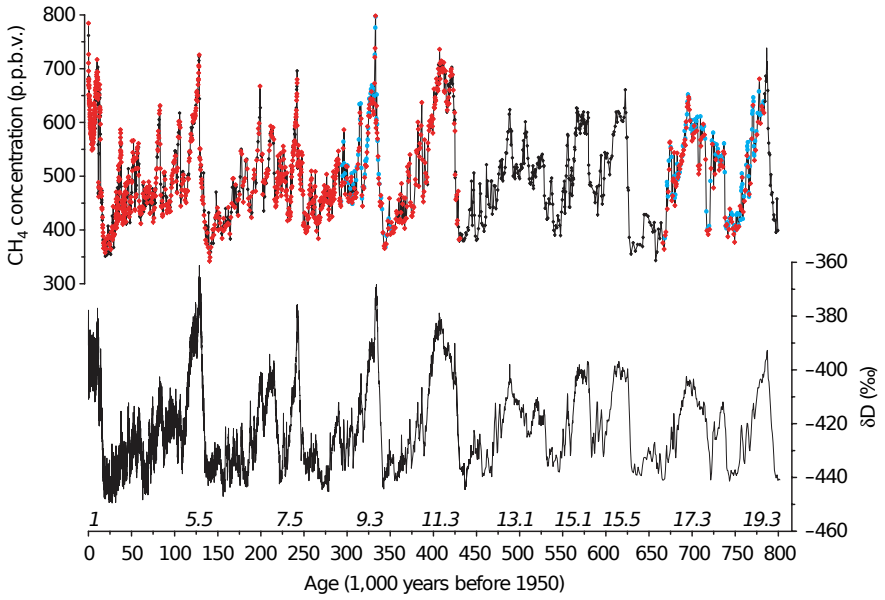

Figure 1.3: Lower panel: Dome C δD record (Jouzel et al., 2007); Upper panel: Dome C CH_4 record (different colors represent estimates from different sources). Adapted from Loulergue et al. (2008).

Figure 1.4 indicates that long-term variability was mainly dominated by variations in Earth's orbital parameters, particularly by the 100 kyr obliquity cycle and the 41 kyr axial precession cycle. It has been suggested that CH_4 variations closely follow, and were initiated by, temperature perturbations. The latter influenced the tropical monsoon system and the location of the Inter-Tropical Convergence Zone (ITCZ), which in turn affected tropical wetland emissions through changes in precipitation. An additional source of variability could have been the extent of glaciers, which controlled CH_4 emissions from periglacial wetlands.

On millenial to decadal time scales, during abrupt climate oscillations (so-called Dansgaard-Oeschger (DO) events), CH_4 changes of 50 to 200 ppb were shown to be in phase with Greenland temperatures (Severinghaus et al., 1998; Severinghaus and

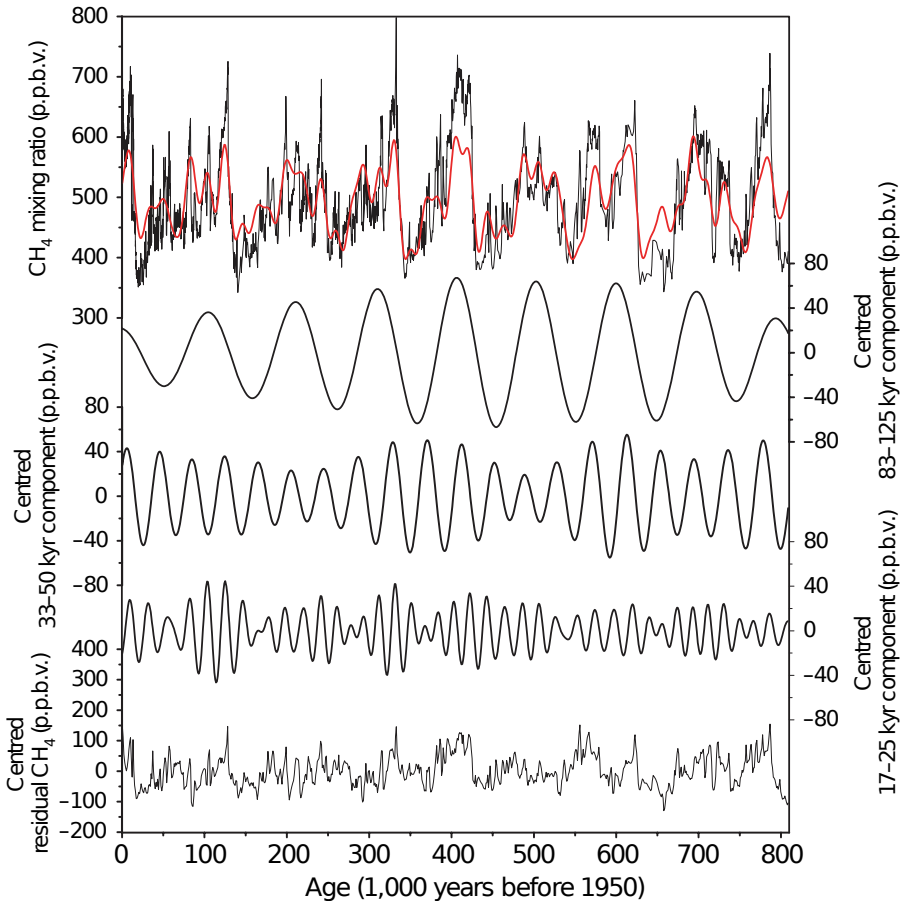

Figure 1.4: Spectal analysis of the Dome C CH_4 record: decomposition of the CH_4 timeseries into orbital components with different pediods (residuals are given in the bottom plot). The red line represents a combination of the three orbital components. Adapted from Loulergue et al. (2008).

Brook, 1999). However, modern climate models fail to explain the magnitude and origin of these CH_4 variations. In particular, neither changes in OH concentrations (Levine et al., 2012) nor changes in the Atlantic meridional overturning circulation (a trigger of DO events) causing migration of the ITCZ and altering tropical wetland emissions (Hopcroft et al., 2011) could generate the amplitude of CH_4 variations observed in the record. In regards to, at least, the last glacial period, Brook et al. (2000) also found no evidence of rapid clathrate degassing in ocean sediments. Despite relatively low CH_4 concentrations compared to the present and the absence of observational evidence that CH_4 was responsible for triggering climate perturbations during the last 800 kyr, variations in CH_4 could still have affected the evolution and magnitude of temperature changes on glacial-interglacial time scales. Nowadays, this historic CH_4 record also places a constraint on possible physical mechanisms responsible for climate variations in the past and may

shed some light on how CH_4 from natural sources may vary in a future warmer climate.

Changes in CH_4 concentrations over the past two thousand years are presented in Fig 1.5 (Etheridge et al., 1998; Mitchell et al., 2011). It shows that during the late preindustrial Holocene, between 1000 and 1800 AD, CH_4 concentrations remained at the level of about 700 ppb with small variations. From then until the present, CH_4 levels experienced an exponential rise related to increasing anthropogenic CH_4 emissions. Figures 1.3 and 1.5 suggest that current CH_4 levels are unprecedented, at least, over the last 800 kyr. This steep rise in atmospheric CH_4 due to anthropogenic activity is suggested (Bindoff et al., 2013) to be partly responsible for the observed global Earth temperature rise since the late 19^{th} century.

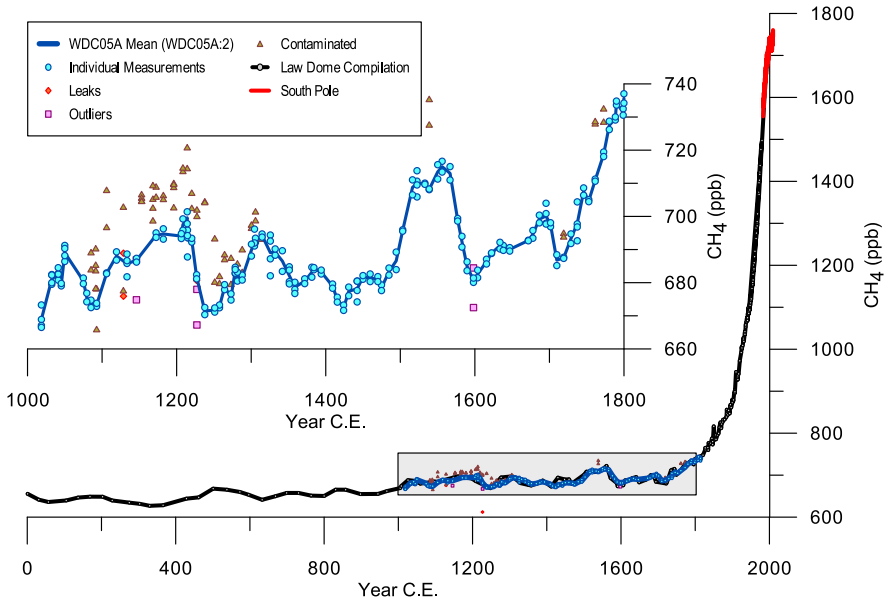

Figure 1.5: A compilation of high temporal resolution Antarctic ice core CH_4 records extending from 2 ka to present. Different colors and shapes correspond to different data sources. Adapted from Mitchell et al. (2011).

Given its current growth rate, the atmospheric abundance of CH_4 may continue to rise in the future if no measures are undertaken to limit anthropogenic emissions. If enforced, measures by emission reduction could have an immediate effect on climate due to the relatively short lifetime of CH_4. Furthermore, the global atmospheric abundance of CH_4 may increase due to wetland emissions that are consistently predicted by models to rise in a warmer climate (Zhang et al., 2017). Release of CH_4 from melting permafrost may occur later in the century if warming continues, but is not expected to be abrupt (Schuur et al., 2015). Ocean clathrate destabilization is a rather slow process that takes place on millenial time scales due to slow propagation of temperature anomalies into the deep

ocean and is unlikely to happen during the current century (Ciais et al., 2013). Potential release of CH_4 from clathrates is limited to the Arctic Ocean, north of Siberia, and the released CH_4 is expected to be converted in the ocean to CO_2, which is a significantly less efficient greenhouse gas. Potential increases in CH_4 sources may also be counteracted by greater chemical destruction by OH in a warmer climate due to increased H_2O and a positive temperature feedback of the OH reaction rate coefficient.

1.2 Atmospheric modelling

To better understand the processes driving the changes in atmospheric CH_4 concentrations, we use an inverse modeling ("top-down") approach, which uses atmospheric observations to indirectly infer sources and sinks of atmospheric CH_4. The latter can also be evaluated using a process-oriented method, referred to as the "bottom-up" approach, which identifies the bulk amount of each major CH_4 emitter and emission rates per unit quantity of each emitter type. This approach is less accurate because it relies on statistical information from the entire world and insufficient knowledge about emission rates under various conditions. Hence, it provides only an approximate estimate, which can potentially be improved using the indirect top-down approach.

The top-down approach to constrain estimates of the CH_4 budget includes several components. First, it includes CH_4 measurements at a global scale. Global coverage is currently provided only by satellite instruments, which are discussed in Section 2.1. The second component is a physical model that takes CH_4 sources and sinks as parameters and relates them to CH_4 observations. The modelling component in this thesis is discussed in Sections 2.2 and 2.3. The third component is an optimization algorithm that adjusts the magnitude of model parameters to best match observations, as described in Section 2.4.

The top-down approach relies on the ability to relate sources and sinks of atmospheric gases to observations using a numerical simulation of atmospheric transport and chemistry. The two main numerical methods used to model atmospheric transport are referred to as the Eulerian and Lagrangian approaches. In the Eulerian approach, tracer evolution is solved on a stationary discretized grid, whereas the Lagrangian method tracks the evolution of each particle following its motion. There are also hybrid approaches which combine Eulerian and Lagrangian transport. The Eulerian approach is convenient for representing the evolution of the entire atmosphere, whereas the Lagrangian approach has advantages for analyzing origins and fate of a particular ensemble of air parcels. The Lagrangian approach is also diffusion-free and is particularly useful for investigation of atmospheric mixing in the vicinity of transport barriers. Since our goal is to simulate

CH_4 concentrations at the location of numerous atmospheric observations, such as those provided by satellite instruments, we prefer the Eulerian approach over the Lagrangian one because of its computational efficiency.

1.3 Limitations of modelling tools

The ability to improve a priori CH_4 emission estimates in an inverse modeling context depends strongly on the information content of the observing system, including its spatial and temporal coverage as well as its sensitivity to vertical CH_4 distributions. However, this ability is also limited by potential biases in both model and measurements. Because CH_4 is well mixed in the troposphere, the signal of emissions at the location of satellite measurements can be rather weak (less than 1% of the total column of CH_4) depending on the type of observing system and the instrument footprint. This puts stringent requirements on the quality of the CH_4 measurements and the modelled CH_4 concentrations: the magnitude of potential biases has to be much smaller than the signal of emissions.

In this thesis, we investigate potential model biases on relatively short (monthly to seasonal) time scales. At such scales, CH_4 chemistry biases play a minor role considering that the seasonal cycle in OH concentrations is understood better than inter-annual variations, and depends primarily on the solar radiation and the abundance of atmospheric ozone and water vapour. The task then can be reduced to evaluation of model transport biases. Measurement biases will be partly discussed in Section 2.1, however, they are not the main focus of this thesis. It is worth mentioning that on long time scales, chemistry biases can either be manifested through incorrect OH fields or caused by biases in temperature fields which affect the OH reaction rate constant $k(T)$ (Fiore et al., 2006; Locatelli et al., 2015).

Chemical transport models (CTMs), which are used to simulate CH_4 abundance in the atmosphere, reduce significantly the computational time compared to general circulation models (GCMs). CTMs are driven by pre-calculated meteorological fields, which are usually archived at reduced temporal resolution due to limited storage space. These metfields may come from a free-running GCM, but are usually derived from a GCM data assimilation system, which uses atmospheric observations to mitigate the impact of model errors on the produced metfields.

A common approach to further speed up CTMs is to coarsen their horizontal or vertical resolution. However, it is relevant to note that running GCMs at coarse resolution may result in misrepresentation of key aspects of atmospheric dynamics (Roeckner et al., 2006;

Rind et al., 2007; Richter et al., 2014). For example, Jablonowski and Williamson (2006) show that at $4^\circ \times 5^\circ$ resolution, a GCM does not capture the evolution of baroclinic waves and starts to converge only at $1^\circ \times 1.25^\circ$. The question of computational time is of significant importance in data assimilation for the purposes of estimating surface emissions of atmospheric gases. The four-dimensional variational data assimilation method (4D-Var) extensively used in the carbon cycle community to constrain surface emissions of greenhouse gases (CO_2, CH_4) is based on an iterative algorithm that integrates the model forward and backward in time repeatedly until the optimal solution is reached; it would be costly to run at high spatial resolution. For example, doubling the model resolution from $4^\circ \times 5^\circ$ to $2^\circ \times 2.5^\circ$ in this thesis increased computational time approximately 4.5 times.

Transport biases can come from errors in the original assimilated GCM metfields, or be native to CTMs. First, the assimilated winds that drive CTMs represent the mean meteorological state, while their uncertainty is not taken into account. Meanwhile, meteorological uncertainty limits predictability of the CH_4 atmospheric state and spatial scales at which it can be inferred (Polavarapu et al., 2016). Moreover, due to the non-linearity of atmospheric dynamics, the atmospheric state generated by ensemble mean winds can be different from the mean of atmospheric states generated by an ensemble of wind fields perturbed according to their uncertainty (Liu et al., 2011). Stohl et al. (2004), Scheele et al. (2005) and Monge-Sanz et al. (2013) also showed that assimilated metfields may be dynamically inconsistent, which results in increased mixing and, for instance, stronger stratosphere-troposphere exchange (STE). Another issue arises from inconsistency between archived horizontal winds (air mass fluxes) and surface pressures in the advection scheme (Jöckel et al., 2001), which leads to violation of mass conservation. This problem is usually solved by implementing a mass (pressure) fixer in the model (Segers et al., 2002; Bregman et al., 2003; Rotman et al., 2004), which, however, may itself produce spurious effect in the tracer concentrations.

The need for a mass fixer is also partly created by the fact that the metfields are usually regridded from the native GCM grid (spectral, cubed-sphere) to the CTM grid (usually, rectilinear longitude-latitude) and are temporally averaged. This process is always associated with some loss of information about eddy transport by convection (Yu et al., 2017) and advection and may cause weakening of vertical transport. This stresses the importance of keeping a consistent numerical grid between the CTM and original GCM where possible. Grell and Baklanov (2011) showed that the loss of information about transport reduces the effective model resolution and can be assessed using a power spectrum of wind fields. The study also stressed that temporal averaging of wind fields

may significantly impact vertical distribution of tracers in the model. However, temporal averaging of metfields does not always have negative effect on tracer simulations. For example, Pawson et al. (2007) showed that the use of 6-hourly averaged wind fields from the GEOS-4 data assimilation system significantly improved transport in the stratosphere by reducing noise in the assimilated metfields.

Another consequence of using a rectilinear grid is the shrinking of the zonal (east-west) size of model boxes at high latitudes, the need to shorten the advection time step in order to meet the Courant-Friedrichs-Lewy (CFL) condition, and special treatment of the polar caps to avoid polar singularities. Different approaches are used to mitigate this problem (Lin and Rood, 1996; Lin, 2004; Prather et al., 2008), however, as shown by Prather et al. (2008), poor treatment of the poles may cause tracer fields to converge to the wrong solution.

Physical parametrization, such as sub-grid convection, is another large source of errors in CTMs. Biases in convection have a significant impact on both tracer vertical distribution and tracer inter-hemispheric exchange (Rind et al., 2007; Patra et al., 2011). Convective transport is usually driven by convective mass fluxes (CMFs), which may either come with assimilated metfields or be re-diagnosed (parameterized) in the CTM in terms of resolved scales at a particular horizontal resolution. The latter approach may be utilized when part of convective transport is resolved in the original high-resolution GCM (and is not accounted for by CMFs), but is lost by coarsening of CTM grid. Meanwhile, original and re-diagnosed fluxes can be very different depending on the convective parametrization scheme. As shown by Orbe et al. (2017), CTMs driven by the same large-scale meteorological fields but with different convective parametrizations may have large differences in simulated tracer fields.

The stratosphere is also one of the most challenging regions for CH_4 simulations. CH_4 in the Earth's stratosphere is not well mixed, and transport errors acting on CH_4 gradients may significantly bias CH_4 fields. A number of studies have found significant discrepancies in stratospheric CH_4 fields between different CTMs (Patra et al., 2011) and mainly positive biases between models and observations (Ostler et al., 2016; Saad et al., 2016). Biases in CH_4 fields are generally related to discrepancies in the stratospheric age of air caused by errors in the STE, the mean residual circulation in the stratosphere and the polar vortex isolation. The transport errors may occur due to a number of factors. For example, as mentioned before, the use of assimilated meteorological fields increases mixing in the model. Additionally, the latter may be increased by coarsening the CTM resolution owing to additional numerical diffusion. Consequently, excessive mixing leads to the increased STE, "leaking" of the tropical pipe in the stratosphere (tropical branch

of the Brewer-Dobson circulation), and weakens transport barriers with strong potential vorticity gradient at the edge of the polar vortex. There are also multiple causes of errors in the strength of the mean residual circulation in the stratosphere, one of which is strength of parametrized gravity wave drag in GCMs.

1.4 Scientific objectives and structure of the thesis

This thesis pursues several objectives that can be formulated as follows:

1. To mitigate GEOS-Chem model biases for CH_4 using advanced data assimilation techniques.

2. To quantitatively characterize transport biases in CH_4 fields modelled by the GEOS-Chem CTM at coarse resolution.

3. To generate optimal initial and boundary conditions for CH_4 transport and data assimilation at high resolution within the North American domain.

The first and second thesis objectives are represented by separate papers, which are currently under review by co-authors. The papers will be submitted to the *Atmospheric Chemistry and Physics* and *Geoscientific Model Development* journals, respectively. The titles of the papers are as follows:

1. *Characterizing model errors in chemical transport modelling of methane: Using GOSAT XCH_4 data with weak constraint four-dimensional variational data assimilation.*

2. *Characterizing model errors in chemical transport modelling of methane: Impact of coarse model resolution.*

The third thesis objective is concerned with biases in CH_4 fields simulated by GEOS-Chem at high resolution over a regional North American domain. High-resolution simulation suffers less from numerical errors, however is expensive to run globally. In such case, one of the major sources of biases over short time scales are boundary conditions (BCs). We investigate the potential impact of these biases on inverted regional emissions and evaluate different methods of generating optimal time-dependent BCs.

The work conducted in the thesis represents the first application of weak constraint four-dimensional variational data assimilation of satellite CH_4 measurements to characterize model errors in a CTM and for producing improved CH_4 boundary and initial conditions.

A number of previous studies investigated the impact of model resolution on simulated CTM tracer fields (Searle et al., 1998; Strahan and Polansky, 2006; Prather et al., 2008). Here, the physical origin of resolution-dependent model errors is more deeply explored, their impact on assimilation analysis of CH_4 surface emissions is assessed, and several solutions are proposed to mitigate these errors.

The majority of the work was accomplished by the author based on models and measurements obtained from public repositories. Proxy CO_2 fields for the GOSAT XCH_4 "proxy" retrievals were generated by Dr. Feng Deng, University of Toronto. The weak constraint 4D-Var method was implemented in GEOS-Chem by Dr. Martin Keller, University of Toronto for assimilation of CO satellite observations.

The thesis is structured as follows. Chapter 2 gives an overview of research tools and methods. It describes the observational datasets that were used to constrain and validate CH_4 simulations. This chapter also describes key aspects of atmospheric CH_4 modelling and introduces the forward GEOS-Chem CTM as well as its adjoint, which were used to simulate CH_4 fields and invert the CH_4 state and CH_4 emissions, respectively. Finally, this chapter gives details about the data assimilation algorithms that were used to optimize CH_4 state and emissions. Each thesis objective is successively addressed in a separate chapter (Chapters 3, 4 and 5, respectively). Chapter 6 provides a summary of the accomplishments and gives suggestions for future work.

Chapter 2

Research tools and methods

2.1 Measurements

Atmospheric observations provide a crucial source of knowledge about CH_4 distributions in the atmosphere and serve multiple purposes. First, observations allow monitoring of changes in atmospheric CH_4 concentrations. Second, they impose constraints on processes responsible for these changes. And third, they provide an important test for the quality of atmospheric chemistry and transport models. CH_4 measurements are performed from a variety of platforms, including Earth-orbiting satellites, stationary surface stations, ships, aircraft and balloons.

Only satellites are able provide global measurement coverage. Satellites carry remote sensing instruments that record atmospheric spectra, which can be used to retrieve CH_4 abundance. Satellites may have limited vertical resolution and coverage depending on the spectral characteristic of the instrument and the observation geometry. Generally, satellite instruments that are used to retrieve CH_4 can be divided into three categories based on the altitude range over which they provide information. Nadir-looking instruments performing measurements in the ShortWave InfraRed (SWIR) spectral band usually have little vertical information about CH_4 distribution and provide estimates of total CH_4 amount in the atmospheric column. These include[1] passive instruments such as the SCIAMACHY instrument that flew on-board Envisat (Schneising et al., 2011), TANSO-FTS on-board GOSAT (Kuze et al., 2009), TROPOMI on-board the recently launched Sentinel-5P (Veefkind et al., 2012), and the future GOSAT-2 (Nakajima et al., 2017) and GeoCarb (Polonsky et al., 2014) satellites. This category also includes the future MERLIN satellite (Kiemle et al., 2014), which will be an active lidar instrument with similar vertical

[1]See List of Acronyms and Abbreviations for the full names of the satellite instruments

sensitivity to the above passive instruments (Kiemle et al., 2011). Thermal InfraRed (TIR) nadir measurements from AIRS (Xiong et al., 2008), TES (Worden et al., 2012), IASI (Xiong et al., 2013) and CrIS (Gambacorta et al., 2016) are passive instruments that primarily provide information about the CH_4 abundance in the middle and upper troposphere and are less sensitive to the lower troposphere due to weak thermal contrast between the atmosphere and the surface. As a consequence, these instruments are less sensitive to direct changes in CH_4 concentrations due to surface emissions except in cases when emitted CH_4 is rapidly injected into the middle and upper troposphere in convective updrafts (Worden et al., 2013). However, TIR measurements can provide greater temporal and spatial coverage relative to SWIR measurements as they do not require sunlight and do not depend on surface spectral reflectivity. Generally, SWIR retrievals are less sensitive to atmospheric temperature profiles and are, potentially, more accurate than TIR retrievals because the latter additionally require temperature to model thermal emissions from each atmospheric layer. Therefore, SWIR CH_4 retrievals are more often used as a constraint on CH_4 surface emissions. Satellite instruments in the third category perform solar occultation and limb measurement, and include instruments such as MIPAS (von Clarmann et al., 2009) and ACE-FTS (Boone et al., 2005). These instruments mainly provide information about CH_4 distributions in the upper troposphere and stratosphere. The tropospheric measurements are subject to errors due to interference with clouds. These measurements have high vertical resolution and are useful for assessing transport in models. They also supply information about polar atmospheric regions not accessible, for example, by nadir SWIR measurements.

In this thesis, we use GOSAT TANSO-FTS CH_4 retrievals as the main source of information about the CH_4 distribution in the atmosphere and as the primary constraint on CH_4 surface emissions. ACE-FTS retrievals are used to validate the optimized CH_4 state and to evaluate the quality of the model transport in the stratosphere. In addition to space-based observations, we also use *in situ* CH_4 measurements from the National Oceanic and Atmospheric Administration (NOAA) Earth System Research Laboratory (ESRL) global cooperative air sampling surface network (Dlugokencky et al., 2016), tall tower network (Andrews et al., 2014) and aircraft program (Sweeney et al., 2015). Additionally, we use CH_4 measurements from the third HIAPER Pole-to-Pole Observations (HIPPO) aircraft campaign (Wofsy et al., 2011) and ground-based XCH_4 (see below) retrievals from the Total Carbon Column Observing Network (TCCON, (Wunch et al., 2011)). As with the ACE-FTS retrievals, these surface and in situ data serve as independent sources of information to evaluate the general model performance and to validate the constrained CH_4 fields.

Most of the observations, except for TCCON and GOSAT, are defined as CH_4 volume mixing ratios (VMR) at a particular location and time. The TCCON and GOSAT datasets provide retrievals of column CH_4 dry-air mole fractions (XCH_4) defined as

$$X_{CH_4} = \frac{\int_0^\infty N_{CH_4}(z)dz}{\int_0^\infty N_{d.air}(z)dz} \tag{2.1}$$

where N_{CH_4} and $N_{d.air}$ are number densities of CH_4 and dry air, respectively. Eq. (2.1) is also often written as

$$X_{CH_4} = 0.2095\frac{\int_0^\infty N_{CH_4}(z)dz}{\int_0^\infty N_{O_2}(z)dz}. \tag{2.2}$$

Quantities derived from Eqs. (2.1) and (2.2) do not depend on spatial and temporal variation in surface pressure and make it easier to interpret spatial variations in the CH_4 observations.

2.1.1 GOSAT

The GOSAT mission (Kuze et al., 2009) was designed specifically for retrievals of greenhouse gases (CO_2 and CH_4) and was launched into orbit on January 23, 2009. It carries two instruments: the Thermal And Near infrared Sensor for carbon Observation Fourier Transform Spectrometer (TANSO-FTS) and the TANSO Cloud and Aerosol Imager (CAI). GOSAT flies in a sun-synchronous 666 km orbit with a 3-day revisit time and performs measurements at about 13:00 local time. TANSO-FTS operates in a cross-track scanning mode. Figure 2.1 shows the GOSAT viewing geometry. Initially it observed five across-track points, separated by about 100 km, however in August 2010, the pattern was switched to three points to reduce pointing errors due to vibrations. Generally, the pointing mechanism is capable of rotating $\pm 35^\circ$ across track and $\pm 20^\circ$ along-track. This also allows observations in glint mode over water and in target mode (staring at one location) for vicarious calibration (for example, at Railroad Valley) and point source emission estimation. Each scene is exposed for 4 sec while an interferogram is recorded. The instrument field-of-view creates a 10.5 km diameter ground footprint.

The spectra are obtained in three SWIR bands (0.76-0.78 μm, 1.56-1.72 μm and 1.92-2.08 μm) and one TIR band (5.6-14.3 μm) at a resolution of about 0.2 cm^{-1} by taking a Fourier transform of the recorded interferogram. The SWIR bands provide almost uniform sensitivity through the entire atmosphere while the TIR band is sensitive to the mid-troposphere. Solar radiation in each SWIR band is additionally split into two orthogonal polarization components (P/S components) so that the instrument obtains

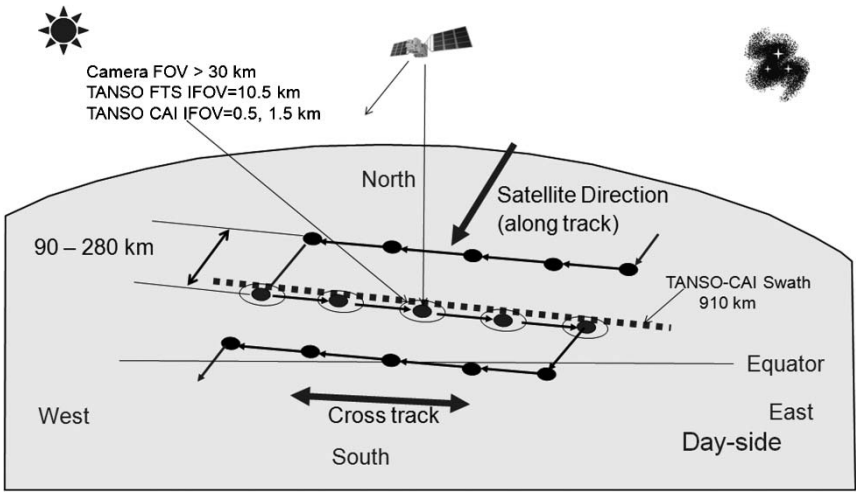

Figure 2.1: GOSAT viewing geometry. Adapted from Kuze et al. (2009).

spectra in seven bands in total. This spectral information is used to retrieve VMRs of CO_2, CH_4 and H_2O. Several CH_4 retrieval products have been produced by different research groups. These include the Full-Physics retrievals from the National Institute for Environmental Studies (NIES, Japan) (Yoshida et al., 2011) and the University of Leicester (UoL) (Parker et al., 2011), the RemoteC retrievals developed at the Netherlands Institute for Space Research (SRON) and Karlsruhe Institute for Technology (KIT) (Butz et al., 2011), as well as the Proxy RemoteC (Butz et al., 2010) and UoL proxy retrievals (Parker et al., 2011).

Because GOSAT observations are central to this study, we provide here a detailed description of the CH_4 retrievals and discuss the implications of assumptions made in the algorithm. We utilize version 5.2 of the UoL Proxy XCH_4 retrievals (Parker et al., 2011, 2015), which are based on the Orbiting Carbon Observatory (OCO) Full-Physics retrieval algorithm (O'Dell et al., 2012). The Proxy approach was first introduced for SCIAMACHY CH_4 retrievals (Frankenberg et al., 2006) and is based on the idea that retrievals of XCO_2 and XCH_4 in nearby spectral bands are subject to similar errors due to photon light path modification (caused by atmospheric scattering by aerosols and clouds) and instrumental effects, both of which would cancel by taking the ratio $\frac{X_{CH_4}}{X_{CO_2}}$. Due to the fact that CO_2 is less variable than CH_4 in the atmosphere, knowledge about XCO_2 from an independent source, such as a CTM, can be used as a proxy for XCH_4:

$$X_{CH_4}^{proxy} = \frac{X_{CH_4}}{X_{CO_2}} X_{CO_2}^{model}. \tag{2.3}$$

The accuracy of XCH_4 retrievals is affected by several factors. Thick cloud and aerosol

layers are major obstacles for accurate XCH_4 estimates. Therefore, such contaminated scenes are identified and filtered in the retrieval. However, thin cloud and aerosol layers are harder to detect. Therefore, Full-Physics retrievals have to take into account atmospheric scattering and fit the properties of the scatterer. This is a challenging task because the retrieval algorithm requires reliable prior knowledge about the distribution and characteristics of scatterers, but there is not enough information in the spectra to directly retrieve them. Eventually, the errors due to scattering may fold into the final retrieval. However, the Proxy method makes the XCH_4 retrievals much less sensitive to the presence of thin atmospheric clouds and aerosol layers, which are usually difficult to filter. This significantly increases the number of potentially observable scenes. Figure 2.2 shows the location and total number of GOSAT observations in February-May 2010, the period considered in the analyses here. The largest density of measurements is over clear-sky deserts, although the tropics are also partly observed. Due to large solar zenith angles (SZAs) during this period, high northern latitudes are sparsely observed.

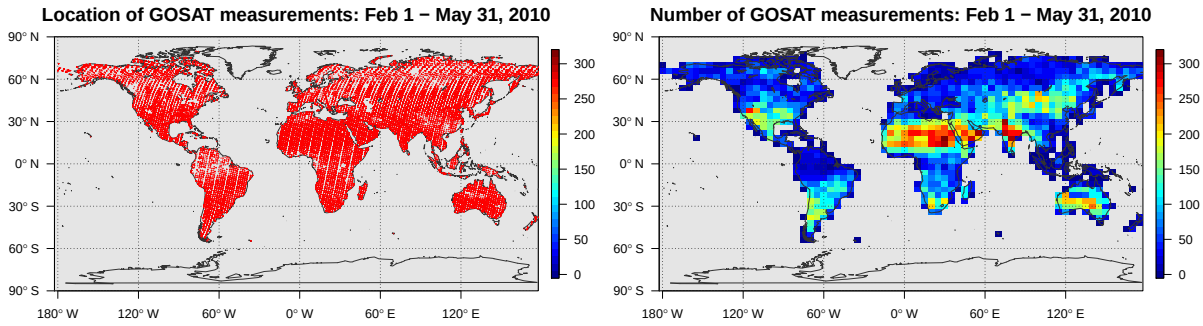

Figure 2.2: The location (left panel) and total number (right panel) of GOSAT observations during the period of February-May 2010.

In the UoL retrieval algorithm, XCH_4 and XCO_2 are retrieved in spectral bands centred at 1.65 μm ($2\nu_3$ CH_4 overtone band) and 1.61 μm, respectively, using the assumption of a non-scattering atmosphere. Also, no light polarization information is used: the two polarization components are combined to produce a single intensity.

The idea behind remote sensing retrievals is to relate the spectra recorded by a spectrometer to the vertical profile of a gas in the atmosphere. This is accomplished using a forward model which simulates atmospheric absorption and reflection spectra for a particular satellite geometry by approximately solving the radiative transfer equation in a plane-parallel atmosphere (Schwarzschild's equation, Liou, 2002). The forward model uses gas mixing ratios as parameters which are adjusted by an optimization algorithm so that the simulated spectra closely match the observed one. In general form, the radiative

transfer equation is defined as

$$\mu \frac{dI_\lambda(\tau, \mu, \phi)}{d\tau} = I_\lambda(\tau, \mu, \phi) - J_\lambda(\tau, \mu, \phi), \tag{2.4}$$

where λ is wavelength, $\mu = \cos(\theta)$, θ and ϕ are observation zenith and azimuth angles, and τ is optical depth. τ replaces the vertical coordinate and is defined as

$$\tau_\lambda(z') = \sum_{m=1}^{M} \int_{z_{TOA}}^{z'} \sigma_m(\lambda, z) N_m(z) dz, \tag{2.5}$$

where M is a number of absorbing gases, N_m is number density of the m^{th} gas and σ_m is absorption cross-section of the m^{th} gas derived from molecular spectroscopic databases. The latter are one of the main sources of bias in CH_4 retrievals and are continuously being improved and updated based on new experimental data and theoretical calculations. I is the intensity of sunlight reflected from the surface and partly absorbed in the atmosphere before and after reflection. The source function J represents the contribution to the total radiation due to scattering of sunlight and can be expressed as

$$\begin{aligned} J_\lambda(\tau, \mu, \phi) = \frac{\tilde{\omega}_\lambda}{4\pi} \int_{-1}^{1} \int_{0}^{4\pi} I_\lambda(\tau, \mu', \phi') P(\mu, \phi, \mu', \phi') d\phi' d\mu' \\ + \frac{\omega(\tau)}{4\pi} P(\mu, \phi, -\mu_0, \phi_0) F_{0,\lambda} e^{-\tau/\mu_0} \end{aligned} \tag{2.6}$$

where $\tilde{\omega}_\lambda$ is single scattering albedo, P is scattering phase function, F_0 is solar irradiance at the top of atmosphere (TOA) while θ_0 and ϕ_0 are solar zenith and azimuth angles. The first term on the r.h.s. of Eq. (2.6) represents the contribution due to multiple scattering of a diffuse light beam, while the second term is due to single scattering of a direct attenuated solar beam. Multiplying both sides of Eq. (2.4) by $e^{-\tau/\mu}$ and integrating from the surface to TOA we obtain intensity at the TOA as

$$I_\lambda(0, \mu, \phi) = I_\lambda(\tau_s, \mu, \phi) e^{-\tau_s/\mu} + \int_0^{\tau_s} J_\lambda(\tau', \mu, \phi) \frac{e^{-\tau'/\mu}}{\mu} d\tau' \tag{2.7}$$

where

$$I_\lambda(\tau_s, \mu, \phi) = \mu_0 F_{0,\lambda} e^{-\tau/\mu_0} R^s_\lambda(\mu, \phi, \mu_0, \phi_0) \tag{2.8}$$

and R^s_λ is surface spectral reflectance (albedo). Due to the small signal-to-noise ratio, retrievals of CH_4 are not possible over surfaces, such as water (except for glint observations), that have low surface reflectance R^s_λ in the near-infrared (NIR) spectral band. In the absence of multiple scattering (the single-scattering approximation), for example, in the

presence of a thin cloud or aerosol layer, in a plane-parallel atmosphere Eq. (2.7) can be integrated to yield

$$I_\lambda(0,\mu,\phi) = \mu_0 F_{0,\lambda} R^s_\lambda(\mu,\phi,\mu_0,\phi_0)\exp\left(-\tau_s\left(\frac{1}{\mu}+\frac{1}{\mu_0}\right)\right) + \\ + \frac{\tilde{\omega}_\lambda \mu_0}{4\pi(\mu+\mu_0)} F_{0,\lambda} P(\mu,\phi,-\mu_0,\phi_0)\left(1-\exp\left(-\tau_s\left(\frac{1}{\mu}+\frac{1}{\mu_0}\right)\right)\right). \tag{2.9}$$

Finally, when scattering is completely ignored, only the first term remains on the r.h.s. of Eq. (2.9).

The UoL XCH_4 Proxy retrievals utilize the LIDORT radiative transfer (RT) model combined with a fast 2-orders-of-scattering vector RT code (Natraj et al., 2008). The forward model simulates the spectrum at high resolution (0.01 cm^{-1}) within the prescribed spectral range and convolves it with the instrument line shape function (ILS). Finally, the observed spectrum $\mathbf{y}$ can be related to state vector $\mathbf{x}$, comprised of atmospheric CH_4 concentrations and other model parameters, by the forward model equation

$$\mathbf{y} = F(\mathbf{x}) + \boldsymbol{\epsilon} \tag{2.10}$$

where F is the non-linear forward model operator, and $\boldsymbol{\epsilon}$ represents the error in the measurements and forward model. Here, the state vector consists of CH_4 and CO_2 VMR profiles with 20 discrete levels, a single scaling factor on H_2O VMR and temperature profiles, surface albedo, and spectral dispersion due to the Doppler line shift and other effects.

The UoL Proxy XCH_4 retrievals are based on the Bayesian optimal estimation method (Rodgers, 2000) which derives a maximum a posteriori (MAP) solution $\hat{\mathbf{x}}$ (see Section 2.4.1 for details) by minimizing the cost function

$$\chi^2 = (\mathbf{y}-F(\mathbf{x}))^T \mathbf{S}_\epsilon^{-1}(\mathbf{y}-F(\mathbf{x})) + (\mathbf{x}-\mathbf{x}_a)^T \mathbf{S}_a^{-1}(\mathbf{x}-\mathbf{x}_a) \tag{2.11}$$

where $\mathbf{S}_\epsilon$ and $\mathbf{S}_a$ are the observation and a priori error covariance matrices, respectively, and $\mathbf{x}_a$ is the a priori state vector. The cost function is minimized iteratively using the Levenberg-Marquardt algorithm. At each iteration i, the algorithm searches for the update $\mathbf{dx}_{i+1}$ on the state vector $\mathbf{x}_i$ which satisfies the equation

$$\left((1+\gamma)\mathbf{S}_a^{-1} + \mathbf{K}_i^T \mathbf{S}_\epsilon^{-1}\mathbf{K}_i\right)\mathbf{dx}_{i+1} = \left(\mathbf{K}_i^T \mathbf{S}_\epsilon^{-1}(\mathbf{y}-F(\mathbf{x}_i)) + \mathbf{S}_a^{-1}(\mathbf{x}-\mathbf{x}_a)\right) \tag{2.12}$$

where γ is the Levenberg-Marquardt parameter and $\mathbf{K}_i$ is the Jacobian matrix that

represents the sensitivity of the simulated spectrum to the state vector and is obtained using the finite perturbation method

$$\mathbf{K} = \frac{\partial F(\mathbf{x})}{\partial \mathbf{x}} \cong \frac{F(\mathbf{x} + \delta\mathbf{x}) - F(\mathbf{x})}{\delta\mathbf{x}}. \tag{2.13}$$

Finally, after convergence, the a posteriori error covariance matrix is obtained as

$$\hat{\mathbf{S}} = \left(\mathbf{K}^T \mathbf{S}_\epsilon^{-1} \mathbf{K} + \mathbf{S}_a^{-1}\right)^{-1} \tag{2.14}$$

while the averaging kernel matrix is given by

$$\mathbf{A} = \frac{\partial \hat{\mathbf{x}}}{\partial \mathbf{x}} = \hat{\mathbf{S}} \mathbf{K}^T \mathbf{S}_\epsilon^{-1} \mathbf{K}. \tag{2.15}$$

X_{CH_4} is calculated as $X_{CH_4} = \mathbf{k}^T \hat{\mathbf{x}}$, where $\mathbf{k}^T = \left(\mathbf{h}^T, \mathbf{0}\right)$ and $\mathbf{h}$ is the pressure weighting vector, which is based on a priori surface pressure and the H_2O VMR profile. The X_{CH_4} averaging kernel function is obtained as follows. Using the identity

$$\frac{\partial X_{CH_4}}{\partial \mathbf{x}} = \mathbf{k}^T \mathbf{A}, \tag{2.16}$$

elements of the column averaging kernel vector are expressed as

$$a_i^{CH_4} = \left(\frac{\partial X_{CH_4}}{\partial \mathbf{x}}\right)_i \frac{1}{h_i} = \left(\mathbf{k}^T \mathbf{A}\right)_i \frac{1}{h_i}, \quad i = \overline{1, q} \tag{2.17}$$

where q is the number of levels in the CH_4 VMR profile. Finally, the XCH_4 retrieval uncertainty is estimated as

$$\sigma_{XCH_4}^2 = \mathbf{k}^T \hat{\mathbf{S}} \mathbf{k}. \tag{2.18}$$

The identical procedure is applied to obtain X_{CO_2}, $\sigma_{XCO_2}^2$ and $\mathbf{a}^{CO_2}$. Then, the $X_{CH_4}^{proxy}$ uncertainty is given by the expression

$$\sigma(X_{CH_4}^{proxy}) = X_{CH_4}^{proxy} \sqrt{\left(\frac{\sigma(X_{CH_4})}{X_{CH_4}}\right)^2 + \left(\frac{\sigma(X_{CO_2})}{X_{CO_2}}\right)^2}. \tag{2.19}$$

The accuracy of the $X_{CH_4}^{proxy}$ estimate also depends on reliable knowledge of the proxy XCO_2. In practice, the latter is also subject to errors. However, these are more challenging to evaluate and are not included in the expression for $\sigma(X_{CH_4}^{proxy})$. As a result, the X_{CH_4} uncertainty is likely to be underestimated. The original UoL XCH_4 retrievals utilize proxy CO_2 calculated as a median of three model CO_2 simulations: GEOS-Chem (from

the University of Edinburgh), LMDZ/MACC-II, and NOAA CarbonTracker, that was smoothed with GOSAT scene-dependent CO_2 averaging kernels. CO_2 fields in all three models were produced by assimilating in-situ surface CO_2 observations. In this thesis, we use a different proxy XCO_2, which is based on optimized CO_2 fields from a GEOS-Chem CO_2 surface flux inversion analysis that used GOSAT XCO_2 retrievals over land (Deng et al., 2014). For the period of February-May 2010, the XCH_4 retrievals using both CO_2 proxies are unbiased against each other with scatter of 3 ppb and a correlation of $R = 0.99$. Figure 2.3 shows the mean difference between the two products and points to some systematic regional discrepancies of up to 8 ppb. However, global mean statistics are also unbiased with 90% of all regional differences smaller than 3 ppb. Generally, the modelled GEOS-Chem CH_4 fields agreed better with the XCH_4 retrievals using this new proxy.

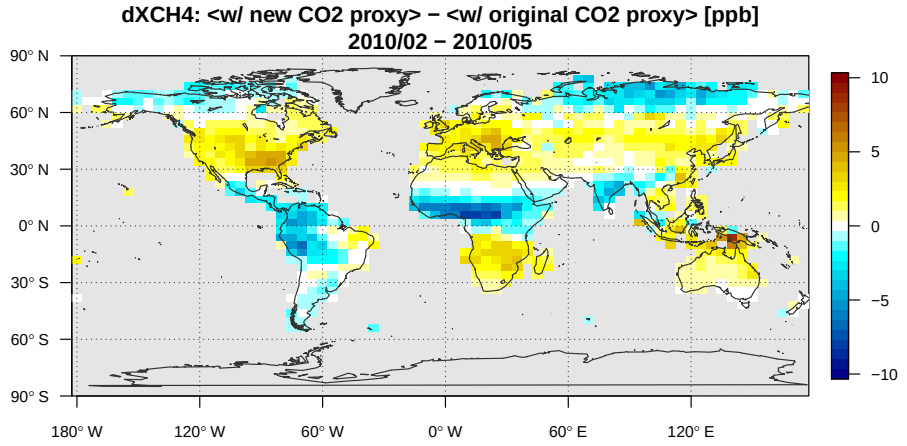

Figure 2.3: Difference between GOSAT XCH_4 retrievals based on two different CO_2 proxy fields. The original CO_2 proxy is based on the median of GEOS-Chem (University of Edinburgh), LMDZ/MACC-II and NOAA CarbonTracker models constrained by in-situ surface CO_2 observations; the new CO_2 fields are from GEOS-Chem CO_2 surface flux inversion constrained by GOSAT ACOS CO_2 retrievals over land.

Spectra over ocean (glint observations) or with a signal-to-noise ratio (SNR) below 50 were not used for retrievals. Cloud-contaminated scenes were filtered if co-located ECMWF surface pressure and clear-sky surface pressure retrieved in the O_2 A band were different by 30 hPa or more. Additionally, we excluded all retrievals over Greenland and to the north of 75°N due to possible biases in retrievals over snow (see Fig. 2.2).

Equation (2.12), which defines the state vector estimate at the next iteration, can be

rewritten as follows, once convergence is achieved

$$\begin{aligned}\hat{\mathbf{x}} &= \mathbf{x}_a + \left(\hat{\mathbf{K}}^T\mathbf{S}_\epsilon^{-1}\hat{\mathbf{K}} + \mathbf{S}_a^{-1}\right)^{-1}\hat{\mathbf{K}}^T\mathbf{S}_\epsilon^{-1}(\mathbf{y} - F(\hat{\mathbf{x}}) + \hat{\mathbf{K}}(\hat{\mathbf{x}} - \mathbf{x}_a)) = \\ &= \mathbf{x}_a + \hat{\mathbf{G}}(\mathbf{y} - F(\hat{\mathbf{x}}) + \hat{\mathbf{K}}(\hat{\mathbf{x}} - \mathbf{x}_a))\end{aligned} \tag{2.20}$$

where $\hat{\mathbf{G}}$ is referred to as the gain matrix. The forward model can also be linearized as

$$y = F(\mathbf{x}) + \boldsymbol{\epsilon} = F(\hat{\mathbf{x}}) + \hat{\mathbf{K}}(\mathbf{x} - \hat{\mathbf{x}}) + \boldsymbol{\epsilon} \tag{2.21}$$

where $\mathbf{x}$ is the true CH_4 profile. Here we simplify the discussions by assuming that the state vector does not contain non-CH_4 elements. Eq. (2.20) can then be rewritten as

$$\begin{aligned}\hat{\mathbf{x}} &= \mathbf{x}_a + \hat{\mathbf{G}}\hat{\mathbf{K}}(\mathbf{x} - \mathbf{x}_a) + \hat{\mathbf{G}}\boldsymbol{\epsilon} \\ &= \mathbf{x}_a + \mathbf{A}(\mathbf{x} - \mathbf{x}_a) + \hat{\mathbf{G}}\boldsymbol{\epsilon} \\ &= (\mathbf{I}_q - \mathbf{A})\mathbf{x}_a + \mathbf{A}\mathbf{x} + \hat{\mathbf{G}}\boldsymbol{\epsilon}.\end{aligned} \tag{2.22}$$

Hence, the retrieved quantity includes contributions from both the a priori and the truth. In the ideal case, all contributions come from the truth and $\mathbf{A}$ is the identity matrix. In practice, the averaging kernel $\mathbf{A}$ reflects the smoothing of the true profile $\mathbf{x}$ and is also referred to as the smoothing matrix. The last term on the r.h.s. of Eq. (2.22) represents the retrieval error due to spectral and forward model errors and is ignored in further discussions for simplicity.

Similarly to $\hat{\mathbf{x}}$, X_{CH_4} is defined as

$$X_{CH_4} = X^a_{CH_4} + \mathbf{h}^T\mathbf{A}(\mathbf{x} - \mathbf{x}_a) = X^a_{CH_4} + \sum_{i=1}^{q} h_i a_i^{CH_4}(\mathbf{x} - \mathbf{x}_a)_i. \tag{2.23}$$

When the true profile is replaced by the modelled profile, $X^{model}_{CH_4}$ provides the modelled dry-air mole fraction of CH_4 as if the model fields were observed by GOSAT

$$X^{model}_{CH_4} = X^a_{CH_4} + \mathbf{h}^T\mathbf{A}(\mathbf{x} - \mathbf{x}_a) = X^a_{CH_4} + \sum_{i=1}^{q} h_i a_i^{CH_4}(\mathbf{x}^{model} - \mathbf{x}_a)_i \tag{2.24}$$

where, for simplicity, $\mathbf{x}$ and $\mathbf{A}$ were assumed to consist only of the elements corresponding to a CH_4 VMR profile. In this context, Eq. (2.24) maps the modelled CH_4 into measurement space and is used for comparing simulated fields with GOSAT observations.

XCH_4 retrievals contain about 1 degree of freedom for signal (DOFS) (defined as the trace of $\mathbf{A}$) and have relatively flat averaging kernels (AKs) in the troposphere that

slowly decrease in the stratosphere. The overall mean GOSAT averaging kernel profile from the UoL Proxy XCH_4 retrieval algorithm is shown in Fig. 2.4 and reveals that the retrieval contains little vertical information. GOSAT has the potential to retrieve vertical information by combining information from the SWIR and TIR spectral bands. However, this has not yet been accomplished due radiometric calibration errors in the TIR band (Kuze et al., 2016).

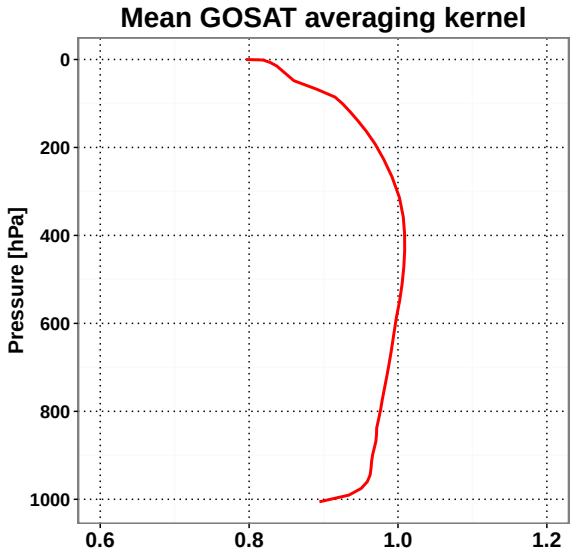

Figure 2.4: The overall mean GOSAT SWIR XCH_4 averaging kernel profile from the UoL Proxy XCH_4 retrieval algorithm.

Errors in GOSAT Proxy XCH_4 retrievals (v5.2), with the original XCO_2 proxy, were assessed against co-located TCCON ground-based retrievals by Hewson et al. (2015). That validation study found that GOSAT retrievals contain random errors of 12.55 ppb and systematic errors of 4.8 ppb (although per-site biases ranged from -2.15 ppb (Wollongong) to 13.44 ppb (Garmisch)). Overall, GOSAT and TCCON were highly correlated with a correlation coefficient of 0.86. However, errors away from TCCON sites could be larger. In principle, the given accuracy would be enough in many regions of the world to improve a priori knowledge of CH_4 surface emissions. However, model errors may significantly undermine this potential.

2.1.2 TCCON

The Total Carbon Column Observing Network (Wunch et al., 2011) is a global network of ground-based high-resolution Fourier transform infrared (FTIR) spectrometers retrieving

CH_4 from solar absorption spectra in the NIR spectrum. TCCON XCH_4 is defined by Eq. (2.2). The retrievals are based on the radiative transfer theory described in Section 2.1.1, but with differences relative to GOSAT mainly due to different instrument geometry (measurements of transmitted sunlight with no surface reflection) and different spectral characteristics of the retrievals (spectral range of 5880 - 6145 cm^{-1}, or 1.63 - 1.7 μm, and 0.02 cm^{-1} resolution). The retrieval algorithm is implemented using the GGG code developed in the Jet Propulsion Laboratory by Geoffrey C. Toon. Typical TCCON XCH_4 averaging kernels for the Lamont site are shown in Fig. 2.5, and have a relatively flat structure. At small SZAs, more information in the retrievals comes from the upper troposphere and the stratosphere, while at high SZAs, it comes from the middle and lower troposphere. We used the GGG2014 version of the TCCON XCH_4 data from multiple stations around the globe (Blumenstock et al., 2017; Griffith et al., 2017; Hase et al., 2017; Kivi et al., 2017; Notholt et al., 2017; Sherlock et al., 2017; Sussmann and Rettinger., 2017; Warneke et al., 2017; Wennberg et al., 2017a,b). The estimated uncertainty and precision of XCH_4 retrievals are less than 0.5% and 0.3%, respectively (Wunch et al., 2015). Retrievals are bias corrected based on comparisons with calibrated aircraft and AirCore profiles measurements. In order to compare modelled CH_4 fields with TCCON observations, we smooth the former with TCCON SZA- and station-dependent XCH_4 averaging kernels using the expression similar to Eq. (2.24).

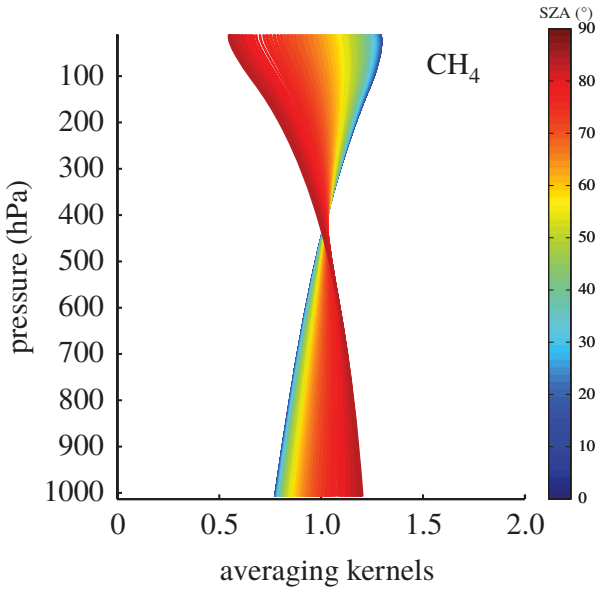

Figure 2.5: SZA-dependent TCCON XCH_4 averaging kernels for the Lamont site. Adapted from Wunch et al. (2011).

2.1.3 ACE

We used data from the ACE-FTS (Atmospheric Chemistry Experiment Fourier Transform Spectrometer (Bernath et al., 2005)) on-board the SCISAT satellite to evaluate the modelled vertical distribution of CH_4 in the stratosphere. SCISAT was launched into orbit on August 12, 2003. The orbit is about 650 km above the surface and has an inclination of 73.9°. The satellite carries ACE-FTS, two imagers, and the Measurement of Aerosol Extinction in the Stratosphere and Troposphere Retrieved by Occultation (MAESTRO) instrument. ACE-FTS is a high-resolution (0.02 cm^{-1}) Fourier transform infrared spectrometer recording atmospheric solar absorption spectra in the spectral range from 750 to 4400 cm^{-1}. Measurements are performed in the limb direction (solar occultation measurements, see Fig. 2.6) over a range of tangent heights.

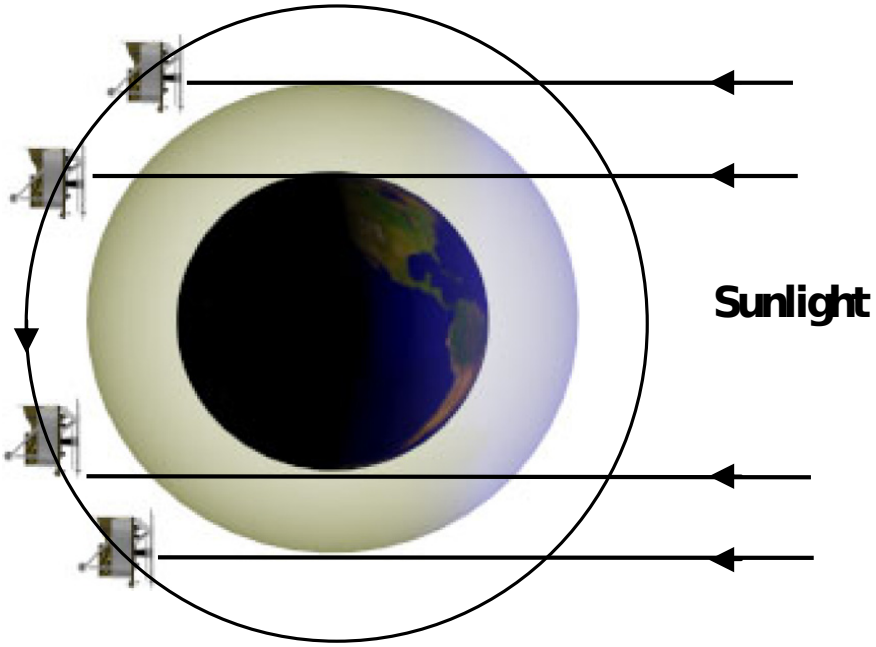

Figure 2.6: ACE-FTS observation geometry. Adapted from Bernath (2017).

The latitudes of the occultations repeat every year. Figure 2.7 shows the typical annual pattern. The satellite makes 15 occultations for both sunrise and sunset per day, separated by about 24° in the longitudinal direction. Measurements cover an altitude range from the cloud tops, at about 5 km, up to 150 km. Spectra are recorded continuously during 2 s scans, which implies that the altitude and tangent point changes slightly during the scan. As a result, the instrument has coarse horizontal resolution of about 300 km in the limb direction. The vertical resolution determined by the instrument field-of-view is about 3 km at a tangent point 3000 km away from the satellite. However, vertical

sampling ranges from 2 to 6 km depending on viewing geometry.

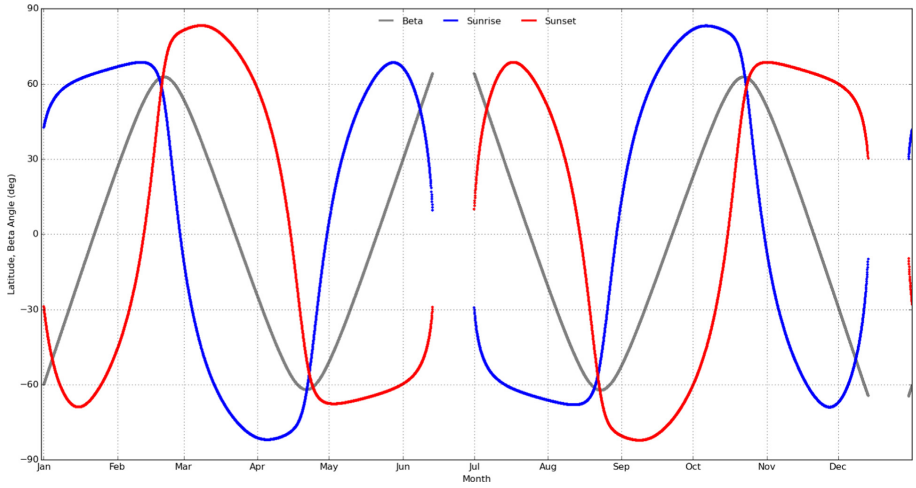

Figure 2.7: Annual pattern of the latitude of ACE occultations at sunrise (blue) and sunset (red), and the angle between the orbital plane and the Earth-Sun vector referred to as beta angle (gray). Adapted from Bernath (2017).

ACE-FTS CH_4 retrievals are performed in several steps (Bernath et al., 2005). First, temperature and pressure profiles, as well as the tangent altitudes, are retrieved using CO_2 absorption lines. The retrievals of CH_4 are performed using the temperature and pressure profiles from the previous step. Retrievals are performed by fitting the simulated spectra to the recorded ones in a set of microwindows defined for each altitude. Atmospheric transmission spectra are modelled using the Beer-Lambert law, the HITRAN 2004 spectral database (Rothman et al., 2005) and the Voigt lineshape function. Retrieved VMR profiles are interpolated onto a vertical grid with 1 km spacing. Here, we use version 3.6 CH_4 retrievals (Boone et al., 2013; Waymark et al., 2014).

A number of studies have performed validation of ACE-FTS CH_4 retrievals. De Mazière et al. (2008) showed that the older v2.2 was accurate to within 10% in the upper troposphere and lower stratosphere, to within 25% from the middle stratosphere up to the lower mesosphere (at about 60 km), and contained significant biases above 60 km. Waymark et al. (2014) evaluated v3.0 and found that this version of CH_4 retrievals was smaller by 10% in the stratosphere between 35 and 40 km than the previous v2.2. Olsen et al. (2017) compared ACE-FTS v3.5 and MIPAS CH_4 vertical profiles coincident with TANSO-FTS measurements, and found small differences except in the tropics. The mean differences were larger than 20% below about 450 hPa, within 5% between 450 and 40 hPa, and larger than 5% above 40 hPa.

2.1.4 In situ measurements

Another source of information about CH_4 distributions is the *in situ* observations from the NOAA-ESRL global cooperative air sampling network (Dlugokencky et al., 2016). Each site in the network collects air samples by opening a stopcock on an evacuated glass flask. Samples are later analyzed at NOAA ESRL in Boulder, Colorado by gas chromatography with flame ionization detection. At stationary sites, samples are collected once per week. Shipborne samples from the Pacific Ocean and South China Sea are collected once every three and one week, respectively, per each latitude zone. The NOAA tall tower network (Andrews et al., 2008) provides daily CH_4 measurements from a number of sites across North America (Andrews et al., 2014) with air samples collected using an automated programmable flask package at altitudes from about 10 to 500 m above ground level (agl). We use data collected at six sites: Argyle, Maine (AMT, 45.03°N, 68.68°W); Erie, Colorado (BAO, 40.05°N, 105.01°W); Beech Island, South Carolina (SCT, 33.406°N, 81.833°W); West Branch, Iowa (WBI, 41.725°N, 91.353°W); Walnut Grove, California (WGC, 38.265°N, 121.4911°W); and Moody, Texas (WKT, 31.32°N, 97.33°W). Surface and tower measurements have precision of 1-3 ppb and absolute accuracy of about 3 ppb (0.2%).

CH_4 measurements were also provided by the network of sites with towers operated by Environment and Climate Change Canada (ECCC) (Worthy et al., 2003). These sites are: Bratt's Lake, Saskatchewan (50.20°N, 104.71°W); Chibougamau, Quebec (49.69°N, 74.34°W); East Trout Lake, Saskatchewan (54.35°N, 104.99°W); Egbert, Ontario (44.23°N, 79.78°W); Estevan Point, British Columbia (49.38°N, 126.54°W); Esther, Alberta (51.67°N, 110.21°W); Fraserdale, Ontario (49.88°N, 81.57°W); Lac La Biche, Alberta (54.95°N, 112.47°W); and Sable Island, Nova Scotia (43.93°N, 60.01°W). Continuous measurements are performed at altitudes from 20 to 105 m above ground level (agl) using an Agilent 6890N gas chromatograph with flame ionization detection, and have precision of approximately 1.5 ppb. We use hourly mean estimates produced by averaging all valid measurements within an hour.

Additionally, we exploit CH_4 measurements from the NOAA aircraft program (Sweeney et al., 2015) over North America. Aircraft flights are performed several times per month, however can also be as frequent as only once per three weeks. During each flight, 12 flask samples are collected at different altitudes (up to 13 km) using the programmable 12-flask sampling system. Data have accuracy and precision of about 1-2 ppb.

Airborne data are also provided by the third HIAPER Pole-to-Pole Observations (HIPPO) aircraft campaign (Wofsy et al., 2011), which took place between 20 March 2010 and 20 April 2010. Measurements sampled the atmosphere from the north pole to the

coast of Antarctica along the central Pacific Ocean and from the surface to 14 km altitude. We used CH_4 measurements performed by a quantum cascade laser spectrometer (QCLS) at 1 Hz frequency. CH_4 was measured by the QCLS with precision of 0.5 ppb and accuracy of 1 ppb, while the mean bias relative to simultaneous flask-based measurements is 0.44 ppb (Santoni et al., 2014). We exploited the Merged 10-second Meteorology, Atmospheric Chemistry, and Aerosol Data product (Wofsy et al., 2012), which was derived from 1-sec measurements by applying a median filter.

2.2 Modelling

2.2.1 Dynamical fields

Dynamical fields that drive tracer transport are generated by numerically solving several governing equations (Kalnay, 2003). The first is the Navier-Stokes equation

$$\frac{d\mathbf{v}}{dt} = -\frac{\nabla p}{\rho} - \nabla\phi + \mathbf{F} - 2\mathbf{\Omega} \times \mathbf{v} \tag{2.25}$$

where $\mathbf{v}$ is the 3D wind velocity vector, ϕ is geopotential, $\mathbf{\Omega}$ is Earth's angular velocity, $\mathbf{F}$ is a frictional force, and ρ is air density. Another is the continuity equation

$$\frac{\partial\rho}{\partial t} + \nabla \cdot (\rho\mathbf{v}) = 0. \tag{2.26}$$

A third is the state equation for an ideal gas

$$p = \rho RT, \tag{2.27}$$

where T is air temperature and R is the gas constant for air. The thermodynamic equation,

$$c_p \frac{1}{\theta}\frac{d\theta}{dt} = \frac{Q}{T} \tag{2.28}$$

is also solved, where c_p is specific heat at constant pressure, Q is the diabatic heating rate and θ is potential temperature. Finally, there are the continuity equations for various gases such as H_2O, O_3, CO_2 and CH_4, etc.

$$\frac{\partial\rho q}{\partial t} + \nabla \cdot (\rho\mathbf{v}q) = E - S \tag{2.29}$$

where q is tracer mass mixing ratio, E is the gas source (e.g., evaporation for H_2O or surface emissions for CH_4) and S is the gas sink (e.g., condensation for H_2O or chemical

destruction for CH_4).

The governing equations are solved on a discretized grid using a variety of numerical methods. Due to the finite size of a grid cell, processes happening on a sub-grid scale cannot be explicitly resolved and have to be parametrized in terms of resolved scales. These processes include convection, turbulent mixing in the boundary layer, radiative heating, chemistry, cloud processes and interaction with radiation, topographic and non-topographic forcing, atmosphere-land and atmosphere-ocean heat and moisture fluxes and others. Therefore, Eqs. (2.26) and (2.29) can be rewritten as

$$\begin{aligned} \frac{\partial \rho}{\partial t} + \nabla \cdot (\rho \mathbf{v}) &= M_a \\ \frac{\partial \rho q}{\partial t} + \nabla \cdot (\rho \mathbf{v} q) &= E - S + M_q \end{aligned} \tag{2.30}$$

where M_a and M_q represent additional air and tracer sources/sinks, respectively, due to, for example, parametrized mixing through convection and turbulence.

In the global domain, the solution of these equations is an initial condition problem, whereas in the regional domain it is also a boundary condition problem. Due to the chaotic nature of the atmosphere, even small but inevitable errors in estimates of the initial conditions may grow quickly in time and produce very different numerical solutions (forecasts). In order to keep the solution trajectory from diverging too far from the truth, the short-term forecast is statistically combined with atmospheric observations using various data assimilation techniques that account for uncertainties in both the model and measurements.

2.2.2 Transport modelling: tracer advection

The action of parametrizing the terms on the r.h.s. of Eq. (2.30) is split into separate steps. Pure tracer advection is addressed by the equation (flux form)

$$\frac{\partial \rho q}{\partial t} + \nabla \cdot (\rho \mathbf{v} q) = 0, \tag{2.31}$$

which can also be written in advective form as

$$\frac{\partial q}{\partial t} + \mathbf{v} \cdot \nabla q = 0. \tag{2.32}$$

A detailed discussion of sub-grid scale turbulence and convective parametrization represented by terms M_a and M_q in Eqs. (2.30) is beyond the scope of this thesis, but a brief description of these parameterizations in the model that is used in the thesis is given in

Section 2.3.3. We just briefly mention that parametrization schemes are one of the most uncertain components of transport and vary between different models.

Most commonly, tracer advection is implemented using finite volume (FV) numerical schemes. Compared to spectral and finite difference methods, these are based on physical principles and have certain advantages. First, they conserve tracer mass by design. Second, they do not produce dispersion errors or spectral ringing at tracer field discontinuities and, therefore, do not heavily rely on *ad hoc* filters and fixers to damp the numerical noise. Third, they are easily configured to guarantee monotonicity and positivity of tracer fields.

In FV schemes, Eq. (2.31), integrated over the model time step and volume of a given grid box, takes the following form

$$\int_{t_n}^{t_{n+1}} \int_{\delta V} \frac{\partial \rho q}{\partial t} dV dt + \int_{t_n}^{t_{n+1}} \int_{\delta V} \nabla \cdot (\rho \mathbf{v} q) dV dt = 0 \tag{2.33}$$

or

$$\Delta V \int_{t_n}^{t_{n+1}} \frac{\partial Q}{\partial t} dt + \Delta t \int_{\delta V} (\nabla \cdot \mathbf{F}) dV = 0 \tag{2.34}$$

where

$$\mathbf{F} = \frac{1}{\Delta t} \int_{t_n}^{t_{n+1}} (\rho \mathbf{v} q) dt$$
$$Q = \frac{1}{\Delta V} \int_{\delta V} (\rho q) dV.$$

After applying the divergence theorem, Eq. (2.34) is transformed to

$$\int_{t_n}^{t_{n+1}} \frac{\partial Q}{\partial t} dt + \frac{\Delta t}{\Delta V} \oiint_{\partial V} \mathbf{F} \cdot \mathbf{n} dS = 0 \tag{2.35}$$

where ∂V is the surface around the grid cell volume and $\mathbf{n}$ is a unit vector normal to the surface and pointing outwards. Assuming a rectangular longitude-latitude horizontal model grid with uniform vertical thickness, Eq. (2.35) can be rewritten in a discretized form as

$$Q^{n+1} = Q^n + F(Q^n) + G(Q^n) + H(Q^n) \tag{2.36}$$

where F, G and H are operators that define increments to Q^n in the zonal, meridional

and vertical directions and can be written as

$$F(Q^n) = \frac{\Delta t}{\Delta S}\left(\Delta y_{i-\frac{1}{2},j}\mathcal{X}_{i-\frac{1}{2},j,k} - \Delta y_{i+\frac{1}{2},j}\mathcal{X}_{i+\frac{1}{2},j,k}\right) \tag{2.37}$$

$$G(Q^n) = \frac{\Delta t}{\Delta S}\left(\Delta x_{i,j-\frac{1}{2}}\mathcal{Y}_{i,j-\frac{1}{2},k} - \Delta x_{i,j+\frac{1}{2}}\mathcal{Y}_{i,j+\frac{1}{2},k}\right) \tag{2.38}$$

$$H(Q^n) = \frac{\Delta t}{\Delta z}\left(\mathcal{Z}_{i,j,k-\frac{1}{2}} - \mathcal{Z}_{i,j,k+\frac{1}{2}}\right) \tag{2.39}$$

where all terms are defined at the grid box edges, ΔS is the model grid cell area, and Δx and Δy are its zonal and meridional extent, $\mathcal{X}$, $\mathcal{Y}$ and $\mathcal{Z}$ are components of the mass flux vector $\mathbf{F} = (\mathcal{X}, \mathcal{Y}, \mathcal{Z})^T$.

The tracer mass flux is a product of the air mass flux and the tracer mass mixing ratio, both of which need to be determined at the grid box edges. This can be done using a sub-grid-scale field reconstruction based on the assumption of either a constant distribution (which is first-order accurate), a piecewise linear distribution (e.g., a van Leer-type, which is second-order accurate), a piecewise parabolic (which is third-order accurate), or a piece-wise cubic sub-grid distribution. For example, the van Leer-type linear distribution in two dimensions is given by Jablonowski and Williamson (2011)

$$h(x, y) = \overline{h} + \Delta a^x x + \Delta a^y y \tag{2.40}$$

where $\overline{h}$ is the grid box average that has to be conserved, and Δa^x and Δa^y are the slopes at the grid box centre in the x and y directions, respectively. The 2D piecewise parabolic (PPM) distribution can be defined as

$$h(x, y) = \overline{h} + \delta a^x x + b^x\left(\frac{1}{12} - x^2\right) + \delta a^y y + b^y\left(\frac{1}{12} - y^2\right) \tag{2.41}$$

where δa^x, b^x, δa^y and b^y are parabolic coefficients. The coefficients are defined using information from several neighbouring grid cells. Usually, a monotonicity constraint is imposed on the reconstructed distribution to ensure that no local maxima or minima (overshoots and undershoots) are created. Such a constraint is used in the advection scheme of the GEOS-Chem chemical transport model described in more detail in Section 2.3. By definition, the monotonicity constraint introduces non-linearity in the advection scheme. Some constraints can be less stringent and require only that the numerical scheme, for example, does not produce negative fields (the so-called *positive definite* constraint). The standard PPM scheme by Colella and Woodward (1984) generates a sub-grid distribution that is within the range of adjacent grid box averaged values or is constant if the the grid

box contains a local extremum of the field. Some modifications of this constraint include the *positive definite* constraint after Lin and Rood (1996), and the "relaxed" constraint after Lin (2004). The constraint is achieved by adjusting the values of coefficients in Eqs. (2.40) and (2.41). In the case of a first-order accurate (constant) distribution, this constraint is referred to as the slope limiter.

2.2.3 Numerical diffusion

A monotonicity constraint inevitably adds diffusion to the numerical scheme, with different types of constraints adding different amounts of implicit diffusion. While the latter is an inherent property of FV schemes with monotonicity constraints, other types of numerical schemes would require the diffusion to be added explicitly. In spectral or finite difference schemes, the added diffusion can be used to reduce numerical noise due to spectral ringing and dispersion errors, to prevent accumulation of energy at small scales and, generally, to ensure numerical stability. Inherent diffusion or diffusion added explicitly to damp numerical noise may also have physical meaning. It can serve as a parametrized representation of sub-grid scale processes, such as vertical transport by turbulent mixing in the planetary boundary layer (PBL) or the sub-grid eddy mass flux of salinity in oceans. However, excessive diffusion can be detrimental for transport, particularly in the presence of sharp field gradients. Therefore, the imposed monotonicity constraint in the FV schemes has to balance the amount of diffusion it introduces with the numerical errors (overshoots/undershoots, negative values, etc.) it leaves undamped.

The advantage of speed in CTMs gained from coarsening the model resolution comes at the cost of increased numerical diffusion in the advection scheme and loss of information on sub-grid scales. Diffusion can be viewed as happening on both inter- and sub-grid scales. On a sub-grid scale, this means that any tracer entering the grid box must entirely fill it according to the pre-defined sub-grid distribution, such as van Leer-type or PPM. Diffusion between model grid boxes is usually caused by the use of non-linear monotonicity constraints designed to prevent over- and undershoots and preserve positivity of the tracer fields (Jablonowski and Williamson, 2011). Although some diffusion must be present implicitly or be added explicitly to the scheme (Whitehead et al., 2011), excessive diffusion can lead to rapid destruction of tracer gradients. The diffusivity of the advection schemes depends on how well they approximate the sub-grid tracer distribution and how much of this information is transferred to the next time step. For example, as shown by Prather et al. (2008), the two commonly used FV schemes, the second-order moments (SOM) algorithm (Prather, 1986) and the Lin and Rood (1996) scheme (LR), have different

effects on simulated tracer fields with coarsening of the model resolution. The LR scheme is described in Section 2.3.2 and is used to drive advection in the GEOS-Chem chemical transport model. The SOM scheme is less diffusive as it keeps two moments of the sub-grid tracer distribution and transfers them to the next step, whereas LR does not maintain any of the moments and produces a new sub-grid tracer distribution each time step based on tracer concentrations in several adjacent cells. Therefore, the SOM scheme is less sensitive to coarsening of model resolution and performs better at preserving strong concentration gradients, for example, at the edges of the polar vortex (Searle et al., 1998).

Eventually, the choice of advection scheme depends on a number of factors such as the particular model application, model resolution, and the number of advected tracers. For example, although less diffusive, the SOM scheme may produce over/under shoots and needs an additional diffusion term to eliminate them, whereas the LR scheme implicitly contains a diffusion term in the form of monotonicity constraints. Also, the SOM scheme is stable only for Courant numbers less than unity, which puts a limit on the length of the transport time step and slows down the numerical simulation, while the LR scheme remains stable for Courant numbers larger than unity by switching to a flux form semi-Lagrangian scheme. Additionally, the SOM scheme requires much more storage to save two moments of sub-grid tracer distribution.

Both horizontal and vertical resolutions are important for reliably simulating the tracer distribution. Vertical resolution is often overlooked, but the gain in performance from increasing vertical spacing can be more substantial than that achieved from a comparable increase in horizontal resolution. Kent et al. (2012) performed a set of experiments using the dynamical core of a GCM where they showed that when increasing the horizontal resolution of the model, convergence of 3D tracer transport to the "true" (very high resolution) solution is strongly diffusion-limited due to too-coarse vertical spacing of the model. Their conclusions are valid for CTMs. For example, Eastham and Jacob (2017) arrived at the same conclusions by examining the impact of vertical resolution on the 3D transport in the GEOS-Chem CTM.

Model resolution is a significant issue in the tropopause region. Unresolved winds and increased mixing due to numerical diffusion can accelerate the STE and significantly bias the vertical distribution of atmospheric gases (Locatelli et al., 2015). Vertical resolution is also important in the PBL as the coarse model spacing may introduce errors in the PBL height and transport of tracers from the PBL to the free troposphere. Both vertical and horizontal diffusion strongly affect tracer fields with sharp concentration gradients. For example, in the troposphere, it may affect the advection of surface emission plumes and transport in narrow frontal zones of extra-tropical cyclones. In the stratosphere,

sharp tracer gradients are found at the borders of dynamic transport barriers, such as the tropopause, the polar vortex, and the stratospheric tropical pipe. Transport of chemicals in the polar vortex has been investigated at different horizontal resolutions and using different advection schemes. Searle et al. (1998) assessed O_3 loss in the Arctic polar vortex in a model driven by the SOM advection scheme. They found weak sensitivity of O_3 loss to model resolution in the range from $1.4^\circ \times 1.4^\circ$ to $5.6^\circ \times 5.6^\circ$. Bregman et al. (2006) showed that the SOM scheme at $3^\circ \times 2^\circ$ performed as well as a more diffusive first-order moments scheme at $1^\circ \times 1^\circ$. Strahan and Polansky (2006) evaluated the isolation of the polar vortex in the LR scheme at different horizontal resolutions. They found that the $4^\circ \times 5^\circ$ resolution was too coarse and allowed too much mixing through the edges of the polar vortex. Significant improvement was achieved by doubling the resolution to $2^\circ \times 2.5^\circ$ with little sensitivity to further doubling ($1^\circ \times 1.25^\circ$). However, their $1^\circ \times 1.25^\circ$ wind fields were linearly interpolated from $2^\circ \times 2.5^\circ$ and did not include additional possible eddy transport. Strahan and Polansky (2006) also showed that at $4^\circ \times 5^\circ$, too much CH_4 leaked from the tropical pipe, however, it remained unclear whether the $2^\circ \times 2.5^\circ$ resolution would be enough to maintain this barrier. Finally, Strahan et al. (2007) evaluated transport in the upper troposphere and lower stratosphere (UTLS) (including cross-tropopause transport) in the same model using a set of observations and concluded that the extratropical tropopause barrier can potentially be maintained using the LR scheme at $2^\circ \times 2.5^\circ$ resolution. Unfortunately, only one model resolution was used, therefore the sensitivity of transport to higher model resolution cannot be ruled out.

Despite the different properties of the various advection schemes available, tracer fields should converge to a single true solution as resolution increases. This was the idea behind the study by Prather et al. (2008), who compared the performance of the SOM and LR schemes in similar model environments. Consistent with earlier studies (e.g., Searle et al., 1998), the SOM scheme showed monotonic convergence to the true solution with weak sensitivity to model resolution in the range from $4^\circ \times 5^\circ$ to $1^\circ \times 1.25^\circ$. The LR scheme did not show similar convergence. However, the differences between the two schemes significantly decreased as the resolution of the LR scheme was doubled from $4^\circ \times 5^\circ$ to $2^\circ \times 2.5^\circ$. Still, the discrepancies between the SOM and LR schemes at the higher resolution were larger than those between different resolutions of the SOM scheme. This again indicated that transport at $4^\circ \times 5^\circ$ resolution using the LR scheme is too diffusive, which is consistent with Strahan and Polansky (2006). Furthermore, tracer transport with the LR scheme at $2^\circ \times 2.5^\circ$ may still contain unresolved numerical errors.

Unfortunately, running simulations at high resolution is not always feasible due to the issue of computational time, especially in data assimilation applications. A number

of assimilation studies have constrained global CH_4 emissions using models at coarse resolution, ranging from about $2° \times 2°$ to $4° \times 6°$ (Chen and Prinn, 2006; Meirink et al., 2008; Bergamaschi et al., 2009, 2013; Fraser et al., 2013; Cressot et al., 2014; Houweling et al., 2014; Monteil et al., 2013; Bruhwiler et al., 2014; Alexe et al., 2015; Locatelli et al., 2015; Feng et al., 2017). The models used different numerical schemes, however, the impact of model resolution on simulated CH_4 fields and surface fluxes has not been thoroughly evaluated. Here we build on the Strahan and Polansky (2006) study and examine the impact of model resolution on the simulation of CH_4 throughout the troposphere and stratosphere.

2.2.4 Chemical modelling of CH_4

The chemical component of modelling can be reduced to three CH_4 reactions with OH, Cl and $O(^1D)$ (reactions (1.1), (1.16) and (1.17), respectively). However, most CH_4 loss is through the first reaction. The rate of reaction (1.1) can be written as

$$-\frac{d[CH_4]}{dt} = k(T)[CH_4][OH] \tag{2.42}$$

where [ ] implies that concentrations are given as number densities and $k(T)$ is the temperature-dependent rate coefficient. The solution of Eq. (2.42) is given by

$$[CH_4](t) = [CH_4]_0 e^{k(T)[OH]t}. \tag{2.43}$$

The rate constant $k(T)$ is often expressed by the empirical Arrhenius equation

$$k(T) = Ae^{\frac{E_a}{RT}}, \tag{2.44}$$

where A is the pre-exponential factor, R is the universal gas constant and E_a is the reaction activation energy. Both A and E_a are determined experimentally. Over a range of atmospheric conditions, they are approximated to be independent of temperature as their effect is noticeably smaller compared to variability of the exponential term.

The most complete way to set up the CH_4 simulations is within a full description of the chemistry where all chemical species are active and their changes feedback on the dynamics. However, such a setup can be computationally expensive and unnecessary depending on the purpose of the simulation. In this thesis, we focus on regional partitioning of sources and sinks of CH_4 and do not aim to evaluate long-term CH_4 emission trends. Because of this, we can make several valid simplifications. First, on short (monthly to seasonal) time

scales, the radiative effect of variations in CH_4 and its oxidation products such as O_3 and H_2O is too small to noticeably affect atmospheric dynamics. Therefore, CH_4 transport can be decoupled from dynamics and the associated radiative effects can be prescribed using gas climatology. Second, the chemical loss of CH_4 is too slow to have regional impacts, although the large-scale OH distribution still matters. Fortunately, changes in the latter caused by seasonal climatological changes in CH_4 concentrations (one of the major *net* sinks of OH) can be credibly predicted. Therefore, on short time scales, OH chemistry can also be decoupled from the CH_4 simulation and OH concentrations can be prescribed by a seasonally varying climatology derived from a separate model simulation with detailed chemistry or from estimates inferred from CH_3CCl_3 measurements. The simplified modelling approach proposed above can be formulated as off-line tracer transport in off-line chemistry mode and is implemented in CTMs driven by assimilated meteorology.

2.3 GEOS-Chem

2.3.1 Metfields

The CH_4 fields are simulated using the configuration of GEOS-Chem from version v9-02 of the model. GEOS-Chem is driven by archived meteorological fields from the Goddard Earth Observing System (GEOS-5) produced by the NASA Global Modelling and Assimilation Office (GMAO) Data Assimilation System (DAS). We use version GEOS-5.2.0 of the GEOS-5 meteorological fields. A detailed description of GEOS-5 model physics and data assimilation system is given in Rienecker et al. (2008).

The atmospheric GCM (AGCM) in the GEOS-5 DAS is driven by a FV dynamic core that is based on the LR flux-form semi-Lagrangian scheme (Lin and Rood, 1996) with vertically Lagrangian control-volume discretization (Lin, 2004). It has a horizontal resolution of $0.5^\circ \times 0.667^\circ$ with 72 hybrid-sigma vertical levels and a model lid at 0.01 hPa. Variables are discretized on a staggered D-grid. The dynamical core is coupled with physics parametrization components under the Earth System Modelling Framework (ESMF). These include parametrization of convection, precipitation, cloud cover, radiation, turbulent mixing in PBL, vertical diffusion, gravity wave drag and surface fluxes from land, ocean and sea ice. The time step of the physics parametrization is 30 min. Convection is parameterized using the Relaxed Arakawa-Schubert (RAS) scheme (Moorthi and Suarez, 1992). Cloud processes, including condensation, evaporation and precipitation, are parametrized according to Bacmeister et al. (2006). The shortwave radiative transfer algorithm is from Chou and Suarez (1999) and includes absorption and

Rayleigh scattering due to water vapor, O_3, clouds and aerosols as well as absorption due to O_2 and CO_2. The longwave radiative transfer model is based on Chou et al. (2001) and includes absorption due to water vapor, CO_2, O_3, N_2O, CH_4, CFCs, clouds and aerosols. CH_4, N_2O, CFC-11, CFC-12, HCFC-22 and stratospheric H_2O are specified from the climatology of the Goddard two-dimensional CTM. O_3 is produced from the O_x family ($O_x = O_3 + O(^3P) + O(^1D)$) which is transported in the model. Turbulent mixing parametrization in the PBL follows Louis et al. (1982) for stable conditions and Lock et al. (2000) for unstable conditions. Gravity wave drag is parametrized in two ways: unresolved orographic waves forced by sub-grid mountains are modelled after McFarlane (1987), while non-orographic waves in the stratosphere and mesosphere are based on Garcia and Boville (1994). Heat and moisture fluxes, as well as exchange of momentum between the atmosphere and land, ocean and sea ice, are parametrized based on Monin-Obukhov similarity theory. Sea surface temperatures and sea ice distribution are prescribed from either observations or climatology. Exchange between the atmosphere and land processes is implemented using the Catchment Land Surface Model (Koster et al., 2000) which combines a catchment-based hydrologic model and a multi-layer snow model.

The GEOS-5 DAS is based on the three-dimensional variational data assimilation (3D-Var) algorithm with a Gridpoint Statistical Interpolation (GSI) solver. The 3D-Var approach estimates the atmospheric state, surface temperatures and coefficients for radiance bias correction at the centre of a 6-hour model time window. The system is constrained by winds, temperature, humidity and surface pressure measurements from a variety of conventional data sources such as radiosondes, balloons, aircraft, Doppler radars, surface stations, ships and buoys. Observations also include wind retrievals from MeteoSat, GOES, QuikSCAT satellites and MODIS instrument, rain rate estimates from SSM/I and the TMI satellite instruments and TOA radiances from a suite of different meteorological satellites.

GEOS-Chem uses assimilated meteorological fields, most of which are archived as 6-hourly averages, while surface pressures are provided as instantaneous fields every 6 hours. Meteorological fields are degraded to a horizontal resolution of $4^\circ \times 5^\circ$ or $2^\circ \times 2.5^\circ$ to perform global simulations. The vertical grid is reduced to 47 levels by binning layers above about 80 hPa. The final vertical spacing ranges from about 150 m in the lower troposphere to about 1 km in the upper troposphere and lower stratosphere to about 4 km in the upper stratosphere. Metfields are interpolated to the internal GEOS-Chem model transport time step of 30 min (15 min) for $4^\circ \times 5^\circ$ ($2^\circ \times 2.5^\circ$) horizontal resolution. In one experiment, we also utilize the nested (regional) capability of GEOS-Chem over North America at the native GEOS-5 horizontal resolution with a 10 min dynamic time

step.

2.3.2 Advection

As mentioned above, advection in GEOS-Chem is implemented using the Lin and Rood (1996) scheme, however, the global and regional (nested) versions of the model have certain differences in the algorithm. The numerical solution for tracer advection in the global domain can be represented by the following formula:

$$\begin{aligned} q^{n+1} = \frac{1}{\rho^{n+1}}\Bigg(\rho^n q^n + F\left(q^n + \frac{1}{2}g(q^n)\right) + \\ + G\left(q^n + \frac{1}{2}f(q^n)\right) + \\ + H\left(q^n + g\left(q^n + \frac{1}{2}f(q^n)\right) + f\left(q^n + \frac{1}{2}g(q^n)\right)\right)\Bigg), \end{aligned} \tag{2.45}$$

where n is a time index, q is the tracer volume mixing ratio, F, G and H are the flux-form advection operators that are given by Eqs. (2.37)-(2.39), f and g are advective form operators derived from Eq. (2.32) using 2^{nd}-order accurate scheme. The numerical scheme in the form of Eq. (2.45) eliminates directional operator splitting errors and preserves linear correlations between advected tracers. It is worth stressing that vertical advection is accomplished on a fixed hybrid-sigma grid where the pressure thickness of the layers changes with surface pressure. Vertical air mass fluxes are calculated based on the divergence of horizontal air mass fluxes. Horizontal air mass fluxes at cell edges are not archived but are derived on-line from pressure and horizontal wind fields, which are degraded from the native resolution cell-centred winds using a pressure weighting procedure (Wang et al., 2004). This method does not conserve mass fluxes at grid cell interfaces between different model resolutions. Moreover, as discussed in Chapter 4, it cancels some of the horizontal motion and, consequently, weakens vertical transport at coarse resolution. In Chapter 4, we partly correct for this issue by driving model advective transport by means of remapped air mass fluxes instead of winds. The cell-averaged winds in the inner advective form operators f and g are also derived from airmass fluxes at the cell edges. Horizontal airmass fluxes are also corrected using a "pressure fixer" (Rotman et al., 2004) so that the vertical integral of the air mass flux divergence remains consistent with the surface pressure tendency in each surface cell.

In the nested domain, at high resolution, advective transport is reduced to two

dimensions and is expressed by

$$q^{n+1} = \frac{1}{\rho^{n+1}}\left(\rho^n q^n + F\left(q^n + \frac{1}{2}g(q^n)\right) + G\left(q^n + \frac{1}{2}f(q^n)\right)\right). \tag{2.46}$$

This 2D advection is performed between two floating vertical Lagrangian surfaces. The tracer distribution is then remapped in a mass conserving way from the predicted Lagrangian surfaces to an Eulerian hybrid-sigma vertical grid at each transport time step.

At high latitudes at each vertical level, when the Courant number in the x-direction (C^x) becomes larger than unity, the algorithm switches to the flux-form semi-Lagrangian scheme, which makes the advection scheme stable for long time steps. C^x is partitioned into K integer and c fractional parts. The semi-Lagrangian scheme performs integer translation for the K grid boxes and the FV scheme accomplishes the remaining advection based on fractional Courant number c. For transport across the polar caps, the tracer fields are averaged in the two most northern (southern) latitudinal bands.

In the standard GEOS-Chem setup, tracer concentrations at cell edges in horizontal directions are reconstructed using the PPM scheme with a full monotonicity constraint (to eliminate both overshoots and undershoots). However, we find that a semi-monotonic constraint (which eliminates only undershoots) is less diffusive and produces better results. A quasi-monotonic method with Huynh's 2^{nd} monotonicity constraint (Huynh, 1997; Lin, 2004) is applied in the vertical.

2.3.3 Parametrization: convection and turbulent mixing

Convection is performed by a moist convective plume scheme that is driven by upward convective mass fluxes and mass detrainment rates (mass deposition rates into each layer) from the GEOS-5 RAS scheme. The coarse resolution fields are obtained by conservative remapping of the original high resolution fields. The scheme represents a slightly modified version of the convective plume model of Allen et al. (1996) inside the GEOS-Chem grid boxes.

Several assumption are made in the model. First, the plume is set to originate anywhere above the second model layer. Second, air in the plume at each level is mixed instantaneously before leaving it. The schematic of the Allen et al. (1996) plume model is shown in Fig. 2.8. We use this diagram with some changes to describe the implementation of the convection scheme in GEOS-Chem. C_k stands for convective mass flux out of the top of the plume in layer k, which is balanced by the downward air mass flux in the rest of the box ($-C_k$). We also use E_k and D_k terms to represent air entrainment into the

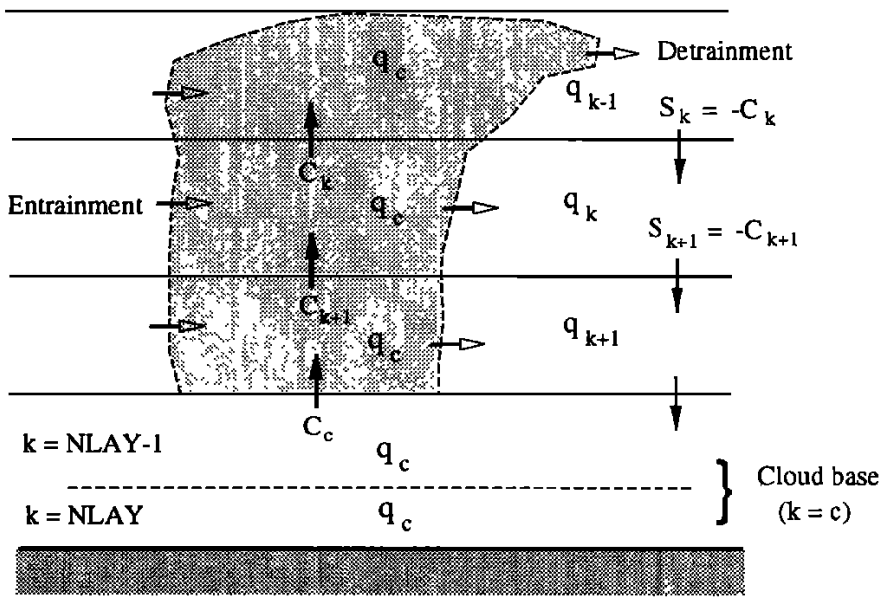

Figure 2.8: Schematic representation of moist convective plume inside the model column. C is convective mass flux at layer edges inside the plume, q is tracer mixing ratio at layer centres and S is mass flux due to subsidence at layer edges in the rest of vertical column. Adapted from Allen et al. (1996).

plume and detrainment out of the plume in layer k, respectively. The air mass balance equation for the plume in layer k is defined as

$$E_k + C_{k+1} = D_k + C_k. \tag{2.47}$$

The general equation for the evolution of the tracer mixing ratio can be written as

$$\frac{\partial q}{\partial t} = g\frac{\partial}{\partial p}\left(C(q_c - q)\right). \tag{2.48}$$

After discretization, Eq. (2.48) is transformed into

$$M_k q_k^{n+1} = M_k q_k^n + \Delta t\left(C_{k+1}(q_{c,k}^{n+1} - q_k^n) - C_k(q_{c,k}^{n+1} - q_{k-1}^n)\right) \tag{2.49}$$

where $M_k = \Delta p_k/g$ is the air mass per unit area, q_k is the tracer mixing ratio in layer k and $q_{c,k}$ is the tracer mixing ratio for the air inside the plume in the same layer that is being transported up to the next level. Here, we use the assumption of instantaneous mixing of air entering the plume. Tracer mixing ratio $q_{c,k}^{n+1}$ inside the plume in layer k at next time step $n+1$ is defined in the following way. For the layer just below the cloud

base $q_{c,k}$ is set equal q_k

$$q_{c,k} = q_k \tag{2.50}$$

and the updated layer tracer mixing ratio q_k^{n+1} is derived from the reduced Eq. (2.49)

$$M_k q_k^{n+1} = M_k q_k^n - \Delta t C_k (q_k^{n+1} - q_{k-1}^n). \tag{2.51}$$

For each subsequent vertical layer comprising the cloud, $q_{c,k}$ is obtained from the balance equation

$$(C_k + D_k)\, q_{c,k}^{n+1} = E_k q_k^n + C_{k+1} q_{c,k+1}^{n+1}. \tag{2.52}$$

Integration is performed from the surface to TOA in several iterations with a reduced internal integration time step of 5 minutes (for better accuracy).

Mixing in the PBL takes place instantaneously from the surface to the height of the mixed layer, which is archived from the GEOS DAS, so that CH_4 attains a constant mixing ratio over the depth of the PBL. The height is based on the bulk Richardson number with surface friction (Holtslag and Boville, 1993). The tracer mixing ratio in the PBL is defined as the mass-weighted mean

$$q^{n+1} = \frac{\sum_{k=1}^{L} M_k q_k^n}{M_s} \tag{2.53}$$

where L is the number of layers in the PBL and $M_s = \sum_{k=1}^{L} M_k$. The other option for turbulent mixing parametrization in GEOS-Chem is a non-local PBL mixing scheme following Lin and McElroy (2010). However, we found that the choice of scheme had only a weak impact on modelled XCH_4 fields.

2.3.4 Sources and sinks

The CH_4 emissions and loss processes in GEOS-Chem are as defined in Wecht et al. (2014). Anthropogenic emissions are based on the 2004 anthropogenic inventory from the Emission Database for Global Atmospheric Research (EDGAR) v4.2, with a $0.1^\circ \times 0.1^\circ$ resolution and no seasonality (European Commission Joint Research Centre/Netherlands Environmental Assessment Agency, 2009). This includes CH_4 emissions from natural gas and oil extraction, coal mining, livestock, landfills, waste water treatment, rice cultivation, biofuel burning and other minor sources. Natural CH_4 sources include termite emissions (Fung et al., 1991), daily fire emissions from the Global Fire Emissions Database Version 3 (GFED3) (van der Werf et al., 2010; Mu et al., 2011) and wetland emissions after Kaplan (2002) and Pickett-Heaps et al. (2011). The emission flux E in molecules of CH_4 per

square meter per second for each model surface grid box in the wetland model is given by the following equation (Pickett-Heaps et al., 2011):

$$E = \delta W F \beta A \exp\left(-\frac{E_0}{T - T_0}\right)\left(\frac{C_1}{\tau_1} + \frac{C_2}{\tau_2}\right) \tag{2.54}$$

where C_1 and C_2 (mol C m^{-2}) represent soil and carbon pools, respectively, with fixed residence times $\tau_1 = 32$ yr and $\tau_1 = 2.8$ yr. $k = A \exp\left(-\frac{E_0}{T-T_0}\right)$ is the Arrhenius factor which specifies the temperature dependence of respiration, with $A = 1.0e^{+3}$, $E_0 = 309$ K, $T_0 = 227$ K and soil temperature T taken as the GEOS-5 skin temperature. β (mol CH_4 per mol C respired) is the methane emission factor, F is an additional scaling factor used to match observed tropical and boreal CH_4 fluxes, W is the maximum potential fraction of wetlands in the model grid box, and $\delta = 1$ if a wetland is actually present over the fraction W, otherwise $\delta = 0$. Wetlands are assumed to be present in the model grid box if the soil moisture, taken from the GEOS-5 metfields, is higher then a predefined threshold. Total CH_4 emissions at different model resolutions are slightly different due to non-linear dependence of wetland emissions on the meteorology. In order to conserve total emissions and separate the effect of transport on the CH_4 fields, we remapped the coarse ($4^\circ \times 5^\circ$) resolution emissions to the higher model resolutions.

The modelled CH_4 lifetime in GEOS-Chem is about 8.9 years. The majority of CH_4 loss is due to oxidation by OH in the atmosphere. Tropospheric OH fields are prescribed as a 3D monthly climatology from a GEOS-Chem simulation of tropospheric chemistry (Park et al., 2004) and result in a tropospheric CH_4 lifetime of 9.9 years. The mean modelled tropospheric OH concentration is about 10.8×10^5 molecules cm^{-3}, which corresponds to the tropospheric methyl chloroform lifetime against OH oxidation of about 5.3 yr (Pickett-Heaps et al., 2011). Stratospheric loss due to reaction with OH, $O(^1D)$ and Cl is estimated based on archived climatology of CH_4 loss frequencies from the NASA Global Modelling Initiative (GMI) model (Murray et al., 2012). The remaining CH_4 sink is due to soil absorption after Fung et al. (1991). The CH_4 simulation is performed in off-line chemistry mode so that OH fields are not altered during a model run, which also simplifies assessment of transport in the model. It should be noted that in the active chemistry mode, the production and loss of atmospheric OH could also be affected by, for example, model resolution which would project onto the CH_4 fields.

2.4 Data assimilation

When given a model simulation and atmospheric measurements of CH_4, together with their corresponding uncertainties, we seek the best representation of the atmospheric CH_4 field that optimally fit observations and a priori constraints. The process of generating such a representation is referred to as data assimilation and can involve adjusting, for example, initial conditions of a short-range forecast as in numerical weather prediction (NWP) models, or model parameters such as CH_4 surface emissions, OH concentrations and others.

Data assimilation can be viewed as probabilistic problem and be defined in the framework of estimation theory where the task is to find the most likely solution given the probability distribution of both the model state and measurements. In inverse theory, it can also be interpreted as search for an inverse solution to infer unknown model parameters provided observational constraints. This approach is often used in satellite remote sensing and geophysics applications to infer geophysical parameters of the atmosphere, surface and solid earth given measurements of radiance or seismic signals. There are also other interpretations of the data assimilation process. One of them is given by control theory where data assimilation can be viewed as the process of searching for the model trajectory in space and time that optimally passes through the available atmospheric measurement. This interpretation is exploited by variational optimization methods such as 4D-Var. Finally, observations can be considered as noisy irregular time series, while data assimilation is a tool (e.g., the Kalman filter approach) to filter this noise and interpolate atmospheric fields to fill gaps in the measurements.

2.4.1 Basics: Optimal interpolation, 3D-Var and the Kalman filter

In the following chapters we introduce the mathematical basics of data assimilation from the standpoint of estimation theory. The atmospheric state ($\mathbf{x}$) generated by the model, together with the associated uncertainties, can be represented by a multidimensional Gaussian probability density function (p.d.f.) of the form $N(\mathbf{x}_a, \mathbf{B})$

$$p(\mathbf{x}) \propto \exp\left(-\frac{1}{2}(\mathbf{x}-\mathbf{x}_a)^T\mathbf{B}^{-1}(\mathbf{x}-\mathbf{x}_a)\right). \tag{2.55}$$

Likewise, atmospheric measurements ($\mathbf{y}$) are distributed according to $p(\mathbf{y})$. The latter can be related to the model state by the expression

$$\mathbf{y} = \mathbf{H}\mathbf{x} + \boldsymbol{\epsilon} \tag{2.56}$$

where $\mathbf{H}$ is the linear observation operator defined by Eq. (2.24) and $\boldsymbol{\epsilon}$ is observation error. Hence, the conditional probability to observe $\mathbf{y}$ given the model state $\mathbf{x}$ is given by p.d.f.

$$p(\mathbf{y}|\mathbf{x}) \propto \exp\left(-\frac{1}{2}(\mathbf{y}-\mathbf{H}\mathbf{x})^T\mathbf{R}^{-1}(\mathbf{y}-\mathbf{H}\mathbf{x})\right), \tag{2.57}$$

where we assume unbiased normally distributed errors $\boldsymbol{\epsilon}$ with covariance matrix $\mathbf{R}$.

The goal of data assimilation is to infer the model state ($\mathbf{x}$) when given atmospheric measurements ($\mathbf{y}$), i.e. to obtain the conditional p.d.f. $p(\mathbf{x}|\mathbf{y})$, which is given by Bayes theorem

$$p(\mathbf{x}|\mathbf{y}) = \frac{p(\mathbf{y}|\mathbf{x})p(\mathbf{x})}{p(\mathbf{y})}. \tag{2.58}$$

After substituting Eqs. (2.55) and (2.57) into (2.58), and considering $p(\mathbf{y})$ as a proportionality constant we obtain that

$$p(\mathbf{x}|\mathbf{y}) \propto \exp\left(-\frac{1}{2}(\mathbf{x}-\mathbf{x}_a)^T\mathbf{B}^{-1}(\mathbf{x}-\mathbf{x}_a) - \frac{1}{2}(\mathbf{y}-\mathbf{H}\mathbf{x})^T\mathbf{R}^{-1}(\mathbf{y}-\mathbf{H}\mathbf{x})\right). \tag{2.59}$$

Here, $p(\mathbf{x}|\mathbf{y})$ is also referred to as the a posteriori distribution.

The estimate of the model state ($\hat{\mathbf{x}}$) can be obtained by maximizing the a posteriori probability (the MAP method) or by minimizing the error variance of $\hat{\mathbf{x}}$ (the minimum variance (MV) method). However, for normally distributed errors and linear operator $\mathbf{H}$, both methods yield identical results. The MAP method can be reduced to minimizing the cost function

$$J(\mathbf{x}) = \frac{1}{2}(\mathbf{x}-\mathbf{x}_a)^T\mathbf{B}^{-1}(\mathbf{x}-\mathbf{x}_a) + \frac{1}{2}(\mathbf{y}+\mathbf{H}\mathbf{x})^T\mathbf{R}^{-1}(\mathbf{y}-\mathbf{H}\mathbf{x}). \tag{2.60}$$

The solution can be defined mathematically as

$$\hat{\mathbf{x}} = \mathbf{x}_a + \mathbf{K}(\mathbf{y}-\mathbf{H}\mathbf{x}) \tag{2.61}$$

where weight matrix $\mathbf{K}$ is given by

$$\mathbf{K} = \mathbf{B}\mathbf{H}^T(\mathbf{H}\mathbf{B}\mathbf{H}^T + \mathbf{R})^{-1}. \tag{2.62}$$

This analytical solution is also referred to as optimal interpolation (OI). In atmospheric modelling, the Hessian matrix $\mathbf{HBH}^T + \mathbf{R}$ is usually large and ill-conditioned, Therefore, computation of the inverse Hessian requires some approximation. The solution can also be found approximately using a search algorithm such as the conjugate gradient method with a limited number of iterations. This approach is usually referred to as the 3D variational (3D-Var) method. The drawback of using 3D-Var and OI methods is that covariances do not take into account the temporal evolution of the atmosphere. They only account for errors at the current assimilation time step. While observation errors ϵ can be assumed to be temporally uncorrelated, the covariance $\mathbf{B}$ has to evolve together with the model dynamics, where growing instabilities in the atmospheric flow amplify the initial estimate of $\mathbf{B}$. This amplification is also a consequence of the chaotic nature of atmospheric flow and is similar to the one predicted by the Fokker-Planck equation (which describes the p.d.f. evolution of the Brownian particle velocity). At the same time, the model dynamics and the observations at the previous time step could attenuate the uncertainty. More advanced data assimilation techniques such as the sequential Kalman filter (KF) or 4D-Var are built to account for the dynamic evolution of the system.

In order to formulate the standard Kalman filter (KF) algorithm we assume a linear forecast model $\mathbf{M}$ which translates the model state $\mathbf{x}_t$ at current time step to the next one:

$$\mathbf{x}_{t+1} = \mathbf{M}\mathbf{x}_t + \mathbf{u}_t \tag{2.63}$$

where $\mathbf{u}_t$ represents model errors at the current time step with unbiased Gaussian statistics $N(0, \mathbf{Q}_t)$. The model state produced by the action of the linear model operator $\mathbf{M}$ is referred to as the "forecast" $\hat{\mathbf{x}}_t^f$ with covariance matrix $\mathbf{P}_t^f$. The estimate of the current state produced by combining the "forecast" with observations is referred to as "analysis" $\hat{\mathbf{x}}_t^a$ with covariance matrix $\mathbf{P}_t^a$. The operator $\mathbf{M}$ acts on the current "analysis" to produce the next "forecast" according to

$$\hat{\mathbf{x}}_{t+1}^f = \mathbf{M}\hat{\mathbf{x}}_t^a. \tag{2.64}$$

The model state covariance evolves as

$$\mathbf{P}_{t+1}^f = \mathbf{M}\mathbf{P}_t^a\mathbf{M}^T + \mathbf{Q}_t. \tag{2.65}$$

The KF theory derives an analytic expression for the "analysis" $\hat{\mathbf{x}}_t^a$ in Eq. (2.64) and

its covariance matrix $\mathbf{P}_t^a$ in Eq. (2.65), which are given by

$$\hat{\mathbf{x}}_t^a = \hat{\mathbf{x}}_t^f + \mathbf{K}_t(\mathbf{y}_t - \mathbf{H}\hat{\mathbf{x}}_t^f), \tag{2.66}$$

$$\mathbf{P}_t^a = (\mathbf{I} - \mathbf{K}_t\mathbf{H})\mathbf{P}_t^f, \tag{2.67}$$

where the Kalman gain matrix $\mathbf{K}$ is defined as

$$\mathbf{K}_t = \mathbf{P}_t^f\mathbf{H}^T(\mathbf{H}\mathbf{P}_t^f\mathbf{H}^T + \mathbf{R}_t)^{-1}. \tag{2.68}$$

It should be noted that observations in the form of $\mathbf{R}_t$ in Eq. (2.68) damp the error growth in Eq. (2.65) through their influence in Eq. (2.67).

Similar to 3D-Var and OI, the KF uses only observations available at a given time step to produce the "analysis". However, the KF can be considered as a special case of the Kalman smoother (see, for example, Bruhwiler et al. (2005)), which can include observations available at any number of time steps. By definition, in the 4D-Var, the "analysis" is also constrained by all available observations in the assimilation time window. Under a perfect model assumption ($\mathbf{Q}_t = \mathbf{0}$), 4D-Var can be viewed as a method of optimizing initial conditions ($\mathbf{x}_0$), or model parameters $\mathbf{p}$, to produce a model trajectory that optimally fits all available observations. Therefore, the 4D-Var trajectory would be smooth and more dynamically consistent, while the KF trajectory would contain jumps in between short assimilation time windows.

Although the described theory is concerned with estimation of the model state, it is straightforward to modify the equations to estimate model parameters. In order to accomplish that, the current state can be related to model parameters through an additional operator, which can be linear in the case of surface emissions.

2.4.2 Weak and strong constraint 4D-Var

For the 4D-Var method, the 3D-Var cost function defined by Eq. (2.60) is transformed into

$$J(\mathbf{x}_0) = \sum_{t=0}^{N} \frac{1}{2}(\mathbf{y}_t - \mathbf{H}\mathbf{x}_t)^T\mathbf{R}_t^{-1}(\mathbf{y}_t - \mathbf{H}\mathbf{x}_t) + \frac{1}{2}(\mathbf{x}_0 - \mathbf{x}_{0,a})^T\mathbf{B}^{-1}(\mathbf{x}_0 - \mathbf{x}_{0,a}), \tag{2.69}$$

where the sum is over all time steps within an assimilation window. J can also be equally defined with respect to model parameters $\mathbf{p}$ with a priori error statistics given by the

normal p.d.f. $N(\mathbf{p}_a, \mathbf{B})$, i.e., Eq. (2.69) can be transformed into

$$J(\mathbf{p}) = \sum_{t=0}^{N} \frac{1}{2}(\mathbf{y}_t - \mathbf{H}\mathbf{x}_t)^T \mathbf{R}_t^{-1}(\mathbf{y}_t - \mathbf{H}\mathbf{x}_t) + \frac{1}{2}(\mathbf{p} - \mathbf{p}_a)^T \mathbf{B}^{-1}(\mathbf{p} - \mathbf{p}_a), \tag{2.70}$$

where the model states at consecutive time steps are related by the expression

$$\mathbf{x}_{t+1} = M(\mathbf{x}_t, \mathbf{p}). \tag{2.71}$$

The previous equation is different from Eq. (2.63) in several ways. First, we do not make assumptions about the linearity of the forward model in contrast to Section 2.4.1. Second, in Eq. (2.71) it is assumed that there are no errors in propagating the state forward in time. Eqs. (2.70) and (2.71) define the cost function of the so-called "strong constraint" (SC) 4D-Var method where the name implies that the model trajectory is used as a strong constraint in the optimization. However, as described by Trémolet (2006), Eq. (2.71) can be modified to account for model errors ("weak constraint") by adding corrections (forcing terms) $\mathbf{u}_{t+1}$ to the CH_4 state at time step $t+1$, so that Eq. (2.71) becomes similar to Eq. (2.63)

$$\mathbf{x}_{t+1} = M(\mathbf{x}_t, \mathbf{p}) + \mathbf{G}\mathbf{u}_{t+1} \tag{2.72}$$

where $\mathbf{u}_t$ represents forward model errors and $\mathbf{G}$ is an operator that maps them into the model state. The operator $\mathbf{G}$ can also be a mask that defines the 3D spatial region where errors in the model state occur. Therefore, the second term on the r.h.s. of Eq. (2.72) can represent additional sources and sinks of CH_4 in the atmospheric region defined by $\mathbf{G}$. The weak constraint 4D-Var method allows evaluation of model errors $\mathbf{u}_t$, which we also refer to interchangeably as state corrections or forcing terms in the rest of this thesis. The WC 4D-Var cost function is given by

$$\begin{aligned} J(\mathbf{p}, \mathbf{u}_t) = &\sum_{t=0}^{N} \frac{1}{2}(\mathbf{y}_t - \mathbf{H}\mathbf{x}_t)^T \mathbf{R}_t^{-1}(\mathbf{y}_t - \mathbf{H}\mathbf{x}_t) + \\ &\frac{1}{2}(\mathbf{p} - \mathbf{p}_a)^T \mathbf{B}^{-1}(\mathbf{p} - \mathbf{p}_a) + \sum_{t=1}^{N} \frac{1}{2}\mathbf{u}_t^T \mathbf{Q}_t^{-1}\mathbf{u}_t \end{aligned} \tag{2.73}$$

and is minimized with respect to both model parameters $\mathbf{p}$ and state corrections $\mathbf{u}_t$. Here, $\mathbf{Q}_t$ defines the a priori model error covariance matrix and model errors are assumed unbiased. As described by Trémolet (2006), $\mathbf{u}_i$ can be considered to represent model errors on time scales as short as each model time step or as long as the full assimilation period, and is assumed to be constant over the appropriate interval. In the case where the

forcing is estimated over the full assimilation window, the optimized forcing will represent a constant model bias over the whole model trajectory.

The WC 4D-Var approach was recently implemented into the GEOS-Chem model by Keller (2014), and here we describe that approach. In variational analysis, the minimum of the cost function (Eq. (2.73)) subject to equality constraints (Eq. (2.72)) can be found using the adjoint method. For simplicity, we show the derivation using the Lagrange multipliers method which, in practice, is identical to the adjoint method. The Lagrangian function is given by the equation

$$\begin{aligned}\mathcal{L}(\mathbf{p}, \mathbf{x}_t, \boldsymbol{\lambda}_t, \mathbf{u}_t) = \frac{1}{2}(\mathbf{p} - \mathbf{p}_a)^T \mathbf{B}^{-1}(\mathbf{p} - \mathbf{p}_a) + \\ \sum_{t=0}^{N} \frac{1}{2}(\mathbf{y}_t - \mathbf{H}\mathbf{x}_t)^T \mathbf{R}_t^{-1}(\mathbf{y}_t - \mathbf{H}\mathbf{x}_t) + \sum_{t=1}^{N} \frac{1}{2}\mathbf{u}_t^T \mathbf{Q}_t^{-1}\mathbf{u}_t - \\ \sum_{t=1}^{N} \boldsymbol{\lambda}_t^T \left(\mathbf{x}_t - M(\mathbf{x}_{t-1}, \mathbf{p}) - \mathbf{G}\mathbf{u}_t\right).\end{aligned} \tag{2.74}$$

We define gradients of the Lagrangian $\mathcal{L}$ with respect to $\boldsymbol{\lambda}_t$, $\mathbf{x}_t$, $\mathbf{p}$ and $\mathbf{u}_t$ by a system of equations

$$\frac{\partial \mathcal{L}}{\partial \boldsymbol{\lambda}_t} = \mathbf{x}_t - M(\mathbf{x}_{t-1}, \mathbf{p}) - \mathbf{G}\mathbf{u}_t \tag{2.75}$$

$$\frac{\partial \mathcal{L}}{\partial \mathbf{x}_t} = -\mathbf{H}^T \mathbf{R}_t^{-1} \left(\mathbf{y}_t - \mathbf{H}\mathbf{x}_t\right) - \boldsymbol{\lambda}_t + \left(\frac{\partial M}{\partial \mathbf{x}_t}\right)^T \boldsymbol{\lambda}_{t+1} \tag{2.76}$$

$$\frac{\partial \mathcal{L}}{\partial \mathbf{x}_N} = -\mathbf{H}^T \mathbf{R}_t^{-1} \left(\mathbf{y}_N - \mathbf{H}\mathbf{x}_N\right) - \boldsymbol{\lambda}_N \tag{2.77}$$

$$\frac{\partial \mathcal{L}}{\partial \mathbf{p}} = \mathbf{B}^{-1}(\mathbf{p} - \mathbf{p}_a) - \sum_{t=1}^{N} \boldsymbol{\lambda}_t^T \frac{\partial M}{\partial \mathbf{p}}(\mathbf{x}_{t-1}, \mathbf{p}) \tag{2.78}$$

$$\frac{\partial \mathcal{L}}{\partial \mathbf{u}_t} = \mathbf{Q}_t^{-1}\mathbf{u}_t + \mathbf{G}^T \boldsymbol{\lambda}_t \tag{2.79}$$

where $\mathbf{M} = \frac{\partial M}{\partial \mathbf{x}_t}$ is the tangent linear model (TLM) and $\mathbf{M}^T$ is its adjoint. At the minimum, the gradients of $\mathcal{L}$ defined by Eqs. (2.75)-(2.79) are equal to zero. Eq. (2.75) then transforms into Eq. (2.72), while Eqs. (2.76)-(2.77) yield the adjoint model equations

$$\begin{aligned}\boldsymbol{\lambda}_N &= -\mathbf{H}^T \mathbf{R}_t^{-1} \left(\mathbf{y}_N - \mathbf{H}\mathbf{x}_N\right) \\ \boldsymbol{\lambda}_t &= \left(\frac{\partial M}{\partial \mathbf{x}_t}\right)^T \boldsymbol{\lambda}_{t+1} - \mathbf{H}^T \mathbf{R}_t^{-1} \left(\mathbf{y}_t - \mathbf{H}\mathbf{x}_t\right).\end{aligned} \tag{2.80}$$

Values of $\boldsymbol{\lambda}_t$ are derived from the forward and the adjoint model integrations and substituted into Eqs. (2.78)-(2.79). In general, $\frac{\partial \mathcal{L}}{\partial \mathbf{u}_t}$ and $\frac{\partial \mathcal{L}}{\partial \mathbf{p}}$ are not equal to zero as the minimum has yet to be reached by iteratively minimizing the Lagrangian function $\mathcal{L}$ using a gradient-based algorithm. In GEOS-Chem, this is done using the L-BFGS-B algorithm (Byrd et al., 1995). In summary, the entire WC 4D-Var algorithm consists of the following steps:

1. Run the forward model (Eq. (2.72)) from time t_1 to t_N using the current estimates of parameters $\mathbf{p}$ and forcing terms $\mathbf{u}_t$.

2. Run the adjoint model and simultaneously accumulate the estimates of $\boldsymbol{\lambda}_t$ based on Eq. (2.80).

3. Calculate the gradients of $\mathcal{L}$ with respect to $\mathbf{p}$ and $\mathbf{u}_t$ using Eqs. (2.78)-(2.79) and estimates of $\boldsymbol{\lambda}_t$.

4. Update the estimates of $\mathbf{p}$ and $\mathbf{u}_t$ using the minimization algorithm (for example, L-BFGS-B) using $\frac{\partial \mathcal{L}}{\partial \mathbf{u}_t}$ and $\frac{\partial \mathcal{L}}{\partial \mathbf{p}}$.

5. Repeat steps 1-4 until convergence is reached.

Similar to the KF, the 4D-Var scheme propagates the covariance matrix $\mathbf{B}$ forward in time with the model dynamics. Unlike the KF, it does not directly calculate the "analysis" covariance matrix, due to the way the cost function is minimized. Different approximate methods exist to obtain estimates of the a posteriori covariance matrix, such as the Monte Carlo approach or using the Davidon-Fletcher-Powell formula to approximate calculation of the Hessian.

Generally, CH_4 surface emissions, but not OH, are optimized as part of assimilation. Variations in the signal of chemical loss are relatively weak and smooth and, therefore, are challenging to constrain. At most, inversion systems may attempt to estimate global scaling factors on a priori prescribed OH concentrations. However, there is a more robust way to do that using methyl chloroform observations (Montzka et al., 2011), which provide global OH estimates with uncertainty of about 15%.

2.4.3 Adjoint

In order to integrate the adjoint model, Eq. (2.80), backward in time, the algorithm requires the adjoint of the tangent linear model $\left(\frac{\partial M}{\partial \mathbf{x}_t}\right)^T$. For these purposes, we use version v35 of the GEOS-Chem adjoint, which is based on version v8-02-01 of the forward

model, with updates up to v9-02. The adjoint model is described by Henze et al. (2007) and has been used for assimilation of CH_4 observations by Wecht et al. (2012, 2014) and Turner et al. (2015). Derivation of the adjoint would be simplified if all processes in the model could be represented in a matrix form. For example, the effect of chemistry and emissions can be represented by simple linear operators acting on the CH_4 state. The adjoint of these operators is straightforward to code and implement. Turbulent mixing parametrization, defined by Eq. (2.53), can be expressed as $\mathbf{q}_{1,L}^{n+1} = \mathbf{H}\mathbf{q}_{1,L}^{n}$, where the linear matrix operator $\mathbf{H}$ is defined as

$$\mathbf{H} = \begin{pmatrix} \frac{M_1}{M_s} & \cdots & \frac{M_L}{M_s} \\ \vdots & \ddots & \vdots \\ \frac{M_1}{M_s} & \cdots & \frac{M_L}{M_s} \end{pmatrix}. \tag{2.81}$$

The adjoint of turbulent mixing would be defined as a transpose of the matrix $\mathbf{H}$. The adjoint of convection defined by Eqs. (2.48)-(2.52) is less straightforward and is calculated using the Tangent and Adjoint Model Compiler (TAMC, Giering and Kaminski, 1998).

Derivation of the advection adjoint in GEOS-Chem is based on the continuous adjoint approach: the equation for the adjoint is first obtained in a continuous form and then discretized. The tracer continuity equation in advective form is given by Eq. (2.32)

$$\frac{\partial q}{\partial t} + \mathbf{v} \cdot \nabla q = 0.$$

Using the concept of tangent linear model, we obtain

$$\frac{\partial \delta q}{\partial t} = -\mathbf{v} \cdot \nabla \delta q = \mathbf{M}\delta q. \tag{2.82}$$

For the adjoint operator $\mathbf{M}^*$, we seek a form that satisfies

$$\frac{\partial \lambda}{\partial t} = \mathbf{M}^* \lambda. \tag{2.83}$$

It is derived from the Lagrange identity

$$\int_{t_0}^{T} \iiint_V (\mathbf{M}\delta q \lambda)\, dV dt = \int_{t_0}^{T} \iiint_V (\delta q \mathbf{M}^* \lambda)\, dV dt. \tag{2.84}$$

Integrating by parts and applying the divergence theorem, we obtain

$$-\int_{t_0}^{T} \oiint_{\partial V} \delta q \lambda \mathbf{v} \cdot \mathbf{n} dS dt + \int_{t_0}^{T} \iiint_V \delta q \left(\nabla \cdot (\mathbf{v}\lambda) - \mathbf{M}^* \lambda\right) dV dt = 0. \tag{2.85}$$

The first term on the l.h.s. contains the surface integral over the boundary of volume V where the unit vector $\mathbf{n}$ is defined at the surface ∂V and points outward. In the global domain, the atmosphere contains only the upper (TOA) and lower (surface) boundaries where the first term vanishes as either $\mathbf{v}$ and $\mathbf{n}$ are orthogonal to each other or $\mathbf{v} = \mathbf{0}$. In one-way nested regions, with prescribed tracer boundary conditions, the adjoint variable λ is set equal to zero at the boundary ($\lambda(\zeta, t) = 0, \forall \zeta \in \partial V$) so that the first term also vanishes. Then, the second term on the l.h.s. should equal zero for any arbitrary perturbations δq, which can be satisfied only if

$$\mathbf{M}^* \lambda = \nabla \cdot (\mathbf{v}\lambda). \tag{2.86}$$

Therefore, the equation for the advection adjoint is defined as

$$\frac{\partial \lambda}{\partial t} = \nabla \cdot (\mathbf{v}\lambda). \tag{2.87}$$

If we define new adjoint variables $\hat{\lambda} = \lambda/\rho$ and $\mathbf{v}_- = -\mathbf{v}$ and assume that grid box density is constant during one integration time step, Eq. (2.87) transforms into

$$\frac{\partial \rho\hat{\lambda}}{\partial t} + \nabla \cdot (\mathbf{v}_- \rho\hat{\lambda}) = 0 \tag{2.88}$$

which is equivalent to Eq. (2.31) (the continuity equation for tracer advection). Therefore, the adjoint of advection can be obtained using the original forward model code. In order to do that, one needs to reverse the sign of the winds, divide the adjoint variables by density fields before integration, and multiply by the density fields afterwards.

Chapter 3

Diagnosing model biases using weak constraint 4D-Var

3.1 Introduction

Significant effort has been put into characterizing surface emissions of CH_4 in order to attribute recent trends in the atmospheric CH_4 concentrations. A number of satellites, such as Envisat carrying SCIAMACHY (Schneising et al., 2011), GOSAT carrying TANSO-FTS (Kuze et al., 2009), Sentinel-5P with TROPOMI on-board (Veefkind et al., 2012), MERLIN (Kiemle et al., 2014), GOSAT-2 (Nakajima et al., 2017), and GeoCarb (Polonsky et al., 2014), have been launched or are proposed to measure atmospheric CH_4 in order to constrain its sources. However, current regional CH_4 emissions remain largely uncertain (Saunois et al., 2016a). One of the biggest challenges for reducing uncertainty on emission estimates is the relatively weak signal of emissions in the atmospheric column of CH_4, which puts tight requirements on the accuracy of satellite measurements. However, while future satellite instruments and improved spectroscopy are expected to provide better CH_4 measurements, errors in the atmospheric models used to simulate CH_4 remain poorly characterized. While random model errors can be accounted for in flux assimilation using various methods, the impact of biases in chemistry and transport are often neglected. In the case of CH_4, which is a relatively long-lived gas with an atmospheric lifetime of about 9 years (Prather et al., 2012), chemistry plays a critical role in long-term trends (McNorton et al., 2016) while transport, alone or coupled with chemistry, defines how total surface emissions are distributed on a regional scale. Therefore, transport errors, such as those produced by numerical advection schemes, biases and uncertainties of meteorological fields, and parametrization of sub-grid scale processes, may significantly undermine our

ability to use models to relate emissions to atmospheric observations, and thus our ability to improve CH_4 emission estimates (Prather et al., 2008; Locatelli et al., 2015; Patra et al., 2011).

One potential solution is to apply a bias correction to the model in the context of the inversion analysis. Simple bias correction schemes with uniform or latitudinally dependent bias estimates have been attempted before (Fraser et al., 2013; Monteil et al., 2013; Alexe et al., 2015; Locatelli et al., 2015). Here we explore the utility of a weak constraint 4D-Var method to characterize forward model errors. In contrast, the traditional strong constraint 4D-Var method assumes that the model is perfect. The WC 4D-Var method was introduced by Sasaki (1970) and used in numerical weather prediction (NWP) models by Derber (1989), Zupanski (1997) and Trémolet (2006, 2007). It was first applied by Keller (2014) in a CTM, to characterize biases in the GEOS-Chem simulation of atmospheric CO. One of the first attempts to apply bias correction in chemical data assimilation was done in the framework of the suboptimal Kalman filter by Lamarque et al. (2004), who used the bias estimation approach of Dee and Da Silva (1998) to constrain the CO state using measurements from the Measurement of Pollution in the Troposphere (MOPITT) instrument. The study pointed to the possibility of errors in the model vertical transport, however most of estimated biases were attributed to poor a priori estimates of CO surface emissions in the model. The major challenge for such type of analyses is the limited information that is available about the global vertical distribution of CH_4 in the atmosphere. There are satellite observations that contain information about the CH_4 distribution in the middle and upper troposphere, such as the thermal infrared CH_4 retrievals from the TES instrument on-board the NASA Aura satellite (Worden et al., 2012), or in the stratosphere, such as the solar occultation measurements from the ACE-FTS (Bernath et al., 2005)) on-board SCISAT satellite. However, the accuracy of these measurements (for example, Wecht et al., 2012; De Mazière et al., 2008) may not be sufficient to detect model errors. The most accurate satellite measurements are those of the dry-air mole fraction of CH_4 in the total atmospheric column (XCH_4) obtained by TANSO-FTS on-board GOSAT. However, these measurements provide less vertical information on CH_4 than those from TES or ACE-FTS. Highly accurate aircraft CH_4 profile measurements would be an ideal source of information, but they are limited in space and time. We explore here the information content of GOSAT CH_4 observations and show that despite being designed to constrain surface emissions, they contain sufficient information to help characterize possible model errors. We assimilate the GOSAT observations using the WC 4D-Var data assimilation approach to estimate biases in GEOS-Chem. This approach is shown to provide a valuable tool for diagnosing and determining the origin of model

errors.

This chapter is organized as follows. Section 3.2 gives an overview of the forward model, observations, and the WC 4D-Var method. It also contains a description of the various sensitivity experiments conducted through a series of Observing System Simulation Experiments (OSSEs). In Section 3.3, we present the results of the sensitivity experiments as well as the results of the assimilation of real GOSAT observations. Section 3.4 provides an interpretation of the pattern of model biases estimated from the GOSAT assimilation. Finally, conclusions are given in Section 3.5.

3.2 Data and methods

3.2.1 The GEOS-Chem model

We use the GEOS-Chem v8-02-01 global forward and adjoint model (Henze et al., 2007), which are described in Sections 2.3 and 2.4.3, respectively. For the analysis presented here, we focus on the period of 1 February 2010 to 31 May 2010. The CH_4 fields were spun up at a resolution of $4^\circ \times 5^\circ$ and $2^\circ \times 2.5^\circ$ for about 5.5 years until July 2009. From July 2009 to January 2010, we assimilated the GOSAT Proxy XCH_4 retrievals (Parker et al., 2015) to obtain monthly mean emission estimates at the $4^\circ \times 5^\circ$ resolution. The optimized emissions were then regridded and used to perform forward model simulations at the $2^\circ \times 2.5^\circ$ resolution for the same period from July 2009 to January 2010. The updated model fields on 1 February 2010 at both model resolutions were taken as initial condition for the analysis period. As a result, the initial conditions at both resolutions contain similar amounts of CH_4 in the atmosphere. However, CH_4 is distributed differently, reflecting the balance between emissions and transport at each model resolution.

3.2.2 Measurements

We obtain information about the CH_4 distribution in the atmosphere from XCH_4 retrievals (Parker et al., 2011) from the TANSO-FTS on-board GOSAT, which are described in Section 2.1.1. We use GOSAT averaging kernels and a priori profiles to smooth the GEOS-Chem CH_4 fields and map them onto the measurement space of the GOSAT retrievals. The absence of vertical information in the measurements is a challenge for constraining the 3D structure of model errors. However, we expect vertical structure to emerge from atmospheric transport patterns. For example, the majority of the CH_4 mass is transported into the North American domain through the western boundary in the jet stream in the upper troposphere. Therefore, XCH_4 observations over North America

would be more sensitive to past CH_4 concentrations in the upper troposphere, upwind over the Pacific and Asia. Here, we explore the potential utility of the weak constraint 4D-Var scheme to discern model biases using the GOSAT XCH_4 data.

Figure 3.1 shows the mean XCH_4 fields from February to May 2010 modelled by GEOS-Chem at $4° \times 5°$ resolution (top panel) and as measured by GOSAT (bottom panel). A number of features in modelled XCH_4 can be identified. There is a clear inter-hemispheric difference with smaller XCH_4 in the Southern hemisphere. Enhanced XCH_4 concentrations can be observed over China, India, equatorial Africa and South America, with weaker signals also present over Europe and the eastern US, which, to first approximation, are related to local surface CH_4 emissions. Major features generally agree between the modelled and observed XCH_4 fields, however there are also a number of discrepancies that are discussed in Section 3.3.

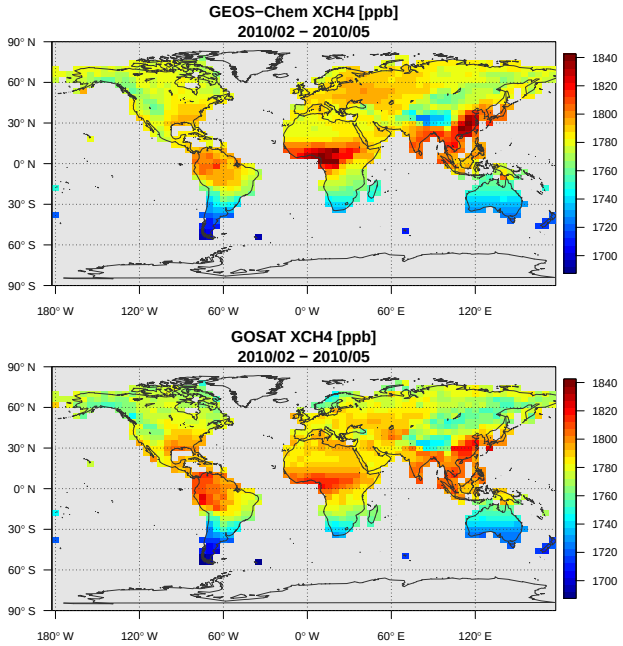

Figure 3.1: Mean XCH_4 fields from February to May 2010. Top: XCH_4 modelled by GEOS-Chem at $4° \times 5°$ resolution, co-located with GOSAT observations and smoothed with GOSAT averaging kernels. Bottom: GOSAT XCH_4 retrievals based on the new CO_2 proxy.

The a priori and constrained model CH_4 fields were also validated against in situ NOAA-ESRL surface CH_4 measurements (Dlugokencky et al., 2016), HIPPO-3 aircraft measurements (Wofsy et al., 2011), TCCON ground-based XCH_4 retrievals (Wunch et al., 2011) and ACE-FTS space-based CH_4 retrievals (Boone et al., 2005), and results are shown in Section 3.3. Description of the datasets and instruments can be found in Sections 2.1.2-2.1.4

3.2.3 Weak constraint 4D-Var approach

The weak constraint (WC) 4D-Var was introduced in Section 2.4.2. Here, we describe the specific configuration of the WC 4D-Var method that was used in this chapter. We utilized the reported uncertainty on the GOSAT XCH_4 retrievals as observation errors (with the median value of approximately 10 ppb) and inflated it to match the GOSAT scatter against TCCON observations. It was assumed that the observation errors are uncorrelated, so that the observation error covariance matrix $\mathbf{R}$ was assumed to be diagonal. The a priori error covariance matrix $\mathbf{B}$ was also assumed to be diagonal, with 50% uncertainty on CH_4 emissions in each surface grid box. Emissions were not split into categories but optimized as monthly totals in each surface grid box. GOSAT provides global coverage with a period of three days. Therefore, we did not attempt to characterize the global model errors on time scales shorter than that and explored keeping the forcing terms constant over a time interval that varied from the minimum of three days up to one month. Little is known about the a priori structure of the model errors, so in the design of the cost function, a priori estimates of model errors were set to zero.

The WC algorithm optimizes scaling factors (SFs) for both the forcing terms and the model parameters (surface emissions). Emission SFs are ratios of optimized emissions to a priori emissions, while forcing SFs are the ratios of optimized forcing terms to some constant scaling parameter $\mathbf{u}_0$. The WC inverse method becomes sensitive to the choice of scaling parameter when working with multidimensional problems. This choice does not affect the Lagrangian $\mathcal{L}$ (Eq. (2.74)), however, it does change the relative magnitude of $\mathcal{L}$ gradients with respect to forcing terms $\frac{\partial \mathcal{L}}{\partial \mathbf{u}_i}$ (Eq. (2.79)) and to surface emissions $\frac{\partial \mathcal{L}}{\partial \mathbf{p}}$ (Eq. (2.78)). The state vector of the WC inversion is largely dominated by a number of forcing SFs as opposed to emission SFs (with the ratio of up to 500:1). Due to the high dimensionality of the problem, the L-BFGS-B optimization algorithm can search only a fraction of parameter space in the direction of the largest gradient descent. Therefore, it becomes sensitive to the relative magnitude of forcing gradients $\frac{\partial \mathcal{L}}{\partial \mathbf{u}_i}$ versus emission gradients $\frac{\partial \mathcal{L}}{\partial \mathbf{p}}$. For large values of $\mathbf{u}_0$ (for example, $\mathbf{u}_0 \geq 50$ ppb), the algorithm descends in the direction of forcing gradient and the WC inversion is transformed into the so-called "full state assimilation". Meanwhile, small values of $\mathbf{u}_0$ (for example, $\mathbf{u}_0 \leq 0.05$ ppb) force the algorithm to minimize the cost function in the direction of emission gradients ("flux assimilation"). The value of $\mathbf{u}_0 = 1.0$ ppb was also empirically chosen to perform simultaneous optimization of the emissions and forcing terms ("flux+state assimilation").

Application of the WC 4D-Var method is sensitive to the specification of the covariance matrix $\mathbf{Q}$, which is difficult to characterize. We adopted a diagonal structure of matrix $\mathbf{Q}$ as our standard option. This implies there was no explicit temporal or spatial correlation

assumed between model errors. However, some correlation is implicitly present in the model and emerges from both atmospheric transport patterns and the definition of constant forcing time window. Still, assigning adequate model error uncertainty is one of the major challenges for using WC method. Generally, there is no single recipe for that, as model errors come from variety of sources, with different characteristics and, moreover, vary on daily to seasonal time scales. Additionally, in practice, there is usually no way to properly validate whether the inversion correctly attributed biases in CH_4 fields as being caused by surface emissions, model errors, or observational biases. This latter statement is related to the fact that surface emission, observational bias, and some model errors may leave similar signatures in the CH_4 fields that would not be easy to distinguish even with perfect observational coverage. The situation may even be worse for CH_4 biases if incorrect emissions and model errors mask each other and do not show up in the model comparison with GOSAT data.

Given these issues, our focus here is not on estimating surface emissions of CH_4. Instead, we use the WC 4D-Var method to optimally constrain the CH_4 state and explore the nature of the errors in the model CH_4 simulation. We performed two types of inversions: "full state assimilation" and "flux+state assimilation". Given that little is known about the distribution of model errors, in both cases we chose a uniform spatial and temporal structure of model error uncertainty q so that the model error covariance is defined as $\mathbf{Q} = q^2\mathbf{I}$.

We conducted a series of parameter tuning experiments where the WC 4D-Var analysis was performed using values of q ranging from 0.05 ppb to about 2000 ppb, and optimized CH_4 fields were validated against independent observations. The experiments showed that for any values of q above 50 ppb, the fit of optimized CH_4 fields to independent observations did not change noticeably. However, for values of q below 50 ppb the fit deteriorated as q became smaller. Therefore, q was set to 50 ppb. Although the latter is too large for the actual model error uncertainty estimate, it reduces the weight of the model error term in the WC cost function defined by Eq. (2.73) and, perhaps, makes the latter easier to minimize. It is important to note that the magnitude of estimated forcing terms change with changing q, but the general pattern of positive and negative corrections was not significantly affected by the choice of q. In the experiments, described in Section 3.2.4, we found that the WC method was still able to significantly improve the model and capture the bias in the CH_4 state. Therefore, we considered a uniform structure for $\mathbf{Q}$ to be a satisfactory assumption for the initial assessment of model errors in the context of the WC 4D-Var analysis.

Generally, at some point during the convergence process, the assimilation will start

fitting the noise in GOSAT observations. This can be prevented by stopping the iterative algorithm when the reduced chi-squared value for the fitted model approximately equals unity. In practice, the real uncertainty on GOSAT XCH_4 retrievals is unknown due to unaccounted errors in the CO_2 proxy fields, for example, so we used a different approach. For each WC inversion that was performed, we monitored the evolution of optimized model fields and compared them to independent observations (from TCCON, the NOAA in situ network, and from the HIPPO-3 aircraft campaign). The iterative process was terminated when the fit to independent observations did not improve any further or started to get worse, based on the assumption that after this threshold the optimization began to fit noise in GOSAT observations. On average, the level of noise was estimated to correspond to GOSAT XCH_4 uncertainty of about 10 ppb.

3.2.4 Sensitivity experiments

To evaluate the performance of the WC 4D-Var scheme, we conducted a series of OSSEs. We began with an analysis of the sensitivity of the GOSAT observational coverage to the CH_4 state in the model. Following Liu et al. (2015) and Byrne et al. (2017), we constructed the sensitivity function

$$J = \sum_{n=1}^{N} (\mathrm{XCH}_4^{model})_n \tag{3.1}$$

where XCH_4^{model} are modelled CH_4 dry-air mole fractions sampled at the times and locations of the GOSAT observations and convolved with GOSAT scene-dependent averaging kernels. The sensitivity function is summed over all N observations available over the assimilation period. The sensitivity of the GOSAT observations to the modelled state is obtained by taking the derivative of J with respect to the state, using the model adjoint

$$\frac{\partial J}{\partial x_{i,j,k,t}} = \sum_{n=1}^{N} \frac{\partial (\mathrm{XCH}_4^{model})_n}{\partial x_{i,j,k,t}} \tag{3.2}$$

where $x_{i,j,k,t}$ is the CH_4 at longitude i, latitude j, altitude k, and time t. The sensitivities are expressed in units of ppb kg^{-1} and can be understood as the propagated backward-in-time GOSAT averaging kernels weighted by the value proportional to the local surface pressure. The sensitivities can be summed in space or time to give an aggregated view of the sensitivity of the GOSAT observational coverage to the modelled CH_4 state.

We then conducted four OSSEs in order to evaluate the performance of the WC 4D-Var method in regards to mitigating artificially introduced model errors for February-May

2010. We investigated model biases from four different sources: surface emissions, vertical transport, chemical loss, and initial conditions. The "true" model state was defined as optimized CH_4 global fields obtained from an inversion analysis to constrain estimates of monthly CH_4 fluxes using GOSAT XCH_4 Proxy retrievals during the same time period. We also refer to these constrained fluxes as "true" CH_4 surface emissions. The CH_4 initial conditions are described in Section 3.2.1. This "true" model state was used to produce pseudo GOSAT XCH_4 measurements by sampling it at the corresponding times and locations of the real GOSAT measurements and then convolving them with GOSAT averaging kernels. The perturbed model was defined by introducing bias in the "true" model from one of the four specified sources of model bias. Then the pseudo-observations were used to constrain and mitigate biases in the perturbed model CH_4 state. The performance of the pseudo-inversion was evaluated by comparing the recovered CH_4 fields to the "true" ones. The analyses were conducted for the standard period of four months (February-May 2010), but most of the results are presented for the second month of the assimilation period, March 2010. This gives the model errors time to accumulate during February, and provides two months of pseudo-data, in April and May, to constrain the CH_4 state in March. No noise was added to the pseudo-observations. Given that and the fact that, usually, the state is most optimally constrained in the middle of the assimilation period, we believe that the OSSEs should reveal the best performance of the WC method.

The emission bias was introduced by replacing the "true" CH_4 emissions with the original a priori emissions. Convection and chemistry were artificially biased by completely turning them off in the model for the duration of the assimilation period. Finally, a bias in initial conditions was introduced by replacing the "true" initial conditions with the ones obtained by running the forward model without convection and with 70% of the a priori emissions from July 1, 2009, to February 1, 2010, the beginning of the assimilation period. Generally, the effect of transport and chemistry on the CH_4 fields in GEOS-Chem is only weakly non-linear which allows us to use large state perturbations. The applied biases were intentionally designed to be extreme; for the real world applications, we expect to deal with less extreme model errors.

We configured the WC method to carry out "full state assimilation" (as described in Section 3.2.3) and have the freedom to determine independently the location of the bias. The constant forcing time window was set equal to three days and forcing terms were optimized throughout the entire atmosphere (mask $\mathbf{G}$ equals unity everywhere). This particular configuration may not be optimal to mitigate a specific type of bias in a real assimilation with limited observational coverage. Here, we intend to investigate the performance of the measurements and the assimilation method when no information is

given about the sources and magnitude of model errors. We also conducted a SC 4D-Var assimilation experiment for comparisons with the WC approach in the OSSE with biased surface emissions.

3.2.5 Assimilation configuration with real GOSAT data

For the assimilation of the real GOSAT CH_4 data, we used the WC 4D-Var configuration as in the OSSEs. The CH_4 initial conditions are described in Section 3.2.1. The CH_4 state was constrained during the standard four-month period of February-May 2010 using GOSAT observations during the same period. Modifications to the WC 4D-Var configuration included tuning the length of constant forcing time window T and the horizontal/vertical structure of the forcing mask $\mathbf{G}$. We also performed additional tuning of the method in order to explore the nature of the model errors. The quality of constrained CH_4 fields was evaluated against independent observations. Additionally, we compared results of the WC inversions with results of the SC surface flux assimilation.

The a priori model validation presented in Section 3.3.2.2 pointed to the fact that the stratosphere in GEOS-Chem at $4^\circ \times 5^\circ$ resolution, particularly, at high latitudes, may be positively biased. A similar result was obtained by Saad et al. (2016). The OSSE results also suggested that the WC assimilation may benefit from additional constraints on stratospheric forcing terms. Therefore, we imposed a negativity bound in the L-BFGS-B algorithm for the optimization of the forcing terms in the extra-tropical stratosphere (above about 210 hPa and poleward of 44°) at $4^\circ \times 5^\circ$ resolution. No bound was imposed on forcing terms in the $2^\circ \times 2.5^\circ$ resolution assimilation.

In one set of experiments, we performed "full state assimilation" and changed the length of the time window over which the forcing terms are held constant in the assimilation. The forcing mask $\mathbf{G}$ comprised the entire atmosphere, and biases in the CH_4 state potentially induced by incorrect surface emissions were treated as just another source of model errors included in forcing terms. The length for the forcing window was varied from three to 30 days. Short time windows would be more appropriate if the model was affected by temporally changing biases such as those related to transient mesoscale eddies. However, the observations may not be able to constrain the short time scales. Also, for short temporal correlation length scales, there is a higher risk that the inversion will fit noise or possible biases in observations. In contrast, the use of long time windows introduces additional temporal correlations between forcing terms that may be suitable only for the mitigation of stationary systematic biases in the model, such as those related to surface emissions, chemistry or stationary transport errors.

Table 3.1: Summary of experiments with real GOSAT data

Parameter	Parameter options	Type of assimilation
Length of forcing time window	3, 7, 14 or 30 days	"full state assimilation"
Vertical extent of forcing mask	• from surface to TOA • from 750 hPa to TOA • from 500 hPa to TOA • from 250 hPa to TOA	"source+state assimilation"
Horizontal extent of forcing mask	• globally • stratosphere + four regions in the troposphere	"source+state assimilation"
Horizontal model resolution	• $4^\circ \times 5^\circ$ • $2^\circ \times 2.5^\circ$	"full state assimilation"

In a different set of experiments, we carried out WC 4D-Var "source+state assimilation' and explored the optimal design of the forcing mask **G**. Here, the forcing window was set equal to three days. First, we explored the vertical structure of **G**. The algorithm was configured to optimize forcing terms in 1) in the whole atmosphere, or 2) above about 750hPa, or 3) above about 500hPa, or 4) above about 200hPa. Then the horizontal structure of **G** was modified as well. Forcing terms were applied globally throughout the stratosphere and in the troposphere only over four separate regions: the three regions defined by the boundaries of the GEOS-Chem nested model domains (North America (NA), Europe (EU), and China with South-East Asia (CH)) and over Equatorial Africa (EQAf). In these experiments we also attempted to narrow down the origin of the biases affecting the model at the location of the TCCON and NOAA measurement sites.

All the above experiments were conducted at the $4^\circ \times 5^\circ$ model resolution. In one additional experiment, we applied WC 4D-Var "full state assimilation" to constrain errors in GEOS-Chem at $2^\circ \times 2.5^\circ$ resolution. We used the standard method configuration with a forcing time window of three days. The only difference between the $4^\circ \times 5^\circ$ and the $2^\circ \times 2.5^\circ$ assimilation was in the initial conditions which are described in Section 3.2.1.

3.3 Results

3.3.1 OSSE experiments

We began with an analysis of the sensitivity of the GOSAT observation coverage to the CH_4 state in the model. Shown in Fig. 3.2 is the total zonal adjoint sensitivity (upper panel), which is a sum of adjoint sensitivities over time and longitude. Additionally, we included a vertical slice of total adjoint sensitivity over 34°N latitude, which is a

sum of adjoint sensitivities over time (lower panel). As suggested by the upper panel in Fig. 3.2, the entire GOSAT observing system from February to May 2010 has the greatest sensitivity to CH_4 changes in the UTLS in the northern hemisphere. This can be explained by the fact that winds in the UTLS region are stronger than in the lower troposphere, hence any change in CH_4 fields in the former region will eventually affect a larger number of GOSAT measurement locations in the model. The sensitivity in the tropics is approximately half that in mid-latitudes. The lower panel in Fig. 3.2 also shows that over the oceans not covered by GOSAT observations (for example, over the Pacific Ocean, between 120°E and 130°W) the sensitivity is reduced near the surface and is increased in the UTLS where most of CH_4 mass flux from Asia enters the North American domain. Increased sensitivity between approximately 30°W and 30°E is due to the large number of GOSAT measurements over the Sahara desert.

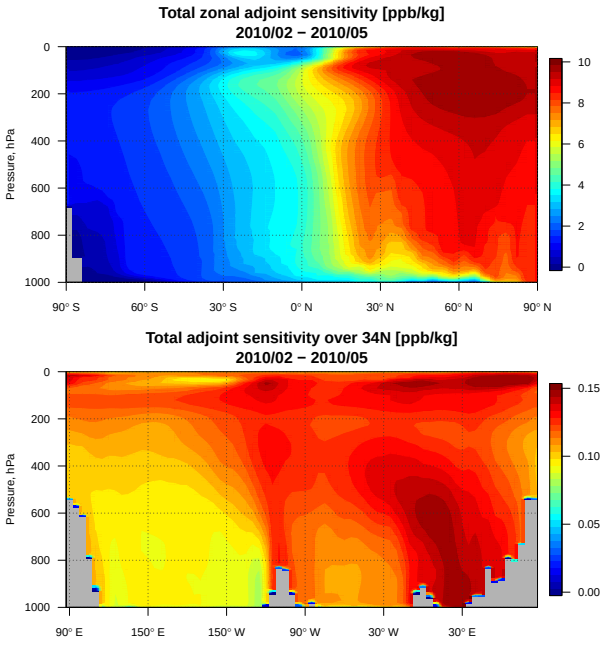

Figure 3.2: Map of the total adjoint sensitivity of GOSAT observations in February-May 2010 to the CH_4 state during the same period (sum over time). Top: total zonal adjoint sensitivity (sum of adjoint sensitivities over longitude). Bottom: slice over 34°N.

In the first OSSE, we tested the ability of both the SC and WC 4D-Var schemes to reproduce mean CH_4 atmospheric concentrations for the case of biased emissions. It is expected that the SC 4D-Var method will produce better results than the WC 4D-Var due to the fact that, when using the SC method, we implicitly supply the assimilation with knowledge about the source of the bias. The results of the OSSE are presented in Fig. 3.3, which shows the mean difference between the recovered state and the "true" CH_4

fields. The results confirm that the SC 4D-Var method is better at removing CH_4 biases due to emissions. As shown in Fig. 3.4, the major challenge for the WC 4D-Var was to constrain CH_4 fields in the boundary layer below about 800 hPa above large emission sources. Here the method failed to properly correct the vertical structure of the model biases. Due to weak vertical sensitivity of the pseudo-data, it is difficult for the WC 4D-Var method to mitigate strong localized vertical bias. Instead, it compensates for the bias by applying relatively weak CH_4 state adjustment of the opposite sign in the column of the atmosphere above, particularly in the stratosphere (see Fig. 3.4).

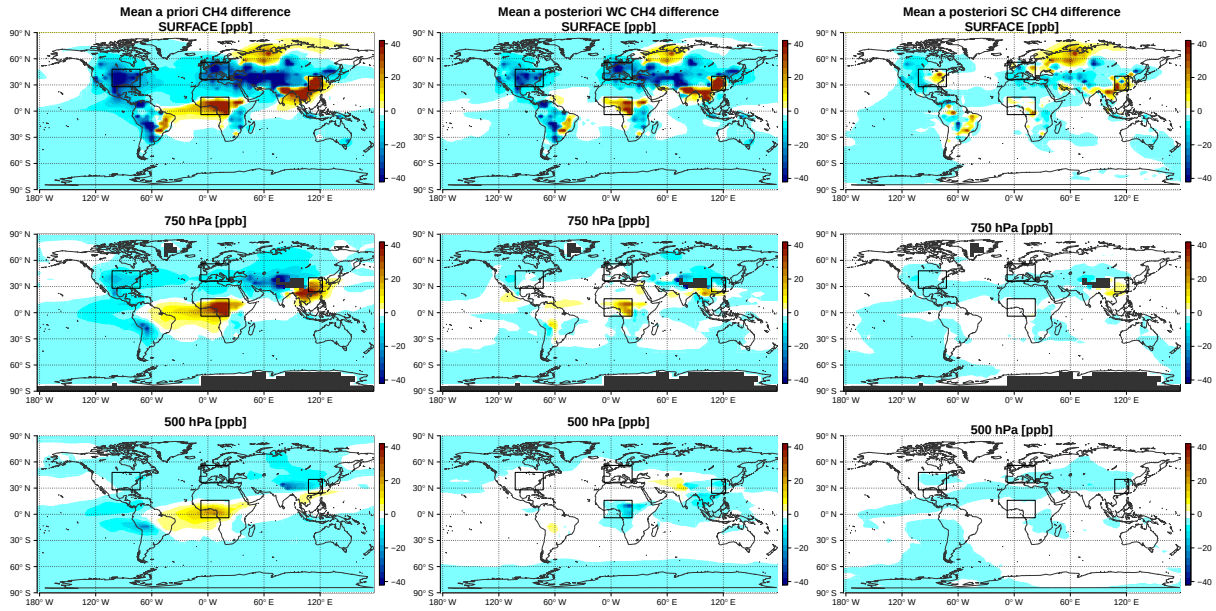

Figure 3.3: Results of the OSSE with biased surface emissions. Mean negative difference in March 2010 between the "true" CH_4 state and the biased CH_4 state (first column), the WC optimized CH_4 state (second column), the SC optimized CH_4 state (third column).

In order to improve the WC 4D-Var performance, additional information is required about the location (which can be specified using forcing mask $\mathbf{G}$) and properties of the model errors. For example, the equivalent of perfect temporal correlation can be accounted for using a constant forcing time window (one month instead of three days for emissions). Improvement in the performance can also be achieved by constraining the magnitude of vertical model errors by assigning non-uniform vertical structure to the forcing error covariance matrix $\mathbf{Q}$, with larger uncertainty in the boundary layer and smaller in the free troposphere. A simple example of gain in the performance by using a 30-day forcing time window is shown in Fig. 3.4. In a another example, shown in the same figure, we changed forcing mask $\mathbf{G}$ so that model errors should be located in the troposphere (approximately, from the surface to 200 hPa). However, this appeared to be a rather loose constraint on

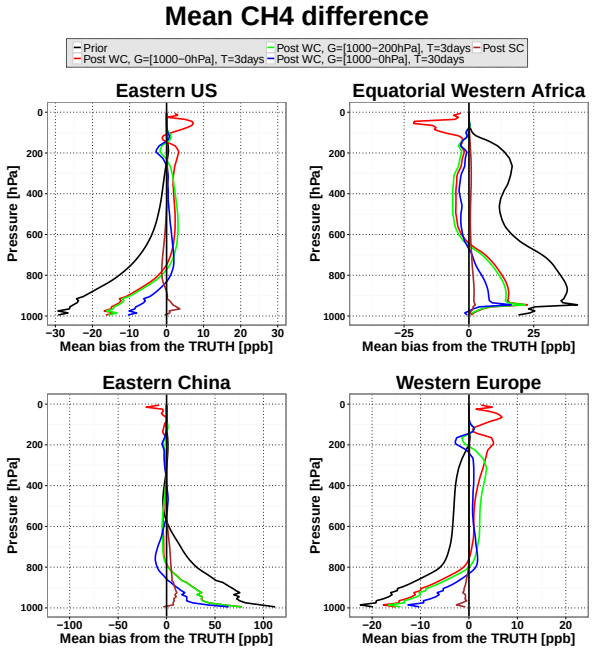

Figure 3.4: Results of the OSSE with biased surface emissions. Mean difference profiles in March 2010 for the four regions depicted in Fig. 3.3 as black boxes. The differences are between the biased a priori and the "true" CH_4 fields (black lines), and between the WC/SC optimized and the "true" CH_4 fields (see colors in the legend). $G = [...]$ represents the vertical extent of the forcing mask, and T is the constant forcing time window.

the potential location of model errors and did not result in a significant improvement in CH_4 state in the troposphere beyond the previous experiments.

In the second OSSE, we investigated the ability of the WC 4D-Var method to mitigate errors in vertical transport by turning off convection in the model. This resulted in enhanced CH_4 concentrations in the lower troposphere and reduced CH_4 in the upper troposphere over the main source regions. Furthermore, the positive CH_4 anomalies in the lower troposphere were partly advected upstream. For example, over Equatorial Africa and South America, instead of being convectively transported up over the continent, CH_4 emissions were transported westwards by winds in the lower and middle troposphere (see Fig. 3.5, first column, third row). As shown, the state corrections capture the general horizontal and vertical structure of the a priori bias. The largest corrections are co-located with the regions of deep moist convection. Positive corrections are found in the upper troposphere and negative corrections in the lower. Still, this was not sufficient to fully mitigate the bias, but, at least, it shows that GOSAT retrievals possess sensitivity to biases in vertical transport and can distinguish them even when the sources and magnitude of model errors are unknown.

Figure 3.6 shows the mean vertical distribution of the a priori and a posteriori residual

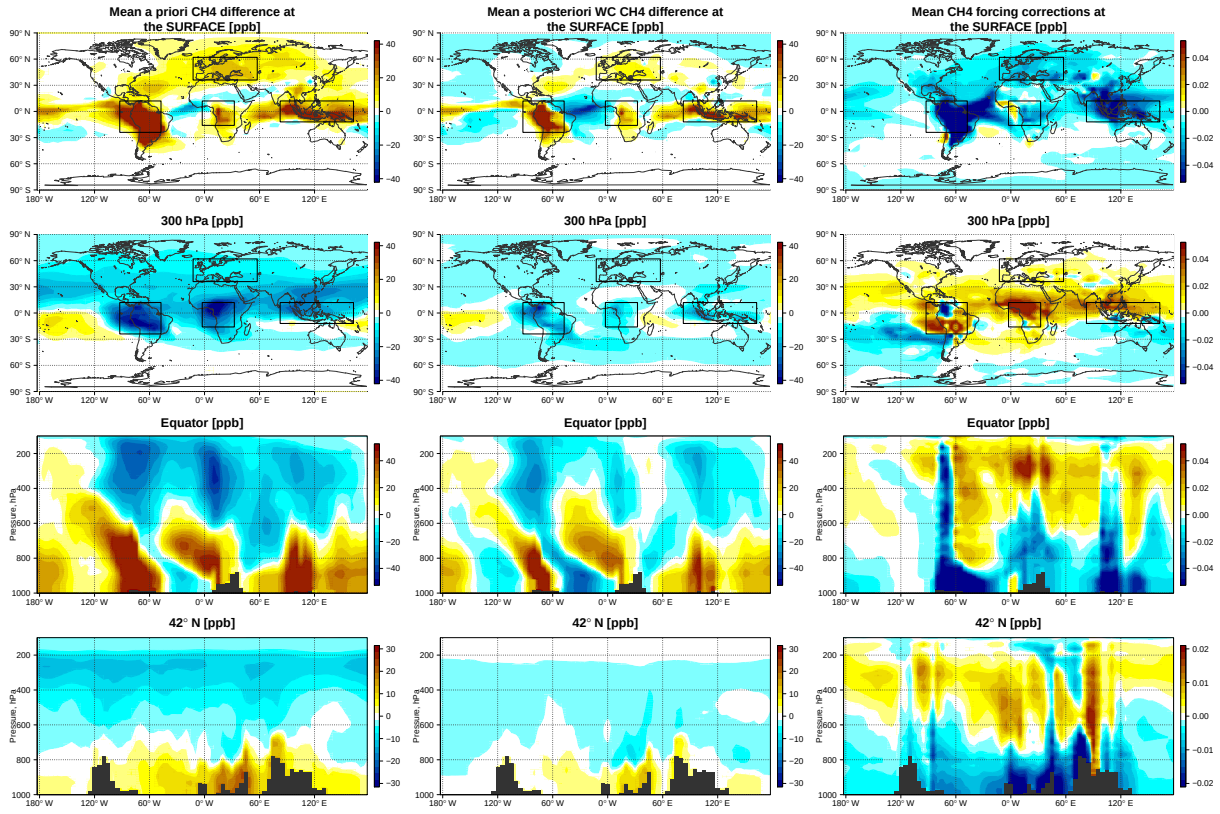

Figure 3.5: Results of the OSSE with biased convection. Mean negative difference in March 2010 between the "true" CH_4 state and the biased CH_4 state (first column), the WC optimized CH_4 state (second column); the mean WC state corrections in March 2010 (third column).

biases in the CH_4 state over four key regions. In mid-latitudes over Europe, the convection bias was much weaker than over the tropics and reached just about 16 ppb near the surface. The WC 4D-Var method was able to strongly mitigate this bias above 800 hPa level and reduce it by more than a factor of two below 800 hPa. The worst results in terms of the fractional reduction of the bias were achieved over Equatorial South-East Asia, most likely due to fewer GOSAT retrievals over this region and limited constraints on the CH_4 distribution in the outflow region. The assimilation has also removed a large fraction of the bias in the CH_4 fields over Equatorial Africa and South America, particularly, in the middle and upper troposphere over Africa and in the lower troposphere over South America.

The chemistry bias created by turning off the reaction of CH_4 with OH was the least challenging for the WC 4D-Var scheme to mitigate. This bias was rather smooth in the troposphere and did not contain small-scale features. Although the actual chemistry bias in the model may have more complex vertical structure, we do not expect chemical biases to be as strongly localized as the biases associated with emissions and vertical transport.

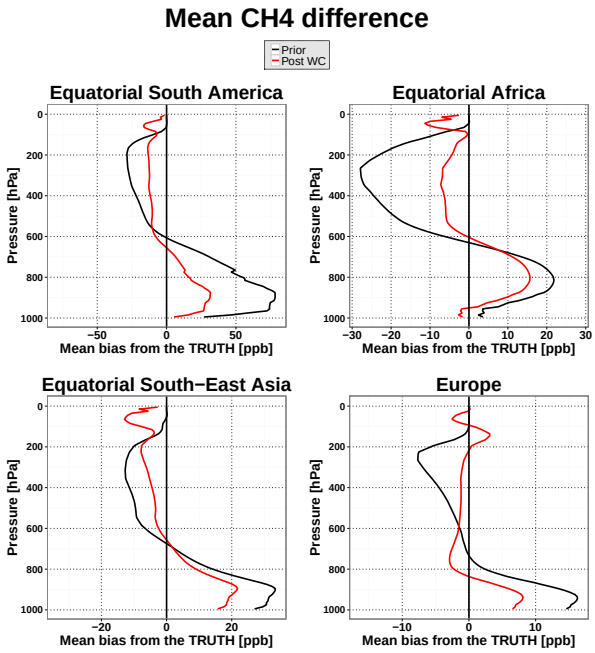

Figure 3.6: Results of the OSSE with biased convection. Mean difference profiles in March 2010 for the four regions depicted in Fig. 3.5 as black boxes. The differences are between the biased a priori and the "true" CH_4 fields (black lines), and between the WC optimized and the "true" CH_4 fields (red lines).

The a priori and a posteriori residual biases, as well as WC forcing terms, are shown in the Fig. 3.7. The WC state optimization performed best over land where the a priori biases were almost completely removed. The optimization was least successful over the oceans in the lower troposphere. This situation is consistent with the distribution of the adjoint sensitivities shown in Fig. 3.2, which points to the lower GOSAT sensitivity to variations in CH_4 in the lower troposphere as compared to the upper troposphere and the absence of GOSAT observations over oceans in our analysis. Shown in Fig. 3.8 are the mean vertical profiles of the prior and posterior bias over the same four regions represented in Fig. 3.6. The model does indeed successfully mitigate the bias. Over the convection regions in the tropics, there is some compensatory corrections in the lower troposphere and in the UTLS, which is probably due to the fast vertical transport in these regions and the limited vertical information in the GOSAT retrievals.

We noticed that forcing terms (Fig. 3.7, third column) decrease in magnitude from the mid-troposphere to the surface. In order to understand this pattern, the GOSAT adjoint sensitivity in Fig. 3.2 should be converted from units of ppb kg^{-1} to units of ppb ppb^{-1}. It appears that the chemistry forcing terms closely follow the pattern of adjoint sensitivity when expressed in units of ppb ppb^{-1}. This is because the imposed chemistry bias in

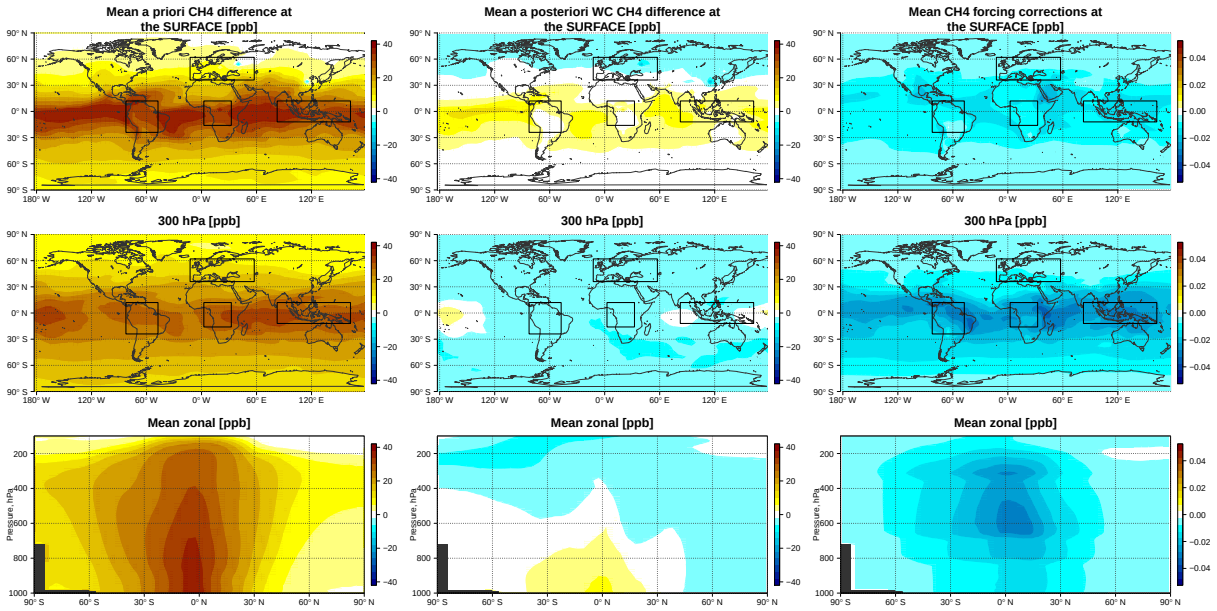

Figure 3.7: Results of the OSSE with biased chemistry. Mean negative difference in March 2010 between the "true" CH_4 state and the biased CH_4 state (first column), the WC optimized CH_4 state (second column); the mean WC state corrections in March 2010 (third column).

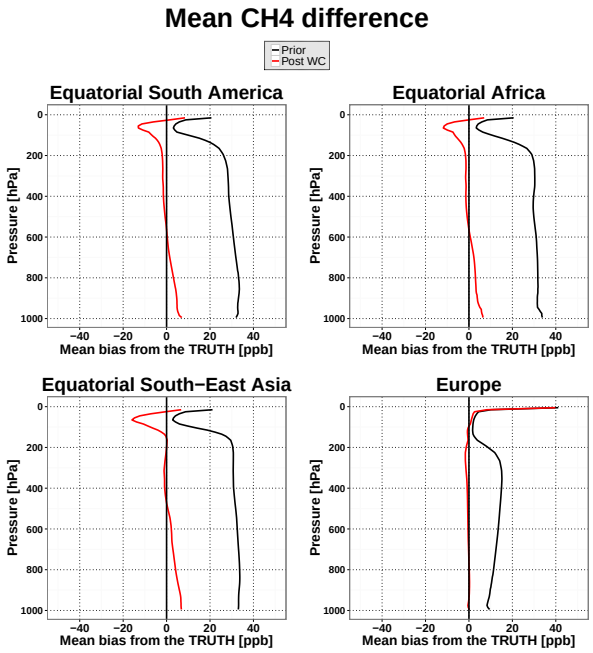

Figure 3.8: Results of the OSSE with biased chemistry. Mean difference profiles in March 2010 for the four regions depicted in Fig. 3.7 as black boxes. The differences are between the biased a priori and the "true" CH_4 fields (black lines), and between the WC optimized and the "true" CH_4 fields (red lines).

units of ppb had almost uniform vertical structure in the troposphere, while WC forcing

terms can be approximated as real model errors convolved with averaging kernels of the entire GOSAT observing system where the latter is represented by the adjoint sensitivity.

In the final OSSE, we biased the initial conditions by introducing biases in both the vertical distribution of CH_4 (due to the absence of convection) and in the total CH_4 mass in the atmosphere (due to running the model with different surface emissions in the previous seven months). The initial condition bias is shown on the left panel in Fig. 3.9. The stratosphere and southern troposphere were positively biased, whereas the northern troposphere was negatively biased. The right panel shows the structure of the a posteriori bias after the WC assimilation, on the last day of the assimilation window, May 31. It shows that the CH_4 state converged to the "true" concentrations everywhere except in the upper stratosphere; the positive upper stratospheric bias was compensated for in the column by a small negative CH_4 bias in the troposphere and the lower stratosphere.

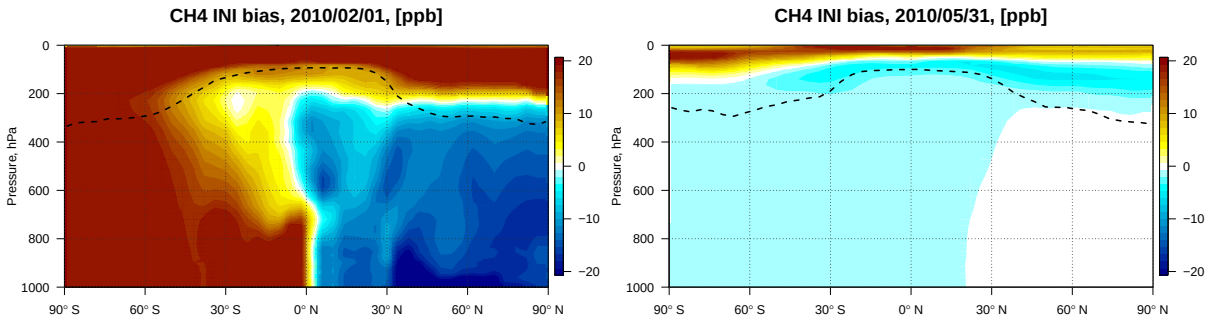

Figure 3.9: Results of the OSSE with biased initial conditions. Left: a priori bias in initial conditions. Right: a posteriori bias at the end of assimilation window. The dashed line represents the mean tropopause height on May 31, 2010 taken from GEOS5 meteorological fields.

In Fig. 3.10, we show the evolution of the initial condition bias, relative to the total atmospheric CH_4 mass, in four altitude bins in each hemisphere. What this figure does not show is how much the bias was adjusted in the actual initial conditions. The perfect observing system would completely remove it on February 1. However, what is shown on February 1 is just an 8% reduction, in each of the eight regions, relative to the a priori with the rest of the bias propagated onto the assimilation period. The different regions converged to the "true" CH_4 mass at different rates. The tropospheric CH_4 burden in both hemispheres (in the 1000-700 hPa, 700-400 hPa, and 400-200 hPa bins) converged mainly during the first month, however, convergence was slower near the surface in the SH. Above 200 hPa, the convergence rate was slow, such that by the third month the CH_4 mass had not fully recovered, particularly, in the SH where there is reduced sensitivity due to the limited GOSAT observational coverage. The slower convergence (compared to the troposphere) is believed to follow from weak vertical mixing in the stratosphere. This

suggests that additional vertical correlation between forcing terms in the stratosphere would be beneficial to accelerate convergence in the stratosphere.

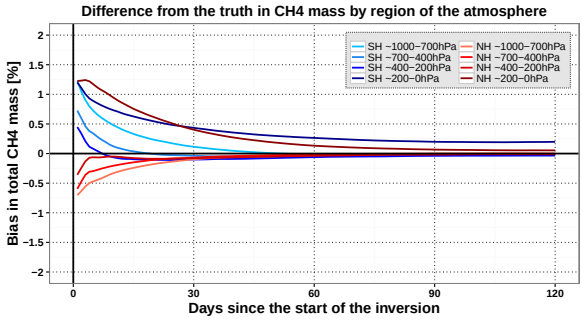

Figure 3.10: Results of the OSSE with biased initial condition. CH_4 mass difference between the WC optimized and the "true" CH_4 fields in eight regions of the atmosphere outlined in the legend ("SH" and "NH" stand for the southern hemisphere and northern hemisphere, respectively).

3.3.2 Assimilation of real GOSAT retrievals

The bias between the GOSAT data and the 4° × 5° a priori and a posteriori model is shown in Fig. 3.11. Here we will refer to the a posteriori results as the **WC_T3_G1000_4x5** assimilation, which is for WC 4D-Var assimilation at 4° × 5° resolution with a three-day forcing time window and a forcing mask **G** comprising the entire atmosphere. As can be seen, there are large positive a priori biases at high latitudes in the northern hemisphere and in some low latitude regions, such as Equatorial Africa and eastern China. The **WC_T3_G1000_4x5** assimilation successfully reduces the a priori bias. There is some residual high-latitude bias, which resembles noise or bias in the GOSAT observations. In Chapter 4, where we examine the impact of model resolution on the modelled CH_4 distribution, we show that the large positive a priori CH_4 bias over China may partly be explained by weakening of the vertical transport in the model due to the coarse 4° × 5° resolution. The large bias in Equatorial Africa may also represent the combined effect of biased vertical transport and incorrect surface emissions. In Chapter 4, we also show that a significant fraction of the high-latitude bias comes from the stratosphere and is a consequence of running the model at 4° × 5° resolution. As a result, here we repeated the GOSAT WC assimilation at a higher resolution of 2° × 2.5°. The results, which are shown in Fig. 3.12, reveal that the high-latitude a priori bias is indeed smaller in the 2° × 2.5° model. At the higher resolution, the WC assimilation also successfully reduces the model bias. For comparison, we repeated the assimilation at 4° × 5°, but optimized the emissions instead of the CH_4 state. The results for this experiment, referred to as **SC_4x5**, are

shown in Fig. 3.13. As can be seen, the SC assimilation leaves significantly larger residual biases. The pattern of the residual bias indicates that there were other biases that the assimilation could not fit at the expense of the emissions. We will investigate possible sources for these biases below.

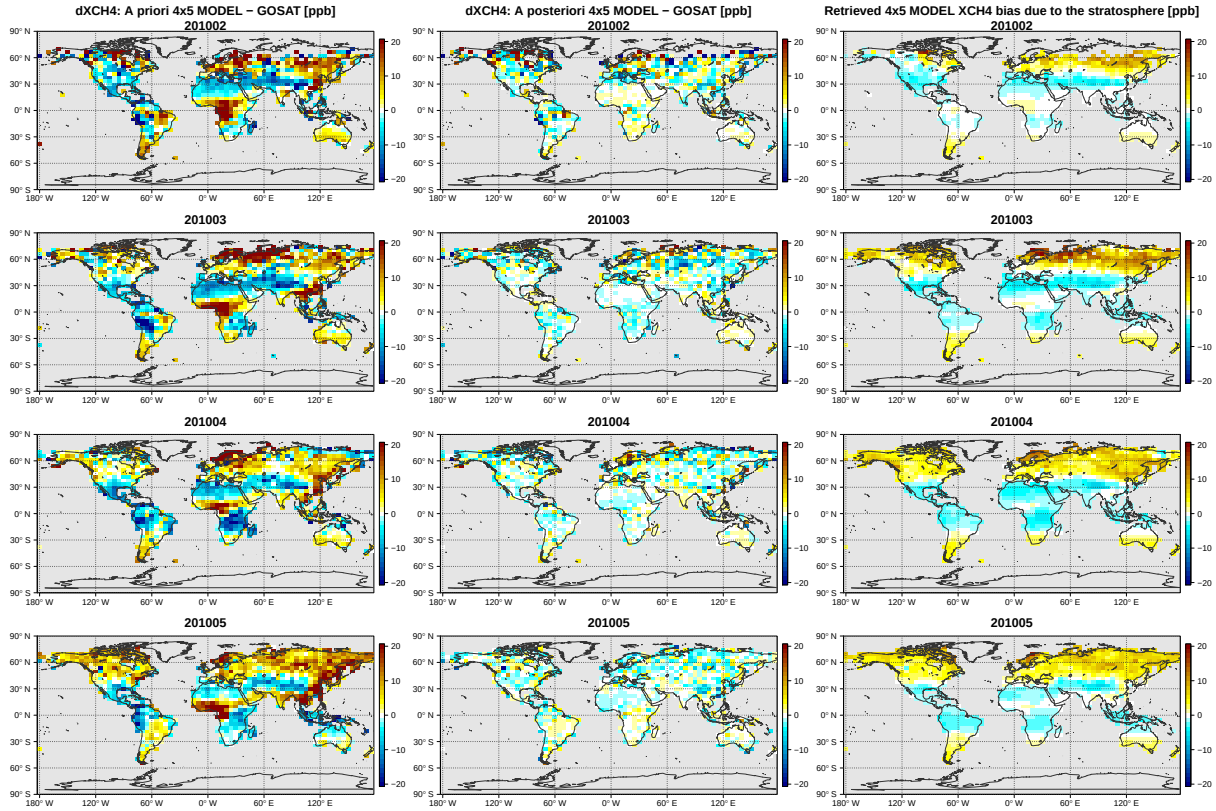

Figure 3.11: The $4° \times 5°$ resolution model mean monthly fields. First column: a priori XCH_4 difference between GEOS-Chem and GOSAT. Second column: a posteriori **WC_T3_G1000_4x5** XCH_4 difference between GEOS-Chem and GOSAT. Third column: the optimized stratospheric XCH_4 bias calculated as difference between forward model runs with optimized forcing terms applied in the troposphere only and throughout the entire atmosphere, co-located with GOSAT observations and smoothed with GOSAT averaging kernels.

The signal of surface emissions is mixed with possible model errors in the troposphere, such as those related to vertical transport. Biases in CH_4 fields caused by incorrect surface emissions will in some cases have identical structure to those caused by biased uplift, which may complicate the interpretation of WC 4D-Var state corrections in the troposphere. On the other hand, it takes much longer for the surface emissions signal to mix into the stratosphere. We assumed that, on the short (four-month) time scale of the simulation, optimized forcing corrections $\mathbf{u}_i$ in the stratosphere can be considered independent from the influence of surface emissions. The third column in Fig. 3.11 and 3.12 shows the actual mean monthly bias in the a priori CH_4 fields that was corrected by the stratospheric

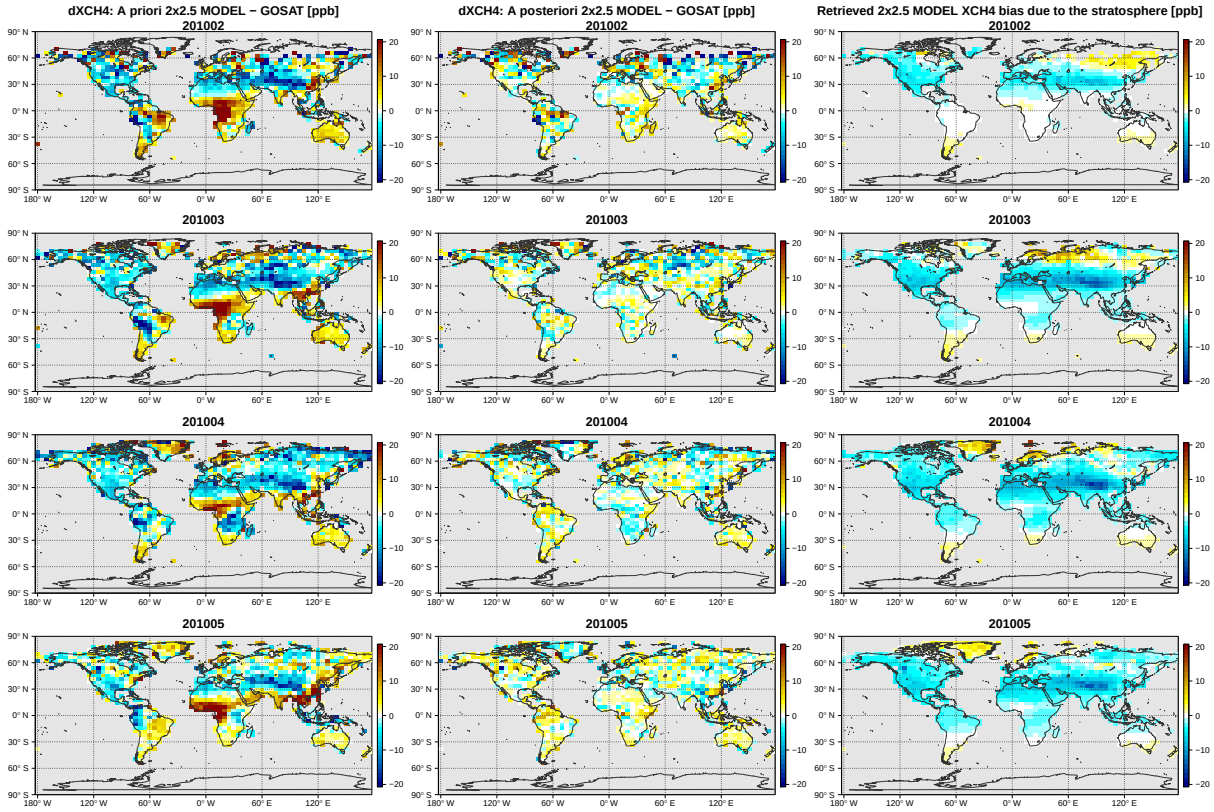

Figure 3.12: Same as Fig. 3.11 but for the 2° × 2.5° resolution model.

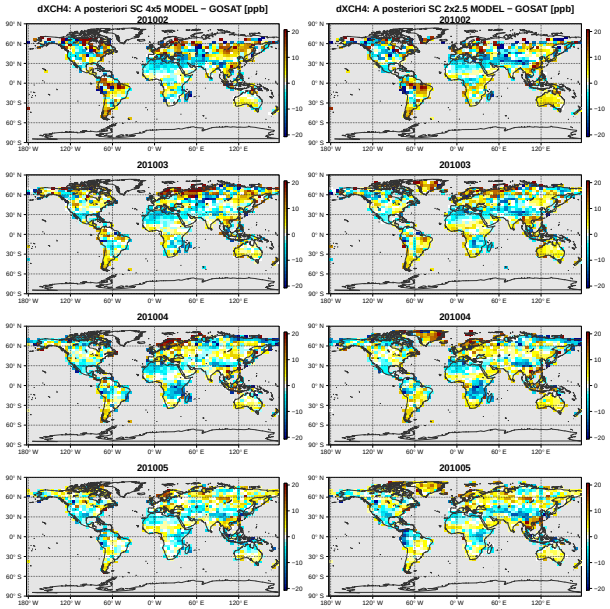

Figure 3.13: Mean monthly a posteriori XCH_4 difference between GEOS-Chem and GOSAT. First column: SC "flux assimilation" at 4° × 5° resolution (**SC_4x5**). Second column: SC "flux assimilation" at 2° × 2.5° resolution (**SC_2x25**).

Table 3.2: Validation of a priori, **SC_4x5** and **WC_T3_G1000_4x5** optimized CH_4 fields using TCCON XCH_4 and NOAA surface *in situ* observation (mean statistics for the period of February-May 2010).

	Bias [ppb]			Scatter [ppb]			Correlation (R)			Slope of regression		
	Prior	SC	WC	Prior	SC	WC	Prior	SC	WC	Prior	SC	WC
TCCON	9.1	8.2	5.3	15.0	13.8	9.9	0.83	0.86	0.93	1.16	1.14	1.07
NOAA	15.1	9.7	9.6	34.5	30.3	28.9	0.88	0.89	0.90	0.90	1.02	0.99

forcing terms alone. The bias corrections in the $2^\circ \times 2.5^\circ$ CH_4 simulation are smaller than for the $4^\circ \times 5^\circ$ simulation, which is consistent with results in Chapter 4, where we showed that part of the stratospheric bias at $4^\circ \times 5^\circ$ resolution is due to the model resolution itself. The WC inversion results suggest that the $4^\circ \times 5^\circ$ model is positively biased in the stratosphere at the high latitudes and weakly negatively biased in the tropics. In contrast, the $2^\circ \times 2.5^\circ$ model is mainly negatively biased in the stratosphere, particularly, around 30-40°N, except for a few high-latitude regions, possibly related to the polar vortex. Generally, the negative bias in the GEOS-Chem stratosphere at the $2^\circ \times 2.5^\circ$ resolution around 30-40°N identified by the WC method agrees with the GEOS-Chem bias against ACE-FTS and HIPPO-3 observations shown in the evaluation discussion below (see the first column in Fig. 3.16).

3.3.2.1 Evaluation with TCCON and NOAA data

Table 3.2 presents the results of the evaluation of the **SC_4x5** and the **WC_T3_G1000_4x5** assimilation with the NOAA in situ and TCCON data, whereas Table 3.3 gives the comparison results at the individual TCCON sites. Based on the OSSE results in Section 3.3.1 and provided that the only model bias is due to incorrect surface emissions, we would anticipate the WC assimilation to produce generally worse fits to the surface measurements than the SC assimilation. The comparisons show that both approaches produced similar improvements in the fit to the NOAA observations, with slightly better performance from the WC method. The SC assimilation also had limited impact on the overall fit to the TCCON XCH_4 retrievals. Table 3.3 shows the benefits of using the WC method, which significantly improved the correlation and reduced the bias between the model and the TCCON observations. The results suggest that GEOS-Chem a priori CH_4 simulation suffered from biases which were not related to incorrect surface emissions.

The evaluation of the WC tuning experiments are summarized in Fig. 3.14. The series of WC experiments described in Section 3.2.5 were organized into four groups. The most

sensitive indicator of the quality of the model-observations fit is the correlation. The scatter was close to the level of GOSAT measurement noise and did not change as much among the different assimilation experiments. In the first group of experiments we changed the vertical extent of the forcing mask **G**. We found that restricting the optimized forcing to the stratosphere (altitudes above 200 hPa) resulted in correlation statistics that were only slightly worse than when we optimized the forcing throughout the whole atmosphere. This suggests that a significant part of model errors above all TCCON stations may be related to the representation of the stratosphere in the model. In addition, the bias and scatter plots show that optimization of forcing terms above 200 hPa produced the best fit to NOAA surface observations. In the second group of experiments, we modified the horizontal extent of the forcing mask **G**. We found that optimization of the forcing throughout the stratosphere and only over North America, Europe, China, and Equatorial Africa in the troposphere, as described in Section 3.2.5, produced almost identical fits to the case of the "full state assimilation". These are major emission source regions and our results suggest that the model above the TCCON sites was likely affected by errors in emissions and the transport of the emission signal over these regions. Henceforth, we refer to these assimilation results as **WC_T3_G-NA+CH+EU+EQAf+STRAT_4x5**. In the third group of experiments, we varied the length of the forcing window. We found that the agreement at some of the stations, such as Lamont, Park Falls, and Sodankyla, were generally insensitive to increasing the length of the forcing window, which could suggest that the model above these stations was affected by slowly varying biases. The model fit at other stations, particularly, Bialystok, Bremen and Karlsruhe, degraded when the window length was increased. The three latter stations are located close to each other and are, probably, affected by the similar model errors on synoptic times scales of about one week.

In the last group of experiments, we compared the performance of the two 4D-Var assimilation modelling approaches (WC "full state assimilation" and SC "flux assimilation") at the two model resolutions ($4^\circ \times 5^\circ$ and $2^\circ \times 2.5^\circ$). The comparison suggested that the SC method brings limited improvements to the a prior CH_4 fields at both resolutions. Indeed, we conclude that the SC assimilation at the $4^\circ \times 5^\circ$ resolution is futile as the a priori model at $2^\circ \times 2.5^\circ$ resolution produces a significantly better fit to the TCCON observations. The performance of the SC assimilation at the $2^\circ \times 2.5^\circ$ resolution was similar to but was surpassed by the "best fit" WC state assimilation at the $4^\circ \times 5^\circ$ resolution in term of its fit to TCCON and NOAA measurements. Overall, the WC state assimilation at $2^\circ \times 2.5^\circ$ resolution generated the best model fit to TCCON observations. However, in all $2^\circ \times 2.5^\circ$ resolution experiments the model bias against NOAA surface

Table 3.3: Validation of a priori, **SC_4x5** and **WC_T3_G1000_4x5** optimized CH_4 fields using TCCON XCH_4 (mean station-wise statistics for the period of February-May 2010).

	Bias [ppb]			Scatter [ppb]			Correlation (R)		
	Prior	SC	WC	Prior	SC	WC	Prior	SC	WC
Sodankyla	30.0	25.7	13.7	18.9	19.1	12.6	0.49	0.50	0.81
Bremen	6.3	3.2	0.7	14.3	15.2	10.5	-0.37	-0.28	0.47
Bialystok	11.9	7.3	5.1	9.3	10.6	8.0	0.39	0.43	0.65
Karlsruhe	6.4	4.4	0.8	9.7	9.9	8.9	0.33	0.29	0.49
Orleans	3.9	3.5	2.5	8.9	9.6	8.3	0.31	0.30	0.51
Garmish	9.9	10.0	5.7	9.0	9.7	8.4	0.46	0.56	0.65
Park Falls	1.9	3.6	2.3	9.7	10.6	8.5	0.37	0.47	0.65
Lamont	1.4	3.7	4.4	11.1	11.5	9.4	0.27	0.30	0.49
Izana	-5.8	-5.3	3.1	7.6	8.2	6.7	0.64	0.58	0.72
Wollongong	7.5	3.9	3.7	8.9	8.8	8.4	0.58	0.55	0.59
Lauder	9.6	9.2	5.9	5.6	5.7	5.4	0.72	0.72	0.73

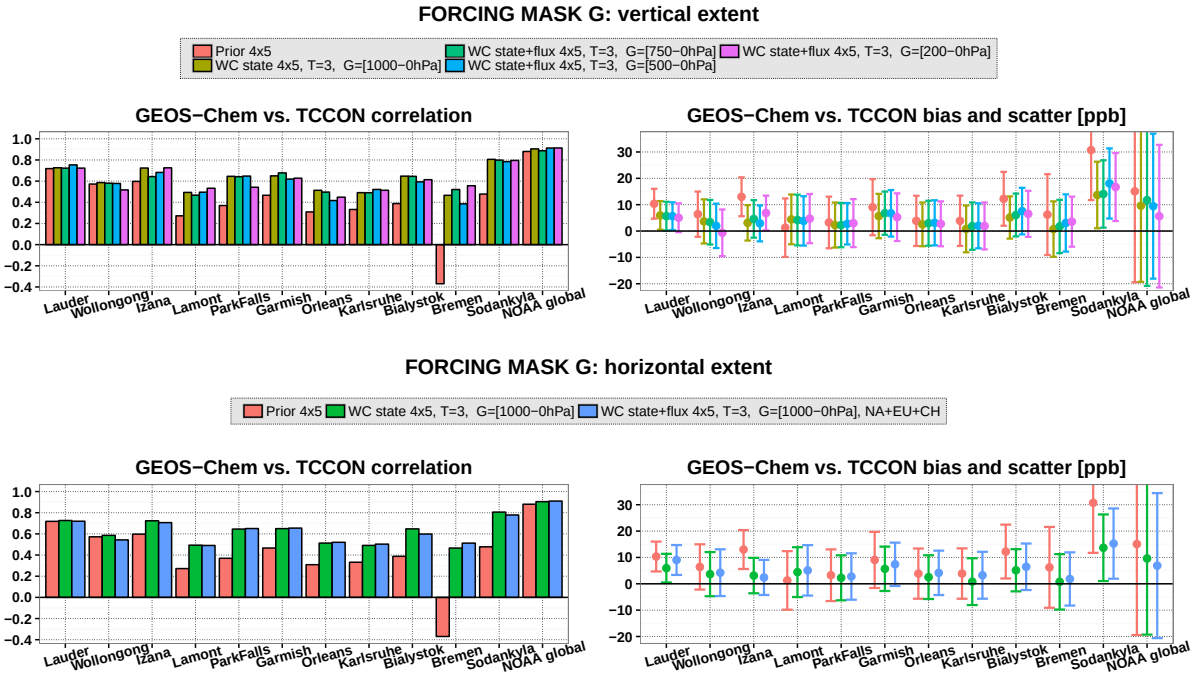

Figure 3.14: Validation of a priori, SC and WC optimized CH_4 fields using TCCON XCH_4 and NOAA surface in situ observation (mean statistics for the period of February-May 2010). Results are shown for a set of WC inversions organized in separate characteristic groups for better representation.

measurements was increased compared to the $4° \times 5°$ experiments. For example, the smallest WC a posteriori bias at $4° \times 5°$ was about 10 ppb, whereas at $2° \times 2.5°$ it was about 17 ppb.

Another important conclusion can be draw from the fact that the WC assimilation at both model resolutions significantly improved the model fit to Izana measurements. The Izana station is located at an altitude of 2370 m above sea level on a small island near the coast of Africa that has no local CH_4 emission sources. The model at 2° × 2.5° and 4° × 5° resolutions is not able to resolve the inland. Therefore, the model transport in the vicinity of high-altitude station, particularly, in the lower troposphere, may be subject to similar errors. Hence, the improvement in the assimilated CH_4 fields should mainly be related to the corrected transport in the upper troposphere and the stratosphere, which also supports the conclusions drawn from the first group of experiments.

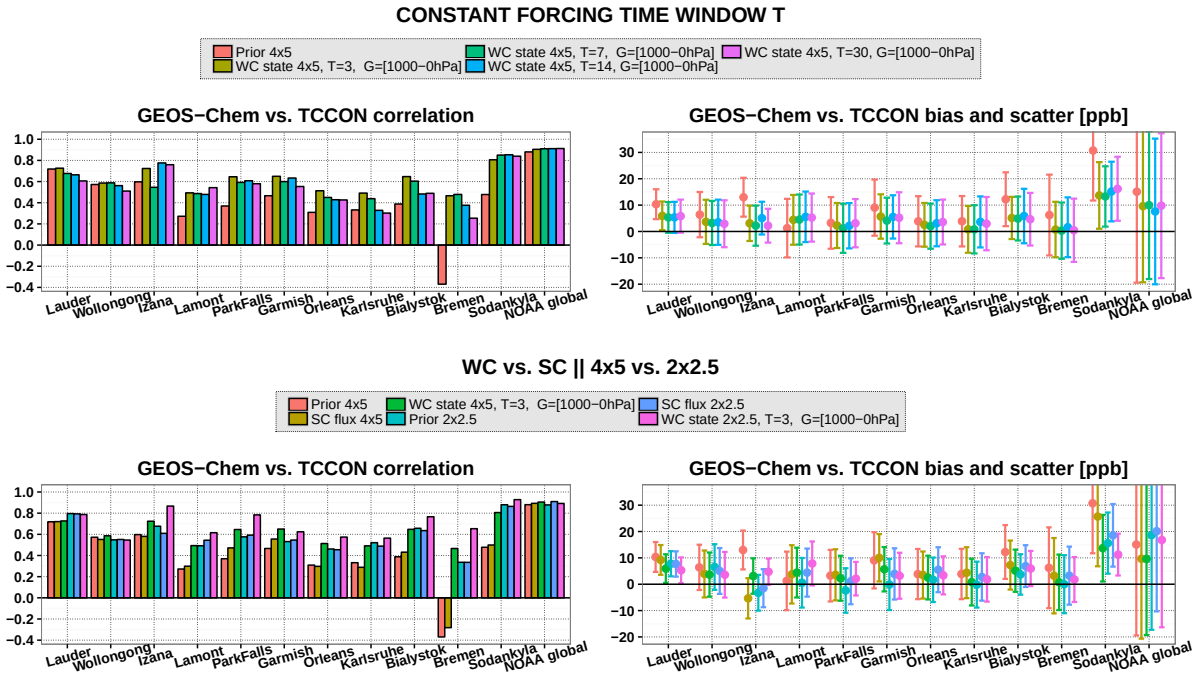

Figure 3.14: Continued.

The WC full state assimilation at 4° × 5° leaves weak positive bias in GEOS-Chem fields against TCCON observations (except at Sodankyla where the bias is significantly larger). Mean a posterior inter-station bias at 4° × 5° (2° × 2.5°) resolution is 3.4 (4.0) ppb (excluding Sodankyla), while scatter equals 8.6 (7.3) ppb (including Sodankyla). It is not clear if the GOSAT data is positively biased or if this could be caused by differences between the GOSAT and TCCON averaging kernels in the stratosphere and the fact that, for example, the stratospheric model bias was not fully recovered by the assimilation, particularly, during the first couple of months of the assimilation period (see Fig. 3.10). The results also do not indicate the presence of a latitudinal bias between TCCON and GEOS-Chem and, hence, between TCCON and GOSAT.

There is larger positive XCH_4 bias between the model and Sodankyla measurements, 12.6 ppb and 11.2 ppb for the WC assimilation at 4° × 5° and 2° × 2.5° resolution, however, the correlation is also high, 0.81 and 0.93, respectively. Tukiainen et al. (2016) and Ostler et al. (2014) pointed to the fact that polar vortex conditions at high latitude stations may induce biases in TCCON XCH_4 retrievals. It has been claimed that a priori profiles in the retrievals do not account for and are not adjusted to these dynamic conditions, hence, they significantly deviate from the real CH_4 profiles. When there is not enough information in the spectra to correct for such discrepancies, the XCH_4 retrievals can be systematically biased. It is possible that both the GOSAT and TCCON could have been affected by the polar vortex conditions in February-April 2010 so that the biases in co-located retrievals are partially cancelled. It should also be noted that the negative a priori correlation between the model and Bremen XCH_4 measurements is partly caused by the limited number (84) of measurements during the four-month assimilation time window.

3.3.2.2 Evaluation with ACE-FTS and HIPPO-3 data

Figures 3.15 and 3.16 show the results of GEOS-Chem comparison with the ACE-FTS and HIPPO-3 data. Model bias versus ACE-FTS data is shown only in the stratosphere in order to exclude potentially biased data due to interference with clouds in the upper troposphere. The mean XCH_4 difference between GEOS-Chem and ACE-FTS that is shown was obtained by applying the GOSAT averaging kernels to the residual CH_4 profiles where hypothetical ACE-FTS CH_4 profiles in the troposphere were assumed to be equal to the GEOS-Chem fields.

Consistent with Saad et al. (2016), the XCH_4 difference reveals that the a priori 4° × 5° model has a positive stratospheric bias as large as 250 ppb in the upper stratosphere (see Fig. 3.15). The HIPPO-3 comparison also showed that the 4° × 5° model is positively biased in the stratosphere and slightly negative in the troposphere. The 4° × 5° WC assimilation reduced the positive stratospheric bias with respect to both HIPPO-3 and ACE-FTS, however, did not remove it completely. For example, the maximum model−ACE-FTS XCH_4 bias due to the stratosphere was reduced from about 40 ppb to 30 ppb. The average negative tropospheric CH_4 bias relative to HIPPO-3 was reduced. It is possible that the WC method was not able to properly localize the stratospheric bias. However, the validation analysis may also reflect the influence of the slow recovery of the stratospheric CH_4 fields from bias in the initial conditions. Therefore, discrepancies in the stratospheric CH_4 field from the initial conditions in the first two months of the WC assimilation could be contributing to the observed HIPPO-3 and ACE-FTS bias.

Unfortunately, the measurement are either too sparse or limited in space and time to verify this assumption.

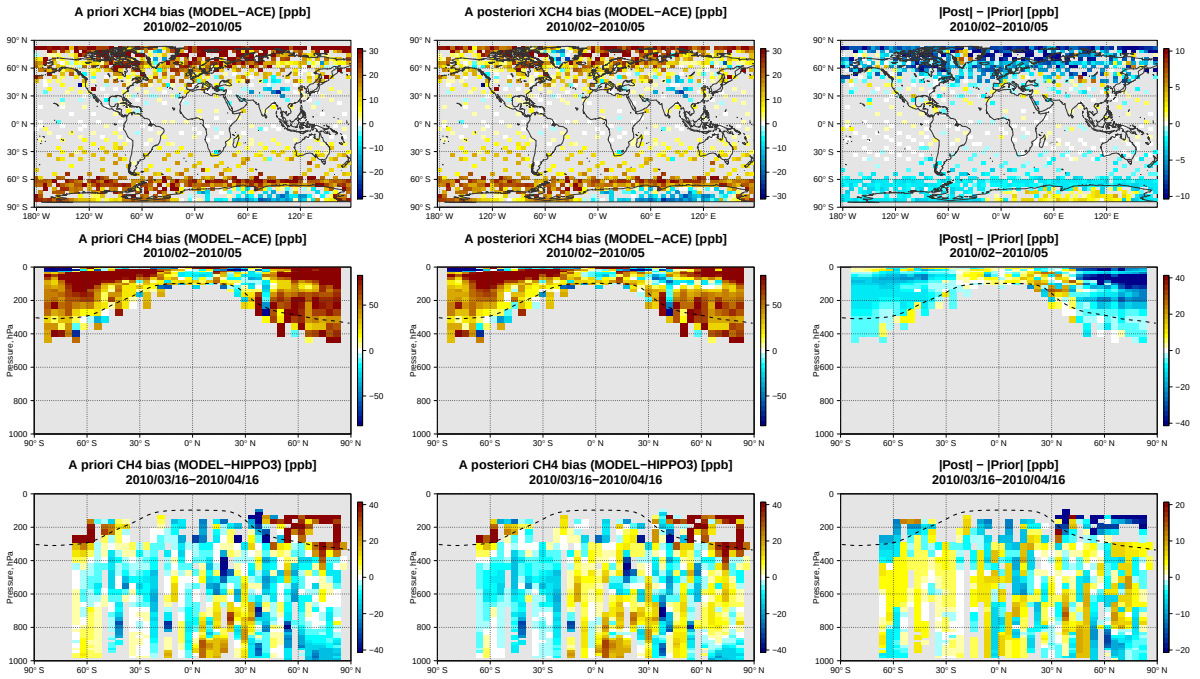

Figure 3.15: Evaluation of the a priori and **WC_T3_G1000_4x5** optimized CH_4 fields using ACE-FTS and HIPPO-3 CH_4 measurements (mean bias for the period of February-May 2010). Columns: a priori bias (left), a posteriori bias (middle), reduction is absolute bias (right). Rows: XCH_4 bias between GEOS-Chem and ACE-FTS (top), CH_4 bias between GEOS-Chem and ACE-FTS zonally averaged among available measurement profiles (middle), CH_4 bias between GEOS-Chem and HIPPO-3 (bottom). We used ACE-FTS retrievals in the stratosphere only. XCH_4 bias between GEOS-Chem and ACE-FTS was obtained by augmenting the ACE-FTS profile in the stratosphere by the GEOS-Chem profile in the troposphere and smoothing the vertical CH_4 bias profile with mean meridional GOSAT averaging kernels. The dashed line represents the mean tropopause height.

The positive a priori stratospheric bias relative to ACE-FTS and HIPPO-3 was significantly reduced at 2° × 2.5° compared to the 4° × 5° resolution (see Fig. 3.16), however, it was not completely removed. Stratospheric CH_4 fields in the NH above 200 hPa even became negatively biased, particularly around 30-40°N, where the absolute bias became larger than at 4° × 5° resolution. The WC method further corrected the positive biases and significantly reduced the negative bias around 30-40°N. As can be inferred from Fig. 3.12, the latter covered the entire latitudinal band but was particularly pronounced over the Himalayas. Despite the reduction of the stratospheric bias, the 2° × 2.5° WC assimilation introduces a positive CH_4 bias relative to HIPPO-3 in the NH lower troposphere.

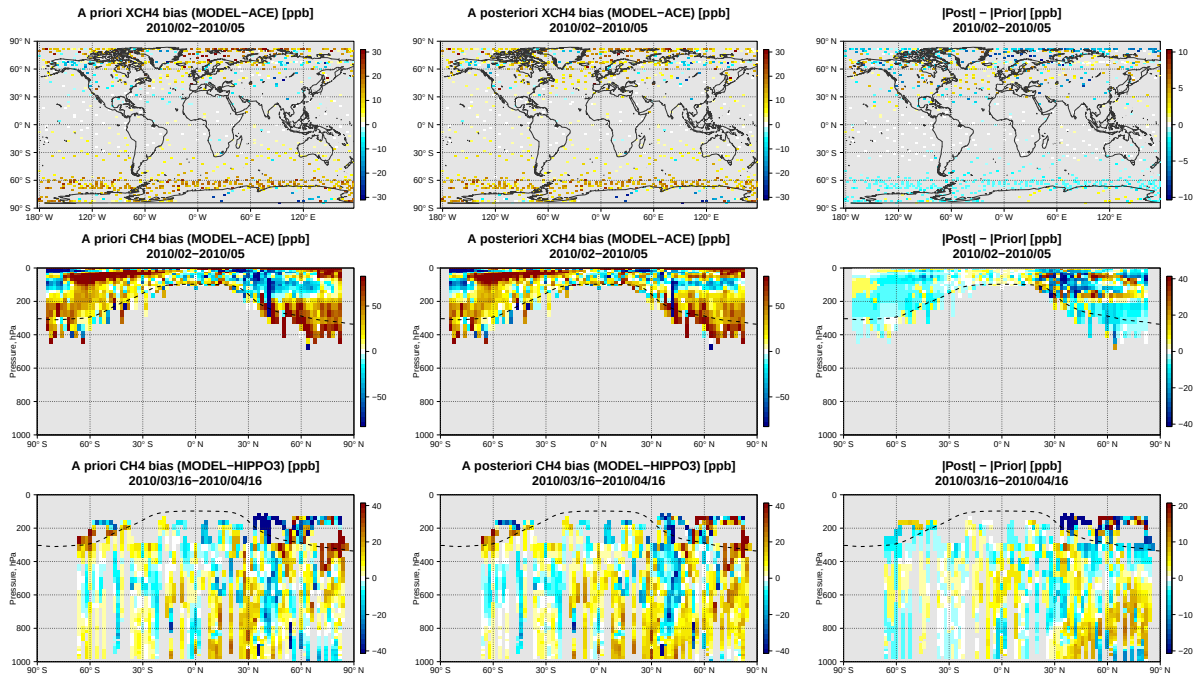

Figure 3.16: Same as Fig. 3.15 but for the 2° × 2.5° resolution model.

The results in Fig. 3.15 were further processed to better illustrate the mean model bias reduction. The zonal stratospheric ACE-FTS bias was averaged into one vertical profile. The zonal HIPPO-3 bias was separated into the tropospheric and stratospheric components and separately averaged to produce tropospheric and stratospheric vertical profiles. The final result is presented in Fig. 3.17 for both the a priori and a posteriori CH_4 fields. The WC assimilation partially mitigated the positive stratospheric bias against ACE-FTS and HIPPO-3 and reduced the negative HIPPO-3 bias in the mid-upper troposphere. Unfortunately, ACE-FTS and HIPPO-3 measure different airmasses, and neither of the datasets is representative of the mean state of the atmosphere or even one particular meridional slice. Therefore, the mean HIPPO-3 and ACE-FTS bias profiles cannot be directly compared to each other.

3.4 Discussion of model biases

3.4.1 Stratospheric bias

The sensitivity experiments carried out in Section 3.2.4 suggested that a stratospheric bias introduced in the system through the initial conditions has the slowest convergence rate. However, by the start of the last month of the assimilation, May 2010, the bias is either removed or does not change much with time. Therefore, we focus the discussion

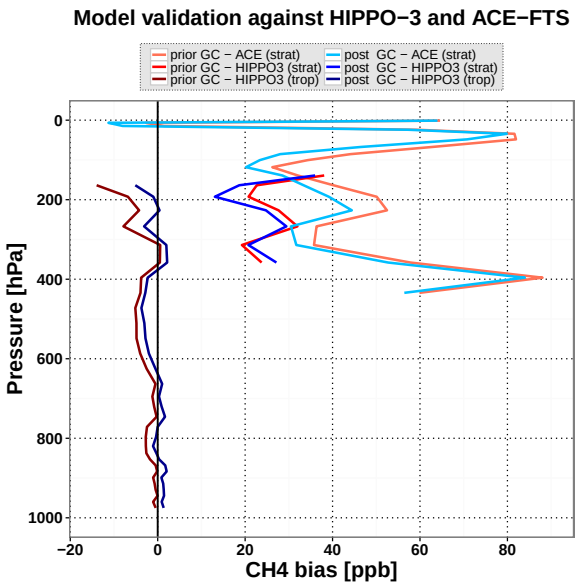

Figure 3.17: Evaluation of a priori and **WC_T3_G1000_4x5** optimized CH_4 fields using ACE-FTS and HIPPO-3 CH_4 measurements (mean bias profiles for the period of February-May 2010). The mean bias profiles were obtained by, first, averaging the biases in zonal and, after that, meridional directions. The HIPPO-3 bias was initially split into the tropospheric and stratospheric components and averaged into separate bias profiles.

here on the stratosphere in the month of May 2010, with the assumption that the model is free of the influence of the initial conditions. Figure 3.18 compares the a priori CH_4 fields to the ones optimized by **WC_T3_G1000_4x5** and **SC_4x5** assimilations. The top panel shows that corrections in the stratospheric CH_4 abundance are the most pronounced feature of the WC optimized CH_4 fields, and that changes are smaller in the zonal mean tropospheric fields. Stratospheric CH_4 was significantly reduced at high latitudes and increased in the tropics relative to the a priori. The changes are more substantial in the northern hemisphere due to the asymmetrically larger number of GOSAT measurements in the northern hemisphere (see Fig. 3.2 with adjoint sensitivity).

Large biases in the stratosphere were also identified in other chemistry transport models (Strahan and Polansky, 2006; Patra et al., 2011; Ostler et al., 2016). The problem was mainly linked to biases in the meridional Brewer-Dobson circulation in the stratosphere and in the rate of stratosphere-troposphere exchange. However, neither mechanism was analysed in detail. Indeed, the observed changes in Fig. 3.18 may partly reflect discrepancies in the Brewer-Dobson circulation projected from the initial conditions. In particular, too-rapid meridional overturning in the months prior to the assimilation would have transported excess of CH_4 from the tropics and to the high latitudes. In Chapter 4, we show that the stratospheric bias in GEOS-Chem can also form due to

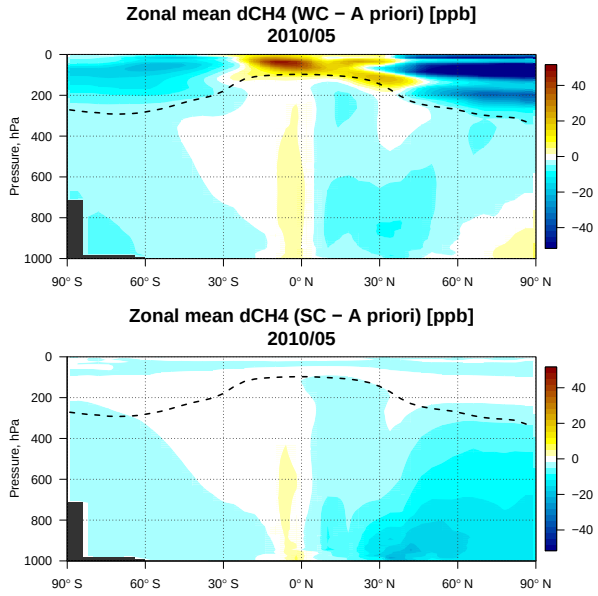

Figure 3.18: Monthly mean CH_4 difference in May 2010. Top: between **WC_T3_G1000_4x5** optimized and a priori fields. Bottom: between **SC_4x5** optimized and a priori fields. Dashed line represents the mean monthly tropopause height.

increased numerical diffusion as a consequence of transport at coarse horizontal model resolution. This leads to additional unphysical horizontal mixing between the troposphere and the stratosphere and between the high latitudes and the tropics in the stratosphere.

The bottom panel in Fig. 3.18 is presented to contrast the behaviour of the two 4D-Var approaches. It shows that the SC assimilation attempts to correct the positive high-latitude stratospheric CH_4 bias at the expense of surface emissions. This results in a negative CH_4 bias in the lower troposphere, while the surface signal hardly impacts the stratosphere.

3.4.2 Tropospheric bias

3.4.2.1 Pattern of forcing terms

The forcing terms are corrections applied to the CH_4 fields at each model time step. This time step is equal to 30 min and 15 min for the $4° \times 5°$ and $2° \times 2.5°$ simulations, respectively. In order to compare the two simulations, we added together state corrections at two successive $2° \times 2.5°$ time steps. Therefore, all forcing terms discussed in this chapter are presented for 30 min time intervals. The first column in Fig. 3.19 presents forcing terms in the troposphere optimized by the **WC_T3_G1000_4x5** assimilation. The observed structure of the forcing terms simultaneously mitigated model errors from

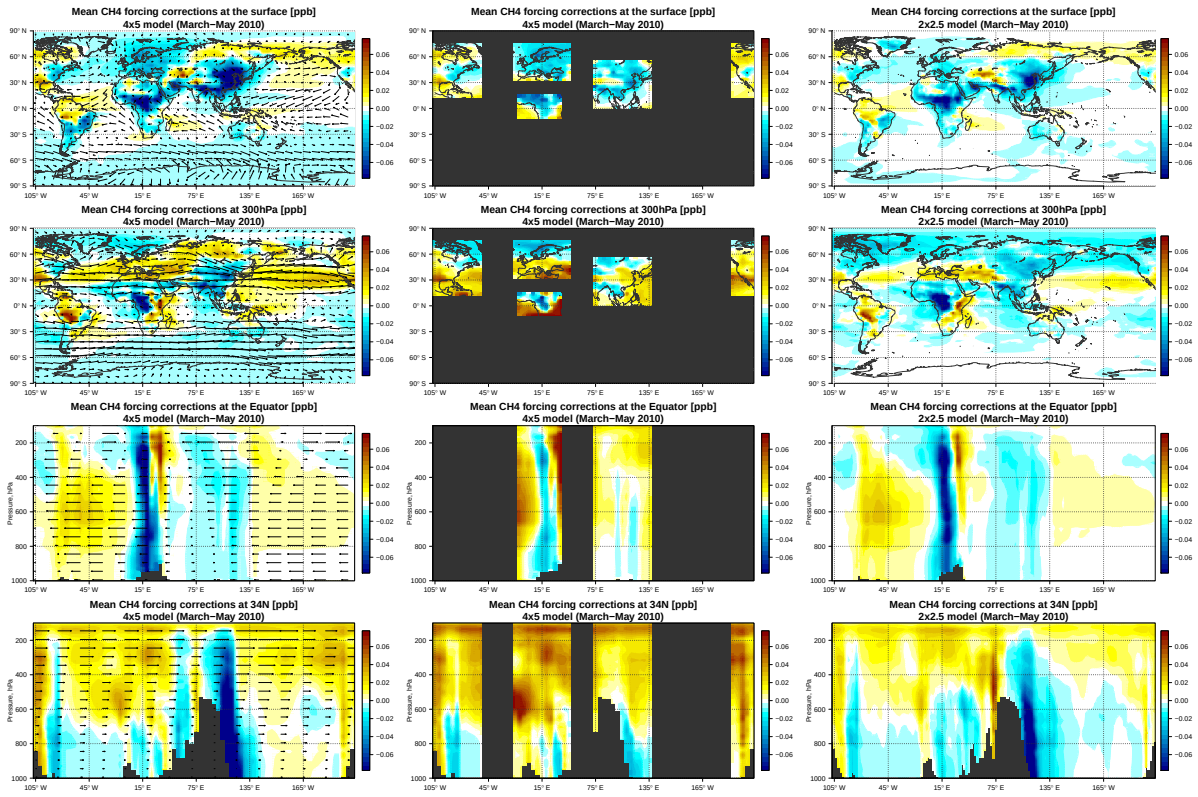

Figure 3.19: Mean optimized forcing terms (state correction) in March-May 2010. Left column: **WC_T3_G1000_4x5** inversion at 4° × 5° resolution. Middle column: **WC_T3_GNA+CH+EU+EQAf+STRAT_4x5** inversion at 4° × 5° resolution. Right column: **WC_T3_G1000_2x25** inversion at 2° × 2.5° resolution. Arrows represent direction and relative magnitude of horizontal winds in each figure.

multiple sources. In this chapter, we attempt to give the most likely explanation of the retrieved pattern of the state correction and identify sources of regional biases.

In general, the original a priori CH_4 fields can be affected by model errors that either occurred during the assimilation period or have been projected onto the assimilation window from the initial conditions. Here, we investigate the former case. Therefore, given the results of the OSSE with biased initial conditions in Section 3.3.1, we focus in Fig. 3.19 on mean forcing terms in the last three months of the assimilation (March-May 2010) as they are much more likely to be related to recent model errors rather than to biases in the initial conditions. The temporally averaged structure also gives insight into systematic model errors and is easier to interpret. Figure 3.19 (the first column) shows that negative forcing terms dominate near the surface and in the lower troposphere, particularly over Europe, Equatorial Africa and East Asia. The CH_4 reduction at the surface was consistent with NOAA observations. Positive state corrections are more frequently found in the upper troposphere, mainly in mid-latitudes over the Pacific and Atlantic oceans as well

as over Europe and significant part of Russia. There are also several regions, such as eastern China and equatorial Africa, where the forcing terms are negative throughout the entire tropospheric column. Vertical slices over mid-latitudes (bottom right panel) show that strong negative corrections over the east coast of Asia and North America are accompanied by positive corrections in the upper troposphere downwind of the continents. Forcing terms are generally weaker in the lower troposphere over the oceans where we lack GOSAT observations.

Generally, corrections of one sign with monotonically decaying magnitude from the surface to the upper troposphere could be associated with biases in the surface emissions, while the dipole structures with corrections of the opposite sign in the upper and lower troposphere could be related to errors in vertical transport. However, it is not feasible to uniquely identify the origin of model errors from the pattern of forcing terms because model errors from separate sources are mixed in the atmosphere and the estimation of the forcing terms is an under-constrained inverse problem.

Still, we may try to identify possible sources of model errors. For example, initial assessment of the state corrections pointed to potential issues in vertical transport. Indeed, the dipole structure of the forcing terms could indicate that upward CH_4 transport in mid-latitudes may be insufficient, particularly, over regions with strong vertical CH_4 gradients that are present over large CH_4 emission sources. In NH mid-latitudes, the major CH_4 emitters are China, the US, and Europe. Moreover, the eastern parts of China and North America are located in regions of significant extra-tropical cyclone activity (Stohl, 2001; Shaw et al., 2016), where CH_4 emitted from the surface is being lifted up in the free troposphere in warm conveyor belts associated with these cyclones (Kowol-Santen et al., 2001; Li et al., 2005; Sinclair et al., 2008; Lin et al., 2010). Moist convection over land could also contribute to the total transport bias, however convective transport is not strong over these mid-latitude regions during the months of February-May. Recently, Andy Jacobson (personal communication) compared SF_6 simulation in GEOS-Chem to observations and showed that the modelled SF_6 fields are too high at the surface at northern hemisphere mid-latitudes, which indicated the reduced vertical transport in the model.

Similar vertical structure of forcing terms was identified above and downwind of eastern North America and China (see Fig. 3.19 (first column, fourth row)). The WC method applied negative corrections over the land, from the surface to the upper troposphere, and large positive corrections in the upper troposphere and weakly negative correction in the lower troposphere over the oceans downwind of the continents. The WC method may suggest that vertical transport over eastern parts of the continents has to be stronger. In

such case, more CH_4 emitted from local sources reaches the middle to upper troposphere and is transported away from the continents by strong westerly winds. Meanwhile, CH_4 concentrations in the entire atmospheric column over land and in the lower troposphere over the adjacent oceans are reduced. Therefore, the large positive a priori bias between the model and GOSAT over China (Fig. 3.11, first column) may partly be attributed to weak local CH_4 uplift.

The observed structure of the forcing terms cannot be uniquely attributed only to biases in vertical transport. The WC method significantly reduced CH_4 in the stratosphere at high latitudes. If biases in the stratospheric CH_4 fields are induced by transport errors, the total CH_4 budget has to be conserved. Therefore, CH_4 removal from the high-latitude stratosphere has to be compensated for in either the tropical stratosphere or the upper troposphere. Hence, the positive forcing terms in the upper troposphere, particularly, in the vicinity of the westerly jet, may also be partly related to model errors in the stratosphere-troposphere exchange and may correct for CH_4 leak from the troposphere to the stratosphere. The negative forcing terms over China and North America may also partly correct for positively biased a priori surface emissions.

Another region of interest, as suggested by the WC assimilation (Fig. 3.19 (first column, third row)), is equatorial Africa. Similar to China, large positive a priori model XCH_4 bias was found here. However, due to the observational coverage, there are limited direct constraints on the CH_4 outflow from Equatorial Africa except for sparse GOSAT observations over South America. While the African XCH_4 bias could be related to positively biased local a priori surface emissions, the WC assimilation also suggested another transport-related explanation. The WC assimilation applied negative CH_4 forcing terms over central Africa and positive forcing terms downwind in the middle troposphere (between 400 and 800 hPa) over the Atlantic Ocean. Such a pattern of state correction could point to potential errors in CH_4 outflow from the African continent. Southern Africa is characterized by a persistent high pressure system that drives easterly outflow from southern tropical Africa to the Atlantic in the lower to middle troposphere (Garstang et al., 1996). In their analysis of the sources of moisture in the Congo Basin, Dyer et al. (2017) showed that there is a strong export of moisture from southern tropical Africa to the Atlantic between 800-500 hPa. Furthermore, Arellano et al. (2006) found, in their inversion analysis of carbon monoxide (CO) data from the MOPITT instrument, a discrepancy between their a posteriori CO and observations at Ascension Island, which they speculated could be due to errors in the altitude dependence of the outflow from Africa in the GEOS-Chem model. It is possible that too-much CH_4 is being convectively lofted to the upper troposphere over central Africa and not enough is exported out over

the Atlantic in the lower troposphere. Figure 3.3 (first column) displays the bias in CH_4 fields when convection was turned off in the model. This caused CH_4 emitted over Africa to take a different transport pathway. Instead of being lifted up over the continent, more CH_4 was transported out to the Atlantic in the lower to middle troposphere between 500 and 900 hPa. Under such conditions, CH_4 is simultaneously depleted over the continent and enhanced over the Atlantic, which is similar to what the WC forcing terms suggest. We cannot determine the exact origin of the XCH_4 bias over Africa, but the forcing terms do suggest the presence of a transport bias.

The estimation of the forcing terms is an under-constrained inverse problem. Consequently, here we evaluate the impact of reducing the dimensionality of the inverse problem by limiting the region of the atmosphere where forcing terms should be applied. This was done in the **WC_T3_G-NA+CH+EU+EQAf+STRAT_4x5** assimilation, in which we restricted the forcing optimization to the stratosphere and over the main CH_4 anthropogenic emission regions in the troposphere. The results presented in Section 3.3.2.1 suggested that the **WC_T3_G1000_4x5** and **WC_T3_G-NA+CH+EU+EQAf+STRAT_4x5** assimilations produced very similar fits to the independent observations. Therefore, errors affecting the model, at least at the location of the validation stations, could emerge from either the NA, CH, EU, EQAf, or STRAT regions. The second column in Fig. 3.19 presents the structure of optimized forcing terms from the **WC_T3_G-NA+CH+EU+EQAf+STRAT_4x5** assimilation where the number of optimized variables was reduced using the forcing mask **G**. Over China and North America, the forcing terms acquired a better defined dipole structure with positive correction in the upper troposphere and negative correction in the lower troposphere. Over equatorial Africa, the region of positive corrections in the mid-troposphere moved closer to the continent.

3.4.2.2 Dependence of the forcing terms on model resolution

Coarsening the model resolution from $2^\circ \times 2.5^\circ$ to $4^\circ \times 5^\circ$ can be considered as introducing errors in the finer resolution model. Results in Chapter 4, as well as Yu et al. (2017), showed that at coarse resolution, vertical transport in GEOS-Chem is weakened due to loss of eddy mass flux and incorrect regridding of meteorological fields. In Chapter 4, we also show that the efficiency of transport barriers is reduced due to increased numerical diffusion, which causes unphysical mixing between the interior and the exterior of the polar vortex, too rapid mixing of CH_4 between the tropical and extratropical branch of the Brewer-Dobson circulation, and the increased stratosphere-troposphere exchange. In Fig. 3.19, we compare the forcing terms from the $4^\circ \times 5^\circ$ assimilation (**WC_T3_G1000_4x5**)

with those from the 2° × 2.5° WC assimilation (**WC_T3_G1000_2x25**). Differences between the 2° × 2.5° and 4° × 5° forcing represent the response of the WC method to the resolution-induced transport errors. We found that the magnitude of the negative forcing term was reduced in the lower troposphere, particularly, over China. Similarly, the magnitude of positive forcing terms was reduced in the upper troposphere. The pattern of forcing terms on the vertical slice at mid-latitudes became significantly weaker. Analysis of Figs. 3.11 and 3.12 also pointed to a significantly weaker magnitude of the stratospheric corrections at the 2° × 2.5° resolution. At the same time, the structure and magnitude of forcing terms at the equator (particularly, over equatorial Africa) was not significantly affected by the increase of resolution.

Several conclusions follow from Fig. 3.19. First, the results suggest that a large fraction of model errors at 4° × 5° resolution, particularly, in the stratosphere and over mid-latitudes in the troposphere are resolution-induced. Second, although the magnitude of forcing terms at the 2° × 2.5° resolution is weaker, the pattern remains similar, which implies that the 2° × 2.5° resolution model may still be affected by the same type of transport errors. Third, the assumptions made about sources of model errors in the tropics, particularly, over equatorial Africa, still apply to the 2° × 2.5° simulation as the structure and magnitude of forcing terms remained unresponsive to the model resolution. Finally, the results strongly suggest that the WC assimilation and the GOSAT observations have actually diagnosed transport errors at both model resolutions.

3.5 Conclusions

In this study, we assessed errors in the global GEOS-Chem chemistry transport model during the four-month period of Ferbuary-May 2010 using the weak constraint 4D-Var data assimilation method at the model resolutions of 4° × 5° and 2° × 2.5°. This was done by constraining simulated CH_4 fields with GOSAT XCH_4 retrievals. This represents the first application of a WC 4D-Var scheme for assimilation of GOSAT XCH_4 retrievals to characterize model errors in a CTM.

An analysis of the sensitivity of the GOSAT measurements to the atmospheric CH_4 state found that the XCH_4 retrievals are most sensitive to CH_4 mass changes in the stratosphere and in the upper troposphere in the northern hemisphere, which was explained by the GOSAT observational coverage and stronger horizontal winds in the UTLS, allowing the CH_4 perturbations to be observed by a larger number of measurements. Sensitivity at the equator was about half that at northern mid-latitudes. In a series of OSSEs, the observations and the WC method were tested to determine the ability of the system to

recover "unknown" errors in CH_4 fields associated with artificially introduced biases in emissions, convection, chemistry, and initial conditions. We found that when not supplied with any information about the errors, the WC method was able to significantly mitigate biases in the CH_4 fields with slowly changing spatial structures, but was not able to correct strongly localized biases, particularly, those in the boundary layer. Despite having almost flat averaging kernels in the troposphere, our analysis showed that the GOSAT XCH_4 retrievals could help constrain the vertical distribution of model errors when convection was turned off in the model. The WC method needed about a month to recover the bias introduced in the initial condition in the troposphere and about two months to do so in the stratosphere. Generally, the method was successful in mitigating model errors of "unknown" origin and magnitude. However, more optimal performance could be achieved by supplying the method with additional information about model errors, such as their temporal and spatial correlation using the model error covariance matrix $\mathbf{Q}$. However, characterizing these correlations will be challenging.

The WC method was tuned in a set of experiments to diagnose real model errors in GEOS-Chem CTM at $4^\circ \times 5^\circ$ resolution. The a posteriori model fit to independent observations, such as ACE-FTS, HIPPO-3, TCCON and NOAA surface measurements, was used to evaluate the assimilation. Initial comparisons suggested that GEOS-Chem was affected by biases not solely related to discrepancies in surface emissions. Results suggested that, modelled CH_4 fields at the location of most NH TCCON stations were affected by slowly varying biases, however, at the location of few stations, such as Bialystok, Bremen and Karlsruhe, CH_4 fields were more likely influenced by errors varying on time scales of one week. The evaluations pointed to a large positive bias in the stratosphere relative to ACE-FTS and HIPPO-3 measurements, and weakly negative bias in the middle to upper troposphere relative to HIPPO-3 data. The WC assimilation was able to mitigate the negative tropospheric bias and partly removed the stratosphere bias. We found that the SC 4D-Var assimilation that optimized the surface emissions had only limited impact on the model fits. Furthermore, the WC assimilation at $4^\circ \times 5^\circ$ resolution performed better than the SC assimilation at $2^\circ \times 2.5^\circ$ resolution. Meanwhile, the results also showed that running the a priori model at $2^\circ \times 2.5^\circ$ resolution produced better agreement with TCCON observations than the a posteriori fields from the SC 4D-Var surface emission optimization at $4^\circ \times 5^\circ$.

State corrections at $4^\circ \times 5^\circ$ resolution also explicitly pointed to issues with vertical transport, suggesting that vertical transport of CH_4 in mid-latitudes over large CH_4 sources in eastern China and North America is too weak. In the tropics, the WC inversion corrected for large positive XCH_4 bias over Equatorial Africa. From the pattern of forcing

terms, it remained unclear whether the bias was related to surface emissions. However, the WC method suggested the possibility of biased CH_4 outflow from the African continent to the Atlantic Ocean in the mid-troposphere, which could be related to a discrepancy in the partitioning between deep convective transport to the upper troposphere and shallow outflow to the Atlantic Ocean.

In Chapter 4 we will examine the impact of model resolution on the CH_4 simulation and show larger model biases at $4^\circ \times 5^\circ$ compared to $2^\circ \times 2.5^\circ$. We found that assimilating the GOSAT data at the higher resolution of $2^\circ \times 2.5^\circ$ produced state corrections that were similar to those obtained at $4^\circ \times 5^\circ$, however, the magnitude of these corrections in the stratosphere and in the mid-latitude troposphere was significantly reduced. This suggested that the model at both resolutions was affected by transport errors of similar origin, although much weaker at $2^\circ \times 2.5^\circ$ resolution, and a significant fraction of these errors was induced by the model resolution itself. The WC assimilation also corrected for the negative CH_4 bias relative to ACE-FTS and HIPPO in the northern mid-latitude stratosphere, found only at $2^\circ \times 2.5^\circ$ resolution, and located this bias particularly over the Himalayas. However, the origin of this bias remained unclear.

In our analysis, we used only GOSAT CH_4 data over land. However, XCH_4 glint measurements over oceans could help better constrain the vertical structure of the model errors. The WC 4D-Var assimilation of shorter-lived species, such as CO, could also help better diagnose model errors, especially when transport and emission errors mask each other in CH_4 fields, although shorter-lived species may also be more strongly affected by errors in chemistry. The advantage of CH_4 is its longer memory of model transport, however shorter-lived gases are more strongly affected by and, hence, may be more sensitive to the same model errors.

Clearly, the detected transport error at $4^\circ \times 5^\circ$ resolution would have considerable impact on inferred emissions if the model were assumed to be perfect, as is the case in SC 4D-Var. Instead of reducing positive high-latitude bias in the stratosphere, the $4^\circ \times 5^\circ$ SC 4D-Var surface flux assimilation negatively biased the lower troposphere. The SC inversion also significantly reduced Chinese CH_4 emissions by incorrectly attributing model errors in vertical transport. Some of the detected transport error were significantly smaller at $2^\circ \times 2.5^\circ$ resolution, while others remained resolution-independent. The effect of these remaining errors at $2^\circ \times 2.5^\circ$ resolution has to be further investigated. One definite outcome of the analysis is that the $2^\circ \times 2.5^\circ$ SC 4D-Var surface flux assimilation had only limited impact on the model fit to independent observations compared to significant improvement when using the WC method.

Potentially, any CTM may be improved if the signal of surface emissions can be

separated from other model errors. This would be rather challenging task for GOSAT XCH_4 measurements. Further analysis is needed on this problem, particularly, focused on a design of model error covariance matrix $\mathbf{Q}$. For example, Trémolet (2007) proposed a design based on statistics of model tendencies. The $\mathbf{Q}$ matrix had a rather primitive structure in our analysis, although sufficient for the objectives of this work. Based on our initial assessment of model errors, the structure of $\mathbf{Q}$ can be further improved. In the meantime, the WC 4D-Var method has a number of immediate useful applications. In general, it is a valuable instrument for diagnosing model errors. It can also be used as a tool to produce a better estimate of the CH_4 state in the model in order to provide boundary and initial conditions for forecasting purposes or regional-scale analysis at higher spatial resolution.

Chapter 4

Impact of coarse model resolution

4.1 Introduction

Chemical transport models are widely used for inverse modelling of surface emissions of environmentally important trace gases such as CO, CO_2 and CH_4. But in this inverse modelling context, model errors become a major issue (Arellano and Hess, 2006; Baker et al., 2006; Chevallier et al., 2010; Houweling et al., 2010; Jiang et al., 2011; Patra et al., 2011; Locatelli et al., 2013; Chevallier et al., 2014; Houweling et al., 2015). Based on the results from ten different simulations in the TransCom-CH_4 model inter-comparison, Locatelli et al. (2013) found that model errors could contribute to discrepancies that are as large as 23%-48% in regional CH_4 source estimates, and as much as 150% in source estimates at the model grid-scale. Until recently, characterizing and mitigating these errors for any given model has been challenging.

In Chapter 3, it was shown that the WC 4D-Var assimilation scheme in GEOS-Chem can be useful for estimating errors in the GEOS-Chem CH_4 simulation. The WC 4D-Var identified large biases in the high-latitude lower stratosphere, which the assimilation system was able to significantly reduce. The WC 4D-Var scheme also identified an issue with vertical transport over the main continental source regions. For example, for eastern North America and East Asia, the estimated corrections to the CH_4 distribution exhibited a dipole structure over and downwind of the source regions, suggesting too much CH_4 is confined close to the source region and not enough is exported over the continent. It was found that the pattern of model corrections was similar, but weaker in magnitude when the model resolution was increased from $4^\circ \times 5^\circ$ to $2^\circ \times 2.5^\circ$, indicating the bias is influenced by the model resolution. Yu et al. (2017) recently investigated the impact of model resolution on transport in GEOS-Chem using ^{222}Rn, ^{210}Pb, and ^{7}Be tracers, and found that vertical transport is reduced in the model at coarse resolution. The analysis

presented in this chapter complements Yu et al. (2017), with a specific focus on the impact of model resolution on the CH_4 simulation and the goal of better understanding the source of the biases identified in Chapter 3.

As discussed in Chapter 1, to reduce computational costs, CTMs use meteorological fields that are archived at lower spatial and temporal resolution than the native resolution of the parent GCM that produced the fields, but this creates a number of issues in the CTM (see Sections 1.3 and 2.2.3). For example, it can lead to inconsistencies between archived horizontal winds (or air mass fluxes) and surface pressures (Jöckel et al., 2001), which can result in the violation of mass conservation in the advection scheme. This lack of mass conservation is typically corrected using a mass (pressure) fixer (Bregman et al., 2003; Segers et al., 2002; Rotman et al., 2004). The degradation of the spatial and temporal resolution and temporal averaging of the meteorological fields is also associated with some loss of information about eddy transport and, consequently, the weakening of vertical motion in the model (Grell and Baklanov, 2011; Yu et al., 2017). Another consequence of reduced model resolution is increased numerical diffusion in the advection scheme, which can lead to rapid destruction of tracer gradients.

As noted in Section 2.2.3, some advection schemes, such as the LR scheme (Lin and Rood, 1996), are more sensitive to changes in the model resolution than others, such as the SOM scheme (Prather, 1986). Strahan and Polansky (2006) evaluated the impact of different horizontal resolutions on the isolation of the polar vortex in the Goddard Space Flight Center (GSFC) three-dimensional CTM, which uses the LR advection scheme. They focused on CH_4, O_3, and the age of air and found that the $4^\circ \times 5^\circ$ resolution allowed too much mixing through the edges of the polar vortex. Significant improvement was achieved by doubling the resolution to $2^\circ \times 2.5^\circ$. In this chapter, we extend the analysis of Strahan and Polansky (2006) and focus on the impact of model resolution on the CH_4 simulation in the troposphere and stratosphere in the GEOS-Chem CTM. There have been a number of inverse modelling studies trying to quantify global CH_4 emissions, and the majority of these have utilized models at coarse horizontal resolution ranging from about $2^\circ \times 2^\circ$ to $4^\circ \times 6^\circ$ (Chen and Prinn, 2006; Meirink et al., 2008; Bergamaschi et al., 2009, 2013; Fraser et al., 2013; Cressot et al., 2014; Houweling et al., 2014; Monteil et al., 2013; Bruhwiler et al., 2014; Alexe et al., 2015; Locatelli et al., 2015; Feng et al., 2017). Because the different studies used different advection schemes, it is not possible to make a general statement about the quality of transport in the models. But our goal here is to quantitatively characterize the resolution-induced errors in the GEOS-Chem CH_4 simulation and assess their potential implications for the use of GEOS-Chem for CH_4 source inversion analyses.

The Chapter is organized as follows. In Section 4.2, we evaluate the forward model simulation at 2° × 2.5° and 4° × 5° using different sets of observations. We then assess the impact of the resolution-induced model biases on optimized CH_4 surface emissions in Section 4.3. In Section 4.4, we investigate the origin of the model errors in the troposphere and the stratosphere using a set of transport tracers, and possible mechanisms responsible for the biases. Finally, in Section 4.5, we present a summary and discussion of our results.

4.2 GEOS-Chem model validation

4.2.1 Comparisons with GOSAT

We simulated CH_4 in GEOS-Chem for the period of four months from 1 February 2010 to 31 May 2010 at the two horizontal resolutions of 4° × 5° and 2° × 2.5°. The time period was chosen to match the analysis period in Chapter 3. Also, for longer time periods, incorrect a priori emissions can become the dominant source of model errors and confound the analysis, whereas our main purpose was to assess transport errors in the model. As in Chapter 3, CH_4 fields at both resolutions were spun up for about 5.5 years until July 2009. From July 2009 to January 2010 monthly mean surface emission optimization was performed using the 4° × 5° resolution model constrained by GOSAT Proxy XCH_4 retrievals described in Section 2.1.1. The regridded optimized emissions were also used to perform the 2° × 2.5° resolution simulation for the same period. The updated model fields on 1 February 2010 at both model resolutions were taken as initial conditions for the analysis period. All results were later converted to, and evaluated at, the 4° × 5° resolution. Modelled CH_4 fields were smoothed with GOSAT scene-dependent averaging kernels. Figure 4.1 (first and second columns) shows GOSAT XCH_4 observations and optimized XCO_2 proxy fields. The third and the fourth columns present the monthly mean difference between the simulated XCH_4 fields at the two resolutions and the GOSAT retrievals. Both difference fields represent the combined effects of errors in transport, chemistry, and the emissions, as well as possible biases in the XCH_4 retrievals. The fact that these differences are generally smaller at 2° × 2.5° resolution implies that there are transport errors in GEOS-Chem that are resolution-dependent and that worsen with decreasing resolution. This is consistent with the model corrections (the forcing terms) found in Chapter 3 using the GEOS-Chem weak constraint 4D-Var assimilation scheme. The difference between the CH_4 fields simulated at the two resolutions, co-located with GOSAT observations and smoothed with GOSAT averaging kernels, is presented in the last column in Fig. 4.1. In general, it shows that at finer resolution, XCH_4 columns are

smaller in the mid- and high latitudes and larger in the tropics. There are also several regional features such as a large positive XCH_4 bias over Northern Europe and Russia that has been reduced but not completely removed at the $2° \times 2.5°$ resolution. In addition, the XCH_4 fields simulated at the $2° \times 2.5°$ resolution have a smaller positive bias relative to the GOSAT observations over China.

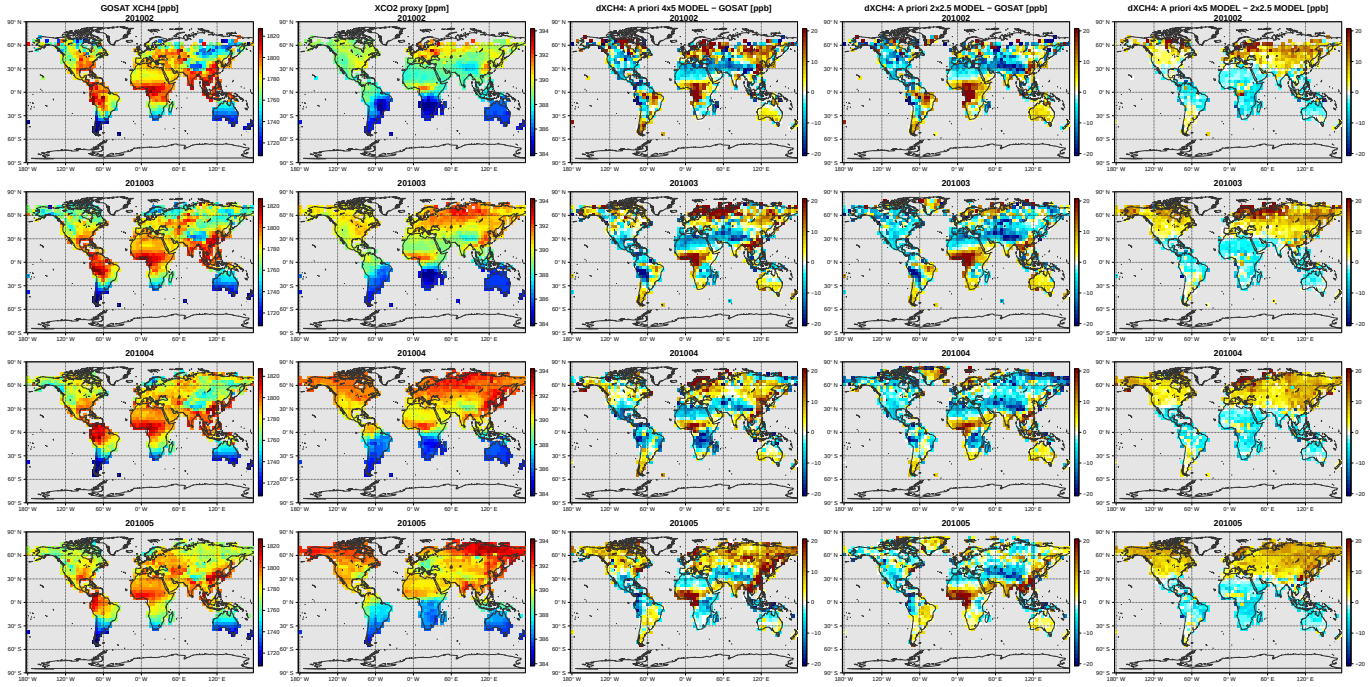

Figure 4.1: Monthly mean fields: GOSAT XCH_4 retrievals (first column) based on new XCO_2 proxy fields (in second column); a priori XCH_4 difference between $4° \times 5°$ resolution GEOS-Chem and GOSAT (third column); a priori XCH_4 difference between $2° \times 2.5°$ resolution GEOS-Chem and GOSAT averaged to $4° \times 5°$ resolution (fourth column); XCH_4 bias calculated as the difference between $4° \times 5°$ and $2° \times 2.5°$ resolution GEOS-Chem CH_4 fields co-located with GOSAT observations and smoothed with GOSAT averaging kernels (fifth column).

It is difficult to say conclusively from this comparison if spatially dependent biases are still present in the $2° \times 2.5°$ simulation. The positive high-latitude bias relative to GOSAT in the northern hemisphere (NH) was reduced compared to the $4° \times 5°$ simulation. However, a weak positive bias over the polar vortex is still present, although it is difficult to say whether this bias is related to transport errors or to possible systematic errors in GOSAT retrievals under the polar vortex conditions. The possibility of a weak positive latitudinal $2° \times 2.5°$ GEOS-Chem bias still exists in the southern hemisphere (SH) and can be observed over southern South America, Australia, and the southern tip of Africa. Negative XCH_4 biases over the Himalayas and Andes were not affected by doubling the model resolution. They could be related to discrepancies in surface pressure between GEOS-Chem and the GOSAT retrievals, however, even filtering of GOSAT retrievals

based on differences in surface pressure did not eliminate them. These biases may also indicate errors in CH_4 uplift over the mountains. Other XCH_4 biases not significantly affected by model resolution are located over Africa, including a positive bias over western Equatorial Africa and a negative bias over southeastern Africa. These biases, as well as biases over mountains, may also be related to the XCO_2 proxy fields used in the GOSAT CH_4 retrievals. The proxy field were obtained by assimilating GOSAT XCO_2 retrievals to constrain CO_2 fluxes in the coarse $4^\circ \times 5^\circ$ resolution GEOS-Chem model. If the CO_2 flux inversion did not remove all biases in CO_2 state, the latter could be projected onto the XCH_4 retrievals. For example, the negative model bias in XCH_4 in southeastern Africa could be related to a positive bias in the XCO_2 proxy due to an overestimate of the regional CO_2 fluxes, which was then transferred to the XCH_4 retrievals.

4.2.2 Comparisons with ACE-FTS

Zonal median differences between GEOS-Chem and ACE-FTS in the stratosphere over the four-month period (February-May 2010) are shown in Fig. 4.2. The figure also shows a comparison of the modelled stratospheric CH_4 fields to the GOSAT a priori stratospheric CH_4 profiles, which come from the TOMCAT (Chipperfield, 2006) model with assimilated ACE-FTS CH_4 retrievals (Parker and GHG-CCI group, 2016). The figure indicates that the GEOS-Chem stratosphere at $4^\circ \times 5^\circ$ resolution is positively biased against ACE-FTS at middle to high latitudes and is weakly negatively biased in the tropics. A strongly positive feature in the NH above 100 hPa, poleward of 45°N, is most likely related to the polar vortex. The mismatch relative to ACE-FTS was significantly reduced at $2^\circ \times 2.5^\circ$ resolution. Furthermore, the CH_4 differences in the NH stratosphere at $2^\circ \times 2.5^\circ$ became even weakly negative, although a positive anomaly remained in the lower stratosphere and in the SH.

Figure 4.3 shows the impact of the CH_4 mismatch in the stratosphere on the XCH_4 fields. The XCH_4 difference between GEOS-Chem and ACE-FTS was obtained by augmenting the ACE-FTS profile in the stratosphere by the GEOS-Chem profiles in the troposphere and smoothing the resulting vertical CH_4 difference profile with mean zonal GOSAT averaging kernels, averaged in 4° latitudinal bands. We used only those ACE-FTS profiles that extended through the entire stratosphere for each GEOS-Chem lon-lat grid cell for a particular time instance. The stratospheric boundary was defined by the dynamic tropopause taken from the archived GEOS-5 meteorological fields. As in Fig. 4.2, the median zonal mean value of the XCH_4 differences was used to avoid the effect of possible outliers and the sparsity of ACE-FTS retrievals. Fig. 4.3 indicates that

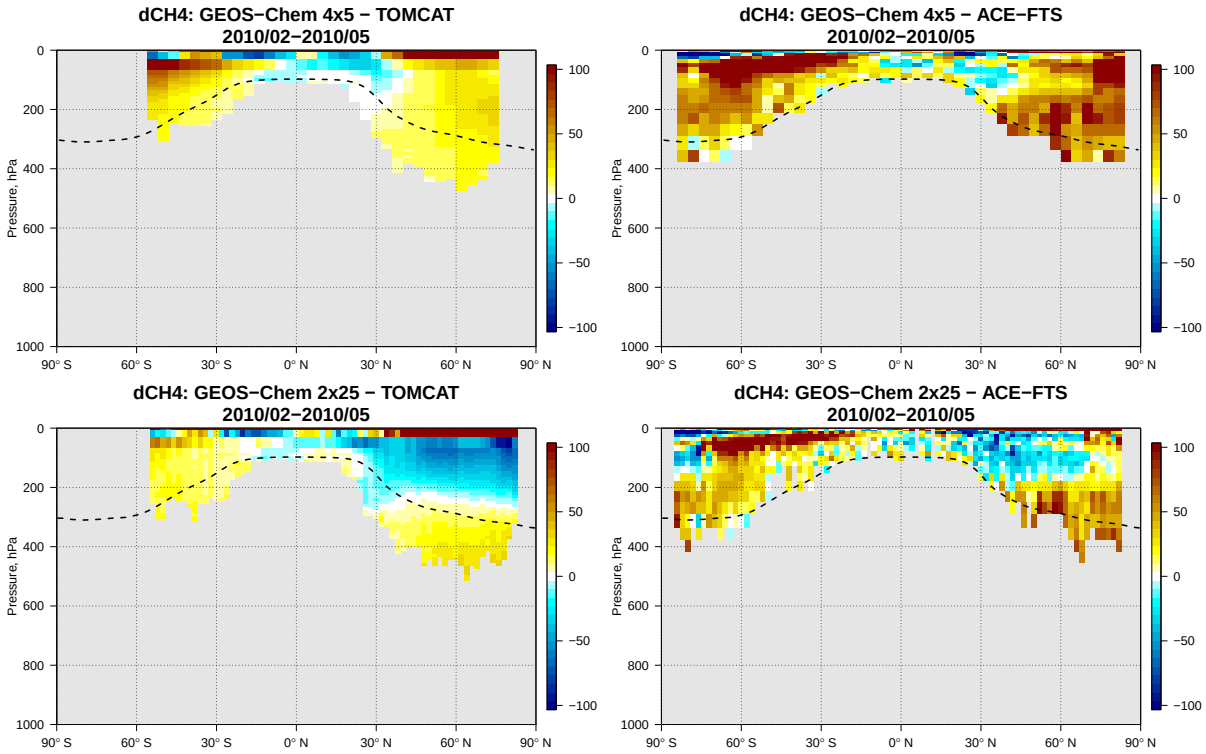

Figure 4.2: CH_4 differences (median value for the period of Feb-May 2010): between GEOS-Chem and GOSAT CH_4 a priori fields in the stratosphere which come from the TOMCAT model with assimilated ACE-FTS CH_4 retrieval (first column), between GEOS-Chem and ACE-FTS CH_4 retrievals in the stratosphere (second column). First (second) row shows CH_4 difference fields for $4° \times 5°$ ($2° \times 2.5°$) model resolution. The dashed line represents the mean dynamic tropopause over February-May 2010 from the archived GEOS-5 meteorological fields.

the XCH_4 differences have a latitudinal structure. The differences are small in the tropics at both resolutions. In NH mid-latitudes (30°-60°N), they reach about 15 ppb at $4° \times 5°$, but are reduced to less than 5 ppb at the $2° \times 2.5°$ resolution. The SH in February-May appears to be less sensitive to model resolution and the reduced XCH_4 difference at $2° \times 2.5°$ resolution was 5 to 10 ppb in this region. We note that these results may be affected by the sparsity of the ACE-FTS measurements and possible biases in ACE-FTS CH_4 retrievals in the lower stratosphere (De Mazière et al. (2008) suggested potential biases of 10% in the older version 2.2 of ACE-FTS CH_4 retrievals in the UTLS region). There is also a sharp positively biased feature in the SH stratosphere, the origin of which is unclear.

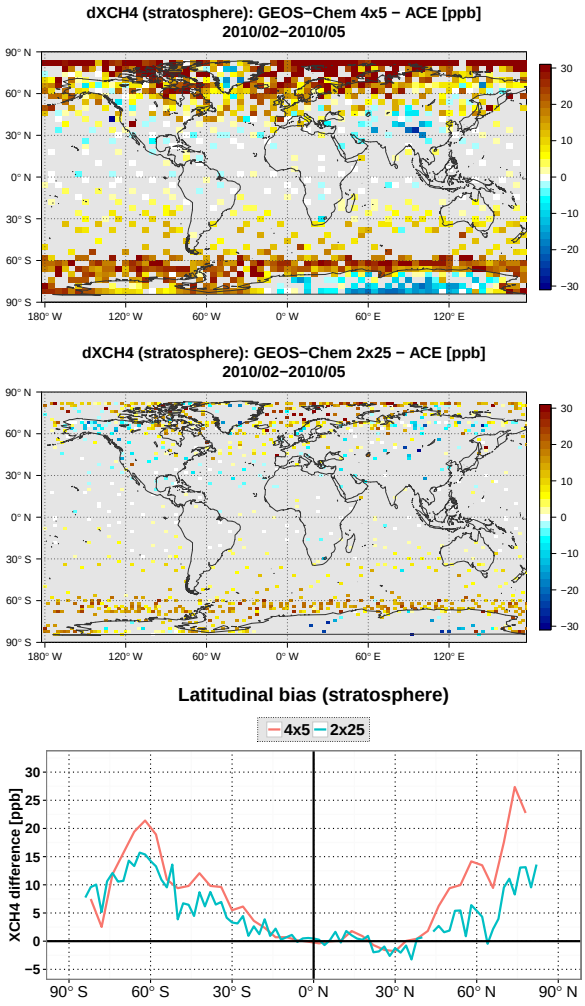

Figure 4.3: "XCH_4" difference between GEOS-Chem and ACE-FTS due to the stratosphere: 4° × 5° model resolution (top), 2° × 2.5° model resolution (middle), zonally averaged for both model resolutions (bottom). "XCH_4" difference was obtained by augmenting the ACE-FTS stratospheric profile with the GEOS-Chem troposphere and smoothing the vertical CH_4 difference profile with the mean meridional GOSAT averaging kernels.

4.2.3 Comparisons with TCCON

The third component of the model validation involved comparisons to ground-based XCH_4 retrievals from TCCON (Wunch et al., 2011). Table 4.1 gives a summary of the model validation against TCCON at the two model resolutions. Similarly to GOSAT, longer analysis periods became dominated by biases in the a priori surface emissions and were less useful for transport validation. The results show that running the model at the 2° × 2.5° resolution significantly improved the correlations and reduced the positive model mismatch against TCCON, except for the northern- and southern-most stations (Lauder, Wollongong and Sodankyla). For the 2° × 2.5° resolution, there is a 7-8 ppb

Table 4.1: Evaluation of the a priori 4° × 5° and 2° × 2.5° resolution GEOS-Chem model fields against TCCON XCH_4 retrievals (mean station-wise statistics for the period of February-May 2010).

	Mean difference [ppb]		Standard deviation [ppb]		Correlation (R)	
	4° × 5°	2° × 2.5°	4° × 5°	2° × 2.5°	4° × 5°	2° × 2.5°
Sodankyla	30.0	15.6	18.9	11.6	0.49	0.88
Bremen	6.3	0.0	14.3	11.0	-0.37	0.34
Bialystok	11.9	3.7	9.3	7.7	0.39	0.67
Orleans	3.9	1.7	8.9	8.4	0.31	0.46
Garmish	9.9	-0.1	9.0	9.7	0.46	0.53
Park Falls	1.9	-2.4	9.7	8.4	0.37	0.58
Lamont	1.4	0.6	11.1	9.4	0.27	0.49
Izana	-5.8	-3.2	7.6	6.8	0.64	0.68
Wollongong	7.5	6.5	8.9	8.7	0.58	0.55
Lauder	9.6	7.8	5.6	4.8	0.72	0.80

difference relative to Wollongong and Lauder in the SH and about a 15 ppb difference relative to Sodankyla in the NH. Similar differences were also observed in model−GOSAT comparisons (Fig. 4.1), with about a 3-4 ppb difference at Wollongong and Lauder and about a 5 ppb difference at Sodankyla. Significant mismatch reduction was achieved for Sodankyla (from 30 ppb to 15.6 ppb), and it is unclear whether the remaining difference is due to the model or the observations. As shown by Tukiainen et al. (2016) and Ostler et al. (2014), Sodankyla XCH_4 retrievals can be subject to systematic errors during polar vortex conditions due to incorrect CH_4 a priori profiles. As with the GOSAT and ACE-FTS comparisons, the TCCON results also suggest that a weak latitudinal bias may still be present in the model at the 2° × 2.5° resolution and, given the results of the ACE-FTS comparisons, it may be related to the stratosphere.

4.3 Impact on surface emissions

The primary reason why we are concerned about the magnitude of biases in the model XCH_4 fields is their possible impact on estimates of CH_4 surface emissions. It was shown in Fig. 4.1 (fifth column) that the resolution-induced bias between 4° × 5° and 2° × 2.5° resolution is comparable in magnitude to the mismatch between the 2° × 2.5° resolution XCH_4 fields and GOSAT data. This suggests that transport errors at 4° × 5° resolution may have an adverse impact on optimized emissions.

We optimized monthly CH_4 surface emissions for the period of February-May 2010 using GEOS-Chem at the two resolutions. Surface emissions were optimized as monthly

totals in each model grid box. Monthly emissions in all four months were adjusted simultaneously in order to best match GOSAT XCH_4 measurements during the same period. We used the strong constraint 4D-Var approach, which was also used in Chapter 3 and assumes that the model is perfect, except for potentially biased CH_4 surface emissions. The SC 4D-Var minimizes the cost function defined by Eq. (2.70) with a constraint given by Eq. (2.71). Both a priori ($\mathbf{R}$) and observational ($\mathbf{B}$) error covariance matrices were assumed to be diagonal. Uncertainty on the a priori emissions in each $4^\circ \times 5^\circ$ and $2^\circ \times 2.5^\circ$ grid box was set to 50% and 100%, respectively, in order to be approximately in accord with the central limit theorem. In designing $\mathbf{R}$, we used XCH_4 retrieval errors as the observational uncertainty and inflated them to match the global mean GOSAT standard deviation (scatter) against TCCON observations (Parker et al., 2015).

Figure 4.4 shows the ratio of optimized to a priori CH_4 emissions, which are referred to as emission scaling factors. The optimized CH_4 fields were evaluated against TCCON and NOAA in situ surface measurements and results are given in Section 3.3.2.1 (see Fig. 3.14). The $4^\circ \times 5^\circ$ inversion suggested lower CH_4 emissions at high latitudes and higher emissions in the tropics compared to the $2^\circ \times 2.5^\circ$ inversion. The differences are particularly large over equatorial Africa and Europe. There are large reductions in the emissions across mid-latitude Eurasia at $4^\circ \times 5^\circ$, whereas the changes in this region were minor at $2^\circ \times 2.5^\circ$. Furthermore, at $2^\circ \times 2.5^\circ$ there were increases in the emissions in western Europe. The discrepancies between the two inversions are probably associated with large positive high-latitude XCH_4 bias at the $4^\circ \times 5^\circ$ resolution.

The CH_4 emissions aggregated into the widely used 11 TransCom regions (Gurney et al., 2004) are plotted in Fig. 4.5. Because of the particular division of the TransCom regions, the aggregated emissions at the two model resolutions were more similar to each other than in Fig. 4.4. The largest changes are observed over Tropical South America where the $2^\circ \times 2.5^\circ$ inversion increased the optimized emissions relative to the a priori emissions by 30% while the $4^\circ \times 5^\circ$ inversions increased them by 60%. Over Temperate South America, Europe and Boreal Eurasia, the $2^\circ \times 2.5^\circ$ emissions remained at their a priori level while the $4^\circ \times 5^\circ$ emissions were reduced by 17%, 26% and 29%, respectively. Additionally, the resulting emissions over Northern Africa, which partly comprised wetland emissions from Equatorial Africa were about 16% smaller for $2^\circ \times 2.5^\circ$ resolution. It is likely that boreal North American emissions would be more biased, however the analysis covered only the time period when local wetland emissions were not significant. The moderate sensitivity of the emissions to the induced biases could be due to the sparse observational coverage of GOSAT. With a greater observational constraint, such as from the Sentinel-5p (Veefkind et al., 2012) or the future MERLIN (Kiemle et al., 2014)

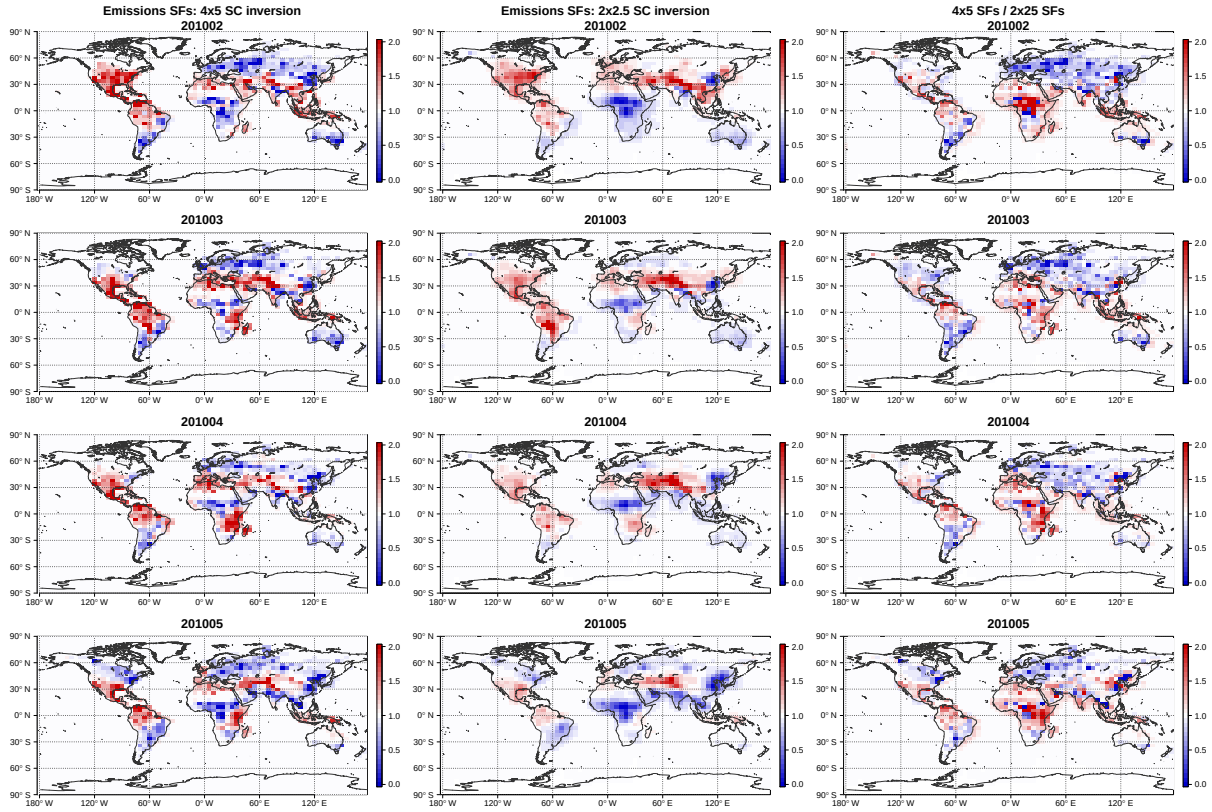

Figure 4.4: Ratio of optimized to a priori CH_4 surface emissions (scaling factors (SFs)). First column: SFs from 4° × 5° resolution inversion. Second column: SFs from 2° × 2.5° resolution inversion. Third column: ratio of the SFs in the first column to the SFs in the second column.

satellites, the optimized emissions may be more sensitive to model errors.

Several studies have tried to address latitudinal biases in CH_4 in models or observations. For example, Turner et al. (2015) applied a mean uniform latitudinal correction to their modelled CH_4 fields prior to performing their inversion analysis, while other studies (Fraser et al., 2013; Alexe et al., 2015) tried to fit a latitudinal correction in their inversion. While this may partly mitigate the problem, a latitudinal correction does not work well if the latitudinal bias is associated with biased initial conditions and surface emissions, for example, due to systematic underestimation/overestimation of a priori CH_4 emissions in the tropics versus mid-latitudes. Moreover, as will be shown below, the actual latitudinal bias may vary in time and may not be zonally uniform, such as features associated with the polar vortex.

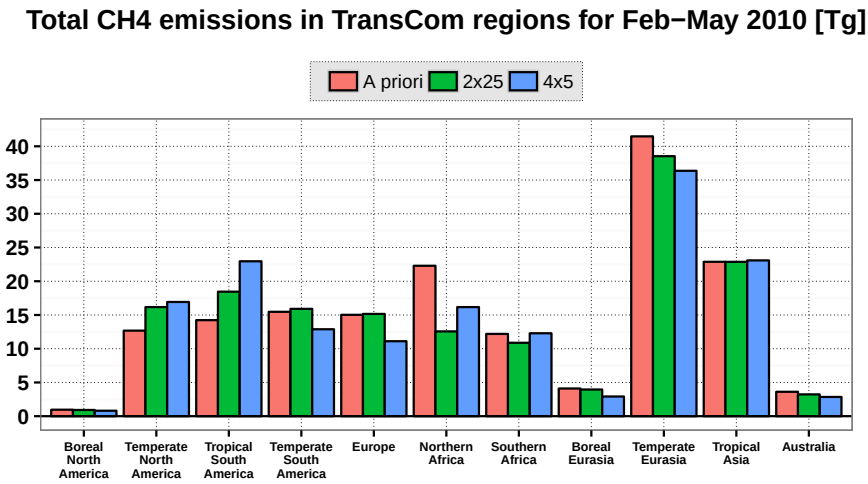

Figure 4.5: Total CH_4 emissions in 11 TransCom regions for the period of Feb-May 2010 including a priori emissions and optimized emissions using the $4° \times 5°$ and $2° \times 2.5°$ resolution GEOS-Chem model.

4.4 Origin of model errors

4.4.1 Mean meridional circulation

To investigate the mechanisms responsible for the differences in transport between the $4° \times 5°$ and $2° \times 2.5°$ model resolutions, we used radon-222 (^{222}Rn) and beryllium-7 (^{7}Be), together with CH_4, as tracers of atmospheric transport. In these experiments, the sources and sinks of the tracers are identical across all model resolutions, so differences in the tracer fields are due solely to transport. ^{222}Rn is emitted from soils by decay of radium-226 (^{226}Ra) and is lost in the atmosphere through radioactive decay to lead-210 (^{210}Pb), with a half-life of 3.8 days (Jacob et al., 1997). Due to its short lifetime and sources at the surface, ^{222}Rn is useful tracer of vertical transport in the troposphere. In GEOS-Chem, land and ocean fluxes of ^{222}Rn are set to 1 and 0.005 atoms cm^{-2} s^{-1}, respectively. Emissions over land in the polar regions beyond 60° are set to 0.005 atoms cm^{-2} s^{-1}. Corresponding emissions are reduced threefold when surface temperatures are below zero. ^{7}Be is produced in the atmosphere (mainly in the stratosphere) in a process of spallation of nitrogen and oxygen atoms by cosmic ray bombardment (Lal and Peters, 1967) and is immediately attached to aerosol particles. It is removed from the atmosphere by radioactive decay with a half-life of 53.3 days and by dry deposition and wet scavenging (Liu et al., 2001). ^{7}Be sources in GEOS-Chem are prescribed following Lal and Peters (1967) and Liu et al. (2001). We used ^{7}Be (as well as CH_4) as a tracer of stratosphere-troposphere exchange (Liu et al., 2016) and stratospheric mixing. However,

it can also be a useful indicator of tropospheric descent.

The experiments were run for two months (February-March 2010). The first month was used to spin up the tracer fields. The first row in Fig. 4.6 gives the mean monthly zonal tracer distribution modelled at the $4° \times 5°$ resolution while the second row presents the zonal mean differences between the $2° \times 2.5°$ and $4° \times 5°$ simulations. The ^{222}Rn experiment indicates that at $4° \times 5°$ there is up to a 40% reduction in the tracer concentrations in the mid-upper troposphere relative to $2° \times 2.5°$, with a noticeable increase in the tracer concentrations in the lower troposphere ranging from 10% to 25% (see Fig. 4.6d). These results suggest that at coarser resolution, vertical transport in GEOS-Chem is reduced. These results are similar to those shown by Yu et al. (2017). Changes in tracer concentrations are aligned along isentropes and are, therefore, most likely related to adiabatic transport as part of the large-scale advection. Figure 4.6d also suggests that biases originate at mid-latitudes. Vertical transport in these regions is associated with baroclinic wave activity: the tracers are lifted in warm conveyor belts that are linked with extratropical cyclones (Stohl, 2001; Eckhardt et al., 2004; Hess, 2005; Parazoo et al., 2011). However, discrepancies in orographic and convergent uplift may also contribute to the total bias. Reduced vertical transport causes ^{222}Rn to remain near the surface and in the cold pocket at lower potential temperature surfaces. The largest fractional overestimate of ^{222}Rn at $4° \times 5°$ resolution is aligned with the 265 K potential temperature surface, while the largest fractional underestimate corresponds to the 310 K surface. There are also large fractional changes in the stratosphere, although the ^{222}Rn concentrations are low there. In the stratosphere at $2° \times 2.5°$, there is much less ^{222}Rn reduction at high latitudes and more in the tropics and in the upper stratosphere. These differences may point to increased cross-tropopause transport at coarser resolution, which may also contribute to lower ^{222}Rn concentrations in the upper troposphere (UT) at $4° \times 5°$. They may also indicate increased isentropic mixing through the boundaries of the tropical pipe in the stratosphere, transporting more air with high levels of ^{222}Rn out of the tropical pipe in the $4° \times 5°$ simulation.

^{7}Be in the $4° \times 5°$ resolution simulation was reduced by up to 20% in the extratropical lower stratosphere (LS) and increased by up to 20% in the tropical UT (see Fig. 4.6e). The extra-tropical LS interacts with the UT across the tropopause through baroclinic waves in the troposphere. Air in the UTLS region is stirred and subsequently mixed by cutoff cyclones, tropopause folds and uplift in warm conveyor belts of extratropical cyclones (Stohl et al., 2003). The ^{7}Be experiment indicates that STE was enhanced at $4° \times 5°$ resolution. The results also suggest that subsidence in the troposphere between the 270 K and 300 K isentropes is stronger at $2° \times 2.5°$ resolution, resulting in higher

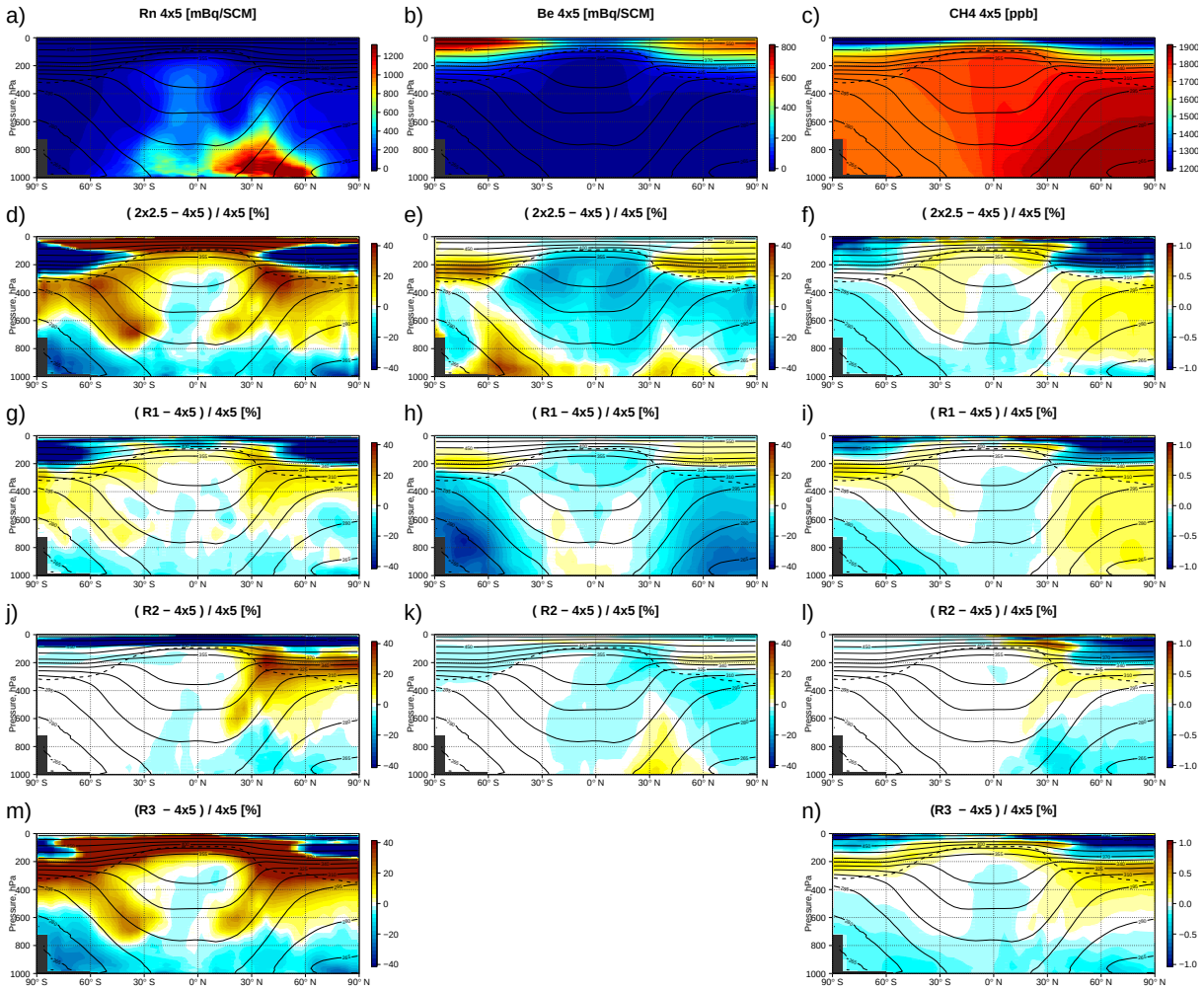

Figure 4.6: Evaluation of the mean meridional circulation in GEOS-Chem using ^{7}Be, ^{222}Rn and CH_4 transport tracers. First column represents results for ^{222}Rn tracer, second column - for ^{7}Be tracer, third column - for CH_4 tracer. First row: mean zonal tracer concentrations in March 2010. Second row: mean difference between 2° × 2.5° and 4° × 5° simulations in March 2010. Third row: mean difference between R1 and 4° × 5° simulations in March 2010. Fourth row: mean difference between R2 and 4° × 5° simulations in March 2010. Fifth row: mean difference between R3 and 4° × 5° simulations in March 2010. R1 is 4° × 5° simulation driven by remapped 2° × 2.5° hAMFs; R2 is 4° × 5° simulation with original calculated hAMFs over NA, EU and CH regions replaced by remapped 0.5° × 0.67° hAMFs; R3 is 4° × 5° simulation driven by remapped 2° × 2.5° hAMFs with additional CH_4 eddy mass flux based on 2° × 2.5° simulation.

^{7}Be concentrations in the lower troposphere at mid-latitudes (up to 35%) and lower ^{7}Be concentrations in the UT in polar regions (up to 20%).

The results of the CH_4 experiment were similar to those from the other two experiments. CH_4 is well mixed in the troposphere and, therefore, is not a good tracer of tropospheric transport. However, the difference plot in Fig. 4.6f shows similar evidence of reduced

vertical transport, with lower CH_4 concentrations below 900 hPa in the NH and higher concentrations above. Higher CH_4 fields in the middle and upper extratropical troposphere in the NH are also explained by a stronger tropopause barrier at $2^\circ \times 2.5^\circ$ resolution, which prevents CH_4 from mixing into the LS and leads to more CH_4 accumulation in the troposphere. Transport in the NH was more strongly affected by model resolution as CH_4 gradients are larger in this region. It could also be explained by the fact that the results are given for the month of March when baroclinic wave activity is stronger in the NH. The ACE-FTS comparisons in Figs. 4.2 and 4.3 showed similar results, with the model biases in the NH more sensitive to changes in model resolution than in the SH.

4.4.2 Polar vortex

The zonal mean plots in Figs. 4.6d-f hide some details of stratospheric transport related to the polar vortex dynamics. To better understand the source of the stratospheric bias, we carried out yearly comparisons of simulated CH_4 fields at both model resolutions with a focus on the polar lower stratosphere. Simulations were run from 1 July 2009 to 1 July 2010 with the identical model setup with the same initial conditions. Figs. 4.7 and 4.8 show mean monthly CH_4 differences at the 50 hPa pressure surface for the NH and SH. The dark blue colors correspond to the regions with lower CH_4 at $2^\circ \times 2.5^\circ$. These regions of lower CH_4 are aligned with and evolve together with the polar vortex, which is illustrated in Fig. 4.9. A vivid example is the vortex splitting event in February 2010. As the polar vortex becomes stronger and develops sharper potential vorticity (PV) gradients at its boundaries, the latter become barriers for mixing. Subsidence inside the polar vortex brings air depleted in CH_4 down from higher altitudes. This air mixes inside the polar vortex but does not mix with the vortex exterior. However, as can be seen in Figs. 4.7-4.8, this barrier is weaker at $4^\circ \times 5^\circ$ and results in higher CH_4 relative to the $2^\circ \times 2.5^\circ$ resolution. As expected, the model CH_4 differences are also aligned with the model$-$GOSAT XCH_4 mismatch in Fig. 4.1 and are substantially reduced at higher horizontal resolution. In case of the vortex splitting event in February 2010 these mismatch were observed over both North America and Eurasia.

4.4.3 XCH_4 bias

As described in Section 2.3, the number of vertical layers in GEOS-Chem, compared to the original GEOS-5 model, can be reduced in the upper stratosphere above 80 hPa. There are 36 vertical levels in this region in the original metfields, which are reduced to just 11 levels here, so that the total number of vertical levels is reduced from 72 to 47.

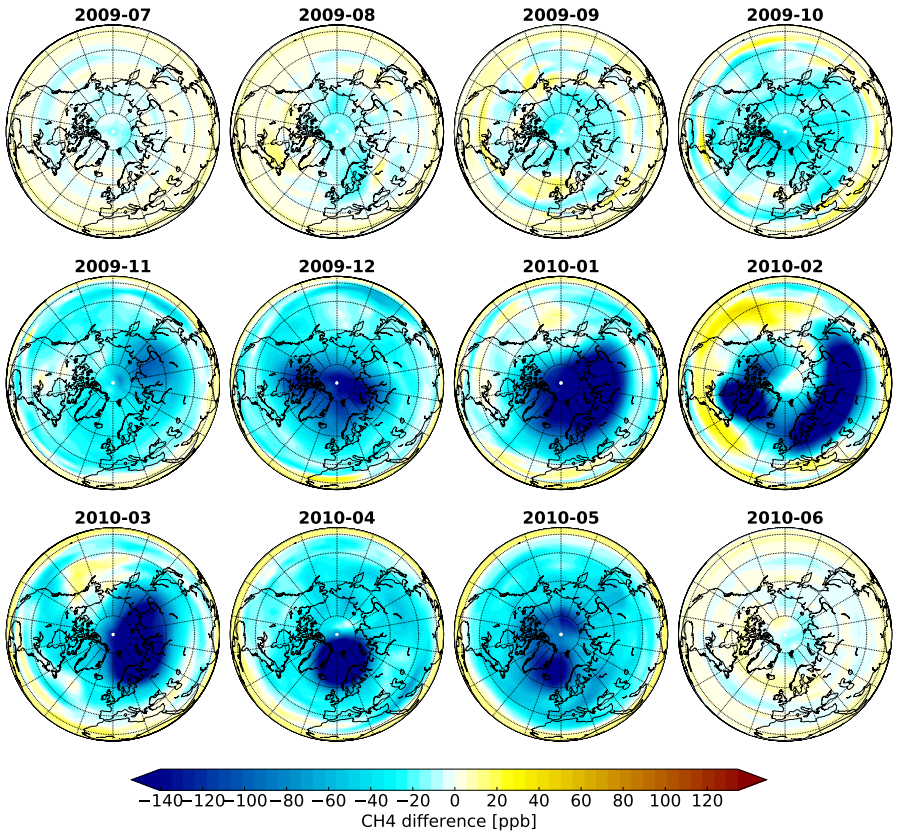

Figure 4.7: Monthly mean difference between 2° × 2.5° and 4° × 5° GEOS-Chem CH_4 simulations at the 50 hPa pressure level (north pole projection).

We also assessed the impact of this vertical remapping on modelled XCH_4 fields. We ran the model with 72 and 47 vertical levels, at both horizontal resolutions. However, for the comparison, all simulations were regridded to the 4° × 5° resolution with 47 vertical levels. The CH_4 differences between the model simulations were vertically smoothed with mean meridional GOSAT averaging kernels, which were averaged in 4° latitudinal bands over the entire period of the observations.

The purpose of these experiments was both to determine regional biases induced in XCH_4 fields by transport errors and to assess their impact on the total atmospheric CH_4 budget. It was shown in previous sections that at 2° × 2.5°, there is less CH_4 in the stratosphere and more in the troposphere. Such redistribution could result in additional CH_4 chemical loss as most of the OH mass is located in the tropical troposphere. Hence, transport errors could potentially project onto an atmospheric CH_4 sink. However, the results did not show any noticeable sensitivity of the CH_4 budget to horizontal resolution and vertical resolution in the upper stratosphere. Changes in the total CH_4 burden in both cases were negligible and didn't exceed 0.05% over the 6-year period.

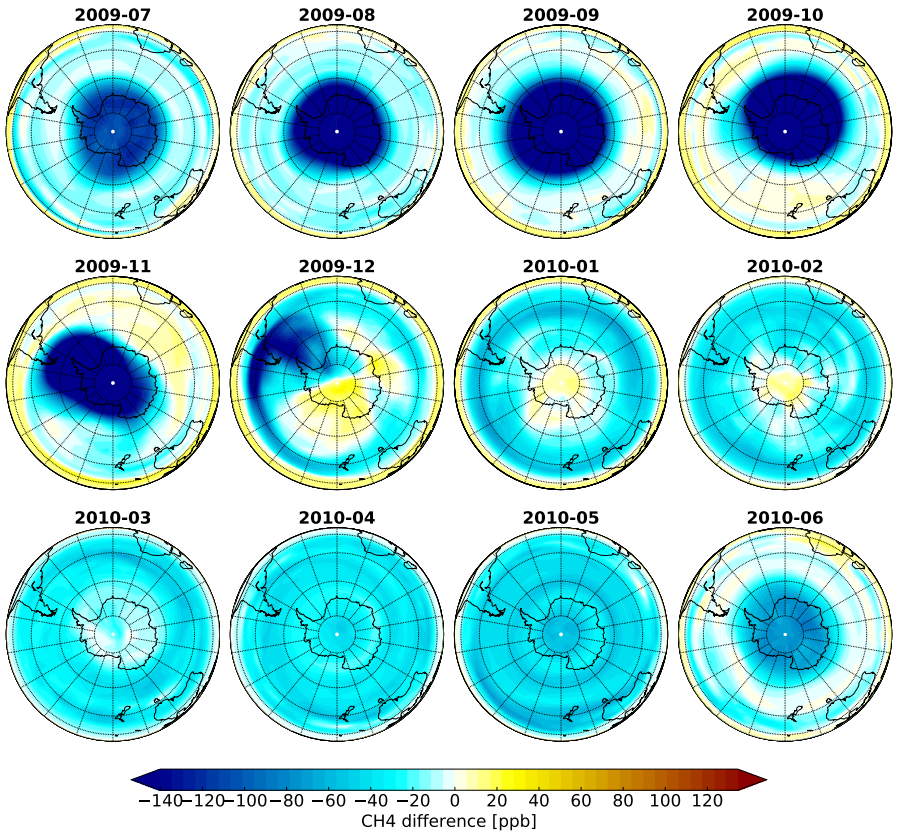

Figure 4.8: Monthly mean difference between 2° × 2.5° and 4° × 5° GEOS-Chem CH_4 simulations at the 50 hPa pressure level (south pole projection).

The results of the experiments are presented in Fig. 4.10 and suggest that increased model vertical resolution in the upper stratosphere had a modest impact on the CH_4 fields. The result is consistent with Strahan and Polansky (2006), however the impact may be larger if the model is run at high horizontal resolution where fine-scale winds in the upper stratosphere could, potentially, produce additional eddy transport sensitive to vertical model spacing. Although we didn't have a chance to fully assess sensitivity to vertical discretization, reduced vertical resolution in the vicinity of the tropopause layer may have a significant adverse effect on modelled CH_4 fields. For example, Locatelli et al. (2015) showed that increased vertical spacing in their model caused an additional leak of tropospheric CH_4 into the stratosphere, significantly biasing vertical CH_4 distribution.

The results of the second experiment with doubling of horizontal resolution show that generally, at 2° × 2.5°, CH_4 is reduced in the column at high latitudes to the north of about 40°N and south of about 50°S and is increased in tropics. As suggested by Fig. 4.6f, the general bias structure is mainly a result of CH_4 redistribution at 2° × 2.5° resolution with more CH_4 in the troposphere and less CH_4 at high latitudes in the stratosphere.

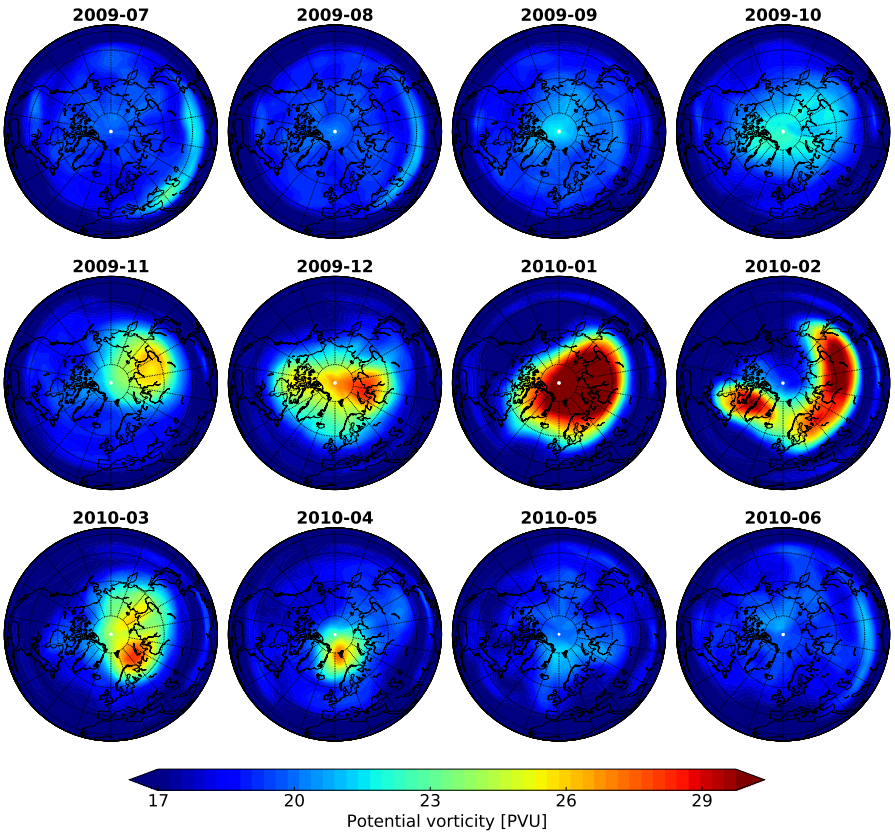

Figure 4.9: Mean monthly potential vorticity on 450 K isentropic surface from the archived GEOS-5 metfields (north pole projection).

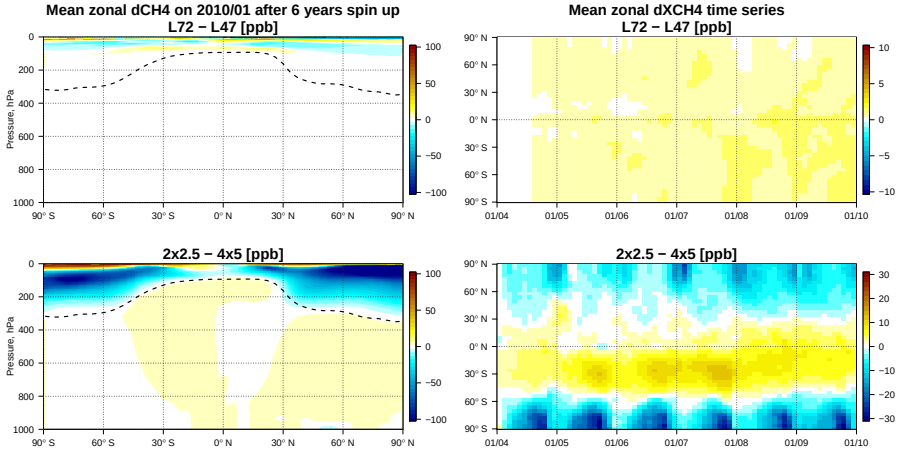

Figure 4.10: First column: mean zonal CH_4 difference (see below) after 6 years of simulation. Second column: mean zonal XCH_4 bias time-series obtained by smoothing CH_4 difference profiles with mean latitudinal GOSAT averaging kernels. First row: difference between GEOS-Chem CH_4 fields modelled using 72 and 47 vertical levels. Second row: difference between GEOS-Chem CH_4 fields modelled at $2° \times 2.5°$ and $4° \times 5°$ horizontal resolution).

Additionally, this pattern is intensified by weaker quasi-isentropic mixing between the tropics and high latitudes in the upper stratosphere at 2° × 2.5° resolution. The XCH_4 increase in the tropics is largely in the SH, however after four years the pattern of biases becomes more symmetric over the equator. The general bias pattern is also modulated by seasonally changing XCH_4 biases associated with the polar vortex in both hemispheres. In the SH where the polar vortex is stronger and more isolated, negative XCH_4 biases are sharp, localized and as large as -31 ppb, while in the NH, the bias fields are more diffused with maximum amplitude of -23 ppb. Strong seasonally varying negative XCH_4 biases in the polar regions are also accompanied by additional positive XCH_4 anomalies of up to 12 ppb in the tropics.

4.4.4 Vertical transport in the troposphere

The tracer experiments in Section 4.4.1 also revealed issues in modelled vertical transport in the troposphere. Here, we investigate possible causes of the reduced vertical transport at the coarse model resolution. The structure of the ^{222}Rn bias between the two model resolutions suggested errors in tracer advection at mid-latitudes. Here we examine possible sources of these transport errors and their impact on the modelled tracer fields.

4.4.4.1 Regridding mass flux versus horizontal winds

Figure 4.11 shows the mean spatial distribution of the vertical air mass fluxes (vAMFs) at about the 590 hPa pressure level in GEOS-Chem at coarse (4° × 5°) and native (0.5° × 0.667°) horizontal resolutions in May 2010 over east Asia. They show that the high-resolution fluxes have more detailed structure due to the complex topography of China, and point to the potential of producing inconsistencies in calculating the vAMFs at different model resolutions due to the fact that at coarse resolution, vAMFs are obtained from degraded coarse resolution cell-centred winds (see Section 2.3.2). To quantify the potential impact of calculating the horizontal AMFs (hAMFs) at the grid cell interfaces from the coarse resolution wind fields, we consider using archived hAMFs remapped from the native resolution GEOS-5.2.0 fields. This ensures consistency between hAMFs at different model resolutions and, therefore, preserves the derived vAMFs.

Unfortunately, neither native resolution hAMFs nor global surface pressure and winds fields at the native GEOS-5.2.0 resolution were available for us, as GMAO has transitioned to version GEOS-5.7.2 of their assimilation system. Instead, we performed two experiments using the 2° × 2.5° and nested GEOS-5.2.0 model fields. In one experiment (R1 experiment), the 2° × 2.5° hAMFs at the grid cell boundaries were remapped to 4°

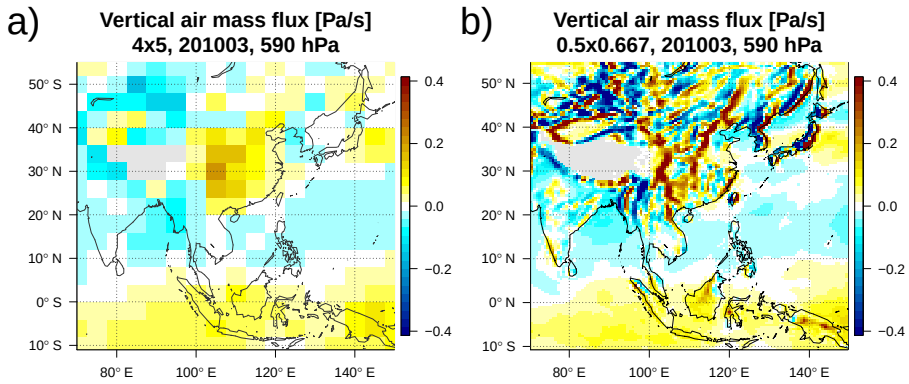

Figure 4.11: Mean advective vAMFs at 4° × 5° and 0.5° × 0.67° resolution in March 2010 at the 590 hPa pressure level.

× 5°. In the other experiment (R2 experiment), we used the native 0.5° × 0.67° hAMFs from the nested model for North America, Europe, and Asia. The remapped native resolution hAMFs in the R2 experiment were merged with the ones calculated at the coarse resolution over the rest of the globe. The hAMFs at 2° × 2.5° and 0.5° × 0.67° were calculated in GEOS-Chem, corrected using the pressure fixer, remapped and saved for each 4° × 5° resolution model transport time step. This also allowed us to turn off the pressure fixer in the R1 experiment as the high-resolution hAMFs already guaranteed mass conservation. Later, the remapped and merged hAMFs were used to drive advection at the coarse 4° × 5° model resolution. Figs. 4.6g-i and Figs. 4.6j-l summarize the results of the R1 and R2 experiments, respectively. The R1 results show that the initial differences between tracer fields at 4° × 5° and 2° × 2.5° resolutions (Figs. 4.6d-f) were partly due to inconsistent AMFs. Using the corrected hAMFs, we were able to partly mitigate vertical transport errors. For example, ^{222}Rn was increased in the upper troposphere by up to 12% in the "fixed" 4° × 5° simulation. Still, the proposed model fix does not explain all the differences between the 4° × 5° and 2° × 2.5° model resolutions. The R2 results suggest that the induced AMF bias between 4° × 5° and native resolution is even larger: regionally remapped native resolution hAMFs had a stronger impact on CH_4 fields at 4° × 5° resolution than globally remapped 2° × 2.5° hAMFs. The general feature of the results obtained is that the tropospheric correction to vertical transport easily propagates into the lower stratosphere at 4° × 5° resolution and further biases the UTLS CH_4 fields. Thus, the weakened tropopause barrier is a major defect of the 4° × 5° model resolution.

Finally, we quantified the impact of the AMF bias on the XCH_4 fields. Figure 4.12 shows the change in absolute bias between the model and GOSAT XCH_4 in the R1 and R2 experiments. Generally, remapped 2° × 2.5° mass fluxes (first column) had a relatively weak impact on XCH_4. Some reduction in the model−GOSAT mismatch was

observed in February at the position of the polar vortex over Europe and North America and in March-May over China. However, this was accompanied by a weak increase in the mismatch in other regions. In the R2 experiment (third column), the reduction in the absolute bias was significantly larger. The transport corrections in R2 reduced the positive XCH_4 misfit at high latitudes. The mean positive misfit over Europe in February was reduced by up to 16 ppb, whereas the positive model−GOSAT misfit over China in March-May was reduced by up to 30 ppb. The model bias over China was caused by weakened vertical advective transport, which we argue was due to a combination of regridding the winds and the strong surface emissions in China, resulting in CH_4 being partly trapped in boundary layer over the continent. Generally, the results suggest that the incorrect hAMFs produce noticeable local biases in the XCH_4 fields.

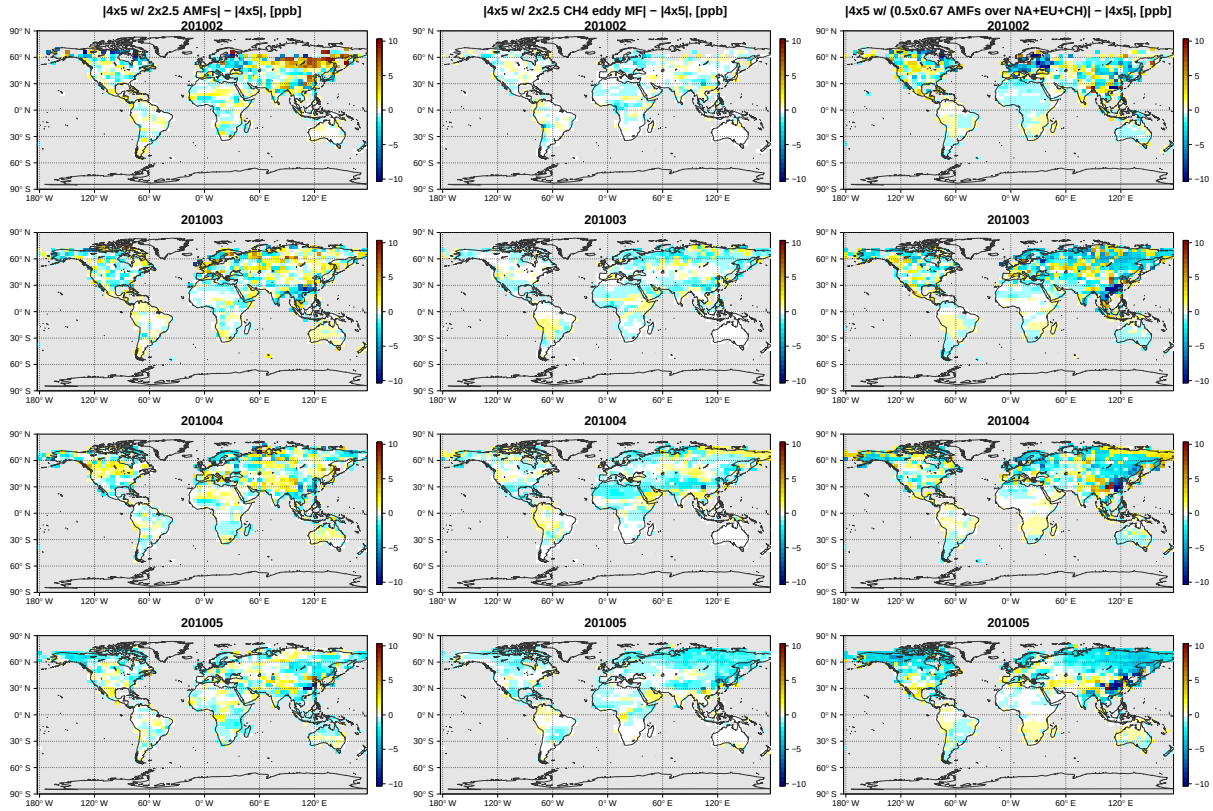

Figure 4.12: Difference in absolute XCH_4 mismatch against GOSAT observations between GEOS-Chem 4° × 5° simulation with corrected transport ("fixed") and original GEOS-Chem 4° × 5° simulation. First column: "fixed" simulation is driven by remapped 2° × 2.5° hAMFs (R1 experiment). Second column: "fixed" simulation is driven by remapped 2° × 2.5° hAMFs with additional CH_4 eddy mass flux based on 2° × 2.5° simulation. Third column: "fixed" simulation is the one with original calculated hAMFs over NA, EU and CH regions replaced by remapped 0.5° × 0.67° hAMFs (R2 experiment).

4.4.4.2 Eddy mass flux

The transport correction implemented in Section 4.4.4.1 only partly accounted for the missing vertical motion as inferred from Fig. 4.6 (third row). Here, we show that the rest of the missing motion can be explained by the loss of tracer eddy mass flux. The continuity equation for the tracer mass in the model grid box in the absence of sources and sinks is defined as

$$\frac{\partial(q\delta p)}{\partial t} + \boldsymbol{\nabla} \cdot (\overline{q\delta p \mathbf{u}}) = 0, \tag{4.1}$$

where q is tracer mixing ratio, δp is the pressure thickness and $\mathbf{u}$ is the 3D velocity. Assuming that both q and $\delta p\mathbf{u}$ vary on sub-grid scales, Eq. (4.1) can be rewritten as

$$\frac{\partial(q\delta p)}{\partial t} + \boldsymbol{\nabla} \cdot (\overline{q} \cdot \overline{\delta p \mathbf{u}}) + \boldsymbol{\nabla} \cdot (q' \cdot (\delta p \mathbf{u})') = 0 \tag{4.2}$$

where $\overline{(\,)}$ is the grid box average and $(\,)'$ is the deviation from the average. The third term on the l.h.s. represents divergence of the tracer eddy mass flux which arises from correlation between q' and $(\delta p\mathbf{u})'$. This divergence term gets lost due to averaging of sub-grid scale fields at coarse resolution.

To better understand the pattern of biases of Fig. 4.6 we briefly revisit the structure of the tropospheric circulation. As shown by Pauluis et al. (2008) from the analysis of atmospheric motion on dry and moist isentropes, tropospheric circulation is best represented by a two-cell structure. In one large hemisphere-size overturning cell, air ascends in the tropics and diverges poleward in the upper troposphere. Part of the air sinks in subtropical regions through radiative cooling while the rest continues poleward motion approximately along isentropes due to mixing by baroclinic waves. At high latitudes, air again descends by radiative cooling and experiences cross-isentropic transport into low latitudes near the surface accompanied by surface sensible heat release. The second smaller circulation cell is similar to the first one but is shorter and confined to mid- and high latitudes where extra-tropical cyclones supplied with moisture from the subtropics in the lower troposphere raise air from the surface to the upper troposphere along moist isentropes. The rest of the motion is as in the first branch. Tracer experiments performed in Section 4.4.1 suggest that model vertical transport is affected by resolution in the second circulation cell.

Vertical transport at middle and high latitudes is largely driven by synoptic scale eddies (extra-tropical cyclones) generated by baroclinic instability (Stohl, 2001; Parazoo et al., 2011). The combined action of convection and advection transports tracers upward and polewards from the surface in warm conveyor belts (WCBs) that originate ahead

of cold fronts and flow above warm fronts of cyclones. They transport air from the boundary layer into the free troposphere, and thereby, are an important mechanism for ventilating the lower troposphere (Kowol-Santen et al., 2001; Sinclair et al., 2008; Ding et al., 2015). At the same time, these cyclones transport upper tropospheric air downward and equatorward at mid-latitudes, following dry intrusions behind the cold fronts. This creates a mean upward tracer flux for tropospheric species such as CH_4 and ^{222}Rn that are emitted at the surface. At NH mid-latitudes, regions of extratropical cyclone activity are located in the western part of the Atlantic and Pacific Oceans and partly overlap with eastern parts of North America and China (Stohl, 2001; Eckhardt et al., 2004; Shaw et al., 2016), which happen to be major CH_4 source regions. This makes WCBs particularly important for upward transport of CH_4 at mid-latitudes. As shown by Stohl et al. (2002), WCB trajectories over China experience rapid ascent and end up in the upper troposphere over the western Pacific, whereas WCB trajectories over North America originate in the PBL and extend to the upper troposphere over Europe.

Frontal uplift, however, may be sensitive to the horizontal resolution of the model. Sinclair et al. (2008) shows that the efficiency of the uplift depends strongly on turbulent mixing in the PBL that raises the tracer to the altitude penetrated by the WCB, and horizontal Ekman transport which supplies the tracer into the frontal region. Furthermore, the coarse-resolution model may not resolve narrow frontal zones and the associated horizontal tracer convergence. Therefore, part of the vertical transport associated with the sub-grid scale correlation between the vAMFs anomalies and the tracer mixing ratio anomalies ("anomalies" = deviations from the coarse grid cell average) is lost. Increased numerical diffusion acting on sharp inter-cell concentration gradients in the frontal zone is another issue that may interfere with vertical transport. Horizontal diffusion would create additional horizontal tracer mass flux which has to be extracted from the vertical mass flux (according to mass conservation), reducing the altitude of tracer penetration into the free troposphere.

In addition to frontal uplift, vertical advective CH_4 transport at mid-latitudes is through convergent uplift in the centre of cyclones and orographic uplift on the lee side of mountains. There mechanisms are of less significance, however they may also be sensitive to model resolution.

Figure 4.13 shows an example of CH_4 fields produced by a cyclone passing over the eastern United States modelled at three resolutions. It gives a snapshot of the cyclone at 12:00 UTC on March 21, 2010. The high-resolution ($0.5° \times 0.67°$) case was simulated using the nested GEOS-Chem model with boundary and initial conditions from the $4° \times 5°$ model run. Both the $4° \times 5°$ and $2° \times 2.5°$ resolution cases have the same initial

CH_4 conditions on 1 March 2010. Figure 4.13 shows that at 0.5° × 0.67° resolution, CH_4 surface concentrations are higher in the frontal zones and the CH_4 plume is lifted higher in the atmosphere along the moist isentropes. Qualitatively, the 2° × 2.5° resolution CH_4 fields are more similar to those at the 0.5° × 0.67° resolution than to those at 4° × 5°. This may suggest that the 2° × 2.5° resolution model approaches the spatial limit at which circulation in frontal zones can be resolved, whereas the 4° × 5° resolution is just too coarse for these purposes.

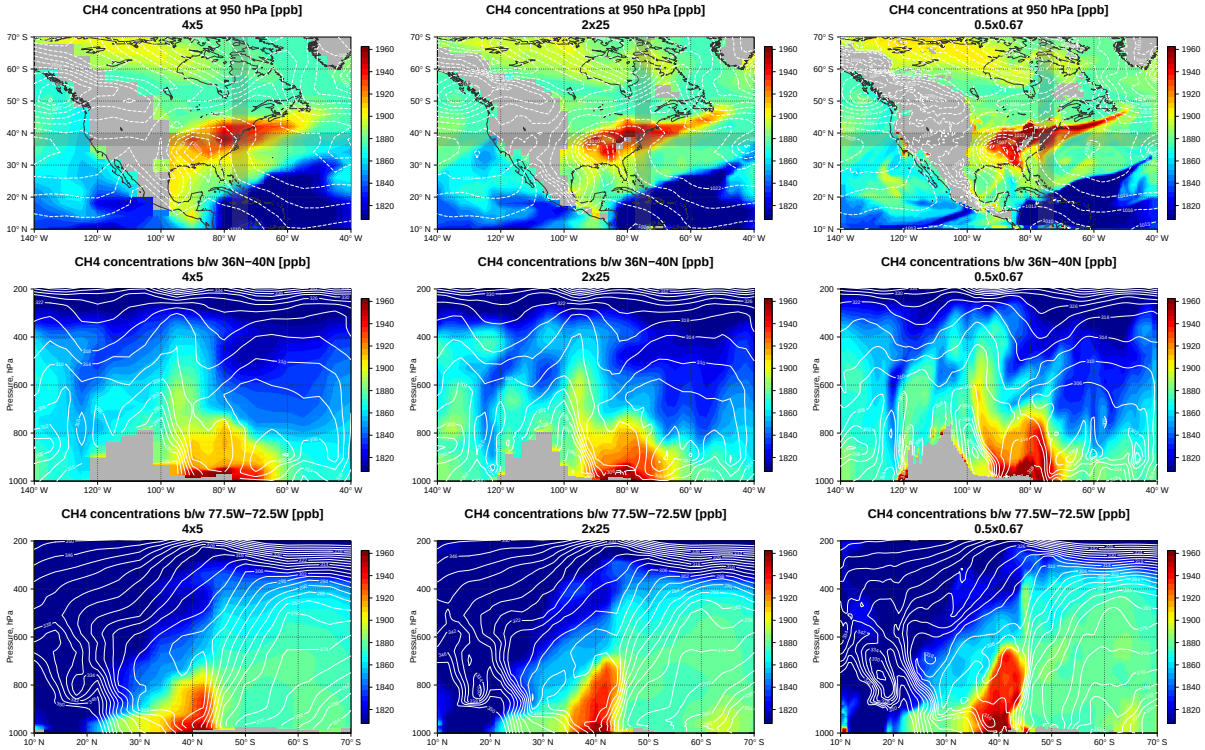

Figure 4.13: GEOS-Chem CH_4 fields at three resolutions at 12:00 UTC on March 21, 2010. First row: at 950 hPa (long-dashed grey lines are contours of sea level pressure). Second and third rows: vertical atmospheric slices through the grey horizontal and vertical bands drawn on the first-row figures (solid grey lines are moist isentropes).

For February-May 2010, we calculated the CH_4 and ^{222}Rn vertical eddy mass fluxes lost by degrading the model resolution from 2° × 2.5° to 4° × 5°. This was done as follows:

1. The 2° × 2.5° vertical tracer and air mass fluxes, and the tracer concentrations were archived from the 2° × 2.5° forward model run and remapped to 4° × 5°.

2. The 4° × 5° tracer mass fluxes were defined as a product of the remapped 2° × 2.5° vertical air mass fluxes and the tracer concentrations.

3. The lost eddy mass flux was set equal to the difference between the remapped 2° × 2.5° tracer mass fluxes in Step 1 and those calculated in Step 2.

Figure 4.14a shows the structure of the CH_4 mass flux at 700 hPa. It can be inferred from the figure that the calculated eddy mass flux is large in the mid-latitude storm track regions of both hemispheres over eastern South America, South Africa, and particularly, over eastern Asia, however, it is rather weak over North America. It also shows up over some mountainous regions, especially over the Himalayas, and in the ITCZ over Africa. The CH_4 eddy mass flux also increased over Europe (particularly, its northern part). One possibility is that this could be related to the ascent in the Icelandic low that moved far east during the extremely negative phase of the North Atlantic Oscillation in the winter/early spring 2010. However, the exact reason has not been determined. Figure 4.14b shows the monthly CH_4 tendency (integral of the eddy mass flux over each global pressure surface) associated with the eddy mass flux, both globally and over North America. For comparison, we also show the CH_4 tendency for the eddy mass flux over North America derived from the 0.5° × 0.67° nested CH_4 simulation. Generally, because CH_4 is well mixed in the troposphere, the tendency terms are rather small. Eddy mass flux acts to reduce CH_4 concentrations from approximately 950 hPa to 600 hPa by as much as 20 ppb month^{-1} and increase it in the upper troposphere by up to 7 ppb month^{-1}. It also increases CH_4 concentrations near the surface below 950 hPa. The North American example also shows that the 0.5° × 0.67° CH_4 tendency in the lower troposphere is about twice as large as 2° × 2.5° tendency.

We used the calculated eddy mass flux as a correction to the advective tracer mass flux at 4° × 5°. Figure 4.6m-n show the impact of the combined eddy mass flux correction and the AMF correction in Section 4.4.4.1 on the zonal structure of ^{222}Rn and CH_4 fields. The corrected 4° × 5° simulation recovers much of the structure of the 2° × 2.5° fields (compare Figs. 4.6m and 4.6d). The issue for both the ^{222}Rn and CH_4 simulations at 4° × 5°, as noted in Section 4.4.4.1, is that corrections to the vertical transport into the troposphere leak into the stratosphere, hence the tracer transport at the coarse resolution cannot be fully recovered. Generally, the eddy correction has a smaller impact on the CH_4 and XCH_4 fields (Fig. 4.12, second column), but has a significant impact on short-lived ^{222}Rn. The influence of the eddy mass flux should be larger if it is derived from the global native resolution simulation.

Generally, the vertical eddy mass flux is species-dependent and there is no way to recover it exactly in the coarse resolution model. However, it may, potentially, be parametrized in the model as an additional diffusive or advective mass flux correction.

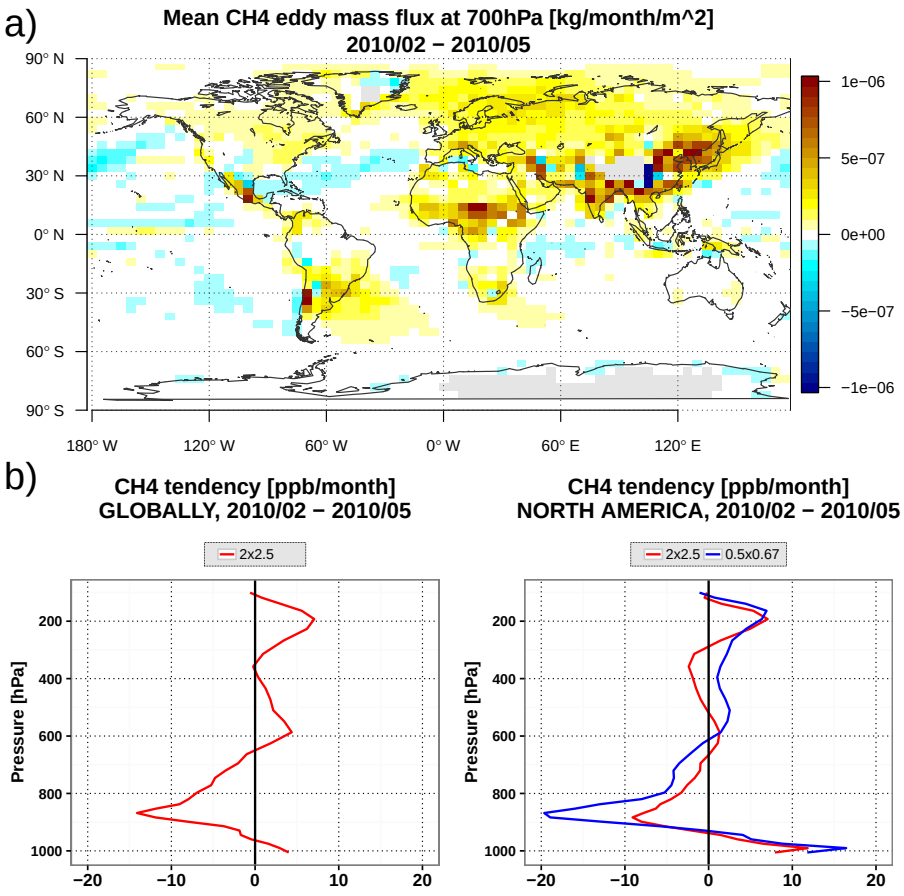

Figure 4.14: Top panel: mean CH_4 eddy mass flux at the 700 hPa pressure level for February-May 2010 lost by degrading the model resolution from 2° × 2.5° to 4° × 5°. Bottom panel: left - additional globally averaged vertical CH_4 tendency caused by the CH_4 eddy mass flux in the first row, right - comparison of additional mean vertical CH_4 tendencies over North America caused by eddy mass flux in the first row ("red") and by eddy mass flux which was lost by degrading model resolution from 0.5° × 0.67° to 4° × 5° ("blue").

The tracer continuity equation in the vertical direction can be modified as

$$\frac{\partial(q\delta p)}{\partial t} + \boldsymbol{\nabla}_p \cdot (q\delta p \mathbf{u}) = \boldsymbol{\nabla}_p \cdot (\kappa \boldsymbol{\nabla}_p \cdot (q\delta p)) \tag{4.3}$$

where the term on the r.h.s. has the form of the diffusion operator, with κ being tracer diffusivity. A similar approach was proposed by Wang et al. (2004). Coefficient κ can be uniform, for example, just to best match the mean zonal vertical tracer distribution however it can also be spatially varying. One possible solution is to set κ in Eq. (4.3) proportional to the squared buoyancy frequency N^2 in order to relate it to the uplift associated with frontal zones of cyclones due to reduced static stability. Ferreira et al. (2005) and Ferreira and Marshall (2006) showed a similar concept to be effective for

mesoscale eddy parametrization in ocean GCMs at coarse resolution.

4.5 Summary and discussion

We used the GEOS-Chem model at the horizontal resolution of 4° × 5° and 2° × 2.5° to understand the sources of resolution-induced biases in the model. We focused on the period of February-May 2010 to match the analysis period in Chapter 3, in which we used a weak constraint 4D-Var assimilation approach to characterize model errors in the GEOS-Chem CH_4 simulation. The GEOS-Chem CH_4 simulation was evaluated using XCH_4 retrievals from TANSO-FTS on-board GOSAT, ground-based XCH_4 retrievals from TCCON, and solar occultation CH_4 retrievals from ACE-FTS on-board SCISAT. Comparison of the model to all three datasets pointed to the presence of significant transport errors at the 4° × 5° resolution, which were greatly reduced at 2° × 2.5°. Discrepancies in the CH_4 fields induced by the model resolution included a latitudinal XCH_4 bias with large positive XCH_4 anomalies at high latitudes and small negative anomalies in the tropics. A significant part of this bias was related to discrepancies in the stratosphere. In addition, a positive XCH_4 bias was associated with the polar vortex. In the troposphere, a positive resolution-induced XCH_4 bias in the model−GOSAT differences was also observed over China and shown to be related to reduced vertical transport at 4° × 5°. The model evaluation against GOSAT, ACE-FTS and TCCON also suggested that a weak latitudinal bias is present in the 2° × 2.5° model and may be related to the stratosphere. We found that the magnitude of the resolution-induced differences between the 4° × 5° and 2° × 2.5° fields was similar in magnitude to the remaining model−GOSAT mismatch at 2° × 2.5° resolution.

We assessed the impact of the resolution-induced model biases on optimized CH_4 surface emissions for February-May 2010 by performing inversion analyses at both model resolutions using the 4D-Var method in GEOS-Chem. The 4° × 5° inversion suggested reduced CH_4 emissions at high latitudes and increased emissions in the tropics relative to the 2° × 2.5° model. The differences were large at grid-box scales, but were less than 30% when the inferred emissions were aggregated to the large TransCom regions. The moderate sensitivity of the emissions to the induced biases may be due to limited data density and observational coverage of GOSAT, particularly at high latitudes. However, the sensitivity to model errors is expected to be higher for data from missions such as TROPOMI, which will provide better observational coverage. Generally, given the magnitude of the model biases, we do not recommend the 4° × 5° GEOS-Chem model for CH_4 inverse modelling. Although the estimated model errors are much smaller at 2° × 2.5° resolution, additional

work is needed to better quantify the resolution-induced errors at 2° × 2.5° and assess their potential impact on inferred CH_4 source estimates.

Using ^{222}Rn, ^{7}Be and CH_4 tracers at the two model resolutions, we investigated the origins of model errors related to coarsening of the model resolution. The results showed that, fundamentally, the majority of the biases are caused by increased numerical diffusion at the 4° × 5° model resolution. Numerical diffusion acts to smear sharp tracer concentration gradients and is particularly detrimental in the regions with strong potential vorticity gradients, including the tropopause layer, boundaries of the tropical pipe, and the polar vortex. The results of this study are consistent with Strahan and Polansky (2006) who also showed that the 4° × 5° resolution model, driven by a similar advection scheme, cannot maintain adequate mixing barriers, which leads to enhanced stratosphere-troposphere exchange across the tropopause and enhanced mixing in the vicinity of the tropical branch of the Brewer-Dobson circulation and the polar vortex. As a consequence, at 4° × 5°, there is less CH_4 in the troposphere and more CH_4 is mixed into the lower stratosphere at high latitudes. Overall, this produces lower XCH_4 fields in the tropics and higher XCH_4 at high latitudes.

The tracer experiments also pointed to a weakening of vertical transport at coarser resolution in the troposphere, mainly at middle to high latitudes. Partly, it was caused by using the coarse resolution wind fields to recalculate the air mass fluxes at the grid box interfaces. Biased AMFs produced non-negligible local biases in the XCH_4 fields such as a large positive bias over China. We showed that this problem can be mitigated in GEOS-Chem by archiving and globally remapping the native resolution horizontal AMFs in order to drive advection at the coarse resolution instead of calculating the horizontal AMFs from the coarse-resolution wind fields. The remaining differences in vertical transport were explained by the loss of tracer eddy mass flux due to coarsening the model resolution and averaging the sub-grid model variability.

GEOS-Chem employs the Lin-Rood scheme for advection and, as mentioned by Prather et al. (2008) and Strahan and Polansky (2006), doubling the resolution of the Lin-Rood scheme from 4° × 5° to 2° × 2.5° may improve the model simulation. However, doubling the horizontal resolution to 2° × 2.5° does not eliminate all of the issues related to the off-line CH_4 transport. Therefore, in order to determine the optimal combination of computational time and accuracy, the ideal experiment would address the sensitivity of CH_4 fields to model transport errors in a cascade of model simplifications starting from an ensemble of on-line GCM simulations, and to the off-line transport modelling at 2° × 2.5° resolution using ensemble mean meteorological fields. The option of using a less diffusive advection scheme as the way to reduce sensitivity of simulated fields to model

resolution could also be explored. Meanwhile, the results of this study can be used as guidelines for future model evaluations and for inverse modelling CH_4 emissions.

Chapter 5

Sensitivity of regional emissions to boundary condition biases

The analysis conducted in the previous chapters indicates that the GEOS-Chem model at coarse spatial resolution contains biases that are reduced as the resolution increases. Although computationally expensive, high-resolution transport modelling offers one possible solution. In order to reduce computational time, simulations can be performed over a small spatial domain such as North America (one-way nested simulation) instead of a global one. However, a regional domain requires boundary and initial conditions which may be evaluated only at coarse temporal or spatial resolution given current observational coverage. Moreover, due to the relatively weak signal of local surface emissions in CH_4 observations, biases in boundary and initial conditions may still have a significant impact on inverse estimates of emissions depending on the type of observing system and measurements (Appendix A provides an in-depth analysis of the impact of boundary conditions on modelled XCH_4 observations).

In a small spatial domain, the memory of the initial conditions is short and the problem may be reduced to evaluating boundary conditions (BCs). One direct way to do that is to spatially and temporally interpolate sparse aircraft measurements in the troposphere over the boundaries of the domain and combine them with modelled stratospheric fields. This approach neglects some of the short-term variability in the background CH_4 arriving from the exterior of the domain. Although part of this variability may be filtered out when estimating, for example monthly-averaged emissions, it may still have a significant impact on shorter time scales. A different option is to optimize surface emissions and BCs simultaneously (for example, as in Wecht et al. (2014)). The disadvantage of this method is that the observations used to constrain the regional CH_4 state may not be able to distinguish between biases in emissions and boundary conditions and may also

produce dynamically inconsistent BC estimates. A third approach is to optimize the global CH_4 state at coarse model resolution and sample it over the region of interest (for example, Jiang et al. (2015); Turner et al. (2015)). This method is able to produce smooth dynamically consistent BCs at high spatial and temporal resolution relative to the other two methods.

This work uses two methods to optimize global CH_4 fields and sample boundary conditions around North America. In one method, we constrained CH_4 surface emission using the SC 4D-Var data assimilation technique. In the other method, WC 4D-Var is used to directly constrain the CH_4 state. Any differences between the models in the sampled BCs would be due to the ability of both methods to fit biases in the CH_4 state. A number of previous studies based upon SC 4D-Var (Turner et al., 2015) or sub-optimal Kalman filtering (Jiang et al., 2015) assumed that the forward model of the inversions is perfect and fitted biases in the state by means of surface emissions only. On the other hand, as shown in Chapter 3, WC 4D-Var is able to remove CH_4 biases that are due to various forward model errors and to produce better estimates of the CH_4 state.

The goal of this study is to compare the performance of the WC and SC 4D-Var methods for generating BCs and to evaluate the impact of differences between BCs on regional CH_4 surface emission estimates. In Section 5.1, we drive the regional GEOS-Chem model with different BCs in order to determine the ones that produce the best fit of simulated CH_4 fields to independent observations. In Section 5.2, we investigate the sensitivity of CH_4 emissions, constrained by real GOSAT observations and pseudo geostationary-like observations, to biases in BCs.

5.1 Boundary condition validation

Chapter 3 described the inversion setup that was used to perform SC and WC 4D-Var inversions in GEOS-Chem at the $4^\circ \times 5^\circ$ and $2^\circ \times 2.5^\circ$ resolutions from February to May 2010. We sample optimized CH_4 fields generated in these inversions over the North American domain every three hours and use them as boundary conditions for regional CH_4 simulations. In particular, we exploited CH_4 fields generated by the WC inversions with a three-day constant forcing time window and a forcing mask covering the entire atmosphere (**WC_T3_G1000_4x5** and **WC_T3_G1000_2x25**), which are referred to as **WC_4x5** and **WC_2x25**, respectively, in this chapter. Strong constraint 4D-Var inversions at $4^\circ \times 5^\circ$ and $2^\circ \times 2.5^\circ$ resolution are referred to as **SC_4x5** and **SC_2x25**, respectively.

We used the nested GEOS-Chem model over the North American domain (140°W to

40°W and 10°N to 70°N) at 0.5° × 0.67° resolution and performed four CH_4 simulations from February to May 2010 with an identical setup, including a priori CH_4 emissions but different boundary and initial conditions, and compared the resulting CH_4 fields with a set of observations. Figure 5.1 shows mean latitudinal XCH_4 difference between the four simulations and GOSAT XCH_4 retrievals. The figure suggests that the simulation with **SC_4x5** BCs contains a latitudinal bias compared to GOSAT, which is almost completely removed after switching to **WC_2x25** BCs. The other two BCs also produce latitudinal biases that are significantly smaller than those for **SC_4x5** BCs.

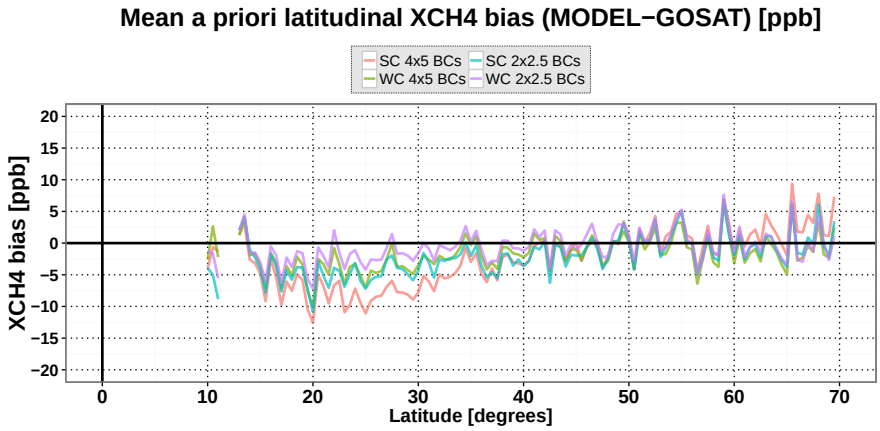

Figure 5.1: Mean latitudinal XCH_4 bias between nested GEOS-Chem CH_4 simulations with four boundary conditions and GOSAT XCH_4 retrievals over the period of February-May 2010. The bias was obtained by first averaging the "model−GOSAT" difference in each 0.5° × 0.67° model grid box, and then averaging zonally.

Table 5.1 presents results of the model comparison against NOAA *in situ* aircraft measurements, NOAA and ECCC *in situ* tall tower data, and TCCON XCH_4 retrievals at Lamont and Park Falls (see Section 2.1 for description of the datasets). These results suggest that neither the increase in resolution nor the use of the weak constraint technique improved the model agreement with *in situ* measurements. There is a significant variation in mean difference ranging from -6 ppb to 12 ppb for surface and from -3 ppb to 7 ppb for aircraft measurements. However, it is not possible to define the best BCs, as the larger mismatch may also imply under/overestimation of regional a priori CH_4 surface emissions.

Comparison to TCCON retrievals points to the benefit of increasing the model resolution and using the weak constraint method for generating BCs. **WC_2x25** BCs showed the best performance in regards to scatter and correlation against TCCON measurements, whereas the mean difference is not a good indicator as stations are located relatively close to CH_4 sources. TCCON comparisons also suggest that the gain from using WC BCs instead of SC BCs is larger than that from doubling the model resolution.

	Lamont			Park Falls		
	Diff. [ppb]	Scatter [ppb]	R	Diff. [ppb]	Scatter [ppb]	R
4° × 5° *BCs*:						
SC	1.8	8.6	0.52	-0.9	9.3	0.43
WC	3.6	7.8	0.64	-1.2	8.4	0.54
2° × 2.5° *BCs*:						
SC	1.9	8.8	0.59	-1.8	9.5	0.49
WC	4.7	7.3	0.69	1.0	8.0	0.61
	NOAA surface (May only)			**NOAA aircraft**		
	Diff. [ppb]	Scatter [ppb]	R	Diff. [ppb]	Scatter [ppb]	R
4° × 5° *BCs*:						
SC	-6.1	43.0	0.33	-3.1	20.2	0.80
WC	-1.3	43.0	0.32	-1.1	20.0	0.81
2° × 2.5° *BCs*:						
SC	11.9	42.4	0.32	6.8	20.7	0.79
WC	9.4	42.6	0.32	3.9	20.1	0.81

Table 5.1: Results of the evaluation (mean difference, scatter (1σ standard deviation) and correlation (R)) of the four modelled CH_4 fields in the nested GEOS-Chem simulation over North America with different boundary conditions (sampled from **WC_4x5**, **WC_2x25**, **SC_4x5** and **SC_2x25** global inversions) against TCCON Lamont and Park Falls XCH_4 and NOAA *in situ* aircraft CH_4 measurements in February-May 2010, and NOAA and ECCC *in situ* tall tower CH_4 measurements in May 2010.

5.2 Inversion of regional emissions: results and discussion

Here, we investigate whether inversions of regional CH_4 emissions are sensitive to the way in which the BCs are generated. We used the same four types of BCs as described above, sampled from the global CH_4 fields constrained by the GOSAT observations, but using different data assimilation methods and at different GEOS-Chem resolutions. Although **WC_2x25** BCs provided the best model fit to regional TCCON measurements, WC 4D-Var state optimization at 2° × 2.5° resolution is more costly to run than, for instance, 4° × 5° SC 4D-Var emissions optimization, and may not be the optimal choice for BCs in the case of weak sensitivity of emissions to the differences in BCs.

The OSSE results in Chapter 3 showed that it may take several months for the WC method to recover biases in the global CH_4 state due to initial conditions, particularly in the stratosphere. Therefore, and also due to the fact that all of our global CH_4 inversions covered only four months from February to May 2010, we used only May 2010 to test the sensitivity of the regional emissions to biases in BCs.

All regional emission inversions were performed using the SC 4D-Var data assimilation method and differed only in the imposed BCs. The inversions were initiated on April 21

but forced by observations only in May 2010. SC 4D-Var simultaneously optimized for mean emissions in May and mean emissions during the last 10-day period in April. We included this 10-day period for the inversion to lose memory of the initial conditions and to reduce potential biases due to regridding the coarse-resolution CH_4 initial conditions to a finer grid over complex terrain.

5.2.1 GOSAT inversions

In the first set of experiments, we used GOSAT observations as a constraint on regional surface emissions. Figure 5.2 shows the results of the inversions for the total optimized North American, US, and Canadian CH_4 emissions in May 2010. It shows that differences in total North American emissions compared to their a priori values, as well as between different inversions, are small (within 10-15%). Inversion with **SC_4x5** BCs produced larger emissions in all three regions compared to the other BCs. Inversions with **WC_2x25**, **SC_2x25** and **WC_4x5** BCs produced similar emission estimates (within about 7% over the USA and total North America and within about 12% over Canada). Larger differences in emissions over Canada may point to model biases in the stratosphere associated with the boundary conditions sampled from the global SC-optimized GEOS-Chem CH_4 fields at $4° \times 5°$ resolution. These biases are particularly large at high latitudes, where Canadian CH_4 sources are located.

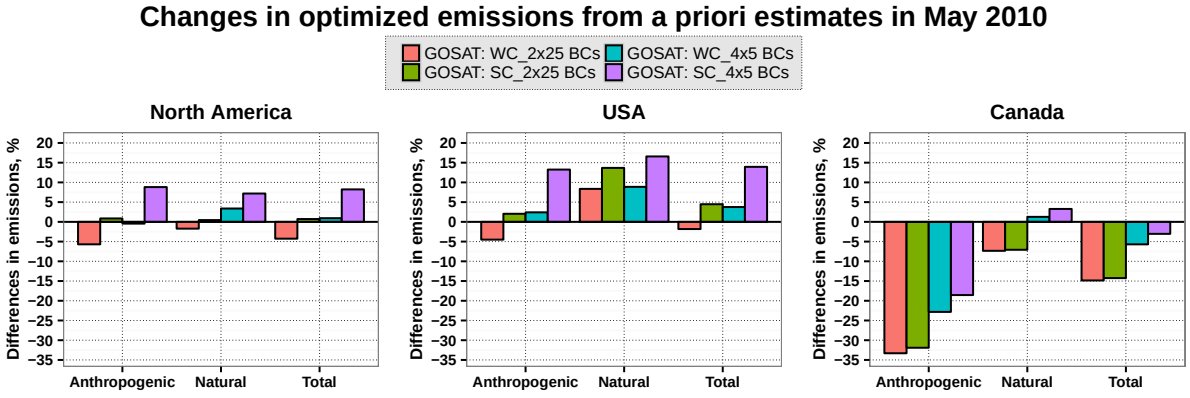

Figure 5.2: Percentage differences between total optimized and a priori surface emissions for North America, the USA and Canada. Emissions were optimized using GOSAT CH_4 observations and strong constraint 4D-Var in the nested GEOS-Chem model driven by four different boundary conditions sampled from **WC_2x25**, **WC_4x5**, **SC_2x25** and **SC_4x5** global inversions.

Figure 5.3 shows changes in total optimized emissions subdivided by sector compared to their a priori values. In order to obtain this result, the distribution of the a priori emissions by sector in each model surface grid box was assumed correct and was multiplied

by the optimized emission SFs to generate the sector-specific emissions. The sector-specific differences are much larger than those shown in Fig. 5.2. The figure again suggests that inversion with **SC_4x5** BCs produced emissions larger than the other inversions by up to 25%, particularly from coal mining, oil and gas extraction and burning, rice production and waste treatment over both Canada and the US. The inversion with **WC_2x25** BCs produced results most similar to the one with **WC_2x25** BCs over the USA and to the one with **SC_2x25** BCs over Canada. However, differences are still within about 10%.

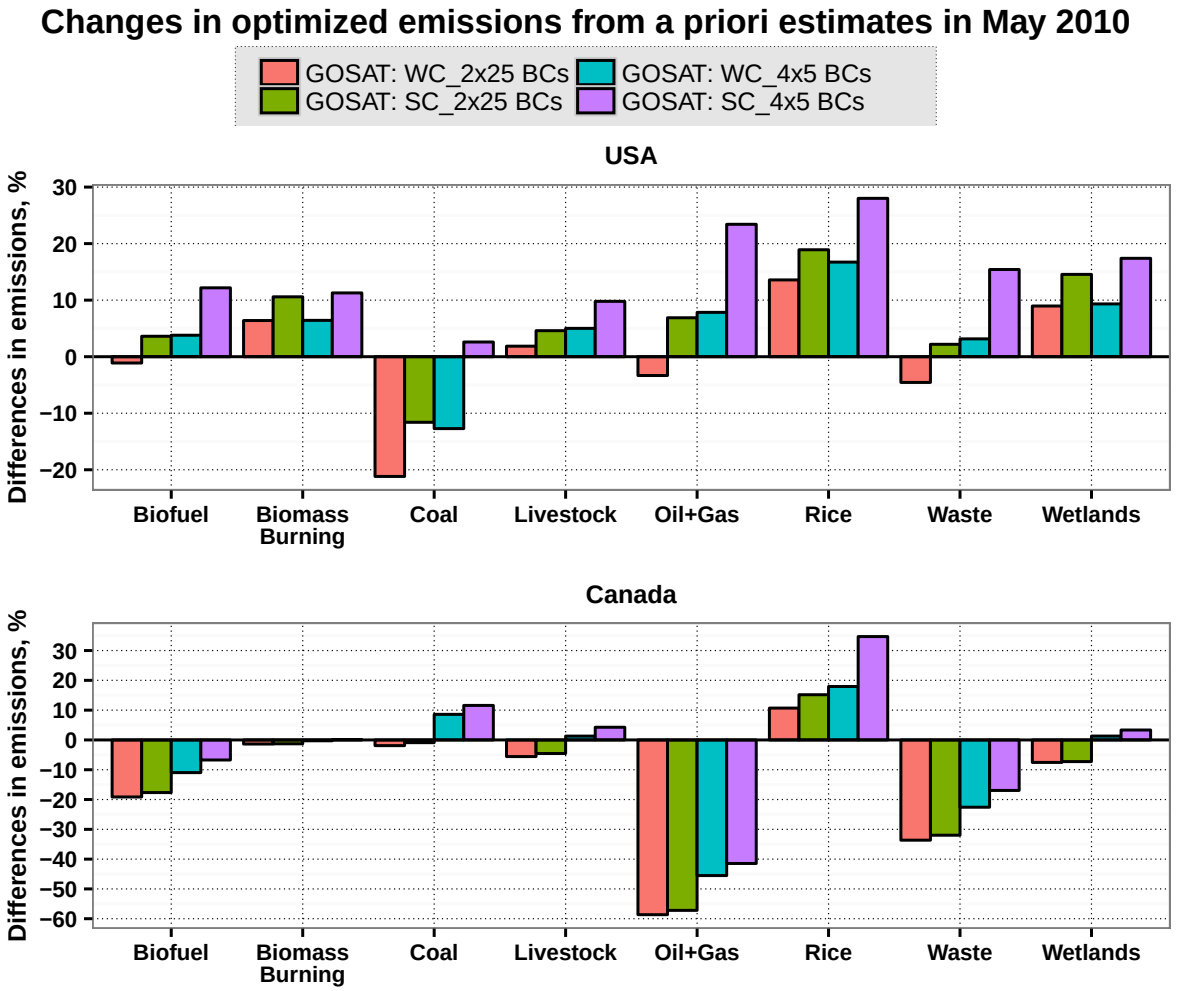

Figure 5.3: Same as Fig. 5.2 but with total US and Canadian emissions subdivided into different sectors (from biofuel burning, biomass burning, oil/gas and coal extraction and combustion, livestock, rice agriculture, waste treatment and wetlands).

The optimized emissions were further subdivided into smaller regions defined by the borders of US states and Canadian provinces and plotted in Fig. 5.4. The figure shows that differences in local emissions are within 20-25% excluding few outliers. As the resolution of the global model increases, SC and WC BCs, as well as corresponding

regional emission estimates converge due to reduction of model biases. Differences in the optimized emissions between **SC_2x25** and **WC_2x25** BCs at regional and local scale, as well as from difference emission sectors, are within about 10%.

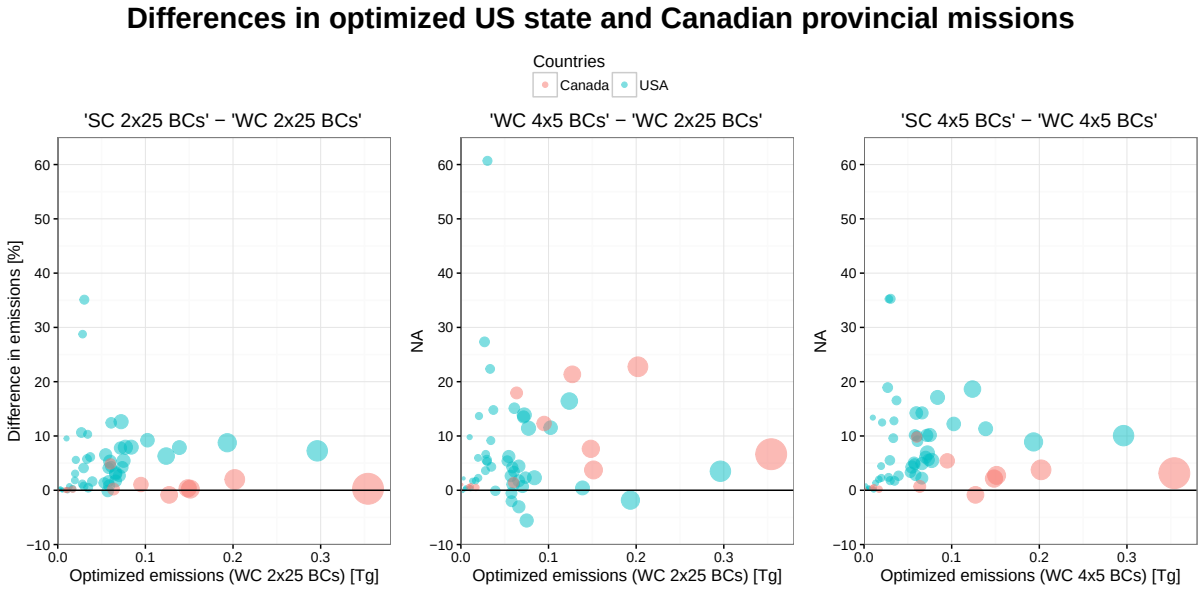

Figure 5.4: Percentage differences between optimized CH_4 surface emissions subdivided locally by borders of US states (blue circles) and Canadian provinces (red circles) from inversions driven by BCs sampled from: *left* - **SC_2x25** and **WC_2x25** global inversions, *middle* - **WC_4x5** and **WC_2x25** global inversions, *right* - **SC_4x5** and **WC_4x5** global inversions. The radius of each circle plotted is proportional to the magnitude of the corresponding local a priori emissions.

5.2.2 OSSEs with a geostationary-like satellite

The sensitivity of regional surface emissions to BC biases depends on the ability of the data assimilation algorithm to fit discrepancies in the CH_4 state at the expense of surface emissions. The greater the information content of an observing system, the higher would be the sensitivity of surface emissions to BC biases. GOSAT observations are still relatively sparse in space and time and provide limited constraints on surface emissions. Therefore, in an identical inversion scenario, surface emissions constrained by GOSAT XCH_4 retrievals may be weakly sensitive to BC biases compared to, for example, hypothetical geostationary observations over North America, which may be available in the future from the GeoCarb satellite (Polonsky et al., 2014).

We carried out a set of OSSEs for a geostationary-like (GEO-like) and GOSAT-like satellite in order to evaluate the sensitivity of regional emissions to BC biases under

different observational coverage. The GOSAT-like satellite performed XCH_4 observations at the time and location of GOSAT observations. The hypothetical geostationary-like satellite was assumed to perform GOSAT-like XCH_4 observations and sample CH_4 fields over North American land region once per hour with a FOV of 4x4 km^2. The number of satellite observations which fell in each $0.5° \times 0.67°$ model grid box was defined by the FOV but was reduced proportionally to the fraction of the grid box covered with clouds. The latter was taken from archived GEOS-5 meteorological fields. Additionally, all geostationary measurements for which the local SZA was larger than 70° were filtered out.

In the OSSEs, we defined the "true" CH_4 state as the one generated using **WC_2x25** BCs ("true" BCs) and the a priori surface emissions ("true" emissions). The "true" CH_4 state was sampled at the times and locations of the geostationary or GOSAT measurements and smoothed with GOSAT-like averaging kernels in order to create XCH4 pseudo-observations. We assumed 12 ppb uncertainty on the pseudo-observations, which is similar to the uncertainty of GOSAT observations, but did not add random noise as we were looking for the systematic component of sensitivity to BCs. In order to investigate the sensitivity, we perturbed the BCs, performed SC 4D-Var surface emission inversion analyses using the archived pseudo-observations and recorded the response of the inverted surface emissions to the perturbation. The "true" BCs were perturbed by successively replacing them with **SC_2x25**, **WC_4x5** and **SC_4x5** BCs. The rest of the inversion setup was kept identical to that in the previous section. In the ideal case with no sensitivity to BC biases, the inverted surface emissions would remain unchanged.

Figures 5.5 and 5.6 show the results of the OSSEs. They suggests that the sensitivity of emissions constrained by geostationary observations to BC biases can be significantly larger than that constrained by low-orbit GOSAT observations. In the latter case, regional anthropogenic and natural emissions change only by up to 7% in response to the introduced BC biases, while in the former case changes are within about 37%. Canadian anthropogenic emissions appeared to be particularly sensitive. This can be explained by sparse GOSAT observational coverage at high latitudes, which prevents the satellite from sampling a significant fraction of biases advected from the BCs. Results also show that the CH_4 state (and hence, boundary conditions) constrained by the satellite with sparse observational coverage should be used carefully in regional inverse modelling analyses where surface emissions are constrained by a different satellite, for example, with denser observation coverage or better information content.

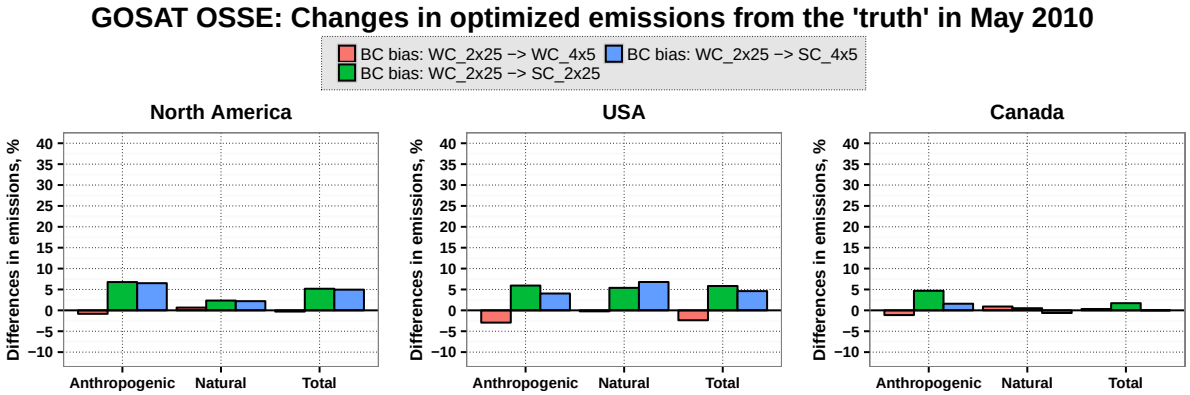

Figure 5.5: Percentage differences between the total emissions constrained by GOSAT XCH_4 pseudo-observations and the "true" surface emissions. Emissions were inverted in a set of OSSEs with biased boundary conditions only, where the "true" BCs were sampled from **WC_2x25** global inversion, while biased BCs were sampled from either **WC_4x5**, **SC_4x5**, or **SC_2x25** global inversions. The legend indicates the type of the imposed BC bias (for example, "WC_2x25 $->$ WC_4x5" implies that BC bias was introduced by replacing the "true" (**WC_2x25**) BCs with **WC_4x5** BCs).

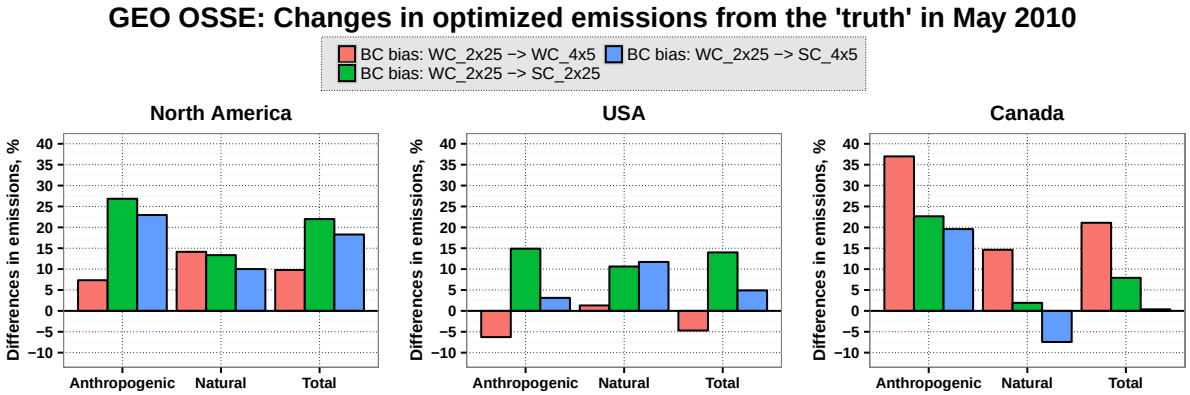

Figure 5.6: Same as Fig. 5.5 but for emissions constrained by geostationary XCH_4 pseudo-observations.

5.3 Discussion

Several conclusions can be drawn based on the results presented in this chapter. It was noticed that BC biases usually have smooth temporal and spatial structures and result in relatively uniform scaling of regional emissions so that the sensitivity of emissions at provincial and state scales is not significantly different from that at country scales. The results of the real GOSAT assimilations showed that even at local scales, differences in monthly emission estimates are generally within 20-25%, which is still a large number given that the BCs were constrained using the same model and measurements. Moderate convergence in the emission estimates was observed when the BCs were sampled from the

SC or WC optimized global 2° × 2.5° resolution CH_4 fields (**SC_2x25** and **WC_2x25** BCs). In this case, differences in the optimized regional- and local-scale emissions, as well as in emissions from difference sectors, were within about 10%. Therefore, errors remaining in the global optimized 2° × 2.5° GEOS-Chem model constrained by GOSAT XCH_4 retrievals may not significantly affect regional North American CH_4 emission estimates in May 2010, and these fields may potentially be used for sampling regional CH_4 boundary and initial conditions.

Despite moderate discrepancies in the emission estimates, the regional surface emission inversions with different boundary conditions suggested that Canadian a priori oil and gas emissions in May 2010 should be strongly reduced by about 40-60%. We were not aware of any study using the same a priori emissions inventory that pointed to the similar overestimation of Canadian CH_4 oil and gas emissions. Robustness of this result has to be further assessed by constraining Canadian emissions using in situ surface and aircraft observations and over the whole seasonal cycle.

As the spatial and temporal coverage of the observing system increases, so does the ability of this system to constrain regional surface emissions. However, as the OSSE results show, the sensitivity of the inverted monthly emissions to BC biases increases as well. In this chapter we tested the sensitivity of North American a priori emissions to BC biases that were defined as uncorrected biases in the CH_4 fields due to GEOS-Chem model errors, relative to the **WC_2x25** assimilation using GOSAT XCH_4 retrievals. Biases in the country-scale natural and anthropogenic emissions in May 2010 constrained by regional GOSAT pseudo-observations due to the introduced BC biases were within 7%. The maximum bias in emissions reached 37% when coverage of the pseudo-observations was changed to approximate that of the hypothetical geostationary satellite. This result also indicates that BCs optimized using one observing system with rather sparse coverage may still be affected by model errors not sampled properly by this system and, when used regionally with the different observing system, may introduce biases in the regional emission estimates.

It is important to note that the present analysis applies to a specific month, May 2010. Due to varying meteorological conditions, model errors, and regional CH_4 emissions, sensitivity to BC biases may be different in other months and should be investigated in future studies. Generally, it would also depend on the spatial (ranging from local to continental) and temporal (ranging from daily to annual) scales analysed. For example, the sensitivity of total annual regional emissions to BC biases may be relatively weak compared to the sensitivity of weekly local emissions.

Chapter 6

Conclusions

The scientific community has been seeking to attribute changes in atmospheric CH_4 concentrations to either variations in the chemical sink of CH_4 or in its emissions. Understanding the processes controlling CH_4 abundance is important for implementing efficient emission reduction policies and for accurate future climate projections. The CH_4 sink is usually evaluated using indirect estimates of the atmospheric OH budget based on measurements of methyl chloroform, while emissions are usually estimated using a "top-down" approach where the CH_4 state is constrained by atmospheric CH_4 measurements with additional constraints such as CH_4 isotopic composition. This thesis addresses a more narrow question: given measurements of global CH_4 distribution, assuming the known CH_4 sink, how well can surface emissions be localized to their geographic origin. Several factors play important roles for addressing this question. First, these include the observational coverage and quality of the CH_4 measurements. Second, particularly when the observational constraint is rather weak, a priori assumptions about CH_4 emissions are important, as the "top-down" approach deals with an under-constrained inverse problem for which a unique solution does not exist. However, the focus of this thesis is on the last set of factors, the quality of the CH_4 simulation, or model errors.

Ideally, the best available model is chosen for the CH_4 simulation that most closely represents reality. In the case of CH_4 with simple linear chemistry, the quality of simulation can be improved by increasing the resolution of the transport model, reducing numerical errors and errors in physical parametrizations. However, the model resolution is constrained by available computational resources. In the 4D-Var data assimilation, computational expenses increase by tens to hundreds of times compared to forward model simulation (depending on a number of iterations until convergence of the algorithm), which limits usability of global high-resolution models for 4D-Var chemical data assimilation. Generally, for a particular transport model, there is a grid spacing limit when resolution-

induced errors become small enough that they do not affect significantly the inferred CH_4 emission estimates (for example, changes in emissions are within 5-10%), and further increase of resolution does not bring significant gain in performance. Evaluation of resolution-induced error as well as other model errors caused, for example, by different physical parametrizations, is the major theme of this thesis.

In order to reduce simulation time and mitigate model errors, a high-resolution models can still be use for data assimilation purposes in a regional domain with imposed boundary conditions sampled from the global coarse-resolution simulation. However, boundary conditions are also affected by errors in the global simulation. Optimization of CH_4 BCs over North America for regional surface emission inversion purposes was the original problem that prompted the rest of the work in the thesis.

6.1 Summary of results

6.1.1 Weak constraint 4D-Var

The initial research objective was to generate an optimal CH_4 state, which can be used for sampling regional BCs, and to diagnose errors in the global CH_4 simulation at model resolutions of $4^\circ \times 5^\circ$ and $2^\circ \times 2.5^\circ$. Traditional strong constraint 4D-Var does not account for model errors. Therefore, the weak constraint method, recently implemented in GEOS-Chem by Martin Keller within the existing 4D-Var code, was used for these purposes and to address the first thesis objective (see Section 1.4). The design of the model error covariance matrix $\mathbf{Q}$ is key to the method performance. We adapted a rather simple structure for $\mathbf{Q}$ with uniform model error uncertainty and no correlation between errors, which implies that no specific assumptions about the structure and magnitude of the model errors were made. This design was validated in a set of OSSEs, where the WC method, using real GOSAT XCH_4 data, was shown to be able to remove artificially imposed model errors and optimize their structure. Although not having the most optimal configuration, the WC method significantly improved the modelled CH_4 fields relative to independent observations in comparison to the SC method, and identified transport errors in the model.

The WC assimilation identified and corrected for the positive bias in the stratospheric CH_4 fields at $4^\circ \times 5^\circ$. Even at $2^\circ \times 2.5^\circ$, the method was able to detect and mitigate the stratospheric bias relative to ACE-FTS and HIPPO-3 measurements. In the GEOS-Chem troposphere, the WC assimilation suggested that vertical transport at mid-latitudes, particularly over eastern China and North America, is too weak. Similar vertical transport

errors were identified at both model resolutions, although they were weaker at 2° × 2.5°. These errors may potentially be reduced by further increasing the model resolution, however, they may also be related to biases in meteorological fields, for example, in the strength of convective motion associated with mid-latitude cyclones. In the tropics, the WC assimilation pointed to the possibility of resolution-independent errors in the CH_4 outflow from the African continent to the Atlantic Ocean, that could also be related to model errors in convection.

Generally, this work showed that the 4° × 5° resolution model contains errors that are too large for the model to be used for CH_4 surface emissions optimization. The 2° × 2.5° model contains similar, but smaller errors and additional work is required to determine the impact of these errors on the inferred CH_4 source estimates. The weak constraint method was proven to be a useful tool for diagnosing model transport errors and for mitigating biases in the global CH_4 fields. The WC optimized CH_4 fields can be used for providing improved boundary and initial conditions for regional analyses at high horizontal resolution. This work also showed that satellite XCH_4 retrievals, used mainly for surface emissions optimization, contain enough information to at least partly mitigate model errors.

6.1.2 Resolution-induced model errors

Based on the results of the WC assimilation we further investigated resolution-induced biases in the GEOS-Chem CH_4 fields in order to better understand their origin and impact on the inverted surface emissions as well as to assess whether model transport at coarse resolution can be improved. This work addressed the second thesis objective from Section 1.4. The focus was on the 4° × 5° and 2° × 2.5° model simulations as these were the only two available global GEOS-Chem resolutions.

Comparison of the model to GOSAT, HIPPO-3, ACE-FTS and TCCON measurements revealed the presence of significant CH_4 biases at 4° × 5°, which were greatly reduced at 2° × 2.5°. Large resolution-dependent biases were found in the stratosphere, particularly at high latitudes, in the vicinity of the polar vortex, and in the troposphere over East Asia. Model validation also suggested that smaller CH_4 biases may still be present in the stratosphere at 2° × 2.5° resolution. The resolution-induced biases resulted in significant differences between CH_4 emissions at small spatial scales estimated using the two model resolutions, while differences were generally within 30% for emissions aggregated in the large TransCom region emissions. Such relatively moderate sensitivity of the emissions to the resolution-induced biases may be the result of sparse sampling of GOSAT retrievals,

particularly at high latitudes.

The origin of resolution-induced errors was investigated in the experiments using ^{222}Rn and ^{7}Be tracers. Results of the experiments showed that a majority of the biases are caused by increased numerical diffusion at the coarse resolution, which acts to smear tracer concentration gradients and weaken transport barriers in regions such as the tropopause layer, the tropical pipe, and the polar vortex in the stratosphere. This leads to enhanced stratosphere-troposphere exchange and enhanced mixing in the stratosphere. The tracer experiments also pointed to a weakening of the vertical transport at coarser resolution, mainly, in mid- to high latitudes. This was partly related to the specific implementation of the advection scheme in GEOS-Chem and was caused by the loss of the air mass fluxes at the grid box interfaces after remapping horizontal winds to coarse resolution. In particular, this resulted in the large positive CH_4 bias over China. The rest of the difference in the vertical transport was explained by the loss of the tracer eddy mass flux due to averaging of sub-grid model variability at coarse resolution. The loss of the eddy mass flux due to coarsening the resolution from $2^\circ \times 2.5^\circ$ to $4^\circ \times 5^\circ$ had a smaller impact on long-lived CH_4 than on the short-lived ^{222}Rn tracer (up to 30% reduction in the upper troposphere). Despite discrepancies in transport, the total CH_4 budget remained insensitive to doubling of the resolution from $4^\circ \times 5^\circ$ to $2^\circ \times 2.5^\circ$.

In this work, we showed that the lost air mass flux can be recovered by changing the configuration of the advection scheme. In the older code, the air mass fluxes were calculated on-line from the coarse resolution wind fields. This was changed, so that the advection could be driven by archived fluxes remapped from the native model resolution.

Generally, the results showed that the resolution-induced errors alone in GEOS-Chem at $4^\circ \times 5^\circ$ have a large impact on surface emissions. The $4^\circ \times 5^\circ$ CH_4 simulation may, potentially, be improved but at additional cost. For example, numerical diffusion at coarse resolution and its sensitivity to the model resolution can be reduced by using a less diffusive advection scheme, such as the SOM, but at the expense of simulation time and storage space. The advection scheme in GEOS-Chem should be updated as described above at no additional cost, except for the space to store air mass fluxes at the original GEOS-5 resolution. The eddy mass flux may, potentially, be parametrized as a correction to the advective tracer mass flux or as an additional diffusive tracer mass flux using machine learning techniques such as neural networks with atmospheric stability (buoyancy frequency) as one of input parameters. These recommendations apply not only to the $4^\circ \times 5^\circ$ model but to the model at any higher resolution if similar errors still persist. Even if $2^\circ \times 2.5^\circ$ resolution does not satisfy quality requirements for inversion of surface emissions (such that an impact of model errors on inferred surface emissions is

limited to 5-10%), running the global 4D-Var assimilation at higher resolution, such as 1° × 1°, is too expensive for global chemical data assimilation. Therefore, transport has to be improved at least at the 2° × 2.5° resolution.

6.1.3 Optimizations of boundary conditions

The other option is to perform regional assimilation at high (0.5° × 0.67°) resolution with optimized regional CH_4 boundary conditions. Optimization of CH_4 BCs over North America motivated work in this thesis in the first place and is the third objective of the thesis (see Section 1.4). Several experiments were performed to evaluate the sensitivity of monthly mean North American CH_4 emissions to BC biases and to determine BCs that most closely imitate reality.

In practice the real biases in BCs are unknown, therefore, a guess has to be made in order to approximate them. Different CH_4 BCs were sampled from the global CH_4 fields optimized at 4° × 5° or 2° × 2.5° using the WC or SC 4D-Var approach. The WC inversion at 2° × 2.5° provided slightly better regional BCs, which was confirmed by comparing the regional CH_4 simulation to a set of independent observations, although the time period for validation was limited. Differences between the **WC_2x25** BCs and the other three BCs were assumed to approximate biases that could have remained after the global CH_4 state or flux assimilation, although the real biases may be even larger due to unaccounted model errors after the global **WC_2x25** assimilation. Four different North American CH_4 emission estimates in May 2010 were obtained based on the regional SC 4D-Var flux assimilation with the four different CH_4 boundary conditions.

All four assimilations strongly reduced (by about 40-60%) Canadian a priori oil and gas emissions in May 2010. However, robustness of this result has to be further addressed by constraining Canadian emissions over the whole seasonal cycle and using in situ surface and aircraft observations. The results also showed that even at provincial/state scales, differences in the monthly emission estimates were generally within 20-25%. However, moderate convergence in these estimates was observed when the BCs were sampled from the global 2° × 2.5° CH_4 fields optimized using either the SC or WC methods. In this case, differences in the optimized monthly emissions at various spatial scales, as well as in emissions from difference sectors, were within about 10%. This could imply that further increase in the resolution of the global model may not be required, and the **WC_2x25** CH_4 fields may be satisfactory for sampling regional CH_4 boundary and initial conditions.

Due to rather sparse coverage, the information content of the GOSAT observing system over North America is significantly smaller than that of the future geostationary

GeoCarb satellite. As the spatial and temporal coverage of the observing system increases, so does the ability of this system to constrain regional surface emissions. However, the sensitivity of the inverted monthly emissions to BC biases increases as well. Therefore, a set of OSSEs was conducted to evaluate the sensitivity of the North American a priori emissions to the previously generated BC biases using pseudo-data from a hypothetical GOSAT satellite and a future geostationary satellite. In the former case, changes in the country-scale natural and anthropogenic emissions in May 2010 in response to the imposed BC biases were within 7%, while in the latter case they were as large as 37% of the "true" emissions. Generally, the OSSE results indicate that regional emissions constrained by future satellites with better observation coverage may be more sensitive to biases in the boundary conditions. However, this also depends on the ability of these satellites to mitigate model errors in the global CH_4 simulation. Additionally, different observing systems may sample and/or mitigate model errors differently and should not be used separately in the assimilation process (for example, one type of measurements for the global state optimization and sampling of BCs and another type for the regional surface emissions optimization).

6.2 Suggestions for future work

The work conducted in the thesis provided only an initial assessment of model errors, ways to correct them, and their impact on inverted CH_4 surface emissions. Therefore, it can be further expanded in a number of directions. Errors in the GEOS-Chem model can be further investigated using the WC 4D-Var method. The identified errors affected the model only in February-May 2010, therefore, further analysis is required to understand their impact in different seasons and years. In the tropics, particularly over Equatorial Africa, the WC state corrections were not sensitive to the model resolution. Therefore, the question about their origin remains open. XCH_4 glint measurements over oceans could help constrain the vertical structure of the local model errors and determine their sources. The WC assimilation of shorter-lived species, such as CO, could also help better diagnose model errors, especially when transport and emission errors mask each other in CH_4 fields. The advantage of CH_4 is its longer memory of model transport, however shorter-lived gases are more strongly affected by and, hence, may be more sensitive to the same model errors.

More optimal performance of the WC 4D-Var can be achieved by supplying the method with additional information about model errors, such as their temporal and spatial correlation, and magnitude, using the model error covariance matrix $\mathbf{Q}$. Further

analysis focused on a design of the **Q** matrix is also required for the method to be able to separate the signal of surface emissions from other model errors in order to improve surface emission estimates. For example, Trémolet (2007) proposed a design based on the statistics of model tendencies. The matrix **Q** had a rather primitive structure in our analysis, although sufficient for the objectives of this work. Based on this initial assessment of model errors, the structure of **Q** can be further improved.

Although doubling of the GEOS-Chem resolution from $4^\circ \times 5^\circ$ to $2^\circ \times 2.5^\circ$ significantly reduced biases in the CH_4 fields, significant errors may still be present in the $2^\circ \times 2.5^\circ$ GEOS-Chem simulation compared to the original high-resolution on-line GEOS-5 simulation. Therefore, their impact on the model transport, including advection, convection and PBL mixing, has to be further explored in order to determine an optimal GEOS-Chem setup for inversions of CH_4 surface emissions, with a compromise between simulation time and the negative impact of model errors. In the future, a full-chemistry simulation of CH_4 may become available, in which OH is an active species, and the CH_4 chemical loss may also be affected by the model resolution and will need to addressed as well.

When further increase of the model resolution does not favour the use of the 4D-Var method due to the increase of computational time, application of different data assimilation techniques, such as the ensemble Kalman Filter (EnKF), should be explored. In the EnKF, an ensemble of model state evaluations can be run in parallel, while 4D-Var in an iterative algorithm where the next iteration depends on the outcome of the previous one. Otherwise, model transport has to be improved at the coarse resolution (for example, as suggested in Section 6.1.2 in regards to advective transport or by Yu et al. (2017) in regards to convective transport).

The analysis conducted to address the sensitivity of the regional emissions to BC biases covered only one specific month, May 2010. The sensitivity to BC biases may differ seasonally and should be investigated in future studies. Generally, it would also depend on the spatial (ranging from local to continental) and temporal (ranging from daily to annual) scales analysed. For example, the sensitivity of total annual regional emissions to BC biases may be relatively weak compared to the sensitivity of weekly local emissions. Due to the fact that a significant fraction of biases in the global CH_4 fields and the CH_4 BCs is located in the stratosphere, the sensitivity of regional emissions to BC biases may be reduced if future satellite retrievals could be made less sensitive to the stratosphere and more sensitive to the troposphere.

6.3 Key findings

The main scientific results can be summarized as follows. The analysis conducted in the thesis showed that space-based observations of atmospheric composition can be used to improve a physical model, which has always been a goal of chemical data assimilation. Although GOSAT XCH_4 observations have previously been used only to constrain surface emission, they contain useful information about atmospheric transport and the distribution of CH_4 in the atmosphere to provide insight into discrepancies in atmospheric transport in the GEOS-Chem model. The results also showed that model errors in GEOS-Chem, including resolution-dependent errors, have significant impact on estimation of CH_4 surface emissions such that the $4^\circ \times 5^\circ$ model resolution appears to be inapplicable for these purposes and even for sampling CH_4 boundary conditions.

Appendix A

XCH_4 variability

The influence of North American BCs on modelled XCH_4 observations over the USA is manifested through the interaction of mid-latitude eddies, which intermittently bring air from the north and the south. We examined data in May-June 2010 to assess the variability of XCH_4 observations at the Lamont TCCON station.

We used the Stochastic Time-Inverted Lagrangian Transport model (STILT) to model XCH_4 at the location of the Lamont TCCON station using the so-called "receptor-oriented" modelling framework. STILT is based on the same mean advection scheme as the Hybrid Single-Particle Lagrangian Integrated Trajectory (HYSPLIT) model (Draxler and Hess, 1998), but has a different turbulence scheme described in Lin et al. (2003). The model was driven by archived reanalysis fields from the National Centers for Environmental Prediction (NCEP) Eta Data Assimilation System (EDAS-40 km, `ftp://www.arl.noaa.gov/pub/archives/edas40/`), which have 40 km horizontal resolution and are archived at 3-hourly timesteps. STILT follows an ensemble of particles released at the measurement (receptor) location backward in time and computes the upstream influence function $I_{\mathrm{CH_4}}(\mathbf{x}_r, t_r|\mathbf{x}, t)$, which links sources/sinks of CH_4, $S(\mathbf{x}, t)$, to concentration $C_{\mathrm{CH_4}}(\mathbf{x}_r, t_r)$ at the receptor point $(\mathbf{x}_r, t_r)$ (Lin et al., 2003)

$$C_{\mathrm{CH_4}}(\mathbf{x}_r, t_r) = \int_{t_0}^{t_r} dt \int_V I_{\mathrm{CH_4}}(\mathbf{x}_r, t_r|\mathbf{x}, t) S(\mathbf{x}, t) d\mathbf{x} + \int_V I_{\mathrm{CH_4}}(\mathbf{x}_r, t_r|\mathbf{x}, t_0) C_{\mathrm{CH_4}}(\mathbf{x}, t_0) d\mathbf{x}. \tag{A.1}$$

The first term on the r.h.s. corresponds to the contribution to $C_{\mathrm{CH_4}}(\mathbf{x}_r, t_r)$ from sources and sinks of the tracer in domain V, while the second term corresponds to the contribution from the tracer advection from initial or boundary conditions. Due to the fact that STILT operates in the troposphere only, the tropopause is defined as one of the boundaries. The surface influence function is also referred to as the surface "footprint" and has units of

ppb per unit emission flux. The final influence function is obtained as an average over an ensemble of particle.

In the standard STILT setup, we run an ensemble of 100 particle trajectories 10 days backward in time. We also added a simple chemical module to the model, which accounts for CH_4 destruction along each particle trajectory by reaction with OH and modifies the influence functions accordingly. XCH_4 concentrations were obtained by modelling the CH_4 profile at Lamont station and smoothing it with Lamont TCCON averaging kernels according to Eq. (2.24). STILT was used to model CH_4 concentrations in the troposphere on a 1 km vertical grid identical to that for the TCCON a priori profiles. The influence functions for CH_4 concentrations at each vertical level were transformed accordingly into the XCH_4 influence functions. The CH_4 boundary and initial conditions and CH_4 concentrations in the stratosphere were sampled from GEOS-Chem model CH_4 fields constrained by GOSAT UoL Proxy XCH_4 retrievals using SC 4D-Var data assimilation at $4^\circ \times 5^\circ$ resolution. OH fields in the chemical module and a priori CH_4 surface emissions were taken from the nested North American version of GEOS-Chem.

Figure A.1 shows the mean surface contribution from a priori emissions to Lamont XCH_4 defined as the integral

$$C^{surf}_{\mathrm{XCH_4}}(\mathbf{x}_r, t_r) = \int_{t_0}^{t_r} dt \int_{V_{1^\circ\times 1^\circ}} I_{\mathrm{XCH_4}}(\mathbf{x}_r, t_r|\mathbf{x}, t) S(\mathbf{x}, t) d\mathbf{x} \tag{A.2}$$

over each $1^\circ \times 1^\circ$ surface grid cell column and averaged over a number of Lamont measurement times during May-June 2010. For comparison, we also show the same surface contribution map for XCH_4 observations made by the University of Toronto Atmospheric Observatory (TAO) FTIR spectrometer (Wiacek et al., 2007). At Lamont, the surface signal of emissions is mainly from the south and even includes a contribution from Florida wetland emissions. On the other hand, the TAO surface signal is strongly localized within about 200 km of the site.

We modelled the XCH_4 timeseries at Lamont from 10 May 2010 to 28 June 2010 using STILT, and compared it to the timeseries modelled by the nested GEOS-Chem model at $0.5^\circ \times 0.67^\circ$ and global GEOS-Chem at $4^\circ \times 5^\circ$ resolution. Both STILT and the nested GEOS-Chem simulations used identical boundary and initial conditions and a priori CH_4 surface emissions. Differences between the simulations are due to the transport modelling approach (Lagrangian versus Eulerian) and the fact that stratospheric CH_4 concentrations at Lamont in STILT were prescribed, while those in nested GEOS-Chem were advected from the BCs. However, due to rapid transport, the stratospheric CH_4 fields in the regional high-resolution model would, mainly, be defined by imposed stratospheric CH_4

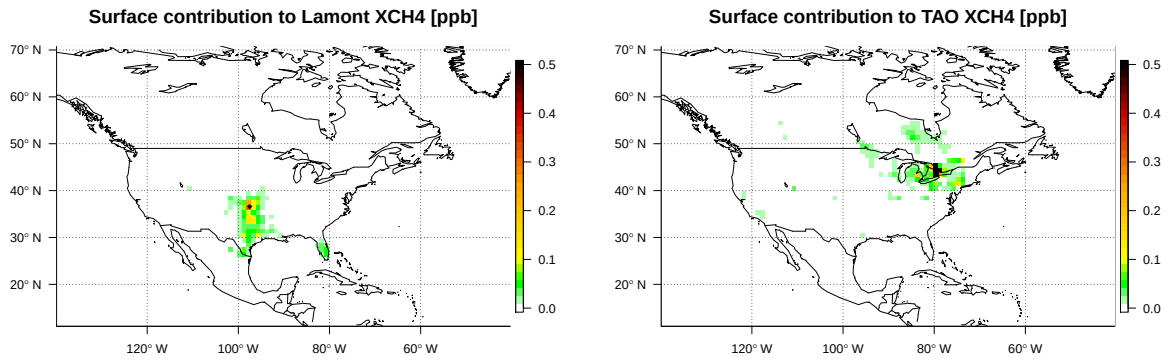

Figure A.1: Mean surface contribution to Lamont and TAO XCH_4 observations from each 1° × 1° surface grid cell over the period from May 10, 2010 to June 28, 2010. See the text above for further details.

BCs. The results of the simulations are given in Fig. A.2.

Figure A.2a shows the measured and modelled Lamont timeseries. For this particular time period, all three modelled timeseries are highly correlated with TCCON measurements and exhibit a positive bias that increases as TCCON XCH_4 decreases. Variations in the modelled timeseries are about 20 ppb on a monthly time scale and are lower by 1-2 ppb than in the measurements. Figure A.2b shows the total magnitude of the surface emissions signal modelled by STILT and nested GEOS-Chem. The result was not influenced by the treatment of the stratosphere as the surface signal did not reach the tropopause. The total surface signal in GEOS-Chem was obtained as the difference between the CH_4 simulations with and without surface emissions. The mean magnitude of the surface emissions signal is about 7-8 ppb. Both models showed similar patterns, but with some discrepancies in magnitude over time. Surface emissions only partly explained the XCH_4 variations in Fig. A.2a. Decreasing surface emissions could only partly reduce the positive mismatch between the modelled and measured XCH_4 timeseries. Therefore, a significant part of the variability and the mismatch is due to background air advected to the site from the boundary conditions (or due to the prescribed stratospheric CH_4 in the case of STILT timeseries).

We found that the tropopause pressure shown in Fig. A.2c was highly correlated with the modelled and measured XCH_4 and, therefore, was a better indicator of XCH_4 variability over Lamont during the given time period. The tropopause at mid-latitudes is determined dynamically by baroclinic eddies (Haynes et al., 2001). When interacting with the north-south XCH_4 gradient, eddies bring air to Lamont with XCH_4-poor air from the south and XCH_4-rich air from the north. Figure A.2d shows the fraction of all STILT tropospheric particle trajectories arriving at Lamont that originated to the south of 25°N

10 days before. This is an even better indicator of changes in XCH_4, which captured most of the features in the modelled and measured timeseries: as the fraction of trajectories from the south increased, the Lamont XCH_4 decreased.

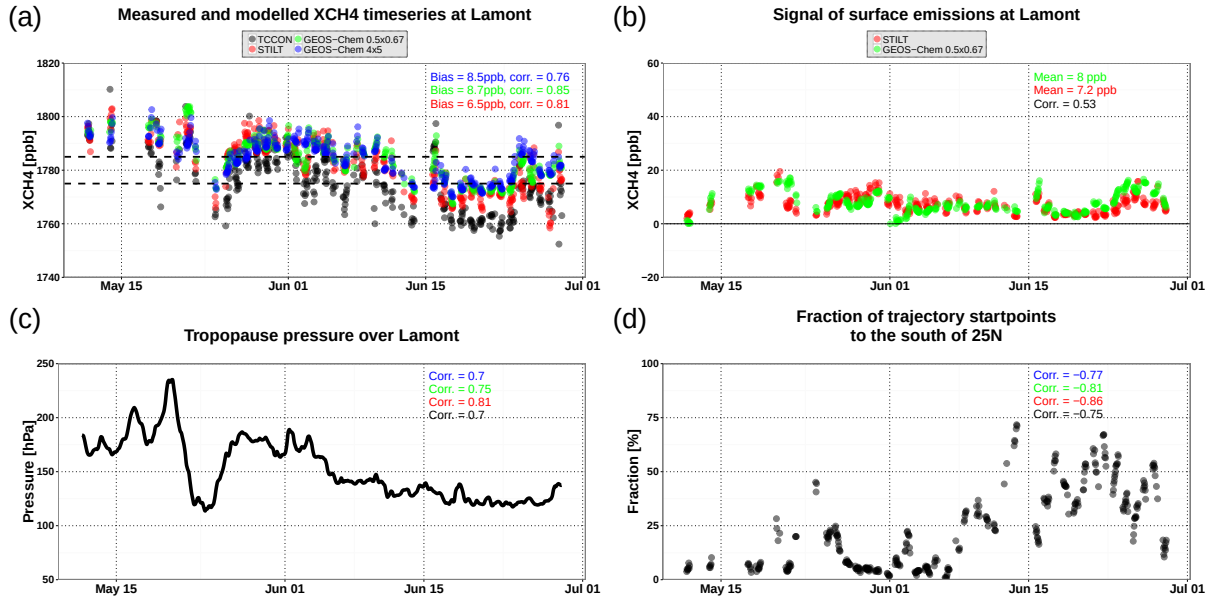

Figure A.2: *(a)*: TCCON XCH_4 timeseries at Lamont from May 10, 2010 to June 28, 2010 with the ones modelled by STILT, high-resolution GEOS-Chem nested over North America, and global GEOS-Chem at $4° \times 5°$ resolution (the legend gives mean difference and correlation (R) of each modelled timeseries with the measurements). *(b)*: signal of surface emissions in XCH_4 at Lamont modelled by STILT and nested GEOS-Chem (the legend gives the mean value of the signal over the entire timeseries and the correlation between both signals). *(c)*: tropopause pressure over Lamont (the legend gives the correlation of the corresponding timeseries in *(a)* with the tropopause pressure). *(d)*: fraction of all tropospheric STILT particle trajectories arriving at Lamont which originated to the south of 25°N 10 days before (the legend gives the correlation of the corresponding timeseries in the upper left figure with the fraction of trajectories from the south).

Figure A.3 shows the spatial probability density function of particle trajectory starting points for two cases: for STILT XCH_4 greater than 1785 ppb (above the upper dashed line in Fig. A.2a) and less that 1775 ppb (below the lower dashed line in the same figure). In the first case, most of trajectories arrived from the western boundary between 30°N and 50°N. In the second case, most of trajectories still originated at the western boundary but to the south of 30°N, however a significant fraction of particles also arrived from the southern and southeastern boundaries.

Although the time period of May-June 2010 is not representative of variability in the entire Lamont TCCON timeseries, the analysis still indicates that a significant fraction of XCH_4 variability may be due to background CH_4 advected from outside of the regional

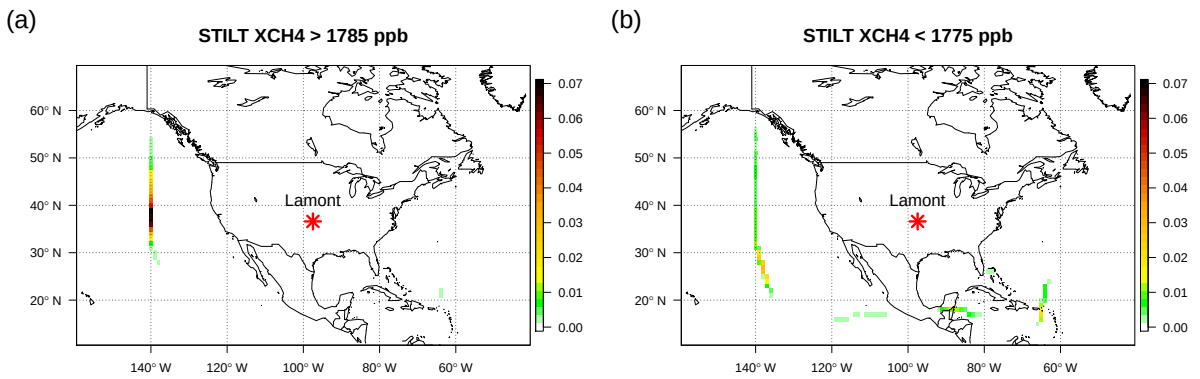

Figure A.3: Spatial probability distribution of modelled Lamont particle trajectory startpoints: *(a)* - for all STILT XCH_4 greater than 1785 ppb, *(b)* - for all STILT XCH_4 less than 1775 ppb.

domain. Small biases in CH_4 boundary conditions may have a significant impact on inverse estimates of local surface emissions, depending on their magnitude. The results also suggest that in our inversions it would not be possible to accurately constrain local surface emissions using the Lamont observations due to potentially large biases in background XCH_4 relative to the surface signal. We believe that, at least part of this bias is due to CH_4 BCs in the stratosphere which were sampled from SC 4D-Var CH_4 surface emissions inversions at $4^\circ \times 5^\circ$ resolution.

Bibliography

Alexe, M., Bergamaschi, P., Segers, A., Detmers, R., Butz, A., Hasekamp, O., Guerlet, S., Parker, R., Boesch, H., Frankenberg, C., Scheepmaker, R. A., Dlugokencky, E., Sweeney, C., Wofsy, S. C., and Kort, E. A.: Inverse modelling of CH_4 emissions for 2010–2011 using different satellite retrieval products from GOSAT and SCIAMACHY, Atmospheric Chemistry and Physics, 15, 113–133, doi:10.5194/acp-15-113-2015, 2015.

Allen, D. J., Kasibhatla, P., Thompson, A. M., Rood, R. B., Doddridge, B. G., Pickering, K. E., Hudson, R. D., and Lin, S.-J.: Transport-induced interannual variability of carbon monoxide determined using a chemistry and transport model, Journal of Geophysical Research: Atmospheres, 101, 28 655–28 669, doi:10.1029/96JD02984, 1996.

Andrews, A., Dlugokencky, E., and Lang, P.: Methane Dry Air Mole Fractions from the NOAA ESRL Surface Network using Programmable Flask Packages (PFP), 1992-2008, Version: 2014-06-23, aftp.cmdl.noaa.gov/data/trace_gases/ch4/flask/surface, 2008.

Andrews, A. E., Kofler, J. D., Trudeau, M. E., Williams, J. C., Neff, D. H., Masarie, K. A., Chao, D. Y., Kitzis, D. R., Novelli, P. C., Zhao, C. L., Dlugokencky, E. J., Lang, P. M., Crotwell, M. J., Fischer, M. L., Parker, M. J., Lee, J. T., Baumann, D. D., Desai, A. R., Stanier, C. O., De Wekker, S. F. J., Wolfe, D. E., Munger, J. W., and Tans, P. P.: CO_2, CO, and CH_4 measurements from tall towers in the NOAA Earth System Research Laboratory's Global Greenhouse Gas Reference Network: instrumentation, uncertainty analysis, and recommendations for future high-accuracy greenhouse gas monitoring efforts, Atmospheric Measurement Techniques, 7, 647–687, doi:10.5194/amt-7-647-2014, 2014.

Arellano, A. F. and Hess, P. G.: Sensitivity of top-down estimates of CO sources to GCTM transport, Geophysical Research Letters, 33, doi:10.1029/2006GL027371, l21807, 2006.

Arellano, A. F., Kasibhatla, P. S., Giglio, L., van der Werf, G. R., Randerson, J. T., and Collatz, G. J.: Time-dependent inversion estimates of global biomass-burning CO

emissions using Measurement of Pollution in the Troposphere (MOPITT) measurements, Journal of Geophysical Research: Atmospheres, 111, doi:10.1029/2005JD006613, 2006.

Aydin, M., Verhulst, K. R., Saltzman, E. S., Battle, M. O., Montzka, S. A., Blake, D. R., Tang, Q., and Prather, M. J.: Recent decreases in fossil-fuel emissions of ethane and methane derived from firn air, Nature, 476, 198, doi:10.1038/nature10352, 2011.

Bacmeister, J. T., Suarez, M. J., and Robertson, F. R.: Rain Reevaporation, Boundary Layer–Convection Interactions, and Pacific Rainfall Patterns in an AGCM, Journal of the Atmospheric Sciences, 63, 3383–3403, doi:10.1175/JAS3791.1, 2006.

Baker, D. F., Law, R. M., Gurney, K. R., Rayner, P., Peylin, P., Denning, A. S., Bousquet, P., Bruhwiler, L., Chen, Y.-H., Ciais, P., Fung, I. Y., Heimann, M., John, J., Maki, T., Maksyutov, S., Masarie, K., Prather, M., Pak, B., Taguchi, S., and Zhu, Z.: TransCom 3 inversion intercomparison: Impact of transport model errors on the interannual variability of regional CO_2 fluxes, 1988–2003, Global Biogeochemical Cycles, 20, doi:10.1029/2004GB002439, gB1002, 2006.

Bergamaschi, P., Frankenberg, C., Meirink, J. F., Krol, M., Villani, M. G., Houweling, S., Dentener, F., Dlugokencky, E. J., Miller, J. B., Gatti, L. V., Engel, A., and Levin, I.: Inverse modeling of global and regional CH_4 emissions using SCIAMACHY satellite retrievals, Journal of Geophysical Research: Atmospheres, 114, doi:10.1029/2009JD012287, 2009.

Bergamaschi, P., Houweling, S., Segers, A., Krol, M., Frankenberg, C., Scheepmaker, R. A., Dlugokencky, E., Wofsy, S. C., Kort, E. A., Sweeney, C., Schuck, T., Brenninkmeijer, C., Chen, H., Beck, V., and Gerbig, C.: Atmospheric CH_4 in the first decade of the 21st century: Inverse modeling analysis using SCIAMACHY satellite retrievals and NOAA surface measurements, Journal of Geophysical Research: Atmospheres, 118, 7350–7369, doi:10.1002/jgrd.50480, 2013.

Bernath, P.: The Atmospheric Chemistry Experiment (ACE), Journal of Quantitative Spectroscopy and Radiative Transfer, 186, 3–16, doi:https://doi.org/10.1016/j.jqsrt.2016.04.006, 2017.

Bernath, P. F., McElroy, C. T., Abrams, M. C., Boone, C. D., Butler, M., Camy-Peyret, C., Carleer, M., Clerbaux, C., Coheur, P.-F., Colin, R., DeCola, P., DeMazière, M., Drummond, J. R., Dufour, D., Evans, W. F. J., Fast, H., Fussen, D., Gilbert, K., Jennings, D. E., Llewellyn, E. J., Lowe, R. P., Mahieu, E., McConnell, J. C.,

McHugh, M., McLeod, S. D., Michaud, R., Midwinter, C., Nassar, R., Nichitiu, F., Nowlan, C., Rinsland, C. P., Rochon, Y. J., Rowlands, N., Semeniuk, K., Simon, P., Skelton, R., Sloan, J. J., Soucy, M.-A., Strong, K., Tremblay, P., Turnbull, D., Walker, K. A., Walkty, I., Wardle, D. A., Wehrle, V., Zander, R., and Zou, J.: Atmospheric Chemistry Experiment (ACE): Mission overview, Geophysical Research Letters, 32, doi:10.1029/2005GL022386, 2005.

Bindoff, N. L., Stott, P. A., AchutaRao, K. M., Allen, M. R., Gillett, N., Gutzler, D., Hansingo, K., Hegerl, G., Hu, Y., Jain, S., et al.: Detection and attribution of climate change: from global to regional, Climate Change 2013: The Physical Science Basis. Contribution of Working Group I to the Fifth Assessment Report of the Intergovernmental Panel on Climate Change, pp. 867–952, 2013.

Blumenstock, T., Hase, F., Schneider, M., Garcia, O., and Sepulveda., E.: TCCON data from Izana, Tenerife, Spain, Release GGG2014.R0, doi:10.14291/tccon.ggg2014.izana01.R0/1149295, 2017.

Boone, C. D., Nassar, R., Walker, K. A., Rochon, Y., McLeod, S. D., Rinsland, C. P., and Bernath, P. F.: Retrievals for the atmospheric chemistry experiment Fourier-transform spectrometer, Applied Optics, 44, 7218–7231, doi:10.1364/AO.44.007218, 2005.

Boone, C. D., Walker, K. A., and Bernath, P. F.: Version 3 Retrievals for the Atmospheric Chemistry Experiment Fourier Transform Spectrometer (ACE-FTS), in: The Atmospheric Chemistry Experiment ACE at 10: A Solar Occultation Anthology, edited by: Bernath, P. F., A, Deepak Publishing, Hampton, Virginia, USA, p. 103–127, 2013.

Bregman, B., Segers, A., Krol, M., Meijer, E., and van Velthoven, P.: On the use of mass-conserving wind fields in chemistry-transport models, Atmospheric Chemistry and Physics, 3, 447–457, doi:10.5194/acp-3-447-2003, 2003.

Bregman, B., Meijer, E., and Scheele, R.: Key aspects of stratospheric tracer modeling using assimilated winds, Atmospheric Chemistry and Physics, 6, 4529–4543, doi:10.5194/acp-6-4529-2006, 2006.

Brook, E. J., Harder, S., Severinghaus, J., Steig, E. J., and Sucher, C. M.: On the origin and timing of rapid changes in atmospheric methane during the Last Glacial Period, Global Biogeochemical Cycles, 14, 559–572, doi:10.1029/1999GB001182, 2000.

Bruhwiler, L., Dlugokencky, E., Masarie, K., Ishizawa, M., Andrews, A., Miller, J., Sweeney, C., Tans, P., and Worthy, D.: CarbonTracker-CH_4: an assimilation system

for estimating emissions of atmospheric methane, Atmospheric Chemistry and Physics, 14, 8269–8293, doi:10.5194/acp-14-8269-2014, 2014.

Bruhwiler, L. M. P., Michalak, A. M., Peters, W., Baker, D. F., and Tans, P.: An improved Kalman Smoother for atmospheric inversions, Atmospheric Chemistry and Physics, 5, 2691–2702, doi:10.5194/acp-5-2691-2005, 2005.

Butz, A., Hasekamp, O. P., Frankenberg, C., Vidot, J., and Aben, I.: CH_4 retrievals from space-based solar backscatter measurements: Performance evaluation against simulated aerosol and cirrus loaded scenes, Journal of Geophysical Research: Atmospheres, 115, doi:10.1029/2010JD014514, 2010.

Butz, A., Guerlet, S., Hasekamp, O., Schepers, D., Galli, A., Aben, I., Frankenberg, C., Hartmann, J.-M., Tran, H., Kuze, A., Keppel-Aleks, G., Toon, G., Wunch, D., Wennberg, P., Deutscher, N., Griffith, D., Macatangay, R., Messerschmidt, J., Notholt, J., and Warneke, T.: Toward accurate CO_2 and CH_4 observations from GOSAT, Geophysical Research Letters, 38, doi:10.1029/2011GL047888, 2011.

Byrd, R. H., Lu, P., Nocedal, J., and Zhu, C.: A Limited Memory Algorithm for Bound Constrained Optimization, SIAM Journal on Scientific Computing, 16, 1190–1208, doi:10.1137/0916069, 1995.

Byrne, B., Jones, D. B. A., Strong, K., Zeng, Z.-C., Deng, F., and Liu, J.: Sensitivity of CO_2 surface flux constraints to observational coverage, Journal of Geophysical Research: Atmospheres, 122, 6672–6694, doi:10.1002/2016JD026164, 2017.

Chen, Y.-H. and Prinn, R. G.: Estimation of atmospheric methane emissions between 1996 and 2001 using a three-dimensional global chemical transport model, Journal of Geophysical Research: Atmospheres, 111, doi:10.1029/2005JD006058, 2006.

Chevallier, F., Feng, L., Bösch, H., Palmer, P. I., and Rayner, P. J.: On the impact of transport model errors for the estimation of CO_2 surface fluxes from GOSAT observations, Geophysical Research Letters, 37, doi:10.1029/2010GL044652, l21803, 2010.

Chevallier, F., Palmer, P. I., Feng, L., Boesch, H., O'Dell, C. W., and Bousquet, P.: Toward robust and consistent regional CO_2 flux estimates from in situ and spaceborne measurements of atmospheric CO_2, Geophysical Research Letters, 41, 1065–1070, doi:10.1002/2013GL058772, 2013GL058772, 2014.

Chipperfield, M. P.: New version of the TOMCAT/SLIMCAT off-line chemical transport model: Intercomparison of stratospheric tracer experiments, Quarterly Journal of the Royal Meteorological Society, 132, 1179–1203, doi:10.1256/qj.05.51, 2006.

Chou, M.-D. and Suarez, M.: A Solar Radiation Parameterization for Atmospheric Studies. NASA Technical Report Series on Global Modelling and Data Assimilation, 15, 1–40, 1999.

Chou, M.-D., Suarez, M., Liang, X., , and Yan, M.-H.: A Thermal Infrared Radiation Parameterization for Atmospheric Studies. NASA Technical Report Series on Global Modelling and Data Assimilation, 19, 1–56, 2001.

Ciais, P., Sabine, C., Bala, G., Bopp, L., Brovkin, V., Canadell, J., Chhabra, A., DeFries, R., Galloway, J., Heimann, M., et al.: Carbon and other biogeochemical cycles, in: Climate Change 2013: The Physical Science Basis. Contribution of Working Group I to the Fifth Assessment Report of the Intergovernmental Panel on Climate Change, pp. 465–570, Cambridge University Press, 2013.

Colella, P. and Woodward, P. R.: The Piecewise Parabolic Method (PPM) for gas-dynamical simulations, Journal of Computational Physics, 54, 174–201, doi:http://dx.doi.org/10.1016/0021-9991(84)90143-8, 1984.

Cressot, C., Chevallier, F., Bousquet, P., Crevoisier, C., Dlugokencky, E. J., Fortems-Cheiney, A., Frankenberg, C., Parker, R., Pison, I., Scheepmaker, R. A., Montzka, S. A., Krummel, P. B., Steele, L. P., and Langenfelds, R. L.: On the consistency between global and regional methane emissions inferred from SCIAMACHY, TANSO-FTS, IASI and surface measurements, Atmospheric Chemistry and Physics, 14, 577–592, doi:10.5194/acp-14-577-2014, 2014.

De Mazière, M., Vigouroux, C., Bernath, P. F., Baron, P., Blumenstock, T., Boone, C., Brogniez, C., Catoire, V., Coffey, M., Duchatelet, P., Griffith, D., Hannigan, J., Kasai, Y., Kramer, I., Jones, N., Mahieu, E., Manney, G. L., Piccolo, C., Randall, C., Robert, C., Senten, C., Strong, K., Taylor, J., Tétard, C., Walker, K. A., and Wood, S.: Validation of ACE-FTS v2.2 methane profiles from the upper troposphere to the lower mesosphere, Atmospheric Chemistry and Physics, 8, 2421–2435, doi:10.5194/acp-8-2421-2008, 2008.

Dee, D. P. and Da Silva, A. M.: Data assimilation in the presence of forecast bias, Quarterly Journal of the Royal Meteorological Society, 124, 269–295, doi:10.1002/qj.49712454512, 1998.

Deng, F., Jones, D. B. A., Henze, D. K., Bousserez, N., Bowman, K. W., Fisher, J. B., Nassar, R., O'Dell, C., Wunch, D., Wennberg, P. O., Kort, E. A., Wofsy, S. C., Blumenstock, T., Deutscher, N. M., Griffith, D. W. T., Hase, F., Heikkinen, P., Sherlock, V., Strong, K., Sussmann, R., and Warneke, T.: Inferring regional sources and sinks of atmospheric CO_2 from GOSAT XCO_2 data, Atmospheric Chemistry and Physics, 14, 3703–3727, doi:10.5194/acp-14-3703-2014, 2014.

Derber, J. C.: A Variational Continuous Assimilation Technique, Monthly Weather Review, 117, 2437–2446, doi:10.1175/1520-0493(1989)117<2437:AVCAT>2.0.CO;2, 1989.

Ding, K., Liu, J., Ding, A., Liu, Q., Zhao, T. L., Shi, J., Han, Y., Wang, H., and Jiang, F.: Uplifting of carbon monoxide from biomass burning and anthropogenic sources to the free troposphere in East Asia, Atmospheric Chemistry and Physics, 15, 2843–2866, doi:10.5194/acp-15-2843-2015, 2015.

Dlugokencky, E.: Trends in Atmospheric Methane as measured by The Global Monitoring Division of NOAA's Earth System Research Laboratory at a globally distributed network of air sampling sites, `https://www.esrl.noaa.gov/gmd/ccgg/trends_ch4/`, 2018.

Dlugokencky, E., Lang, P., Crotwell, A., Mund, J., Crotwell, M., and Thoning, K.: Atmospheric Methane Dry Air Mole Fractions from the NOAA ESRL Carbon Cycle Cooperative Global Air Sampling Network, 1983-2015, doi:Path:ftp://aftp.cmdl.noaa.gov/data/trace_gases/ch4/flask/surface/, 2016.

Dlugokencky, E. J., Steele, L. P., Lang, P. M., and Masarie, K. A.: The growth rate and distribution of atmospheric methane, Journal of Geophysical Research: Atmospheres, 99, 17 021–17 043, doi:10.1029/94JD01245, 1994.

Draxler, R. R. and Hess, G.: An overview of the HYSPLIT_4 modelling system for trajectories, Australian meteorological magazine, 47, 295–308, 1998.

Dyer, E. L. E., Jones, D. B. A., Nusbaumer, J., Li, H., Collins, O., Vettoretti, G., and Noone, D.: Congo Basin precipitation: Assessing seasonality, regional interactions, and sources of moisture, Journal of Geophysical Research: Atmospheres, 122, 6882–6898, doi:10.1002/2016JD026240, 2017.

Eastham, S. D. and Jacob, D. J.: Limits on the ability of global Eulerian models to resolve

intercontinental transport of chemical plumes, Atmospheric Chemistry and Physics, 17, 2543–2553, doi:10.5194/acp-17-2543-2017, 2017.

Eckhardt, S., Stohl, A., Wernli, H., James, P., Forster, C., and Spichtinger, N.: A 15-Year Climatology of Warm Conveyor Belts, Journal of Climate, 17, 218–237, doi:10.1175/1520-0442(2004)017<0218:AYCOWC>2.0.CO;2, 2004.

Etheridge, D. M., Steele, L. P., Francey, R. J., and Langenfelds, R. L.: Atmospheric methane between 1000 A.D. and present: Evidence of anthropogenic emissions and climatic variability, Journal of Geophysical Research: Atmospheres, 103, 15 979–15 993, doi:10.1029/98JD00923, 1998.

Etminan, M., Myhre, G., Highwood, E. J., and Shine, K. P.: Radiative forcing of carbon dioxide, methane, and nitrous oxide: A significant revision of the methane radiative forcing, Geophysical Research Letters, 43, 12,614–12,623, doi:10.1002/2016GL071930, 2016.

European Commission Joint Research Centre/Netherlands Environmental Assessment Agency: Emission Database for Global Atmospheric Research (EDGAR), release version 4.0, URL `http://edgar.jrc.ec.europa.eu`, 2009.

Feng, L., Palmer, P. I., Bösch, H., Parker, R. J., Webb, A. J., Correia, C. S. C., Deutscher, N. M., Domingues, L. G., Feist, D. G., Gatti, L. V., Gloor, E., Hase, F., Kivi, R., Liu, Y., Miller, J. B., Morino, I., Sussmann, R., Strong, K., Uchino, O., Wang, J., and Zahn, A.: Consistent regional fluxes of CH_4 and CO_2 inferred from GOSAT proxy $XCH_4 : XCO_2$ retrievals, 2010–2014, Atmospheric Chemistry and Physics, 17, 4781–4797, doi:10.5194/acp-17-4781-2017, 2017.

Ferreira, D. and Marshall, J.: Formulation and implementation of a "residual-mean" ocean circulation model, Ocean Modelling, 13, 86–107, doi:10.1016/j.ocemod.2005.12.001, 2006.

Ferreira, D., Marshall, J., and Heimbach, P.: Estimating eddy stresses by fitting dynamics to observations using a residual-mean ocean circulation model and its adjoint, Journal of Physical Oceanography, 35, 1891–1910, doi:10.1175/JPO2785.1, 2005.

Fiore, A. M., Horowitz, L. W., Dlugokencky, E. J., and West, J. J.: Impact of meteorology and emissions on methane trends, 1990–2004, Geophysical Research Letters, 33, doi:10.1029/2006GL026199, 2006.

Frankenberg, C., Meirink, J. F., Bergamaschi, P., Goede, A. P. H., Heimann, M., Körner, S., Platt, U., van Weele, M., and Wagner, T.: Satellite chartography of atmospheric methane from SCIAMACHY on board ENVISAT: Analysis of the years 2003 and 2004, Journal of Geophysical Research: Atmospheres, 111, doi:10.1029/2005JD006235, 2006.

Fraser, A., Palmer, P. I., Feng, L., Boesch, H., Cogan, A., Parker, R., Dlugokencky, E. J., Fraser, P. J., Krummel, P. B., Langenfelds, R. L., O'Doherty, S., Prinn, R. G., Steele, L. P., van der Schoot, M., and Weiss, R. F.: Estimating regional methane surface fluxes: the relative importance of surface and GOSAT mole fraction measurements, Atmospheric Chemistry and Physics, 13, 5697–5713, doi:10.5194/acp-13-5697-2013, 2013.

Fung, I., John, J., Lerner, J., Matthews, E., Prather, M., Steele, L. P., and Fraser, P. J.: Three-dimensional model synthesis of the global methane cycle, Journal of Geophysical Research: Atmospheres, 96, 13 033–13 065, doi:10.1029/91JD01247, 1991.

Gambacorta, A., Barnet, C., Smith, N., Pierce, R., Smith, J., Spackman, J., and Goldberg, M.: The NPP and J1 NOAA Unique Combined Atmospheric Processing System (NUCAPS) for atmospheric thermal sounding: recent algorithm enhancements tailored to near real time users applications., in: AGU Fall Meeting Abstracts, 2016.

Garcia, R. R. and Boville, B. A.: "Downward Control" of the Mean Meridional Circulation and Temperature Distribution of the Polar Winter Stratosphere, Journal of the Atmospheric Sciences, 51, 2238–2245, doi:10.1175/1520-0469(1994)051<2238:COTMMC>2.0.CO;2, 1994.

Garstang, M., Tyson, P. D., Swap, R., Edwards, M., Kållberg, P., and Lindesay, J. A.: Horizontal and vertical transport of air over southern Africa, Journal of Geophysical Research: Atmospheres, 101, 23 721–23 736, doi:10.1029/95JD00844, 1996.

Giering, R. and Kaminski, T.: Recipes for Adjoint Code Construction, ACM Transactions on Mathematical Software, 24, 437–474, doi:10.1145/293686.293695, 1998.

Grell, G. and Baklanov, A.: Integrated modeling for forecasting weather and air quality: A call for fully coupled approaches, Atmospheric Environment, 45, 6845 – 6851, doi:https://doi.org/10.1016/j.atmosenv.2011.01.017, modeling of Air Quality Impacts, Forecasting and Interactions with Climate., 2011.

Griffith, D. W. T., Velazco, V. A., Deutscher, N., Murphy, C., Jones, N., Wilson, S., Macatangay, R., Kettlewell, G., Buchholz, R. R., and Riggenbach., M.: TCCON

data from Wollongong, Australia, Release GGG2014.R0, doi:10.14291/tccon.ggg2014.wollongong01.R0/1149291, 2017.

Gurney, K. R., Law, R. M., Denning, A. S., Rayner, P. J., Pak, B. C., Baker, D., Bousquet, P., Bruhwiler, L., Chen, Y.-H., Ciais, P., Fung, I. Y., Heimann, M., John, J., Maki, T., Maksyutov, S., Peylin, P., Prather, M., and Taguchi, S.: Transcom 3 inversion intercomparison: Model mean results for the estimation of seasonal carbon sources and sinks, Global Biogeochemical Cycles, 18, doi:10.1029/2003GB002111, 2004.

Hanel, R. A., Schlachman, B., Rogers, D., and Vanous, D.: Nimbus 4 Michelson Interferometer, Applied Optics, 10, 1376–1382, doi:10.1364/AO.10.001376, 1971.

Hase, F. a. T. B., Dohe, S., Gross, J., and Kiel., M.: TCCON data from Karlsruhe, Germany, Release GGG2014.R0, doi:10.14291/tccon.ggg2014.karlsruhe01.R0/1149270, 2017.

Haynes, P., Scinocca, J., and Greenslade, M.: Formation and maintenance of the extratropical tropopause by baroclinic eddies, Geophysical Research Letters, 28, 4179–4182, doi:10.1029/2001GL013485, 2001.

Henze, D. K., Hakami, A., and Seinfeld, J. H.: Development of the adjoint of GEOS-Chem, Atmospheric Chemistry and Physics, 7, 2413–2433, doi:10.5194/acp-7-2413-2007, 2007.

Hess, P. G.: A comparison of two paradigms: The relative global roles of moist convective versus nonconvective transport, Journal of Geophysical Research: Atmospheres, 110, doi:10.1029/2004JD005456, 2005.

Hewson, W., Bösch, H., and Parker, R.: ESA Climate Change Initiative (CCI) Comprehensive Error Characterisation Report: University of Leicester proxy retrieval algorithm for XCH_4 CRDP-OCPR v5.2, 2015.

Holtslag, A. A. M. and Boville, B. A.: Local Versus Nonlocal Boundary-Layer Diffusion in a Global Climate Model, Journal of Climate, 6, 1825–1842, doi:10.1175/1520-0442(1993)006<1825:LVNBLD>2.0.CO;2, 1993.

Hopcroft, P. O., Valdes, P. J., and Beerling, D. J.: Simulating idealized Dansgaard-Oeschger events and their potential impacts on the global methane cycle, Quaternary Science Reviews, 30, 3258–3268, doi:https://doi.org/10.1016/j.quascirev.2011.08.012, 2011.

Houweling, S., Aben, I., Breon, F.-M., Chevallier, F., Deutscher, N., Engelen, R., Gerbig, C., Griffith, D., Hungershoefer, K., Macatangay, R., Marshall, J., Notholt, J., Peters, W., and Serrar, S.: The importance of transport model uncertainties for the estimation of CO_2 sources and sinks using satellite measurements, Atmospheric Chemistry and Physics, 10, 9981–9992, doi:10.5194/acp-10-9981-2010, 2010.

Houweling, S., Krol, M., Bergamaschi, P., Frankenberg, C., Dlugokencky, E. J., Morino, I., Notholt, J., Sherlock, V., Wunch, D., Beck, V., Gerbig, C., Chen, H., Kort, E. A., Röckmann, T., and Aben, I.: A multi-year methane inversion using SCIAMACHY, accounting for systematic errors using TCCON measurements, Atmospheric Chemistry and Physics, 14, 3991–4012, doi:10.5194/acp-14-3991-2014, 2014.

Houweling, S., Baker, D., Basu, S., Boesch, H., Butz, A., Chevallier, F., Deng, F., Dlugokencky, E. J., Feng, L., Ganshin, A., Hasekamp, O., Jones, D., Maksyutov, S., Marshall, J., Oda, T., O'Dell, C. W., Oshchepkov, S., Palmer, P. I., Peylin, P., Poussi, Z., Reum, F., Takagi, H., Yoshida, Y., and Zhuravlev, R.: An intercomparison of inverse models for estimating sources and sinks of CO_2 using GOSAT measurements, Journal of Geophysical Research: Atmospheres, 120, 5253–5266, doi:10.1002/2014JD022962, 2014JD022962, 2015.

Huynh, H. T.: Schemes and constraints for advection, in: Fifteenth International Conference on Numerical Methods in Fluid Dynamics: Proceedings of the Conference Held in Monterey, CA, USA, 24–28 June 1996, pp. 498–503, Springer Berlin Heidelberg, doi:10.1007/BFb0107151, 1997.

Jablonowski, C. and Williamson, D. L.: A baroclinic instability test case for atmospheric model dynamical cores, Quarterly Journal of the Royal Meteorological Society, 132, 2943–2975, doi:10.1256/qj.06.12, 2006.

Jablonowski, C. and Williamson, D. L.: The pros and cons of diffusion, filters and fixers in atmospheric general circulation models, in: Numerical Techniques for Global Atmospheric Models, pp. 381–493, Springer, doi:10.1007/978-3-642-11640-7_13, 2011.

Jacob, D.: Introduction to Atmospheric Chemistry, Princeton University Press, 1999.

Jacob, D. J., Prather, M. J., Rasch, P. J., Shia, R.-L., Balkanski, Y. J., Beagley, S. R., Bergmann, D. J., Blackshear, W. T., Brown, M., Chiba, M., Chipperfield, M. P., de Grandpré, J., Dignon, J. E., Feichter, J., Genthon, C., Grose, W. L., Kasibhatla, P. S., Köhler, I., Kritz, M. A., Law, K., Penner, J. E., Ramonet, M., Reeves, C. E.,

Rotman, D. A., Stockwell, D. Z., Van Velthoven, P. F. J., Verver, G., Wild, O., Yang, H., and Zimmermann, P.: Evaluation and intercomparison of global atmospheric transport models using ^{222}Rn and other short-lived tracers, Journal of Geophysical Research: Atmospheres, 102, 5953–5970, doi:10.1029/96JD02955, 1997.

Jiang, Z., Jones, D. B. A., Kopacz, M., Liu, J., Henze, D. K., and Heald, C.: Quantifying the impact of model errors on top-down estimates of carbon monoxide emissions using satellite observations, Journal of Geophysical Research: Atmospheres, 116, doi: 10.1029/2010JD015282, d15306, 2011.

Jiang, Z., Jones, D. B. A., Worden, J., Worden, H. M., Henze, D. K., and Wang, Y. X.: Regional data assimilation of multi-spectral MOPITT observations of CO over North America, Atmospheric Chemistry and Physics, 15, 6801–6814, doi:10.5194/ acp-15-6801-2015, 2015.

Jöckel, P., von Kuhlmann, R., Lawrence, M. G., Steil, B., Brenninkmeijer, C. A. M., Crutzen, P. J., Rasch, P. J., and Eaton, B.: On a fundamental problem in implementing flux-form advection schemes for tracer transport in 3-dimensional general circulation and chemistry transport models, Quarterly Journal of the Royal Meteorological Society, 127, 1035–1052, doi:10.1002/qj.49712757318, 2001.

Jouzel, J., Masson-Delmotte, V., Cattani, O., Dreyfus, G., Falourd, S., Hoffmann, G., Minster, B., Nouet, J., Barnola, J. M., Chappellaz, J., Fischer, H., Gallet, J. C., Johnsen, S., Leuenberger, M., Loulergue, L., Luethi, D., Oerter, H., Parrenin, F., Raisbeck, G., Raynaud, D., Schilt, A., Schwander, J., Selmo, E., Souchez, R., Spahni, R., Stauffer, B., Steffensen, J. P., Stenni, B., Stocker, T. F., Tison, J. L., Werner, M., and Wolff, E. W.: Orbital and Millennial Antarctic Climate Variability over the Past 800,000 Years, Science, 317, 793–796, doi:10.1126/science.1141038, 2007.

Kai, F. M., Tyler, S. C., Randerson, J. T., and Blake, D. R.: Reduced methane growth rate explained by decreased Northern Hemisphere microbial sources, Nature, 476, 194–197, 2011.

Kalnay, E.: Atmospheric modeling, data assimilation and predictability, Cambridge University Press, 2003.

Kaplan, J. O.: Wetlands at the Last Glacial Maximum: Distribution and methane emissions, Geophysical Research Letters, 29, 31–34, doi:10.1029/2001GL013366, 2002.

Kasting, J. F.: Methane and climate during the Precambrian era, Precambrian Research, 137, 119–129, doi:https://doi.org/10.1016/j.precamres.2005.03.002, 2005.

Katz, M. E., Pak, D. K., Dickens, G. R., and Miller, K. G.: The Source and Fate of Massive Carbon Input During the Latest Paleocene Thermal Maximum, Science, 286, 1531–1533, doi:10.1126/science.286.5444.1531, 1999.

Keller, M.: Mitigating model error in CO emission estimation, Ph.D. thesis, University of Toronto (Canada), 2014.

Kennedy, M., Mrofka, D., and Von Der Borch, C.: Snowball Earth termination by destabilization of equatorial permafrost methane clathrate, Nature, 453, 642–645, doi:10.1038/nature06961, 2008.

Kent, J., Jablonowski, C., Whitehead, J. P., and Rood, R. B.: Assessing Tracer Transport Algorithms and the Impact of Vertical Resolution in a Finite-Volume Dynamical Core, Monthly Weather Review, 140, 1620–1638, doi:10.1175/MWR-D-11-00150.1, 2012.

Kiemle, C., Quatrevalet, M., Ehret, G., Amediek, A., Fix, A., and Wirth, M.: Sensitivity studies for a space-based methane lidar mission, Atmospheric Measurement Techniques, 4, 2195–2211, doi:10.5194/amt-4-2195-2011, 2011.

Kiemle, C., Kawa, S. R., Quatrevalet, M., and Browell, E. V.: Performance simulations for a spaceborne methane lidar mission, Journal of Geophysical Research: Atmospheres, 119, 4365–4379, doi:10.1002/2013JD021253, 2014.

Kivi, R., Heikkinen, P., and Kyro., E.: TCCON data from Sodankyla, Finland, Release GGG2014.R0, doi:10.14291/tccon.ggg2014.sodankyla01.R0/1149280, 2017.

Kopp, R. E., Kirschvink, J. L., Hilburn, I. A., and Nash, C. Z.: The Paleoproterozoic snowball Earth: A climate disaster triggered by the evolution of oxygenic photosynthesis, Proceedings of the National Academy of Sciences of the United States of America, 102, 11 131–11 136, doi:10.1073/pnas.0504878102, 2005.

Koster, R. D., Suarez, M. J., Ducharne, A., Stieglitz, M., and Kumar, P.: A catchment-based approach to modeling land surface processes in a general circulation model: 1. Model structure, Journal of Geophysical Research: Atmospheres, 105, 24 809–24 822, doi:10.1029/2000JD900327, 2000.

Kowol-Santen, J., Beekmann, M., Schmitgen, S., and Dewey, K.: Tracer analysis of transport from the boundary layer to the free troposphere, Geophysical Research Letters, 28, 2907–2910, doi:10.1029/2001GL012908, 2001.

Kuze, A., Suto, H., Nakajima, M., and Hamazaki, T.: Thermal and near infrared sensor for carbon observation Fourier-transform spectrometer on the Greenhouse Gases Observing Satellite for greenhouse gases monitoring, Applied Optics, 48, 6716–6733, doi:10.1364/AO.48.006716, 2009.

Kuze, A., Suto, H., Shiomi, K., Kawakami, S., Tanaka, M., Ueda, Y., Deguchi, A., Yoshida, J., Yamamoto, Y., Kataoka, F., Taylor, T. E., and Buijs, H. L.: Update on GOSAT TANSO-FTS performance, operations, and data products after more than 6 years in space, Atmospheric Measurement Techniques, 9, 2445–2461, doi:10.5194/amt-9-2445-2016, 2016.

Lal, D. and Peters, B.: Cosmic ray produced radioactivity on the earth, in: Kosmische Strahlung II/Cosmic Rays II, pp. 551–612, Springer, doi:10.1007/978-3-642-46079-1_7, 1967.

Lamarque, J.-F., Khattatov, B., Yudin, V., Edwards, D. P., Gille, J. C., Emmons, L. K., Deeter, M. N., Warner, J., Ziskin, D. C., Francis, G. L., Ho, S., Mao, D., Chen, J., and Drummond, J. R.: Application of a bias estimator for the improved assimilation of Measurements of Pollution in the Troposphere (MOPITT) carbon monoxide retrievals, Journal of Geophysical Research: Atmospheres, 109, doi:10.1029/2003JD004466, 2004.

Levine, J., Wolff, E., Hopcroft, P., and Valdes, P.: Controls on the tropospheric oxidizing capacity during an idealized Dansgaard-Oeschger event, and their implications for the rapid rises in atmospheric methane during the last glacial period, Geophysical Research Letters, 39, 2012.

Li, Q., Jacob, D. J., Park, R., Wang, Y., Heald, C. L., Hudman, R., Yantosca, R. M., Martin, R. V., and Evans, M.: North American pollution outflow and the trapping of convectively lifted pollution by upper-level anticyclone, Journal of Geophysical Research: Atmospheres, 110, doi:10.1029/2004JD005039, 2005.

Lin, J. C., Gerbig, C., Wofsy, S. C., Andrews, A. E., Daube, B. C., Davis, K. J., and Grainger, C. A.: A near-field tool for simulating the upstream influence of atmospheric observations: The Stochastic Time-Inverted Lagrangian Transport (STILT) model, Journal of Geophysical Research: Atmospheres, 108, doi:10.1029/2002JD003161, 2003.

Lin, J.-T. and McElroy, M. B.: Impacts of boundary layer mixing on pollutant vertical profiles in the lower troposphere: Implications to satellite remote sensing, Atmospheric Environment, 44, 1726–1739, doi:https://doi.org/10.1016/j.atmosenv.2010.02.009, 2010.

Lin, M., Holloway, T., Carmichael, G. R., and Fiore, A. M.: Quantifying pollution inflow and outflow over East Asia in spring with regional and global models, Atmospheric Chemistry and Physics, 10, 4221–4239, doi:10.5194/acp-10-4221-2010, 2010.

Lin, S.-J.: A "Vertically Lagrangian" Finite-Volume Dynamical Core for Global Models, Monthly Weather Review, 132, 2293–2307, doi:10.1175/1520-0493(2004)132<2293:AVLFDC>2.0.CO;2, 2004.

Lin, S.-J. and Rood, R. B.: Multidimensional Flux-Form Semi-Lagrangian Transport Schemes, Monthly Weather Review, 124, 2046–2070, doi:10.1175/1520-0493(1996)124<2046:MFFSLT>2.0.CO;2, 1996.

Liou, K.-N.: An introduction to atmospheric radiation, vol. 84, Academic Press, 2002.

Liu, H., Jacob, D. J., Bey, I., and Yantosca, R. M.: Constraints from ^{210}Pb and ^{7}Be on wet deposition and transport in a global three-dimensional chemical tracer model driven by assimilated meteorological fields, Journal of Geophysical Research: Atmospheres, 106, 12 109–12 128, doi:10.1029/2000JD900839, 2001.

Liu, H., Considine, D. B., Horowitz, L. W., Crawford, J. H., Rodriguez, J. M., Strahan, S. E., Damon, M. R., Steenrod, S. D., Xu, X., Kouatchou, J., Carouge, C., and Yantosca, R. M.: Using beryllium-7 to assess cross-tropopause transport in global models, Atmospheric Chemistry and Physics, 16, 4641–4659, doi:10.5194/acp-16-4641-2016, 2016.

Liu, J., Fung, I., Kalnay, E., and Kang, J.-S.: CO_2 transport uncertainties from the uncertainties in meteorological fields, Geophysical Research Letters, 38, doi:10.1029/2011GL047213, 2011.

Liu, J., Bowman, K. W., and Henze, D. K.: Source-receptor relationships of column-average CO_2 and implications for the impact of observations on flux inversions, Journal of Geophysical Research: Atmospheres, 120, 5214–5236, doi:10.1002/2014JD022914, 2015.

Locatelli, R., Bousquet, P., Chevallier, F., Fortems-Cheney, A., Szopa, S., Saunois, M., Agusti-Panareda, A., Bergmann, D., Bian, H., Cameron-Smith, P., Chipperfield, M. P., Gloor, E., Houweling, S., Kawa, S. R., Krol, M., Patra, P. K., Prinn, R. G., Rigby, M., Saito, R., and Wilson, C.: Impact of transport model errors on the global and regional methane emissions estimated by inverse modelling, Atmospheric Chemistry and Physics, 13, 9917–9937, doi:10.5194/acp-13-9917-2013, 2013.

Locatelli, R., Bousquet, P., Saunois, M., Chevallier, F., and Cressot, C.: Sensitivity of the recent methane budget to LMDz sub-grid-scale physical parameterizations, Atmospheric Chemistry and Physics, 15, 9765–9780, doi:10.5194/acp-15-9765-2015, 2015.

Lock, A. P., Brown, A. R., Bush, M. R., Martin, G. M., and Smith, R. N. B.: A New Boundary Layer Mixing Scheme. Part I: Scheme Description and Single-Column Model Tests, Monthly Weather Review, 128, 3187–3199, doi:10.1175/1520-0493(2000)128<3187:ANBLMS>2.0.CO;2, 2000.

Louis, J., Tiedtke, M., and Geleyn, J.: A short history of the PBL parameterization at ECMWF, Proc. ECMWF Workshop on Planetary Boundary Layer Parameterization, Reading, United Kingdom, ECMWF, 19, 59–80, 1982.

Loulergue, L., Schilt, A., Spahni, R., Masson-Delmotte, V., Blunier, T., Lemieux, B., Barnola, J.-M., Raynaud, D., Stocker, T. F., and Chappellaz, J.: Orbital and millennial-scale features of atmospheric CH_4 over the past 800,000 years, Nature, 453, 383, 2008.

McFarlane, N. A.: The Effect of Orographically Excited Gravity Wave Drag on the General Circulation of the Lower Stratosphere and Troposphere, Journal of the Atmospheric Sciences, 44, 1775–1800, doi:10.1175/1520-0469(1987)044<1775:TEOOEG>2.0.CO;2, 1987.

McNorton, J., Chipperfield, M. P., Gloor, M., Wilson, C., Feng, W., Hayman, G. D., Rigby, M., Krummel, P. B., O'Doherty, S., Prinn, R. G., Weiss, R. F., Young, D., Dlugokencky, E., and Montzka, S. A.: Role of OH variability in the stalling of the global atmospheric CH_4 growth rate from 1999 to 2006, Atmospheric Chemistry and Physics, 16, 7943–7956, doi:10.5194/acp-16-7943-2016, 2016.

Meirink, J. F., Bergamaschi, P., Frankenberg, C., d'Amelio, M. T. S., Dlugokencky, E. J., Gatti, L. V., Houweling, S., Miller, J. B., Röckmann, T., Villani, M. G., and Krol, M. C.: Four-dimensional variational data assimilation for inverse modeling of atmospheric methane emissions: Analysis of SCIAMACHY observations, Journal of Geophysical Research: Atmospheres, 113, doi:10.1029/2007JD009740, 2008.

Mitchell, L. E., Brook, E. J., Sowers, T., McConnell, J. R., and Taylor, K.: Multidecadal variability of atmospheric methane, 1000–1800 C.E., Journal of Geophysical Research: Biogeosciences, 116, doi:10.1029/2010JG001441, 2011.

Monge-Sanz, B. M., Chipperfield, M. P., Dee, D. P., Simmons, A. J., and Uppala, S. M.: Improvements in the stratospheric transport achieved by a chemistry transport model

with ECMWF (re)analyses: identifying effects and remaining challenges, Quarterly Journal of the Royal Meteorological Society, 139, 654–673, doi:10.1002/qj.1996, 2013.

Monteil, G., Houweling, S., Butz, A., Guerlet, S., Schepers, D., Hasekamp, O., Frankenberg, C., Scheepmaker, R., Aben, I., and Röckmann, T.: Comparison of CH_4 inversions based on 15 months of GOSAT and SCIAMACHY observations, Journal of Geophysical Research: Atmospheres, 118, 11,807–11,823, doi:10.1002/2013JD019760, 2013.

Montzka, S. A., Krol, M., Dlugokencky, E., Hall, B., Jöckel, P., and Lelieveld, J.: Small Interannual Variability of Global Atmospheric Hydroxyl, Science, 331, 67–69, 2011.

Moorthi, S. and Suarez, M. J.: Relaxed Arakawa-Schubert. A Parameterization of Moist Convection for General Circulation Models, Monthly Weather Review, 120, 978–1002, doi:10.1175/1520-0493(1992)120<0978:RASAPO>2.0.CO;2, 1992.

Mu, M., Randerson, J. T., van der Werf, G. R., Giglio, L., Kasibhatla, P., Morton, D., Collatz, G. J., DeFries, R. S., Hyer, E. J., Prins, E. M., Griffith, D. W. T., Wunch, D., Toon, G. C., Sherlock, V., and Wennberg, P. O.: Daily and 3-hourly variability in global fire emissions and consequences for atmospheric model predictions of carbon monoxide, Journal of Geophysical Research: Atmospheres, 116, doi:10.1029/2011JD016245, 2011.

Murray, L. T., Jacob, D. J., Logan, J. A., Hudman, R. C., and Koshak, W. J.: Optimized regional and interannual variability of lightning in a global chemical transport model constrained by LIS/OTD satellite data, Journal of Geophysical Research: Atmospheres, 117, doi:10.1029/2012JD017934, 2012.

Myhre, G., Shindell, D., Bréon, F.-M., Collins, W., Fuglestvedt, J., Huang, J., Koch, D., Lamarque, J.-F., Lee, D., Mendoza, B., et al.: Anthropogenic and natural radiative forcing, Climate change 2013: The Physical Science Basis. Contribution of Working Group I to the Fifth Assessment Report of the Intergovernmental Panel on Climate Change, pp. 658–740, 2013.

Nakajima, M., Yajima, Y., Hashimoto, M., Shiomi, K., Suto, H., and Imai, H.: The current status of the mission instruments of GOSAT-2, in: EGU General Assembly Conference Abstracts, vol. 19 of *EGU General Assembly Conference Abstracts*, p. 11324, 2017.

Natraj, V., Boesch, H., Spurr, R. J. D., and Yung, Y. L.: Retrieval of from simulated Orbiting Carbon Observatory measurements using the fast linearized R-2OS radiative

transfer model, Journal of Geophysical Research: Atmospheres, 113, doi:10.1029/2007JD009017, 2008.

Nisbet, E. G., Dlugokencky, E. J., Manning, M. R., Lowry, D., Fisher, R. E., France, J. L., Michel, S. E., Miller, J. B., White, J. W. C., Vaughn, B., Bousquet, P., Pyle, J. A., Warwick, N. J., Cain, M., Brownlow, R., Zazzeri, G., Lanoisellé, M., Manning, A. C., Gloor, E., Worthy, D. E. J., Brunke, E., Labuschagne, C., Wolff, E. W., and Ganesan, A. L.: Rising atmospheric methane: 2007–2014 growth and isotopic shift, Global Biogeochemical Cycles, 30, 1356–1370, doi:10.1002/2016GB005406, 2016.

Notholt, J., Petri, C., Warneke, T., Deutscher, N., Buschmann, M., Weinzierl, C., Macatangay, R., and Grupe., P.: TCCON data from Bremen, Germany, Release GGG2014.R0, doi:10.14291/tccon.ggg2014.bremen01.R0/1149275, 2017.

O'Dell, C. W., Connor, B., Bösch, H., O'Brien, D., Frankenberg, C., Castano, R., Christi, M., Eldering, D., Fisher, B., Gunson, M., McDuffie, J., Miller, C. E., Natraj, V., Oyafuso, F., Polonsky, I., Smyth, M., Taylor, T., Toon, G. C., Wennberg, P. O., and Wunch, D.: The ACOS CO_2 retrieval algorithm – Part 1: Description and validation against synthetic observations, Atmospheric Measurement Techniques, 5, 99–121, doi:10.5194/amt-5-99-2012, 2012.

Olsen, K. S., Strong, K., Walker, K. A., Boone, C. D., Raspollini, P., Plieninger, J., Bader, W., Conway, S., Grutter, M., Hannigan, J. W., Hase, F., Jones, N., de Mazière, M., Notholt, J., Schneider, M., Smale, D., Sussmann, R., and Saitoh, N.: Comparison of the GOSAT TANSO-FTS TIR CH_4 volume mixing ratio vertical profiles with those measured by ACE-FTS, ESA MIPAS, IMK-IAA MIPAS, and 16 NDACC stations, Atmospheric Measurement Techniques, 10, 3697–3718, doi:10.5194/amt-10-3697-2017, 2017.

Olson, S. L., Reinhard, C. T., and Lyons, T. W.: Limited role for methane in the mid-Proterozoic greenhouse, Proceedings of the National Academy of Sciences, 113, 11 447–11 452, doi:10.1073/pnas.1608549113, 2016.

Orbe, C., Waugh, D. W., Yang, H., Lamarque, J.-F., Tilmes, S., and Kinnison, D. E.: Tropospheric transport differences between models using the same large-scale meteorological fields, Geophysical Research Letters, 44, 1068–1078, doi:10.1002/2016GL071339, 2017.

Ostler, A., Sussmann, R., Rettinger, M., Deutscher, N. M., Dohe, S., Hase, F., Jones, N., Palm, M., and Sinnhuber, B.-M.: Multistation intercomparison of column-averaged

methane from NDACC and TCCON: impact of dynamical variability, Atmospheric Measurement Techniques, 7, 4081–4101, doi:10.5194/amt-7-4081-2014, 2014.

Ostler, A., Sussmann, R., Patra, P. K., Houweling, S., De Bruine, M., Stiller, G. P., Haenel, F. J., Plieninger, J., Bousquet, P., Yin, Y., Saunois, M., Walker, K. A., Deutscher, N. M., Griffith, D. W. T., Blumenstock, T., Hase, F., Warneke, T., Wang, Z., Kivi, R., and Robinson, J.: Evaluation of column-averaged methane in models and TCCON with a focus on the stratosphere, Atmospheric Measurement Techniques, 9, 4843–4859, doi:10.5194/amt-9-4843-2016, 2016.

Parazoo, N. C., Denning, A. S., Berry, J. A., Wolf, A., Randall, D. A., Kawa, S. R., Pauluis, O., and Doney, S. C.: Moist synoptic transport of CO_2 along the mid-latitude storm track, Geophysical Research Letters, 38, doi:10.1029/2011GL047238, 2011.

Park, R. J., Jacob, D. J., Field, B. D., Yantosca, R. M., and Chin, M.: Natural and transboundary pollution influences on sulfate-nitrate-ammonium aerosols in the United States: Implications for policy, Journal of Geophysical Research: Atmospheres, 109, doi:10.1029/2003JD004473, 2004.

Parker, R. and GHG-CCI group: ESA Climate Change Initiative (CCI) Algorithm Theoretical Basis Document Version 5 (ATBDv5) - The University of Leicester Full-Physics Retrieval Algorithm for the retrieval of XCO_2 and XCH_4, 2016.

Parker, R., Boesch, H., Cogan, A., Fraser, A., Feng, L., Palmer, P. I., Messerschmidt, J., Deutscher, N., Griffith, D. W. T., Notholt, J., Wennberg, P. O., and Wunch, D.: Methane observations from the Greenhouse Gases Observing SATellite: Comparison to ground-based TCCON data and model calculations, Geophysical Research Letters, 38, doi:10.1029/2011GL047871, 2011.

Parker, R. J., Boesch, H., Byckling, K., Webb, A. J., Palmer, P. I., Feng, L., Bergamaschi, P., Chevallier, F., Notholt, J., Deutscher, N., Warneke, T., Hase, F., Sussmann, R., Kawakami, S., Kivi, R., Griffith, D. W. T., and Velazco, V.: Assessing 5 years of GOSAT Proxy XCH_4 data and associated uncertainties, Atmospheric Measurement Techniques, 8, 4785–4801, doi:10.5194/amt-8-4785-2015, 2015.

Patra, P. K., Houweling, S., Krol, M., Bousquet, P., Belikov, D., Bergmann, D., Bian, H., Cameron-Smith, P., Chipperfield, M. P., Corbin, K., Fortems-Cheiney, A., Fraser, A., Gloor, E., Hess, P., Ito, A., Kawa, S. R., Law, R. M., Loh, Z., Maksyutov, S., Meng, L., Palmer, P. I., Prinn, R. G., Rigby, M., Saito, R., and Wilson, C.: TransCom model

simulations of CH_4 and related species: linking transport, surface flux and chemical loss with CH_4 variability in the troposphere and lower stratosphere, Atmospheric Chemistry and Physics, 11, 12 813–12 837, doi:10.5194/acp-11-12813-2011, 2011.

Pauluis, O., Czaja, A., and Korty, R.: The global atmospheric circulation on moist isentropes, Science, 321, 1075–1078, doi:10.1126/science.1159649, 2008.

Pawson, S., Stajner, I., Kawa, S. R., Hayashi, H., Tan, W.-W., Nielsen, J. E., Zhu, Z., Chang, L.-P., and Livesey, N. J.: Stratospheric transport using 6-h-averaged winds from a data assimilation system, Journal of Geophysical Research: Atmospheres, 112, doi:10.1029/2006JD007673, 2007.

Pickett-Heaps, C. A., Jacob, D. J., Wecht, K. J., Kort, E. A., Wofsy, S. C., Diskin, G. S., Worthy, D. E. J., Kaplan, J. O., Bey, I., and Drevet, J.: Magnitude and seasonality of wetland methane emissions from the Hudson Bay Lowlands (Canada), Atmospheric Chemistry and Physics, 11, 3773–3779, doi:10.5194/acp-11-3773-2011, 2011.

Polavarapu, S. M., Neish, M., Tanguay, M., Girard, C., de Grandpré, J., Semeniuk, K., Gravel, S., Ren, S., Roche, S., Chan, D., and Strong, K.: Greenhouse gas simulations with a coupled meteorological and transport model: the predictability of CO_2, Atmospheric Chemistry and Physics, 16, 12 005–12 038, doi:10.5194/acp-16-12005-2016, 2016.

Polonsky, I. N., O'Brien, D. M., Kumer, J. B., O'Dell, C. W., and the geoCARB Team: Performance of a geostationary mission, geoCARB, to measure CO_2, CH_4 and CO column-averaged concentrations, Atmospheric Measurement Techniques, 7, 959–981, doi:10.5194/amt-7-959-2014, 2014.

Prather, M. J.: Numerical advection by conservation of second-order moments, Journal of Geophysical Research: Atmospheres, 91, 6671–6681, doi:10.1029/JD091iD06p06671, 1986.

Prather, M. J., Zhu, X., Strahan, S. E., Steenrod, S. D., and Rodriguez, J. M.: Quantifying errors in trace species transport modeling, Proceedings of the National Academy of Sciences, 105, 19 617–19 621, doi:10.1073/pnas.0806541106, 2008.

Prather, M. J., Holmes, C. D., and Hsu, J.: Reactive greenhouse gas scenarios: Systematic exploration of uncertainties and the role of atmospheric chemistry, Geophysical Research Letters, 39, doi:10.1029/2012GL051440, 2012.

Rice, A. L., Butenhoff, C. L., Teama, D. G., Röger, F. H., Khalil, M. A. K., and Rasmussen, R. A.: Atmospheric methane isotopic record favors fossil sources flat in 1980s and 1990s with recent increase, Proceedings of the National Academy of Sciences, 113, 10 791–10 796, doi:10.1073/pnas.1522923113, 2016.

Richter, J. H., Solomon, A., and Bacmeister, J. T.: Effects of vertical resolution and nonorographic gravity wave drag on the simulated climate in the Community Atmosphere Model, version 5, Journal of Advances in Modeling Earth Systems, 6, 357–383, doi:10.1002/2013MS000303, 2014.

Rienecker, M., Suarez, M., Todling, R., Bacmeister, J., Takacs, L., Liu, H.-C., Gu, W., Sienkiewicz, M., Koster, R., Gelaro, R., et al.: The GEOS-5 Data Assimilation System—Documentation of Versions 5.0.1, 5.1.0, and 5.2.0. NASA Technical Report Series on Global Modelling and Data Assimilation, 27, 1–118, 2008.

Rigby, M., Montzka, S. A., Prinn, R. G., White, J. W. C., Young, D., O'Doherty, S., Lunt, M. F., Ganesan, A. L., Manning, A. J., Simmonds, P. G., Salameh, P. K., Harth, C. M., Mühle, J., Weiss, R. F., Fraser, P. J., Steele, L. P., Krummel, P. B., McCulloch, A., and Park, S.: Role of atmospheric oxidation in recent methane growth, Proceedings of the National Academy of Sciences, 114, 5373–5377, doi:10.1073/pnas.1616426114, 2017.

Rind, D., Lerner, J., Jonas, J., and McLinden, C.: Effects of resolution and model physics on tracer transports in the NASA Goddard Institute for Space Studies general circulation models, Journal of Geophysical Research: Atmospheres, 112, doi:10.1029/2006JD007476, 2007.

Rodgers, C. D.: Inverse methods for atmospheric sounding: theory and practice, vol. 2, World Scientific, 2000.

Roeckner, E., Brokopf, R., Esch, M., Giorgetta, M., Hagemann, S., Kornblueh, L., Manzini, E., Schlese, U., and Schulzweida, U.: Sensitivity of Simulated Climate to Horizontal and Vertical Resolution in the ECHAM5 Atmosphere Model, Journal of Climate, 19, 3771–3791, doi:10.1175/JCLI3824.1, 2006.

Rothman, L., Jacquemart, D., Barbe, A., Benner, D. C., Birk, M., Brown, L., Carleer, M., Chackerian, C., Chance, K., Coudert, L., Dana, V., Devi, V., Flaud, J.-M., Gamache, R., Goldman, A., Hartmann, J.-M., Jucks, K., Maki, A., Mandin, J.-Y., Massie, S., Orphal, J., Perrin, A., Rinsland, C., Smith, M., Tennyson, J., Tolchenov, R., Toth, R., Auwera,

J. V., Varanasi, P., and Wagner, G.: The HITRAN 2004 molecular spectroscopic database, Journal of Quantitative Spectroscopy and Radiative Transfer, 96, 139–204, doi:https://doi.org/10.1016/j.jqsrt.2004.10.008, 2005.

Rotman, D. A., Atherton, C. S., Bergmann, D. J., Cameron-Smith, P. J., Chuang, C. C., Connell, P. S., Dignon, J. E., Franz, A., Grant, K. E., Kinnison, D. E., Molenkamp, C. R., Proctor, D. D., and Tannahill, J. R.: IMPACT, the LLNL 3-D global atmospheric chemical transport model for the combined troposphere and stratosphere: Model description and analysis of ozone and other trace gases, Journal of Geophysical Research: Atmospheres, 109, doi:10.1029/2002JD003155, 2004.

Saad, K. M., Wunch, D., Deutscher, N. M., Griffith, D. W. T., Hase, F., De Mazière, M., Notholt, J., Pollard, D. F., Roehl, C. M., Schneider, M., Sussmann, R., Warneke, T., and Wennberg, P. O.: Seasonal variability of stratospheric methane: implications for constraining tropospheric methane budgets using total column observations, Atmospheric Chemistry and Physics, 16, 14 003–14 024, doi:10.5194/acp-16-14003-2016, 2016.

Santoni, G. W., Daube, B. C., Kort, E. A., Jiménez, R., Park, S., Pittman, J. V., Gottlieb, E., Xiang, B., Zahniser, M. S., Nelson, D. D., McManus, J. B., Peischl, J., Ryerson, T. B., Holloway, J. S., Andrews, A. E., Sweeney, C., Hall, B., Hintsa, E. J., Moore, F. L., Elkins, J. W., Hurst, D. F., Stephens, B. B., Bent, J., and Wofsy, S. C.: Evaluation of the airborne quantum cascade laser spectrometer (QCLS) measurements of the carbon and greenhouse gas suite – CO_2, CH_4, N_2O, and CO – during the CalNex and HIPPO campaigns, Atmospheric Measurement Techniques, 7, 1509–1526, doi:10.5194/amt-7-1509-2014, 2014.

Sasaki, Y.: Some basic formalisms in numerical variational analysis, Monthly Weather Review, 98, 875–883, doi:10.1175/1520-0493(1970)098<0875:SBFINV>2.3.CO;2, 1970.

Saunois, M., Bousquet, P., Poulter, B., Peregon, A., Ciais, P., Canadell, J. G., Dlugokencky, E. J., Etiope, G., Bastviken, D., Houweling, S., et al.: The global methane budget 2000-2012, Earth System Science Data, 8, 697, 2016a.

Saunois, M., Jackson, R. B., Bousquet, P., Poulter, B., and Canadell, J. G.: The growing role of methane in anthropogenic climate change, Environmental Research Letters, 11, 120 207, 2016b.

Schaefer, H., Fletcher, S. E. M., Veidt, C., Lassey, K. R., Brailsford, G. W., Bromley, T. M., Dlugokencky, E. J., Michel, S. E., Miller, J. B., Levin, I., Lowe, D. C., Martin,

R. J., Vaughn, B. H., and White, J. W. C.: A 21st-century shift from fossil-fuel to biogenic methane emissions indicated by 13CH4, Science, 352, 80–84, doi:10.1126/science.aad2705, 2016.

Scheele, M. P., Siegmund, P. C., and Velthoven, P. F. J.: Stratospheric age of air computed with trajectories based on various 3D-Var and 4D-Var data sets, Atmospheric Chemistry and Physics, 5, 1–7, doi:10.5194/acp-5-1-2005, 2005.

Schneising, O., Buchwitz, M., Reuter, M., Heymann, J., Bovensmann, H., and Burrows, J. P.: Long-term analysis of carbon dioxide and methane column-averaged mole fractions retrieved from SCIAMACHY, Atmospheric Chemistry and Physics, 11, 2863–2880, doi:10.5194/acp-11-2863-2011, 2011.

Schuur, E., McGuire, A. D., Schädel, C., Grosse, G., Harden, J., Hayes, D., Hugelius, G., Koven, C., Kuhry, P., Lawrence, D., et al.: Climate change and the permafrost carbon feedback, Nature, 520, 171–179, doi:10.1038/nature14338, 2015.

Schwietzke, S., Sherwood, O. A., Bruhwiler, L. M., Miller, J. B., Etiope, G., Dlugokencky, E. J., Michel, S. E., Arling, V. A., Vaughn, B. H., White, J. W., et al.: Upward revision of global fossil fuel methane emissions based on isotope database, Nature, 538, 88, doi:10.1038/nature19797, 2016.

Searle, K. R., Chipperfield, M. P., Bekki, S., and Pyle, J. A.: The impact of spatial averaging on calculated polar ozone loss: 2. Theoretical analysis, Journal of Geophysical Research: Atmospheres, 103, 25 409–25 416, doi:10.1029/98JD02089, 1998.

Segers, A., van Velthoven, P., Bregman, B., and Krol, M.: On the computation of mass fluxes for Eulerian transport models from spectral meteorological fields, Computational Science—ICCS 2002, pp. 767–776, 2002.

Severinghaus, J. P. and Brook, E. J.: Abrupt climate change at the end of the last glacial period inferred from trapped air in polar ice, Science, 286, 930–934, 1999.

Severinghaus, J. P., Sowers, T., Brook, E. J., Alley, R. B., and Bender, M. L.: Timing of abrupt climate change at the end of the Younger Dryas interval from thermally fractionated gases in polar ice, Nature, 391, 141, 1998.

Shaw, T., Baldwin, M., A. Barnes, E., Caballero, R., Garfinkel, C., Hwang, Y.-T., Li, C., A. O'Gorman, P., Rivière, G., R. Simpson, I., and Voigt, A.: Storm track processes and the opposing influences of climate change, Nature Geoscience, 9, 656–664, doi:10.1038/ngeo2783, 2016.

Sherlock, V., Connor, B., Robinson, J., Shiona, H., Smale, D., and Pollard., D.: TCCON data from Lauder, New Zealand, 125HR, Release GGG2014.R0, doi:10.14291/tccon.ggg2014.lauder02.R0/1149298, 2017.

Simpson, I. J., Andersen, M. P. S., Meinardi, S., Bruhwiler, L., Blake, N. J., Helmig, D., Rowland, F. S., and Blake, D. R.: Long-term decline of global atmospheric ethane concentrations and implications for methane, Nature, 488, 490, doi:10.1038/nature11342, 2012.

Sinclair, V. A., Gray, S. L., and Belcher, S. E.: Boundary-layer ventilation by baroclinic life cycles, Quarterly Journal of the Royal Meteorological Society, 134, 1409–1424, doi:10.1002/qj.293, 2008.

Stohl, A.: A 1-year Lagrangian "climatology" of airstreams in the northern hemisphere troposphere and lowermost stratosphere, Journal of Geophysical Research: Atmospheres, 106, 7263–7279, doi:10.1029/2000JD900570, 2001.

Stohl, A., Eckhardt, S., Forster, C., James, P., and Spichtinger, N.: On the pathways and timescales of intercontinental air pollution transport, Journal of Geophysical Research: Atmospheres, 107, ACH 6–1–ACH 6–17, doi:10.1029/2001JD001396, 2002.

Stohl, A., Wernli, H., James, P., Bourqui, M., Forster, C., Liniger, M. A., Seibert, P., and Sprenger, M.: A New Perspective of Stratosphere–Troposphere Exchange, Bulletin of the American Meteorological Society, 84, 1565–1573, doi:10.1175/BAMS-84-11-1565, 2003.

Stohl, A., Cooper, O. R., and James, P.: A Cautionary Note on the Use of Meteorological Analysis Fields for Quantifying Atmospheric Mixing, Journal of the Atmospheric Sciences, 61, 1446–1453, doi:10.1175/1520-0469(2004)061<1446:ACNOTU>2.0.CO;2, 2004.

Strahan, S. E. and Polansky, B. C.: Meteorological implementation issues in chemistry and transport models, Atmospheric Chemistry and Physics, 6, 2895–2910, doi:10.5194/acp-6-2895-2006, 2006.

Strahan, S. E., Duncan, B. N., and Hoor, P.: Observationally derived transport diagnostics for the lowermost stratosphere and their application to the GMI chemistry and transport model, Atmospheric Chemistry and Physics, 7, 2435–2445, doi:10.5194/acp-7-2435-2007, 2007.

Sussmann, R. and Rettinger., M.: TCCON data from Garmisch, Germany, Release GGG2014.R0, doi:10.14291/tccon.ggg2014.garmisch01.R0/1149299, 2017.

Sweeney, C., Karion, A., Wolter, S., Newberger, T., Guenther, D., Higgs, J. A., Andrews, A. E., Lang, P. M., Neff, D., Dlugokencky, E., Miller, J. B., Montzka, S. A., Miller, B. R., Masarie, K. A., Biraud, S. C., Novelli, P. C., Crotwell, M., Crotwell, A. M., Thoning, K., and Tans, P. P.: Seasonal climatology of CO2 across North America from aircraft measurements in the NOAA/ESRL Global Greenhouse Gas Reference Network, Journal of Geophysical Research: Atmospheres, 120, 5155–5190, doi:10.1002/2014JD022591, 2015.

Trémolet, Y.: Accounting for an imperfect model in 4D-Var, Quarterly Journal of the Royal Meteorological Society, 132, 2483–2504, doi:10.1256/qj.05.224, 2006.

Trémolet, Y.: Model-error estimation in 4D-Var, Quarterly Journal of the Royal Meteorological Society, 133, 1267–1280, doi:10.1002/qj.94, 2007.

Tukiainen, S., Railo, J., Laine, M., Hakkarainen, J., Kivi, R., Heikkinen, P., Chen, H., and Tamminen, J.: Retrieval of atmospheric CH_4 profiles from Fourier transform infrared data using dimension reduction and MCMC, Journal of Geophysical Research: Atmospheres, 121, 10,312–10,327, doi:10.1002/2015JD024657, 2016.

Turner, A. J., Jacob, D. J., Wecht, K. J., Maasakkers, J. D., Lundgren, E., Andrews, A. E., Biraud, S. C., Boesch, H., Bowman, K. W., Deutscher, N. M., Dubey, M. K., Griffith, D. W. T., Hase, F., Kuze, A., Notholt, J., Ohyama, H., Parker, R., Payne, V. H., Sussmann, R., Sweeney, C., Velazco, V. A., Warneke, T., Wennberg, P. O., and Wunch, D.: Estimating global and North American methane emissions with high spatial resolution using GOSAT satellite data, Atmospheric Chemistry and Physics, 15, 7049–7069, doi:10.5194/acp-15-7049-2015, 2015.

Turner, A. J., Frankenberg, C., Wennberg, P. O., and Jacob, D. J.: Ambiguity in the causes for decadal trends in atmospheric methane and hydroxyl, Proceedings of the National Academy of Sciences, doi:10.1073/pnas.1616020114, 2017.

van der Werf, G. R., Randerson, J. T., Giglio, L., Collatz, G. J., Mu, M., Kasibhatla, P. S., Morton, D. C., DeFries, R. S., Jin, Y., and van Leeuwen, T. T.: Global fire emissions and the contribution of deforestation, savanna, forest, agricultural, and peat fires (1997–2009), Atmospheric Chemistry and Physics, 10, 11 707–11 735, doi:10.5194/acp-10-11707-2010, 2010.

Veefkind, J., Aben, I., McMullan, K., Förster, H., de Vries, J., Otter, G., Claas, J., Eskes, H., de Haan, J., Kleipool, Q., van Weele, M., Hasekamp, O., Hoogeveen, R., Landgraf, J., Snel, R., Tol, P., Ingmann, P., Voors, R., Kruizinga, B., Vink, R., Visser, H., and Levelt, P.: TROPOMI on the ESA Sentinel-5 Precursor: A GMES mission for global observations of the atmospheric composition for climate, air quality and ozone layer applications, Remote Sensing of Environment, 120, 70–83, doi:http://dx.doi.org/10.1016/j.rse.2011.09.027, 2012.

von Clarmann, T., M., H., S., K., A., L., S., C., B., F., U., G., N., G., M., K., T., S., G.P., S., and S., V.: Retrieval of temperature, H_2O, O_3, HNO_3, CH_4, N_2O, $ClONO_2$ and ClO from MIPAS reduced resolution nominal mode limb emission measurements, Atmospheric Measurement Techniques, 2, 159–175, doi:10.5194/amt-2-159-2009, 2009.

Wang, Y. X., McElroy, M. B., Jacob, D. J., and Yantosca, R. M.: A nested grid formulation for chemical transport over Asia: Applications to CO, Journal of Geophysical Research: Atmospheres, 109, doi:10.1029/2004JD005237, 2004.

Warneke, T., Messerschmidt, J., Notholt, J., Weinzierl, C., Deutscher, N., Petri, C., Grupe, P., Vuillemin, C., Truong, F., Schmidt, M., Ramonet, M., and Parmentier., E.: TCCON data from Orleans, France, Release GGG2014.R0, doi:10.14291/tccon.ggg2014.orleans01.R0/1149276, 2017.

Waymark, C., Walker, K., Boone, C., and Bernath, P.: ACE-FTS version 3.0 data set: validation and data processing update, Annals of Geophysics, 56, doi:10.4401/ag-6339, 2014.

Wecht, K. J., Jacob, D. J., Wofsy, S. C., Kort, E. A., Worden, J. R., Kulawik, S. S., Henze, D. K., Kopacz, M., and Payne, V. H.: Validation of TES methane with HIPPO aircraft observations: implications for inverse modeling of methane sources, Atmospheric Chemistry and Physics, 12, 1823–1832, doi:10.5194/acp-12-1823-2012, 2012.

Wecht, K. J., Jacob, D. J., Frankenberg, C., Jiang, Z., and Blake, D. R.: Mapping of North American methane emissions with high spatial resolution by inversion of SCIAMACHY satellite data, Journal of Geophysical Research: Atmospheres, 119, 7741–7756, doi:10.1002/2014JD021551, 2014.

Wennberg, P. O., Roehl, C., Wunch, D., Toon, G. C., Blavier, J.-F., Washenfelder, R., Keppel-Aleks, G., Allen, N., and Ayers., J.: TCCON data from Park Falls, Wisconsin, USA, Release GGG2014.R0, doi:10.14291/tccon.ggg2014.parkfalls01.R0/1149161, 2017a.

Wennberg, P. O., Wunch, D., Roehl, C., Blavier, J.-F., Toon, G. C., Allen, N., Dowell, P., Teske, K., Martin, C., and Martin., J.: TCCON data from Lamont, Oklahoma, USA, Release GGG2014.R0, doi:10.14291/tccon.ggg2014.lamont01.R0/1149159, 2017b.

Whitehead, J. P., Jablonowski, C., Rood, R. B., and Lauritzen, P. H.: A Stability Analysis of Divergence Damping on a Latitude–Longitude Grid, Monthly Weather Review, 139, 2976–2993, doi:10.1175/2011MWR3607.1, 2011.

Wiacek, A., Taylor, J. R., Strong, K., Saari, R., Kerzenmacher, T. E., Jones, N. B., and Griffith, D. W. T.: Ground-Based Solar Absorption FTIR Spectroscopy: Characterization of Retrievals and First Results from a Novel Optical Design Instrument at a New NDACC Complementary Station, Journal of Atmospheric and Oceanic Technology, 24, 432–448, doi:10.1175/JTECH1962.1, 2007.

Wofsy, S. et al.: HIPPO Merged 10-Second Meteorology and Atmospheric Chemistry and Aerosol Data (R_20121129), Carbon Dioxide Information Analysis Center, Oak Ridge National Laboratory and Oak Ridge and Tennessee.[Avaialble at http://dx.doi.org/10.3334/CDIAC/hippo_010,(Release 20121129)], 2012.

Wofsy, S. C., Team, H. S., Modellers, C., and Teams, S.: HIAPER Pole-to-Pole Observations (HIPPO): fine-grained, global-scale measurements of climatically important atmospheric gases and aerosols, Philosophical Transactions: Mathematical, Physical and Engineering Sciences, 369, 2073–2086, 2011.

Worden, J., Kulawik, S., Frankenberg, C., Payne, V., Bowman, K., Cady-Peirara, K., Wecht, K., Lee, J.-E., and Noone, D.: Profiles of CH_4, HDO, H_2O, and N_2O with improved lower tropospheric vertical resolution from Aura TES radiances, Atmospheric Measurement Techniques, 5, 397–411, doi:10.5194/amt-5-397-2012, 2012.

Worden, J., Wecht, K., Frankenberg, C., Alvarado, M., Bowman, K., Kort, E., Kulawik, S., Lee, M., Payne, V., and Worden, H.: CH_4 and CO distributions over tropical fires during October 2006 as observed by the Aura TES satellite instrument and modeled by GEOS-Chem, Atmospheric Chemistry and Physics, 13, 3679–3692, doi:10.5194/acp-13-3679-2013, 2013.

Worthy, D. E. J., Platt, A., Kessler, R., Ernst, M., Braga, R., and Racki, S.: The Canadian atmospheric carbon dioxide measurement program: Measurement procedures, data quality and accuracy, In: Report of the 11th WMO/IAEA Meeting of Experts on Carbon Dioxide Concentration and Related Tracer Measurement Techniques, Tokyo,

Japan, September 2001, edited by: Toru, S. and Kazuto, S., World Meteorological Organization Global Atmosphere Watch, pp. 112–128, 2003.

Wunch, D., Toon, G. C., Blavier, J.-F. L., Washenfelder, R. A., Notholt, J., Connor, B. J., Griffith, D. W. T., Sherlock, V., and Wennberg, P. O.: The Total Carbon Column Observing Network, Philosophical Transactions of the Royal Society of London A: Mathematical, Physical and Engineering Sciences, 369, 2087–2112, doi:10.1098/rsta.2010.0240, 2011.

Wunch, D., Toon, G. C., Sherlock, V., Deutscher, N. M., Liu, C., Feist, D. G., and Wennberg, P. O.: The total carbon column observing network's GGG2014 data version, Carbon Dioxide Information Analysis Center, Oak Ridge National Laboratory, Oak Ridge, Tennessee, USA, 10, 2015.

Xiong, X., Barnet, C., Maddy, E., Sweeney, C., Liu, X., Zhou, L., and Goldberg, M.: Characterization and validation of methane products from the Atmospheric Infrared Sounder (AIRS), Journal of Geophysical Research: Biogeosciences, 113, doi:10.1029/2007JG000500, 2008.

Xiong, X., Barnet, C., Maddy, E. S., Gambacorta, A., King, T. S., and Wofsy, S. C.: Mid-upper tropospheric methane retrieval from IASI and its validation, Atmospheric Measurement Techniques, 6, 2255–2265, doi:10.5194/amt-6-2255-2013, 2013.

Yoshida, Y., Ota, Y., Eguchi, N., Kikuchi, N., Nobuta, K., Tran, H., Morino, I., and Yokota, T.: Retrieval algorithm for CO_2 and CH_4 column abundances from short-wavelength infrared spectral observations by the Greenhouse gases observing satellite, Atmospheric Measurement Techniques, 4, 717–734, doi:10.5194/amt-4-717-2011, 2011.

Yu, K., Keller, C. A., Jacob, D. J., Molod, A. M., Eastham, S. D., and Long, M. S.: Errors and improvements in the use of archived meteorological data for chemical transport modeling, Geoscientific Model Development Discussions, 2017, 1–22, doi:10.5194/gmd-2017-125, 2017.

Zahnle, K., Claire, M., and Catling, D.: The loss of mass-independent fractionation in sulfur due to a Palaeoproterozoic collapse of atmospheric methane, Geobiology, 4, 271–283, doi:10.1111/j.1472-4669.2006.00085.x, 2006.

Zhang, Z., Zimmermann, N. E., Stenke, A., Li, X., Hodson, E. L., Zhu, G., Huang, C., and Poulter, B.: Emerging role of wetland methane emissions in driving 21st century climate

change, Proceedings of the National Academy of Sciences, doi:10.1073/pnas.1618765114, 2017.

Zupanski, D.: A General Weak Constraint Applicable to Operational 4DVAR Data Assimilation Systems, Monthly Weather Review, 125, 2274–2292, doi:10.1175/1520-0493(1997)125<2274:AGWCAT>2.0.CO;2, 1997.